Characterizing Near-Surface Velocity and Attenuation Structures and Evaluating Spatiotemporal *b*-Value Variations in the Marmara Sea Region

DISSERTATION
zur Erlangung des akademischen Grades

Doktor der Naturwissenschaften
(Dr. rer. Nat.)

In der Wissenschaftsdisziplin Geophysik
eingereicht an der Geowissenschaftlichen Fakultät
der Freien Universität Berlin

vorgelegt von Christina Raub
Berlin, Januar 2017

Eidesstattliche Erklärung

Ich erkläre hiermit an Eides statt, dass ich die vorliegende Dissertation selbstständig und nur unter Verwendung der angegebenen Quellen und Hilfsmittel angefertigt habe.

Berlin, den 06.01.2017

Referent: Prof. Dr. Marco Bohnhoff

Korreferent: Prof. Dr. Frederik Tilmann

Datum der Disputation: 04.05.2017

Freie Universität Berlin

Fachbereich Geowissenschaften

Institut für Geologische Wissenschaften

Malteserstr. 74 – 100

12249 Berlin

Summary

The North Anatolian Fault Zone (NAFZ) is one of the most active fault zones in Eurasia. The NAFZ segment below the Sea of Marmara in northwestern Turkey is the only fault segment that did not rupture in the last century, and thus, poses a high seismic hazard to the city of Istanbul. One of the most ambitious goals of seismology is a realistic seismic hazard assessment. For this task a comprehensive understanding of all components involved in creating hazard is necessary. Most important is knowledge about 1) the geometry and kinematics of faults 2) recurrence models to predict future seismicity, and 3) a ground motion model to predict ground motions during a potential earthquake. To progress towards an improved knowledge about these points in the Istanbul metropolitan area this thesis comprises two main studies, one analyzing near-surface rock properties which strongly affect ground motions, and the other dealing with spatiotemporal b-value variations. The b-value describes the distribution of magnitudes in an earthquake catalog and is a standard parameter in recurrence models. Furthermore, the b-value is suggested to reflect the current state of stress on a fault.

Starting in Sep 2012 the GONAF (Geophysical Observatory of the North Anatolian Fault) network was installed around the eastern Sea of Marmara consisting of seven ~300 m deep boreholes. The first borehole was completed on the Tuzla peninsula, in southeast Istanbul. The borehole is equipped with seismometers at the surface and at 71, 144, 215, and 288 m depth. By analyzing the first seismic recordings from the GONAF-Tuzla borehole an earthquake swarm of ~100 microseismic events, overlooked by surface networks, was detected based on a cross-correlation algorithm. This is a promising sign from the new borehole observatory improving the seismic monitoring in the eastern Sea of Marmara.

The first main study of this thesis is based on a set of microseismicity recordings from the GONAF-Tuzla borehole. With deconvolution interferometry Green's functions of excellent signal-to-noise ratio were obtained. They reveal surface reflections, near-surface amplification, and reflections from a strong impedance contrast. To determine the velocity and attenuation (Q) structure below the Tuzla site the Green's functions were forward modeled in time domain. The determined quality factors Q need to be interpreted with care. Because of simplifications that were applied during the forward modeling procedure, the Q value here is an apparent value which is a mixture of impedance effects, and scattering and intrinsic attenuation. The seismic velocities of the P- and S-waves below the Tuzla site are unusually high, and between ~90 and ~140 m depth is a velocity inversion. This complex velocity structure, especially the low-velocity layer that leads to impedance amplification, is suggested to have a significant influence on the ground motion during an earthquake.

In the second main study spatiotemporal b-value variations along the western NAFZ were analyzed. The study is based on a combined hypocenter catalog from the Izmit-Düzce region and the eastern Sea of Marmara. Near the cities Izmit and Düzce two M>7 earthquakes occurred within three month in 1999. Therefore, the dataset from the Izmit-Düzce region comprises seismicity from pre-, inter-, and post-seismic times. To ensure a dataset of homogeneous magnitude, necessary for comparing b-values throughout time and region, moment magnitudes were newly calculated in this study. For the eastern Sea of Marmara b-value maps and depth sections were generated, and for the Izmit-Düzce region map and depth views were analyzed for the pre-, inter-, and post-seismic times. Large variations in the b-value distribution reflect the complex fault structure of the western NAFZ. Furthermore, a comprehensive analysis of the b-value distribution indicates that the b-value cannot be unambiguously interpreted. The b-value most likely depends on several fault characteristics like the stress on a fault, heterogeneity or fault complexity, and distribution of damage in the

crust. As a consequence, a biased discussion towards either one parameter may lead to erroneous conclusions, and without supporting knowledge about the study area it may not be possible to infer the state of stress on a fault from the b-value.

Finally, the heterogeneous b-value distribution and the complex velocity structure below the Tuzla site suggest that using a constant b-value and a standard site classification in probabilistic seismic hazard assessment are too simplified assumptions for the Marmara region. Therefore, the b-value study and the study of near-surface rock properties are a progress towards making seismic hazard assessment as fault and site specific as possible.

Zusammenfassung

Die Nordanatolische Verwerfungszone (NAFZ) ist eine der seismisch aktivsten Verwerfungen in Eurasien. Das einzige Segment der NAFZ welches nicht im letzten Jahrhundert durch ein großes Erdbeben brach liegt unter dem Marmarameer im Nordwesten der Türkei. Daher stellt es für die Stadt Istanbul eine große seismische Gefährdung dar. Eines der ambitioniertesten Ziele der Seismologie ist eine realistische Beurteilung der seismischen Gefährdung. Dazu bedarf es eines umfangreichen Verständnisses aller Komponenten die zur seismischen Gefährdung beitragen. Am wichtigsten sind dabei Kenntnisse über 1) die Geometrie und Kinematik von Verwerfungen, 2) Modelle zur Wiederkehrperiode zum Vorhersagen zukünftiger Seismizität und 3) Modelle zur Bodenbewegung, um die Bodenbewegung während zukünftiger Erdbeben vorhersagen zu können. Diese Dissertation umfasst zwei Hauptstudien um die Kenntnisse über die oben genannten Punkte in der Metropolregion Istanbul zu verbessern. In der ersten werden Gesteinseigenschaften in oberflächennahen Schichten untersucht, welche einen starken Einfluss auf Bodenbewegungen haben und in der zweiten Studie werden zeitliche und räumliche Variationen vom b-Wert untersucht. Der b-Wert beschreibt die Magnitudenverteilung eines Erdbebenkataloges und ist ein Standardparameter in Modellen zur Wiederkehrperiode. Darüber hinaus wird diskutiert, ob der b-Wert den Spannungszustand der Verwerfung wiederspiegelt.

Beginnend im September 2012 wurde das GONAF (Geophysical Observatory of the North Anatolian Fault) Netzwerk um das östliche Marmarameer aufgebaut. Es besteht aus sieben ~300 m tiefen Bohrlöchern. Das erste Bohrloch wurde auf der Tuzla Halbinsel im Südosten Istanbuls im Januar 2013 fertiggestellt. Es ist mit Seismometern an der Oberfläche und in 71, 144, 215 und 288 m Tiefe ausgestattet. Bei Untersuchungen erster seismischer Aufzeichnungen vom GONAF-Tuzla Bohrloch wurde ein Erdbebenschwarm mit ~100 Mikrobeben mittels Kreuzkorrelation detektiert, welche von Oberflächennetzwerken übersehen wurden. Dies ist ein vielversprechendes Signal des neuen Bohrloch-Observatoriums, das eine Verbesserung der seismischen Überwachung im östlichen Marmarameer ankündigt.

Die erste Hauptstudie dieser Dissertation basiert auf mikroseismischen Aufzeichnungen vom GONAF-Tuzla Bohrloch. Mit Interferometrie mittels Dekonvolution wurden Greens Funktionen zwischen den Tiefenstockwerken der Bohrlochsensoren und der Oberfläche mit exzellentem Signal-Rausch-Verhältnis bestimmt. Sie lassen Oberflächenreflexionen, Amplitudenverstärkung nahe der Oberfläche und Reflexionen an einem starken Impedanzkontrast erkennen. Um die Geschwindigkeits- und Dämpfungsstruktur (Q) unter dem Tuzla-Standort zu bestimmen, wurden die Greens Funktionen im Zeitbereich vorwärts modelliert. Der hierbei bestimmte Qualitätsfaktor Q muss mit Vorsicht interpretiert werden. Da während der Vorwärtsmodellierung bestimmte Vereinfachungen angenommen wurden, ist dieser Q-Wert ein scheinbarer Wert, der eine Mischung aus Impedanzeffekten, Dämpfung durch Streuung und intrinsischer Dämpfung ist. Die seismischen Geschwindigkeiten der P- und S-Wellen unter dem Tuzla-Standort sind ungewöhnlich hoch und zwischen ~90 und ~140 m Tiefe ist eine Geschwindigkeitsinversion. Diese komplexe Geschwindigkeitsstruktur, insbesondere die Niedriggeschwindigkeitsschicht, welche zur Impedanzverstärkung führt, hat einen starken Einfluss auf die Bodenbewegung während eines Erdbebens.

In der zweiten Hauptstudie wurden zeitliche und räumliche b-Wert-Variationen entlang der westlichen NAFZ untersucht. Die Studie basiert auf einem zusammengesetzten Hypozentrenkatalog von der Izmit-Düzce Region und dem östlichen Marmarameer. Nahe den Städten Izmit und Düzce ereigneten sich 1999 innerhalb von drei Monaten zwei M>7 Erdbeben. Daher enthält der Datensatz der Izmit-Düzce Region Seismizität von pre-, inter-,

und post-seismischen Zeiträumen. Um einen Datensatz mit homogener Magnitude sicher zu stellen, was für einen Zeit und Regionen übergreifenden Vergleich vom b-Wert nötig ist, wurden Momentenmagnituden in dieser Studie neu bestimmt. Für das östliche Marmarameer wurden b-Wert-Karten und Tiefensektionen erstellt und für die Izmit-Düzce Region wurden Karten- und Tiefenansichten von pre-, inter- und post-seismischer Zeit untersucht. Die großen Variationen in der b-Wert-Verteilung spiegeln die komplexe Struktur der Verwerfung der westlichen NAFZ wieder. Darüber hinaus weist eine detaillierte Untersuchung der b-Wert-Verteilung darauf hin, dass b-Werte nicht eindeutig interpretiert werden können. Sehr wahrscheinlich hängt der b-Wert von verschiedenen Eigenschaften der Verwerfung ab, wie dem Spannungszustand, Heterogenität oder Komplexität der Verwerfung und die Verteilung von Zerstörung in der Kruste.

Die heterogene Verteilung der b-Werte und die komplexe Geschwindigkeitsstruktur unter dem Tuzla-Standort weisen darauf hin, dass die Annahme einer Standard-Standortklassifizierung und eines konstanten b-Werts in Wahrscheinlichkeitsabschätzungen seismischer Gefährdung zu große Vereinfachungen für die Marmara Region sind. Daher ist die b-Wert-Studie und die Studie der oberflächennahen Gesteinseigenschaften ein Schritt hin zu einer so standort- und verwerfungsspezifischen seismischen Gefährdungsabschätzung wie möglich.

Contents

1 General Introduction

In the last century the right-lateral strike-slip North Anatolian Fault Zone (NAFZ) has produced a series of systematically westward propagating earthquakes of $M>7$, rupturing ~900 km of the NAFZ (Stein *et al.*, 1997). The most recent of them were the M_W7.4 Izmit and M_W7.1 Düzce earthquakes occurring Aug 17th and Nov 12th 1999 less than 100 km to the east from the historical city center of Istanbul (Figure 1.1, top; e.g. Tibi *et al.*, 2001). The Izmit rupture terminated in the eastern Sea of Marmara in the Çınarcık basin close to the Princes Islands segment (Fig. 1.1, bottom). In 1912 to the west of Istanbul a M_S7.3 earthquake ruptured the Ganos fault terminating in the western Sea of Marmara (Bohnhoff *et al.*, 2016a). This leaves the ~150 km long NAFZ section below the Sea of Marmara as the only fault segment that did not rupture since 1766. From historical earthquake catalogs the recurrence period of M~7 earthquakes in the Sea of Marmara is estimated to be ~250 years (Bohnhoff *et al.*, 2016a). Thus, it is assumed that the Sea of Marmara segment is in its final stage of the seismic cycle.
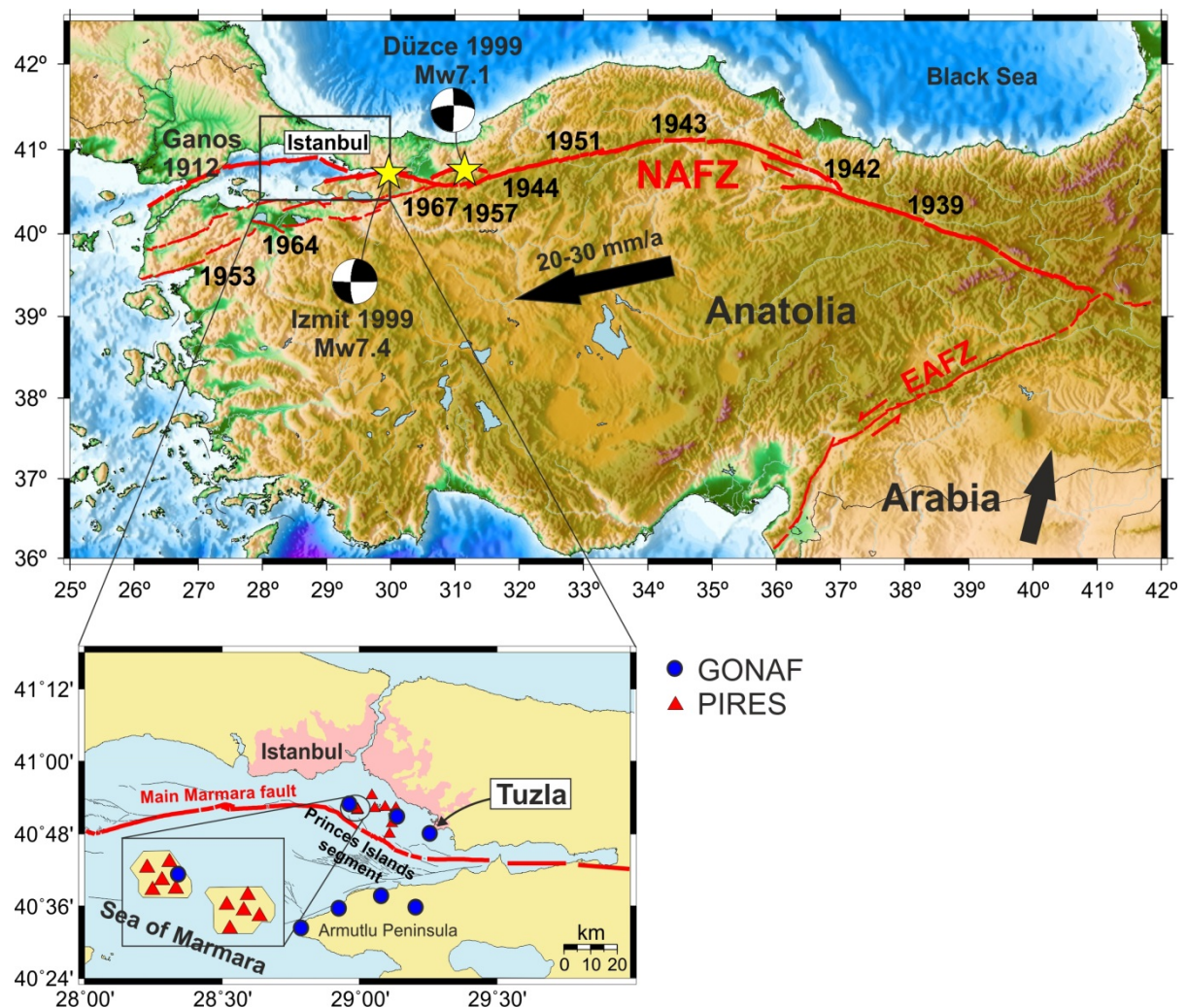
Figure 1.1: Top) Location map of the North and East Anatolian Fault Zones (NAFZ, EAFZ) and the $M>7$ earthquakes on the NAFZ in the last century (marked by their year of occurrence). Black arrows indicate the direction of motion of the Anatolian and Arabian plate. The epicenter locations and focal mechanisms of the Izmit and Düzce earthquakes are after Örgülü and Aktar (2001) and Özalaybey et al. (2002). **Bottom)** Map of eastern Sea of Marmara showing the locations of the PIRES and GONAF networks.

Due to the presence of the Sea of Marmara regional seismometer networks have a poor spatial coverage around the main branch of the NAFZ below the sea and only few stations close to the fault, resulting in a large magnitude of completeness of ~2.6 and a poor hypocenter location precision (Bulut *et al.*, 2009). To improve the monitoring and to determine the seismotectonic setting of the eastern part of the 'Marmara seismic gap', in 2006 the permanent PIRES (Prince Islands Real-time Earthquake System) seismometer network was installed on the Princes Islands only a few kilometers north of the Princes Islands segment of the NAFZ directly offshore Istanbul (Fig. 1.1, bottom; Bulut *et al.*, 2009; 2011). The microseismicity recordings of the PIRES network from 2006 to 2010 reveal an improvement of the magnitude of completeness by approximately one unit and of hypocenter location precision in the eastern Sea of Marmara. Based on this four-year PIRES catalog a ~30 km long and ~10 km deep aseismic patch was identified on the Princes Islands segment which is interpreted as completely locked and as possible nucleation point of the pending Marmara earthquake (Bohnhoff *et al.*, 2013).

The Princes Islands segment in a distance of ~20 km from the megacity Istanbul imposes a severe seismic hazard to the metropolitan area. Therefore, significant efforts are conducted in hazard assessment and medication of risk. One of them is the Geophysical Observatory at the North Anatolian Fault (GONAF) being a joint research venture of GFZ in Potsdam, Germany, and AFAD Disaster and Emergency Management Presidency of Turkey (Bohnhoff *et al.*, submitted). The installation of the GONAF network started 2012 and complements the PIRES network by seven ~300 m deep vertical borehole seismometer arrays around and in the eastern Sea of Marmara, with its first well completed on the Tuzla peninsula in Oct 2012 (Fig. 1.1, bottom). The borehole environment enables relatively noise free recordings in an urban area, and adds the depth dimension to the data providing ideal conditions to study wave propagation in the shallow subsurface and related site effects on surface recordings.

1.1   Motivation

Seismic hazard analyses like probabilistic seismic hazard assessment depend on assumptions about a seismotectonic source model which defines fault or areal zones of seismic potential, a predictive ground motion model possibly taking local site effects into account, and an earthquake-recurrence model (Cornell, 1968; Wiemer *et al.*, 2009). This thesis based on two main studies contributes to the above by addressing several points needed for realistic hazard assessment; the first study analyzing near-surface rock characteristics needed for site effect evaluation, and the second study dealing with spatiotemporal *b*-value variations to improve assumptions about the seismotectonic setting and recurrence models.

The response of the shallow subsurface to strong shacking, i.e. the site response characterized by site effects, is essential for predicting ground shaking during strong earthquakes on which for example seismic hazard maps and building codes are based. It has been observed that the pattern of peak ground shaking is linked to the underlying site conditions, for example a sediment layer amplifies waves and prolongs the duration of shaking in comparisons to bedrock (Kanlı, 2006).

In areas of strong seismicity like California, ground-motion recordings of strong earthquakes can be directly used to create maps of maximum shaking during strong earthquakes. In places devoid of strong earthquakes, like the Sea of Marmara during the last century of instrumental seismology, maximum shaking during strong earthquakes can be predicted from site effects estimated from weak-motion recordings. However, the translation of weak motions to strong motions may not be straight forward, since the linear relationships used to describe weak motions do not hold for very strong motions, because of non-linear soil behavior when a certain strength of ground shaking is reached (Sleep and Erickson, 2014).

Nevertheless, for seismic hazard assessment for the city of Istanbul it is of great value to have accurate information about the subsurface rock characteristics below the city, even though near-surface properties are valid only for a particular site due to lateral heterogeneities. However, having a few sites with precise subsurface information is currently the best available, and may form the basis for a slight improvement of the preparedness of the city for any expected severe ground shaking. Therefore, in the first study of this thesis using recordings from the first completed GONAF borehole seismometer array wave propagation effects in shallow layers are studied to derive the velocity and attenuation structure at the Tuzla site based on a seismic interferometry approach.

For realistic seismic hazard assessment knowledge about the seismotectonic setting to define the seismic potential of individual fault segments is needed as well. However, the kinematics of the fault system in the eastern Sea of Marmara is still under debate, some describing the Çınarcık basin as being mainly under the influence of a strike-slip stress regime (Bulut *et al.*, 2009), and others suggesting a predominant normal-faulting stress regime (Korkusuz Öztürk *et al.*, 2015). Furthermore, it is under debate whether or not the Princes Islands segment is looked or creeping (Bohnhoff *et al.*, 2013). Modeling earthquake scenarios for the Sea of Marmara taking several fault geometries, nucleation points, and initial stress states into account show a great influence of these parameters on the seismic hazard (Oglesby and Mai, 2012; Aochi and Ulrich, 2015).

To address the question of the state of stress on the Princes Islands segment, in the second main study of this thesis based on the four-year PIRES catalog spatial variations of the Gutenberg-Richter b-value are analyzed following the suggestion of recent studies to map locked and creeping fault patches by b-value anomalies (e.g. Wiemer and Wyss, 1997). Since the Sea of Marmara segment of the NAFZ is at its final stage of the seismic cycle the b-value study there is complemented with a b-value study in the Izmit-Düzce region based on a local catalog of pre-, inter-, and post-seismic times to evaluate if the temporal b-value variations in the Izmit-Düzce region have implications for the Marmara region.

Furthermore, the Gutenberg-Richter a- and b-values describe the magnitude frequency distribution on which the prediction of the occurrence of future seismicity is based (Bender, 1983; Youngs and Coppersmith, 1985). In general in probabilistic seismic hazard assessment recurrence models are described with an overall constant b-value in the whole study area (Frankel, 1995). However, in light of increasing observations of the spatial variability of b the trend in recent hazard assessments is towards refined methodologies that take b-value variations into account (Pace *et al.*, 2006; Wiemer *et al.*, 2009). Therefore, identifying b-value anomalies along the western NAFZ contributes to an improved hazard assessment of the city of Istanbul.

1.2   Outline

This thesis comprises the following chapters.

Chapter 2 presents parts of a publication which I co-authored published in *International Journal of Earth Sciences*. Details about the design, installation, and instrumentation of the GONAF network are given. Afterwards, the generation of the first datasets from the GONAF-Tuzla array on which the studies in section 2.3 and chapter 4 are based is described. This is followed by a presentation of the analysis of an earthquake swarm sequence of ~100 microearthquakes recorded with the GONAF-Tuzla borehole array, which demonstrates the improved monitoring conditions inside a borehole.

Chapter 3 describes how shallow geological structures alters the seismic recording at the surface and how near-surface properties, in particular the quality factor Q, can be determined with the spectral ratio technique. Furthermore, the concept of seismic interferometry is introduced, and the theory of computing synthetic seismograms with the Thomson-Haskell propagator method is presented.

In the manuscript published in *Bulletin of the Seismological Society of America* presented in chapter 4 the first-order wave propagation effects at the GONAF-Tuzla site are analyzed using a seismic interferometry technique based on deconvolution and a simple forward modeling approach to estimate near-surface apparent quality factors and seismic velocities of P- and S-waves. The near-surface seismic velocity structure at the Tuzla site comprises unusual high seismic velocities and a low-velocity layer between ~90 and ~140 m depth. These heterogeneities lead to strong interference effects of up- and down-going waves in the borehole recordings. The velocity model is confirmed by sonic-log measurements and uncertainties are evaluated by synthetic tests.

Chapter 5 introduces the current state of research on the Gutenberg-Richter b-value. Methods for calculating the b-value and estimating its uncertainty are described. Furthermore, theories that form the base of common interpretations of spatial and temporal b-value variations are discussed. Additionally, it is explained how moment magnitudes are calculated for the study presented in chapter 6, and a modified methodology for determining the magnitude of completeness is described.

Chapter 6 presents a manuscript which was recently submitted to *Tectonophysics*. The study focusses on analyzing spatiotemporal b-value variations in the Izmit-Düzce and eastern Sea of Marmara region. Based on a hypocenter catalog of homogeneous moment magnitudes that comprises seismicity of pre-, inter- and post-seismic times b-value variations are studied throughout the region and at different stages of the seismic cycle. Most likely the b-value depends on a combination of several fault-zone characteristics like local stress conditions, heterogeneity of the crust, and damage distribution, leading to several possible interpretations of one and the same observation. The results of this study indicate that a biased discussion towards stress or another individual parameter may lead to erroneous conclusions.

Chapter 7 summarizes the main findings of this thesis. In a joint discussion of the results from the b-value study and analysis of near-surface rock properties at the GONAF-Tuzla site implications for the seismic hazard assessment in the Istanbul region are given. Afterwards perspectives are presented.

2   The GONAF downhole observatory

The publication Prevedel *et al.* (2015) 'Downhole geophysical observatories: best installation practices and a case history from Turkey'[1] which I co-authored, describes very comprehensively permanent downhole monitoring systems in general, and in particular the design and installation of the GONAF network. Section 2.1 presents a summary about the design and installation of the GONAF network based on Prevedel *et al.* (2015). Afterwards, in section 2.2 the compilation of the first datasets from the GONAF-Tuzla array is presented (not part of Prevedel *et al.* (2015)). Then, in section 2.3 the analysis of the first downhole seismic recordings from the GONAF-Tuzla array is presented in its original form as it is published in Prevedel *et al.* (2015).

2.1   Design and installation of the GONAF network

The GONAF network is focused on long-term earthquake monitoring along the Marmara segment of the NAFZ, immediately south of the city of Istanbul. The locations of these on-land stations were selected to be as close as possible to the offshore fault segment and include two Princes-Islands-based sites (Fig. 2.1). Combined with data from the existing Princes Islands surface arrays (PIRES) and selected stations from permanent regional networks, the GONAF network is expected to lower the local magnitude-detection threshold by at least one order of magnitude due to the improved signal-to-noise ratio in a borehole (Fig. 2.3, left). The aim of this project is to monitor earthquake activity at low magnitude-detection threshold not achievable with surface recordings. It hopes thereby to provide new insights into the physical processes acting on a fault segment prior, during and after a large earthquake. It is also aimed at calibrating and refining ground shaking models, based on site effect studies that analyze waveforms from short-period instruments at different depth levels as well as broadband and strong-motion data recorded at the wellhead of each GONAF borehole, and furthermore, to contribute to near-real-time hazard assessments for the megacity of Istanbul.

The GONAF network was planned to comprise eight ~300 m deep boreholes. Each is equipped with a five-stage array of seismometers (Fig. 2.2). The first GONAF borehole completed in 2012 is a test installation on the Tuzla peninsula (southeastern Istanbul). It was followed in 2013 by two standardized sites on the Armutlu peninsula along the southern shore of the Sea of Marmara (Fig. 2.1).

2.1.1   GONAF sensor selection and installation

A typical GONAF borehole was planned to consist of a short-period 1 Hz three-component (3-C) seismometer, and a strong-motion and broadband instrument at the surface, and downhole instruments are 1 Hz vertical (1-C) geophones every ~75 m along the wellbore, and

---

[1] Published in *Int. J. Earth Sci. (Geol. Rundsch.)* as Prevedel, B., B. Fatih, M. Bohnhoff, C. Raub, R.F. Kartal, F. Alver and P.E. Malin (2015). Downhole geophysical observatories: best installation practices and a case history from Turkey. pp. 1-11, doi: 10.1007/s00531-015-1147-5

at the bottom of the borehole at ~300 m depth a combination of short-period 1, 2, and 15 Hz 3-C seismometers are installed (Fig. 2.2 and 2.4, right).

The setup at the bottom of the borehole allows covering a broad frequency range, including higher frequencies of microearthquakes. The 15 Hz Geospace DS2500 sensor was selected as a failsafe in case of large bottom-hole tilt, because its high natural frequency makes it tilt insensitive. The potential tradeoffs of this sensor were both more limited bandwidth and potential low signal-to-noise ratios at lower frequencies. Thus, the Geospace HS-1 2 Hz sensor was selected in addition to cover the latter possibility and was gimbal mounted to correct for tilts as large as ~15° or more (Fig. 2.3, right). The 2 and 15 Hz 3-C sensors were integrated into a single sonde. The 1 Hz 3-C sensor - Mark Products L4 seismometer - was included to add both, low frequency bandwidth and higher amplitude output signals, to ensure overcoming the self-noise of the data logger. Because of its much larger diameter, length, and tilt sensitivity compared with the other two sensor types, the decision to add a 1 Hz 3-C sensor at depth also came with a tradeoff. The issue was borehole diameter versus tilt compensation.

The large borehole diameter required for the 1 Hz 3-C sensor was beyond the aims of the first test-borehole in Tuzla. Thus, the Tuzla borehole is equipped at the bottom only with the 2 and 15 Hz sensors.
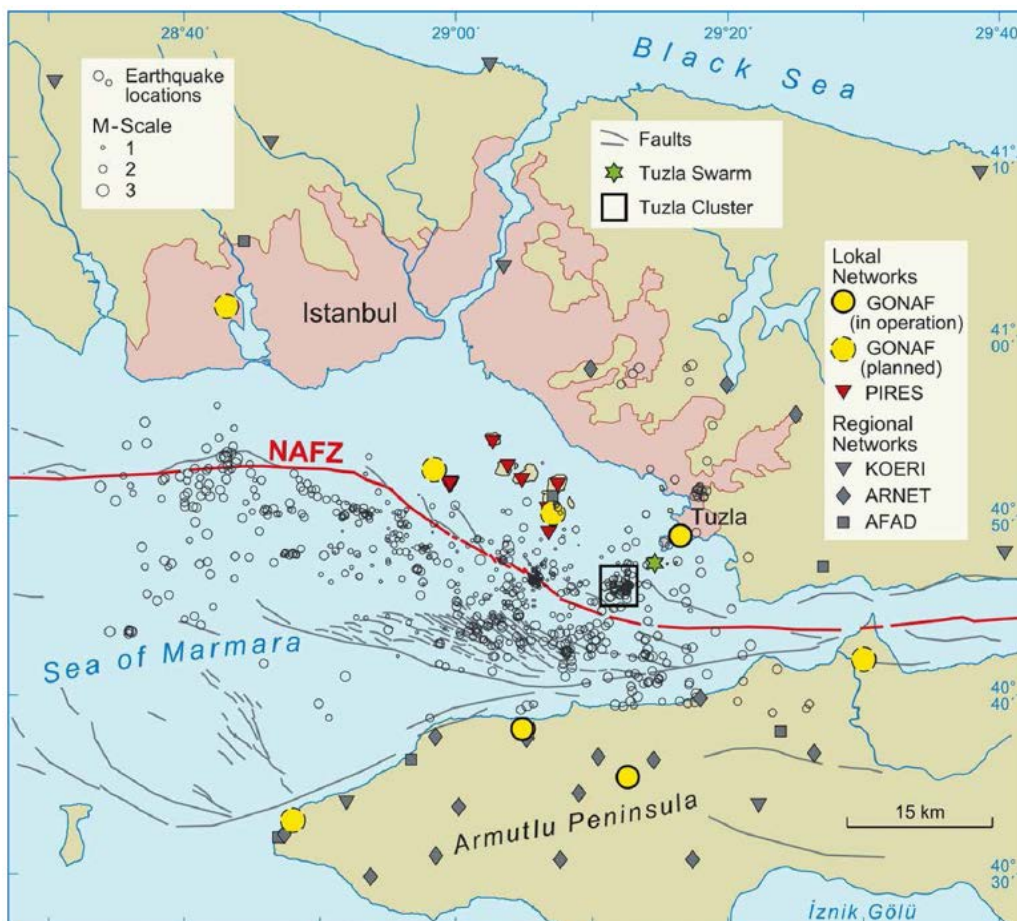
Figure 2.1: Location map of the greater Istanbul metropolitan region in northwestern Turkey. The red line marks the Princes Islands segment as the main branch of the North Anatolian Fault Zone (NAFZ) below the eastern Sea of Marmara. Gray symbols are stations of the regional permanent networks. Yellow points are borehole locations of the GONAF network, while those with a solid frame (on the Tuzla and Armutlu peninsulas) have already been drilled and instrumented in 2012/2013. (From Prevedel *et al.*, 2015)

Figure 2.2: Borehole instrumentation of a standardized GONAF well. Only the Tuzla borehole does not contain a 1Hz-3C seismometer at the bottom of the borehole.

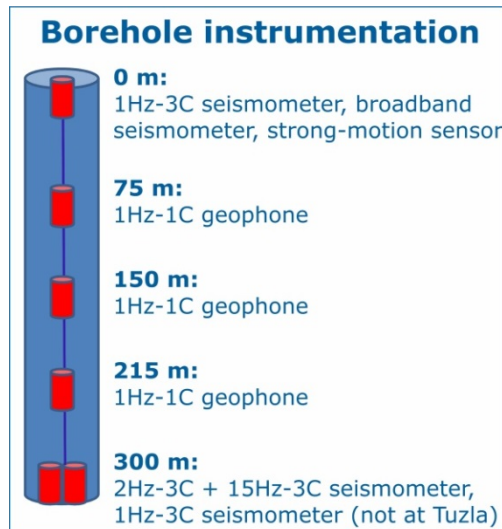Drilling at Tuzla started on Sep 7th 2012, with a truck-mounted rig. The borehole inclination was measured during the drilling operation as a minimum in 30-m intervals. With some effort, the borehole was kept within a degree or two of vertical and reached its final depth of 301 m on Oct 15th 2012. Cuttings were taken every 2 m throughout the drilling, and logging measurements were conducted down to 258 m depth. The sensors were lowered into the hole by banding them onto the cementing trim tube as displayed in Fig. 2.4, center. Finally, the entire well was filled with cement to ensure optimum coupling of the sensors.
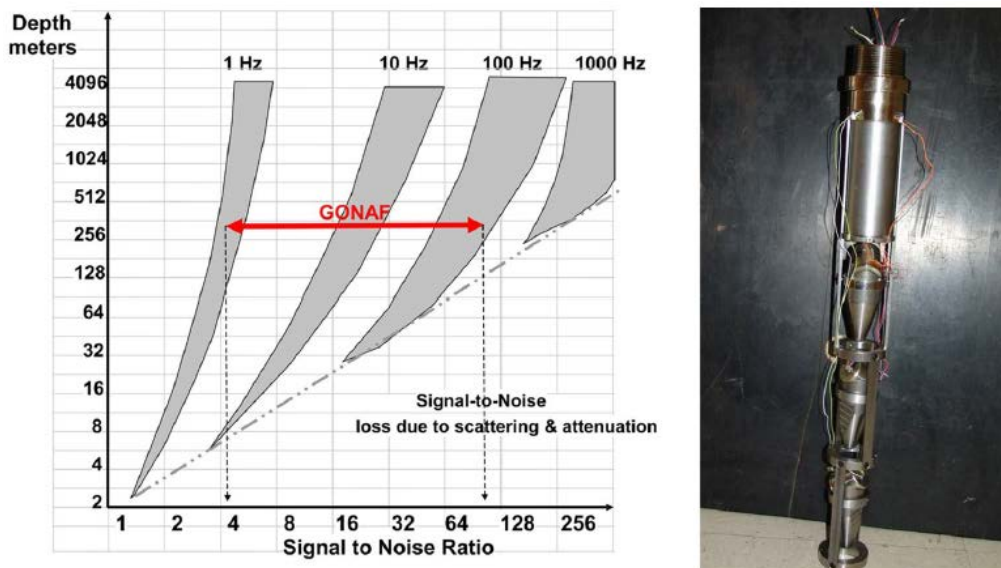
Figure 2.3: Left) Anticipated noise attenuation and signal improvement with depth as proposed by P.E. Malin. The red arrow indicates the expected frequency band for microseismic recordings and subsequent improvements in signal-to-noise ratio with respect to surface for the downhole seismometers deployed in the frame of the GONAF project. **Right)** Fully gimbaled seismometer suspensions for 2-directional tilts, to be installed in a high-pressure housing filled with viscous damping fluid. The geophones embedded in carefully balanced counterweights shown are Geospace 57° Gal'perin position HS-1 4.5 Hz velocity sensors. The enclosed cylinder above these sensors contains a three-component (3-C) MEM accelerometer. (From Prevedel *et al.*, 2015)

7

Figure 2.4: Left) Sensors of the first GONAF instrumentation at the Tuzla borehole. **Right)** The optimized array after the Tuzla test: from left to right are three 1 Hz vertical L4s, a sonde containing the 2 and 15 Hz 3-C, and a 1Hz 3-C L4 instrument. **Center)** One of the 1 Hz vertical L4 sensors banded to the cementing/installation pipe on its way downhole at the Tuzla site. (From Prevedel *et al.*, 2015)

Data is recorded at the surface with an 18-channel data logger designed by Guralp Company. The signals from each sensor are A/D-converted at the surface, and the data is sampled initially with 2000 Hz at the Tuzla site and with 500 Hz at the other GONAF sites. Waveform recordings are transferred in real-time via Internet to end users in Turkey and Germany for further processing. In case of failure of the online data transmission system, the data is always stored locally as backup for manual download at the respective site.

The GONAF surface recording facilities consist of a 10-feet container hosting the data logger, GPS antenna, communication system, power supply, and surface short-period, broadband, and strong-motion sensors. The short-period seismometer at the surface was installed in Jan 2013 and the broadband and strong-motion sensors will be added in future.

The successful drilling of the Tuzla test-well implied that the 1 Hz 3-C sensor at the bottom of the borehole (which was not included into the Tuzla-borehole design because of its large diameter and tilt sensitivity) can be included into the standardized GONAF borehole design. Starting in fall 2013 the drilling of two borehole sites on the Armutlu peninsula the standard GONAF borehole design was successfully realized. The instrument complement of the Tuzla borehole and of a standardized GONAF borehole is shown in Fig. 2.4 left and right, respectively.

Initially seismic recordings from the GONAF Tuzla site contained strong electronical noise introduced through the power net with maxima at 50 Hz and multiples. This was reduced by galvanic separation from the public power net of Istanbul by using a battery power supply with a DC charger, and grounding conditions were refined, leading to a substantially improved data quality. Thus the same actions were consequently taken for the other GONAF sites as well. Furthermore, the selected sites were pre-surveyed using short-term dense seismic arrays in order to understand to what extend surrounding noise might interfere with the downhole environment.

2.2   First datasets from the GONAF-Tuzla array

After the borehole construction and sensor installation at the Tuzla site was completed the real-time online data transmission from Tuzla in Turkey to GFZ in Germany was set up. I contributed to that on the GFZ side by setting up the software 'Scream' in our computer system. Initially, the real-time data transmission suffered from data gaps. To identify and cure the cause of the data gaps extensive testing with the software on the Turkish and GFZ side was conducted. Finally, a stable online data transmission was enabled. During the first half year of operation of the GONAF-Tuzla array the data was strongly contaminated by electronical noise. To diminish the electronical noise several types of power supply were tested to which I contributed by analyzing the waveform recordings. Afterwards, the raw continuous recordings were processed to compile the first datasets from the GONAF-Tuzla array.

To automatically detect earthquakes in continuous seismic recordings a waveform cross-correlation algorithm and a short-time-average/long-time-average (STA/LTA) trigger were used.
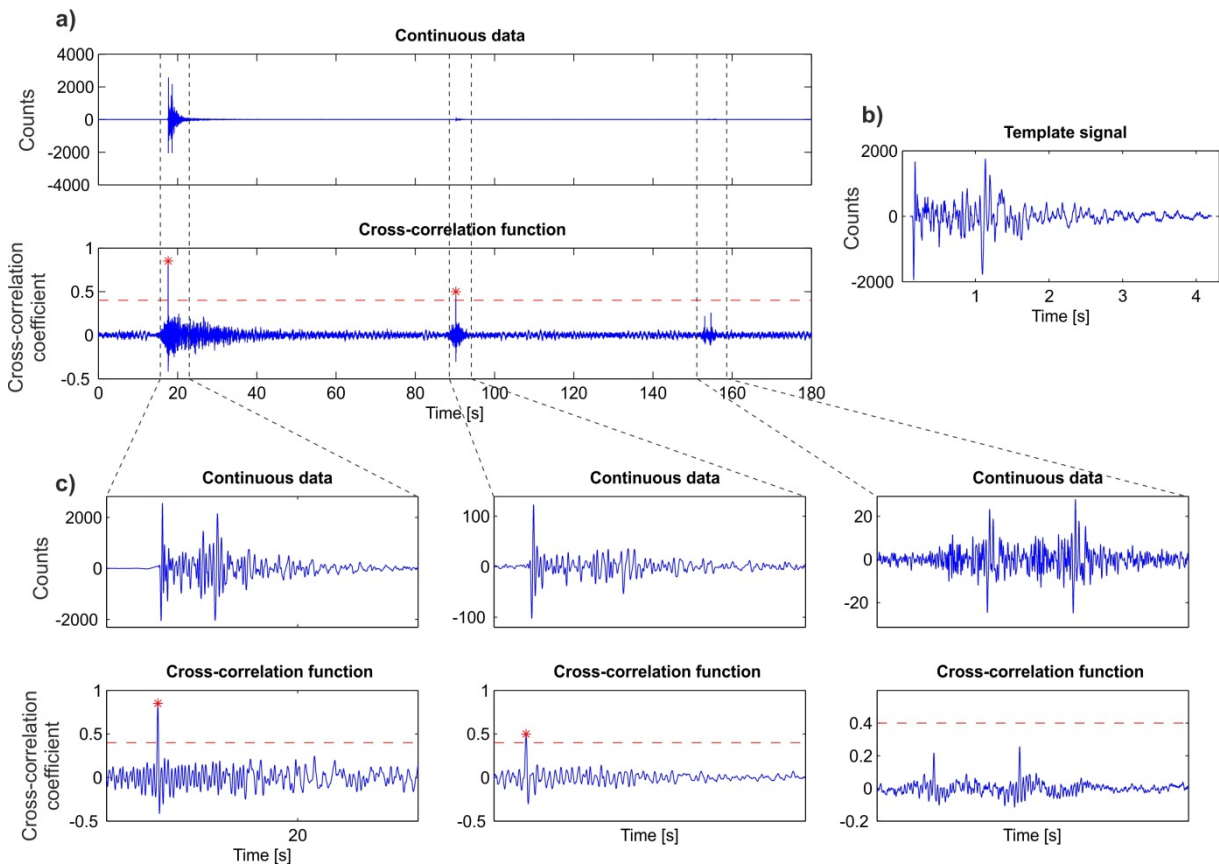
Figure 2.5: Illustration of earthquake detection based on a cross-correlation algorithm applied to recordings from the 1 Hz 1-C sensor at 215 m depth: **a)** On top continuous data from Apr 20th 2013 (around 1:30 am) bandpass filtered between 3 and 40 Hz is presented. Below the cross-correlation function obtained from cross-correlating the template signal (b) with the continuous data is shown. The red dashed line indicates the detection threshold of 0.4 and red stars mark detections. **b)** As template signal the M_D1.6 event on Apr 20th 2013 (9:09 pm) is used. **c)** Close-ups of (a) showing two earthquakes that were detected and two successive earthquakes which yielded cross-correlation coefficients below the threshold.

2.2.1 Cross-correlation algorithm

To detect earthquakes too weak for being recognized by standard detection algorithms a waveform cross-correlation technique was applied. A template signal is cross-correlated with the continuous waveform data by shifting it across the data in steps of one sample. A high cross-correlation coefficient indicates a high waveform similarity. When the cross-correlation coefficient exceeds a threshold a signal is detected. This is illustrated in Figure 2.5 based on an example of an earthquake swarm sequence from Apr 20th 2013 which is discussed in detail in section 2.3. As template signal (Fig. 2.5b) serves the recording of a M_D1.6 earthquake. The template signal was cross-correlated with continuous data surrounding Apr 20th. Figure 2.5a shows an example of three minutes of continuous data ~20 hours before the template event occurred and the corresponding cross-correlation function. To set the detection threshold several values were tested by manually inspecting detected signals. Here a conservative value of 0.4 is used leading to a loss of a few very weak earthquakes as seen in Figure 2.5c. However, a lower detection threshold would have resulted in numerous false detections as well.

2.2.2 STA/LTA trigger

To compile a local hypocenter catalog a STA/LTA trigger was used. The ratio of the average absolute amplitudes of a short time data window and a long time data window is continuously calculated by shifting the windows sample-wise across the data which is filtered in the desired frequency band (Fig. 2.6). When the ratio exceeds a predefined threshold a signal is detected. The length of the long time window determines the sensitivity of the trigger to temporal changes in background noise, while the length of the short time window determines the trigger sensitivity to seismic events.

To reduce the number of false detections the STA/LTA trigger is applied to all stations of the PIRES network and of the GONAF-Tuzla array. This is followed by a coincidence trigger to declare only those detections as 'true' earthquake detections when the signal was detected on a certain number of stations within a given time period. The STA/LTA trigger parameters, window lengths and detection threshold, were fine-tuned manually by visual inspection of detected signals (Fig. 2.6).

After earthquake detection an event database was compiled from all available PIRES stations and stations from the regional KOERI (Kandilli Observatory and Earthquake Research Institute) and AFAD (Turkish Disaster and Emergency Management Authority) networks. Subsequently, P- and S-wave arrivals and coda length were manually picked on the waveforms and hypocenter locations were determined with the *HYPOCENTER* computer code (Lienert *et al.*, 1986). Based on the resulting hypocenter catalog near-surface rock characteristics were studied (chapter 4).
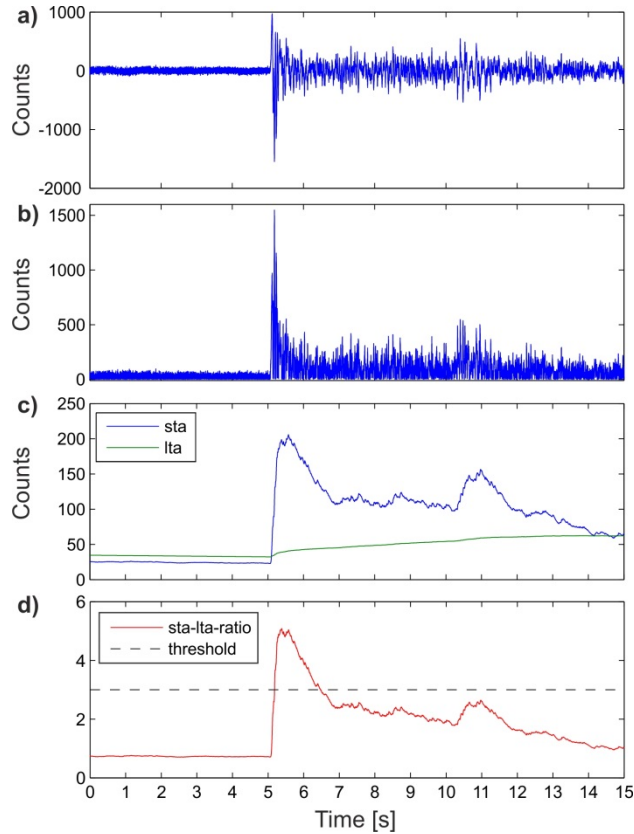
Figure 2.6: Illustration of STA/LTA trigger algorithm: **a)** Example of a raw earthquake recording at the vertical component of the surface station from the GONAF-Tuzla array. **b)** Absolute amplitude of (a). **c)** Short-time-average (STA) and long-time-average (LTA) computed from (b) with a STA and LTA window length of 0.6 and 20 s, respectively. **d)** STA/LTA ratio and threshold-ratio set to 3.

2.3   First downhole monitoring results from the GONAF-Tuzla site

At Apr 20th 2013 a few months after the first GONAF station was completed on the Tuzla peninsula, a local M_D1.6 earthquake was detected by permanent regional seismic networks and localized south of the Tuzla peninsula (Fig. 2.1, green star). This event served to elaborate on the improvements provided by downhole recordings for studying the seismic activity associated with somewhat larger events.

The region in which the M_D1.6 event occurred is close to the so-called Tuzla earthquake cluster. Here, seismicity swarms were activated two days after the M_W 7.4 Izmit earthquake on Aug 17th 1999, and ever since had a nearly constant earthquake occurrence rate (Karabulut *et al.*, 2011). Analysis of the GONAF downhole recordings revealed that the M_D1.6 event in April was only the largest event of a whole earthquake sequence that remained undetected from surface networks. Due to the reduced noise level at the borehole sensors and the relatively short distance between the borehole and the earthquake hypocenters, it was possible to detect a total of 114 additional earthquakes with smaller magnitudes framing the time of the M_D1.6 event.

As detection algorithm, we applied a cross-correlation technique to the channel with the highest signal-to-noise ratio from all channels of the Tuzla borehole array, which is the 1 Hz vertical sensor at 215 m depth. This channel is least affected by 50 Hz noise, and it is the deepest one of the 1 Hz seismometers. The complete waveform including P- and S-wave coda

11

of the $M_D 1.6$ event was used as a template signal, which was correlated with the continuous waveform recordings for the time period April‑May 2013 by shifting it across the data in steps of one sample. The resulting cross-correlation coefficients are a measure of the similarity between the template signal and the continuous waveform recordings, with "0" meaning completely uncorrelated and "1" identical. When the cross-correlation coefficient exceeded a threshold of 0.4, an earthquake was declared. This low threshold was used to ensure we obtain the largest possible number of events related to this specific swarm region during the considered time interval. In this 2-month time period, 20 of the events observed at the downhole Tuzla sensors were also recorded by the closest station of the PIRES array on the Princes Islands, but at significantly lower signal-to-noise ratio (Fig. 2.7).

The main portion of the seismic activity lasted approximately five days from April 18th to 23rd 2013. The magnitude distribution, with a mean duration (coda) magnitude of −0.42 ± 0.4, resembles a typical behavior of an earthquake swarm with random magnitude distribution rather than a mainshock-aftershock sequence (Fig. 2.8).
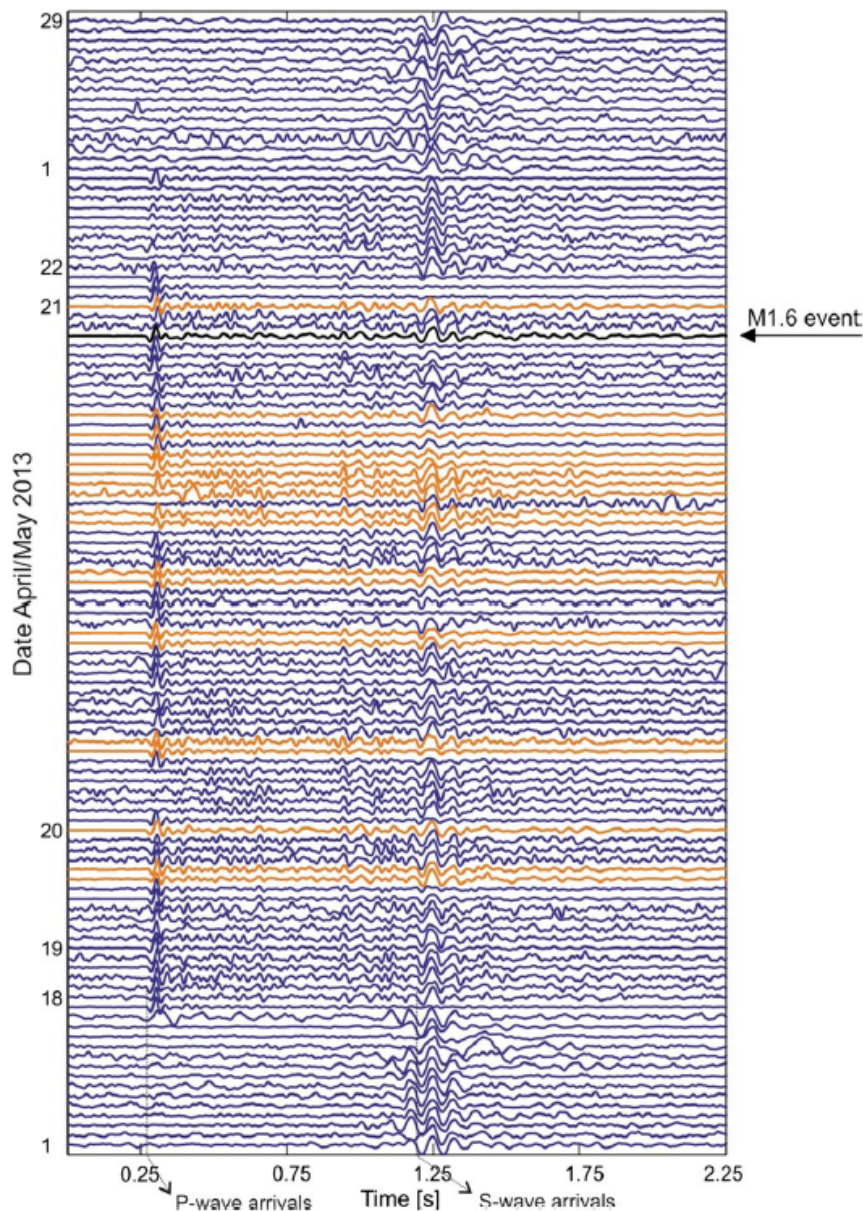
Figure 2.7: Waveform recordings of the Tuzla earthquake swarm of April‑May 2013. The traces shown are recordings of the 1 Hz vertical seismometer in the GONAF-Tuzla borehole at 215 m depth. While only one event ($M_D 1.6$) was detected and located by the regional permanent seismic network (bold black trace), another 19 smaller-magnitude events were also detected by the closest surface station on the Princes Islands, on the southeastern-most island of Baliciada (orange traces). Using a cross-correlation technique, additional 95 earthquakes could be detected by the GONAF-Tuzla borehole array (blue traces). All events belong to one earthquake swarm within a narrow hypocentral region close to the Tuzla cluster (see Fig. 2.1).

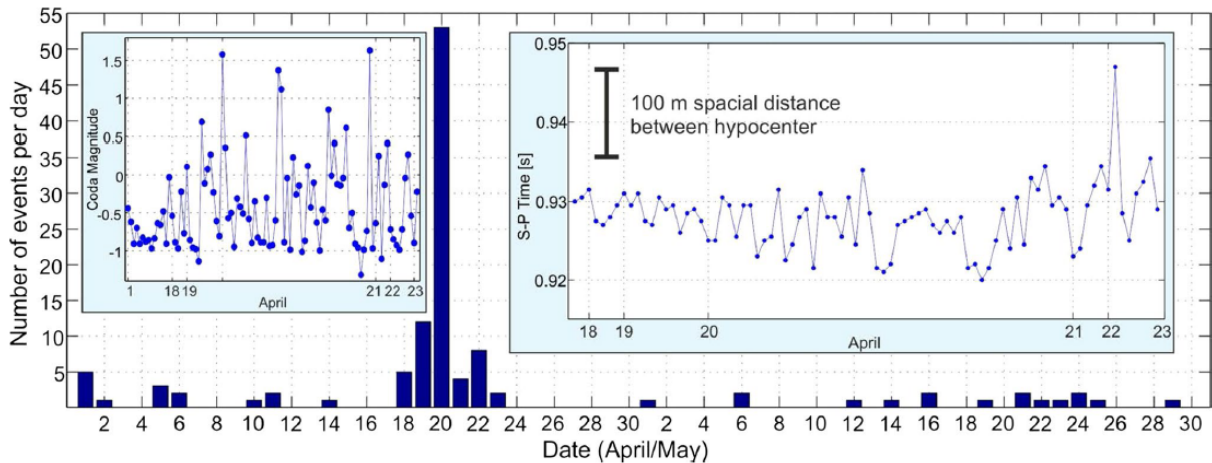**Figure 2.8:** Temporal evolution of the Tuzla earthquake swarm (daily event rate). While the main activity of the swarm occurred during April 18th – 23rd 2013, several additional events with highly similar waveforms were detected during the framing 2-month period. The **upper left insert** shows the temporal evolution of the earthquake magnitudes indicating a swarm-type behavior rather than a mainshock-aftershock sequence. In the **upper right**, the S-P times are plotted, indicating no major internal migration of hypocenters.

The right inset in Figure 2.8 shows the S‑P times, which vary with a standard deviation of only 0.01 s; hence, the movement of the earthquakes toward or away from Tuzla is limited to ~80 m. Although the variation in S‑P times of ~0.01 s is very small, the high sampling rate of 2000 samples per second and precise relative arrival times derived from cross-correlation make it possible to achieve such high temporal resolution. In addition to S‑P times, also the highly correlated waveforms (average cross-correlation coefficient of 0.62 for events of the main swarm activity from April 18th to 23rd) indicate that the swarm events occur all in a similar source region and are generated by the same source mechanism.

Such seismic swarms are common for volcanic active regions where they are associated with crustal fluid migration. The seismicity of the observed Tuzla swarm might therefore also be related to upward migration of fluids and gases, in this case at branches and splay faults of the Princes Islands segment of the NAFZ (Geli *et al.*, 2008). However, a direct link between gas emissions at the sea bottom located at the epicenter of the swarm activity and the Tuzla swarm is difficult to verify, but needs further investigation. The gas composition seems to indicate a shallower source depth than the depth of the earthquake swarm at 7 km, and therefore, might be interpreted as a decoupled process (Bourry *et al.*, 2009).

2.4   Conclusions and current status of GONAF

The successful completion of the GONAF test-site on the Tuzla peninsula suggested that it is possible to incorporate into a standardized GONAF borehole a 1 Hz 3-C seismometer at the bottom of the borehole. This challenging goal was successfully met at six GONAF sites, with the last borehole being finished in 2015 (see map in Fig. 1.1 (bottom) for locations; Bohnhoff *et al.*, submitted). Recordings of an earthquake swarm of magnitudes below 0 with the GONAF-Tuzla well shows that the local magnitude-detection threshold could be lowered below 0, and it indicates an improved waveform quality of low-magnitude events.

3 Analysis of near-surface properties

For many geophysical applications it is important to quantify how shallow subsurface geological features influence seismic recordings. For example, many earthquake source models predict a too high portion of high-frequency energy when comparing with field recordings (Blakeslee and Malin, 1991). Either microearthquake sources emit less high-frequency energy as anticipated or the emitted high-frequency energy is attenuated, most likely due to site effects at the receiver. Hauksson *et al.* (1987) and Abercrombie and Leary (1993) compared source parameters determined on seismic recordings from a seismometer in a borehole with those from a surface station and found that near-surface attenuation severely affected the spectral content of the surface recording, resulting in a significantly lower corner frequency. Therefore, it is necessary to account for near-surface effects when analyzing source parameters.

Site effects also play an essential role in ground motion estimations, or otherwise the predicted ground motions can be significantly under- or over-estimated, as discussed for example in Pulido *et al.* (2004) and Sørensen *et al.* (2006; 2007) who computed ground motion estimates for the Sea of Marmara region for various earthquake scenarios with and without taking site effects into account.

The amplitude and frequency of seismic recordings at the surface are influenced by shallow subsurface geological structures through

- amplification due to near-surface low-impedance layers, which can be explained with conservation of energy,
- resonance effects caused by strong impedance contrasts between soft sediment layers above bedrock, introducing reverberations in the seismic recording,
- attenuation related to scattering of high-frequency energy, and
- intrinsic attenuation, i.e. material damping, for example, energy transfer to heat.

Furthermore, the free-surface effect amplifies SH waves by a factor of 2, and P- and SV-waves by a factor of approximately 2 or smaller depending on the incidence angle (Shearer and Orcutt, 1987).

Classical methods to characterize the site response from a pair of stations are reviewed for example by Şafak (1997). The seismic wavefield U recorded with a seismometer can be described as a convolution of the source, path, and site effects (S, P, and G, respectively), and the transfer function I of the instrument. In the frequency domain with frequency f this is (Steidl *et al.*, 1996):

$$U(f) = S(f)P(f)I(f)G(f). \tag{3.1}$$

The path effects include all effects which alter the waveform along the travel path from the source to the receiver, e.g. geometrical spreading and scattering. Many techniques are based on spectral ratios between the site of interest and a reference station, such as a surface-to-downhole seismometer pair. When the station-to-station distance is significantly smaller than the hypocentral distances, it can be assumed that the source and path terms are nearly identical on both stations. Thus, after instrument response correction the spectral ratio between the two recordings can be associated solely with site effects.

One parameter of interest is the quality factor Q which describes the attenuation of the medium. It is related to the spectral ratio as follows. The surface recording at depth $z = 0$ expressed by the borehole recording at depth z is (Aki and Richards, 2002)

$$U_{z=0}(f) = 2U_z(f)\exp(-\alpha f), \tag{3.2}$$

where α is the attenuation coefficient being

$$\alpha = \frac{\pi z}{vQ} = \frac{\pi \Delta t}{Q}, \tag{3.3}$$

and v and Δt are the effective velocity and the traveltime difference between the borehole and surface sensors. The factor 2 in equation 3.2 accounts for the free-surface amplification. In most studies it is simply set to 2, because small incident angles are assumed. When assuming that Q is frequency independent it can be determined by fitting the slope m of the logarithmic spectral ratio:

$$\ln\left(\frac{U_0(f)}{2U_z(f)}\right) = \frac{-\pi \Delta t f}{Q}, \tag{3.4}$$

$$Q = \frac{-\pi \Delta t}{m}. \tag{3.5}$$

If the subsurface between the surface and borehole sensors contains heterogeneities this Q value is an effective value corresponding to an equivalent homogeneous layer.

This technique has been applied in numerous studies of seismic recordings from borehole arrays (e.g. Malin *et al.*, 1988; Parolai *et al.*, 2007; Ge *et al.*, 2009). However, downhole seismograms are affected by downgoing surface or near-surface reflections. They cause destructive interference peaks in the spectrum, which can lead to an erroneous Q estimation. It has been shown that the spectral decay due to attenuation can be masked by resonance effects and near-surface amplification (Blakeslee and Malin, 1991; Trampert *et al.*, 1993). To avoid this problem and to make use of the complete wavefield seismic interferometry is applied in this study (chapter 4) for deriving the attenuation and velocity structure at the GONAF-Tuzla site.

3.1 Seismic interferometry

Seismic interferometry is the study of the interference of seismic related signals (Curtis *et al.*, 2006). It is used to extract the impulse response between two sensors without the need to know the model parameters. Many seismic interferometry studies are based on cross-correlation (Curtis *et al.*, 2006). However, recently deconvolution interferometry has been applied more frequently, because in contrast to correlation-based interferometry deconvolution interferometry eliminates the source function (Snieder and Şafak, 2006; Vasconcelos and Snieder, 2008a; Nakata and Snieder, 2012).

Let the signal recorded at the borehole sensor at depth z be $U_{z,s}(f)$ which includes the source function and all propagation effects between the source location s and the sensor. Then the wavefield recorded at the surface ($z = 0$) is in frequency domain

$$U_{0,s}(f) = G_{0,z}(f)U_{z,s}(f). \tag{3.6}$$

$G_{0,z}(f)$ is the plane-wave Green's function propagating from depth z to the surface. The cross-correlation of the surface signal with the borehole signal is

$$C_{0,z}(f) = U_{0,s}(f)U_{z,s}^*(f) = G_{0,z}(f)|U_{z,s}(f)|^2, \qquad (3.7)$$

where $*$ denotes the complex conjugate. The deconvolution of the surface signals with the borehole signal is

$$D_{0,s}(f) = \frac{U_{0,s}(f)}{U_{z,s}(f)} = G_{0,z}(f). \qquad (3.8)$$

Equation 3.8 obviously has the advantage over equation 3.7 of being free of the source and path effects. In correlation-based interferometry this problem is handled by stacking over many correlation functions between one receiver and sources distributed at all directions around the receiver. Such source-and-receiver geometry is not given in this study. Therefore, deconvolution interferometry is preferred. Additionally, to improve the signal-to-noise ratio of the resulting Green's function, the deconvolved seismograms obtained from all earthquake recordings used in this study are stacked as well.

Examples of deconvolved seismograms are presented in Figures 4.6 and 4.7. Either, the surface or the borehole station serves as reference station, i.e. the denominator in equation 3.8. When using the surface station as reference Trampert *et al.* (1993) has shown that in the case of SH-wave propagation the spikes on the time axis symmetric around time zero depend only on the velocity and thickness of the layer, while the amplitude ratio of these spikes is related to the quality factor of the layer. Van Vossen *et al.* (2004) and Mehta *et al.* (2007) presented how the deconvolution results can be also related to P- and SV-wave propagation in a lossless and lossy medium, respectively, showing that also in the P-SV case the velocity structure and attenuation of the medium controls the position in time and amplitudes of the spikes. Thus, in the study presented in chapter 4, the amplitude and the times of spikes in the deconvolved seismograms (the Green's functions) are forward modeled to determine the attenuation and velocity structure between the borehole and surface sensors. The deconvolution technique and forward modeling approach are described in detail in section 4.4 and 4.7, respectively, and how the synthetic seismograms needed for the forward modeling are calculated is described below.

3.2   Computation of synthetic seismograms

Synthetic seismograms for a 1-D velocity model were computed with the orthonormalyzed matrix propagator method in the frequency-wavenumber domain of Wang (1999) which is based on the Thomson-Haskell propagator method (Thomson, 1950; Haskell, 1953). With the Thomson-Haskell propagator method the displacement vector is calculated from layer to layer via a chain rule in a stack of horizontally homogeneous layers overlaying a homogeneous half space (Fig. 3.1).

The equation of motion can be converted with the Fourier-Hankel transform to a system of ordinary differential equations and is written in matrix form as (Wang, 1999; Aki and Richards, 2002)
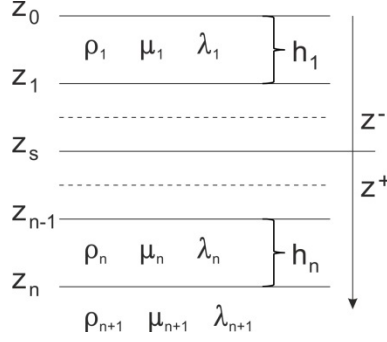
$$\frac{d\mathbf{f}}{dz} = \mathbf{Af}, \qquad (3.9)$$

Figure 3.1: Sketch of a stack of n homogeneous layers over a homogeneous half space with a seismic source at depth z_s. The medium is described by the density ρ and the Lamé moduli λ and μ which are constant within one layer. h is the layer thickness.

where $\mathbf{f}$ is the $n \times 1$ column generalized displacement vector in the frequency-wavenumber domain and $\mathbf{A}$ is the $n \times n$ coefficient matrix whose entries depend on the elastic parameters of the medium and is constant within each layer. In the P-SV case $\mathbf{f} = (U, V, P, S)^T$, where U and V are the displacement components in the frequency-wavenumber domain, P and S are the elastic surface force on a horizontal plane, and T denotes the transpose of the vector. The entries of $\mathbf{A}$ are given for example in Aki and Richards (2002) (their eq. 7.28). To take attenuation into account the elastic properties in $\mathbf{A}$ are replaced with anelastic ones.

A point source is incorporated into the system in form of a discontinuity of the solution vector $\mathbf{f}$ across the source plane at $z = z_s$

$$\mathbf{f}_-^+ = \mathbf{f}(z_s^+) - \mathbf{f}(z_s^-) = \Delta\mathbf{f}_s, \tag{3.10}$$

where '$+$' and '$-$' denote the lower and upper side of the source plane, respectively (Fig. 3.1), and $\Delta\mathbf{f}_s$ is the Hankel-transformed source function.

The solution of $\mathbf{f}$ should satisfy the boundary conditions at the free surface (no traction) and at depth infinity (no motion) and the continuity condition of displacement and stresses across the interfaces between each layer. The solution of $\mathbf{f}$ can be written for a homogeneous layer in the form

$$\mathbf{f} = \mathbf{F}\mathbf{w} = \mathbf{E}\mathbf{\Lambda}\mathbf{w}. \tag{3.11}$$

$\mathbf{F}$ is the layer matrix factorized in a matrix $\mathbf{E}$ containing the eigenvectors of $\mathbf{A}$, times a diagonal matrix $\mathbf{\Lambda}$ containing the vertical wavenumbers of the P- and SV-waves. For entries of $\mathbf{E}$ and $\mathbf{\Lambda}$ for the P-SV case see equation 7.55 in Aki and Richards (2002). $\mathbf{w} = (A_+, B_+, A_-, B_-)^T$ is a constant vector to be determined, where A and B are the displacement amplitudes of the down- $(+)$ and up-going $(-)$ P- and SV-waves, respectively.

With the Thomson-Haskell propagator matrix $\mathbf{P}$ the displacement vector at the free surface, $\mathbf{f}(z_0)$, can be related to that at the half space at depth z_n via a chain rule

$$\mathbf{f}(z_0) = \mathbf{P}(z_0, z_1) \cdots \mathbf{P}(z_{n-2}, z_{n-1})\mathbf{P}(z_{n-1}, z_n)\mathbf{f}(z_n) = \left(\prod_{i=1}^{n} \mathbf{P}(z_{i-1}, z_i)\right)\mathbf{f}(z_n). \tag{3.12}$$

This also works inversely, constructing the displacement vector at the half space by starting the vector propagation at the free surface. When expressing the displacement vector $\mathbf{f}$ with the

eigenvectors and eigenvalues of $\mathbf{A}$ as in equation 3.11 the propagator matrix $\mathbf{P}$ for layer i can be defined as (Wang, 1999; Aki and Richards, 2002)

$$\mathbf{P}(z_{i+1}, z_i) = \mathbf{P}(h_i) = \mathbf{E}_i \mathbf{\Lambda}_i(h_i) \mathbf{E}_i^{-1}, \tag{3.13}$$

where $h_i = z_{i+1} - z_i$ is the thickness of the layer.
Due to the boundary conditions the displacement vector at the free surface is

$$\mathbf{f}(z_0) = (U, V, 0, 0)^T, \tag{3.14}$$

and at the interface between the lowest layer and the half space at depth z_n it is

$$\mathbf{f}(z_n) = \mathbf{E}_n(0, 0, A_-, B_-)^T. \tag{3.15}$$

From equations 3.14 and 3.15 starting values for the initial value problem can be determined (see Wang, 1999). Then the displacement vector at the free surface is propagated downwards through the medium to the source depth z_s, and the displacement vector at depth z_n is propagated upwards to z_s. The final solution is obtained by superposition of both results so that the source condition given in equation 3.10 is satisfied.
The original Thomson-Haskell propagator method suffers from numerical instabilities when waves become evanescent, e.g. in a thick layer. Therefore, an additional orthonormalization procedure is inserted into the propagation loop which is described in detail in Wang (1999).

4 Seismic-wave propagation in shallow layers at the GONAF-Tuzla site, Istanbul, Turkey[2]

Summary

Using the first dataset available from the downhole Geophysical Observatory of the North Anatolian Fault (GONAF), we investigated near-surface seismic-wave propagation on the Tuzla Peninsula, Istanbul, Turkey. We selected a dataset of 26 seismograms recorded at Tuzla at sensor depths of 0, 71, 144, 215, and 288 m. To determine near-surface velocities and attenuation structures, the waveforms from all sensors were pairwise deconvolved and stacked. This produced low-noise empirical Green's functions for each borehole depth interval. From the Green's functions we identified reflections from the free surface and a low-velocity layer between ~90 and ~140 m depth. The presence of a low-velocity zone was also confirmed by a sonic log run in the borehole. This structure plus high near-surface P- and S-wave velocities of ~3600 – 4100 m/s and ~1800 m/s lead to complex interference effects between up- and down-going waves. As a result, the determination of quality factors (Q) with standard spectral ratio techniques was not possible. Instead we forward modeled the Green's functions in time domain to determine effective Q values and to refine our velocity estimates. The effective Q_P values for the depth intervals of 0–71, 0–144, 0–215 and 0–288 m were found to be 19, 35, 39 and 42. For the S-waves we obtained an effective Q_S of 20 in the depth interval of 0–288 m. Considering the assumptions made in our modeling approach, it is evident that these effective quality factors are biased by impedance contrasts between our observation points. Our results show that even after correcting for a free-surface factor of 2, the motion at the surface was found to be 1.7 times greater than that at 71 m depth. Our efforts also illustrate some of the difficulties of dealing with site effects in a strongly heterogeneous subsurface.

4.1   Introduction

For numerous scientific applications such as earthquake source parameter studies (e.g. Hauksson *et al.*, 1987; Abercrombie and Leary, 1993) it is important to quantify how near-surface geological structures influence the waveforms and amplitudes of seismic waves. Shallow subsurface geological features affect the seismic wavefield through amplification due to near-surface low-impedance layers, resonance effects caused by strong impedance contrasts, and high-frequency attenuation due to scattering, and intrinsic attenuation. Studies of these effects are usually based on a two-geographical-location comparison method. A common practice is to compare recordings from the site of interest to those from a close-by reference station, preferably one installed on outcropping bedrock or in a deep borehole – the optimum being a vertical array of seismometers from the surface down to competent rock (Steidl *et al.*, 1996). In the latter circumstance, with a sufficient number of sensors the mechanical properties of the soil can be measured directly for different depth intervals.

Such an arrangement exists at the Tuzla Peninsula site of the Geophysical Observatory of the North Anatolian Fault (GONAF), southeastern Istanbul, Turkey (Fig. 4.1). The GONAF-Tuzla array includes five levels of borehole seismometers extending down to ~300 m depth (Fig. 4.2). It was the first of seven GONAF vertical arrays to be installed around the eastern Sea of Marmara (Prevedel *et al.*, 2015). The seismic data collected at Tuzla provide a base for a better understanding of wave propagation in the shallow geological layers around this site, and improve source parameter and ground motion estimates that are necessary for preparing hazard scenarios locally and in the immediate surrounding area of Istanbul, with its 15 million inhabitants.

We focus here on the 1 kHz sampling-rate seismograms of 26 nearby microearthquakes recorded at Tuzla (Tab. 4.1). Our study is an initial investigation of this site's amplification, attenuation (quality factor Q), seismic velocity and shallow wave propagation effects. Spectral ratio techniques are widely used to determine near-surface amplification and the quality factor (e.g. Malin *et al.*, 1988; Şafak, 1997; Assimaki *et al.*, 2008). However, as discussed later in the text, the high seismic velocities and heterogeneities at the Tuzla site lead to strong interference effects between up- and down-going waves, the latter ones being reflected at the surface and at reflectors between the borehole seismometers. These interference effects cause complicated spectra, which makes a stable determination of Q based on spectral ratios difficult (Trampert *et al.*, 1993; Bethmann *et al.*, 2012). As a result, our application of them failed to give meaningful results.

Accordingly, we chose to apply an alternative approach based on deconvolution interferometry which makes use of the complete wavefield and takes advantage of the surface reflected wave, instead of regarding it as a troublesome source of interference. The method also enables us to determine the velocity structure between the borehole seismometers and to evaluate amplification and shallow wave propagation effects.

Deconvolution interferometry is used to estimate the impulse response between two receivers (e.g. Vasconcelos and Snieder, 2008a). It is applied, for example, for imaging purposes (Vasconcelos and Snieder, 2008b), retrieving building response to ground shaking (Snieder and Şafak, 2006; Bindi *et al.*, 2015) and for determining near-surface velocities (van Vossen *et al.*, 2004; Parolai *et al.*, 2009; Nakata and Snieder, 2012). Deconvolution interferometry has also found applications in estimating site specific Q values. Parolai *et al.* (2010) determined site related Q values by fitting the amplitude spectrum of the deconvolved wavefield using analytical models, and Parolai *et al.* (2012) derived Q by performing a full inversion of the spectrum.
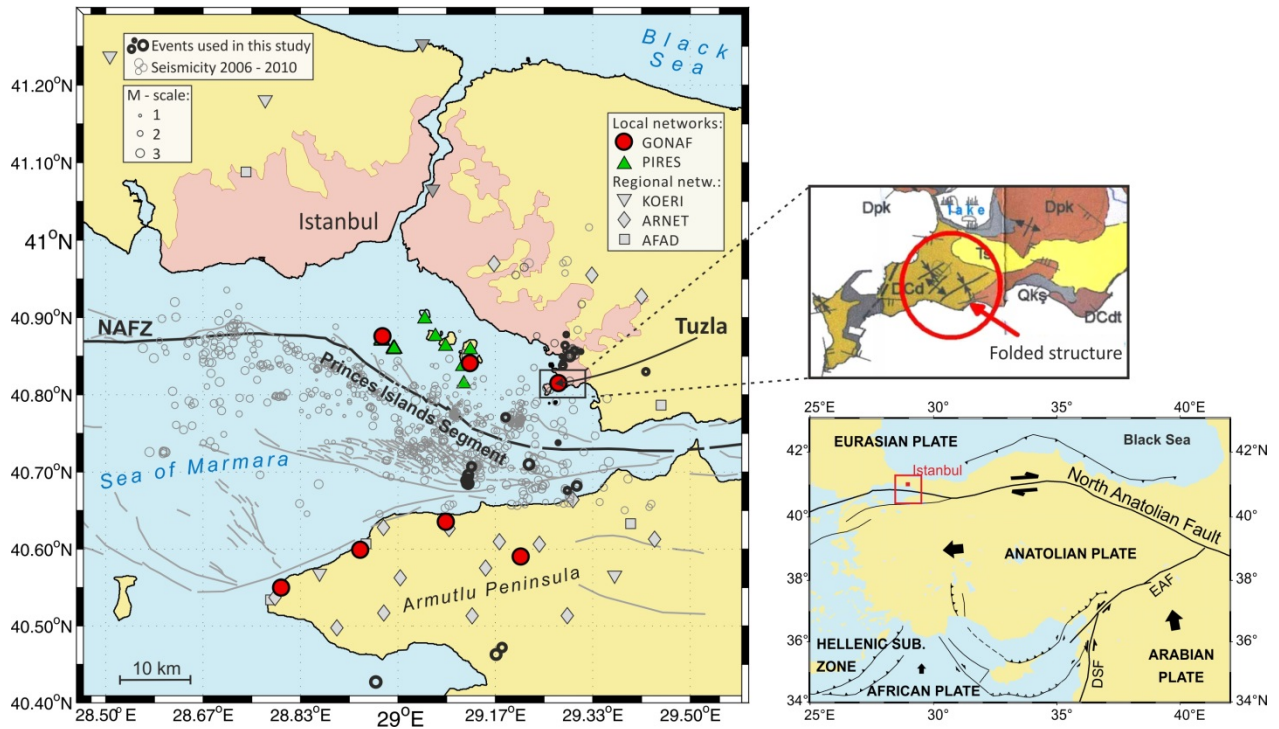
Figure 4.1: Right, bottom) Location map of the Anatolian region with the main tectonic features forming the North Anatolian Fault. The box marks the study area (enlarged left). Bold black arrows indicate the direction of plate motion with respect to stable Eurasia. **Left)** Map of the eastern Sea of Marmara showing the local microseismic activity (light gray circles, after Bohnhoff *et al.*, 2013) obtained from the island-based PIRES network and selected regional seismometer stations during 2006 – 2010. The GONAF wells with vertical seismometer arrays are indicated by bold filled circles. Black open circles are the earthquakes used in this study. Fault locations are from Armijo *et al.* (2005). The bold black line marks the Princess Islands segment and adjacent portions as the main branch of the NAFZ below the eastern Sea of Marmara. **Right, top)** Geological map showing the vicinity of the Tuzla area as the location of the GONAF borehole array (E. Arpat, personal comm. and report, 2012).

Time domain approaches for the estimation of Q are less common. For example Snieder and Şafak (2006) determined Q_S in a building by fitting the slopes of the logarithm of envelopes of deconvolved seismograms. Trampert *et al.* (1993) estimated Q_S between a 500 m deep borehole geophone and a surface seismometer by a time domain SH-propagator inversion. The theory of the propagator inversion technique was extended by Mehta *et al.* (2007) for the P-SV case for attenuating media. However, their paper did not provide an application of it to actually determine Q values.

In our data analysis we pairwise deconvolve the downhole recordings of the 26 events with their surface recordings. The deconvolution was also checked in the reverse sense, using the deepest sensor as reference. Instead of performing an inversion as proposed by Trampert *et al.* (1993), or analyzing the deconvolved wavevield in the frequency domain as proposed by Parolai *et al.* (2010, 2012), we forward modeled the deconvolved seismograms in time domain. With a grid search we found the seismic velocities for P- and S-waves V_P, V_S and quality factors Q_P and Q_S that best fit the data in a least squares sense.

For the estimation of effective velocities and quality factors we assumed a single homogeneous layer above each borehole sensor. With the further assumption that the P- and S-wave parameters can be determined independently the modeling procedure could be reduced to a simple 2-D grid search. Given that the interferometric results and logging data reveal the presence of a low-velocity layer, these strong heterogeneities bias our Q estimates.

The resulting Q values need to be regarded as apparent values that are mixtures of intrinsic and scattered attenuation and impedance effects.

4.2   Tectonic setting and the GONAF project

The North Anatolian Fault Zone (NAFZ) is a right-lateral strike-slip transform fault. It spans ~1300 km from eastern Anatolia to the northern Aegean Sea (e.g. Barka, 1992). It forms the plate boundary between the Anatolian plate in the south and the Eurasian plate in the north and slips at a rate of 20 – 30 mm/a (McClusky *et al.*, 2000). This kinematic framework is driven by the northward pushing Arabian plate in the east and the southward pulling rollback of the Hellenic subduction zone in the west (Flerit *et al.*, 2004; Bohnhoff *et al.*, 2005) (Fig. 4.1, right, bottom).

In the last century ~900 km of the NAFZ ruptured in a series of M > 6.7 earthquakes that started in 1939 near Erzincan in eastern Anatolia. This series then systematically propagated westward towards the Istanbul-Marmara area (Stein *et al.*, 1997). The most recent events occurred near Izmit and Düzce in 1999, which suffered M_W 7.4 and 7.1 earthquakes respectively (Tibi *et al.*, 2001; Barka *et al.*, 2002).

The only NAFZ segment that has not experienced a major earthquake since 1766 lies to the west of the Izmit rupture and below the Sea of Marmara. It is considered to be in the final stage of its seismic cycle, with a 35 – 70 % probability for a M > 7 earthquake to occur by 2034 (Hubert-Ferrari *et al.*, 2000; Parsons, 2004). The eastern part of this 'Marmara seismic gap' is located within 20 km of Istanbul's historic city center. Due to this regional seismic hazard and its associated risks, numerous local and regional seismic monitoring projects are being conducted along the seismic gap. One focus of these studies is the eastern part of the Marmara region offshore Istanbul.

For example, Bohnhoff *et al.* (2013) studied microearthquakes recorded by a near-fault seismic network on the Princes Islands – the PIRES network (Bulut *et al.*, 2009, 2011). Based on a four-year hypocenter catalogue, these authors identified a ≥ 30-km long aseismic fault patch extending down to 10 km depth south of the Princes Islands. They concluded that this sub-segment might be locked and thus represents a potential nucleation point for an impending Marmara earthquake. This view is also supported by GPS data (Ergintav *et al.*, 2014).

The recently implemented GONAF borehole observatory is part of an intensified monitoring effort in the eastern Marmara region. It includes seven vertical arrays of seismometers in ~300-m-deep boreholes. Five of these are on-land and two are on-island sites surrounding the eastern Sea of Marmara (Fig. 4.1, left). These stations are unique in that they make use of the only possible long-term on-land and near-fault sites surrounding the seismicity gap. Their borehole designs enable monitoring under low-noise conditions even in this highly populated area. As a consequence, the GONAF network has lowered the magnitude-detection threshold in the study area by two magnitude units with respect to the present regional networks, allowing the detection of nearly 2 orders of magnitude more seismic events (Prevedel *et al.*, 2015).

In this study we use recordings from the first GONAF borehole, completed in January 2013 on the Tuzla peninsula southeast of Istanbul (Fig. 1, left). The GONAF-Tuzla array consists of a three component (3C) Mark Products L4 seismometer with a natural frequency of 1 Hz at the surface, three L4 vertical component (1C) seismometers at ~75 m depth-spacing and a bottom sonde with two 3C Geospace geophones of 2 Hz and 15 Hz natural frequency, both in the same housing at 288 m depth (Fig. 4.2). More detailed information about the borehole construction and instrumentation is given in Prevedel *et al.* (2015). In the current study we use

data from May 2013. Up to mid May 2013 the sampling rate was 2000 Hz. It was reduced to 1000 Hz thereafter.

4.2.1 Local geology at Tuzla

The Tuzla peninsula was selected for a GONAF site due to its short distance to the Princes Islands seismic gap and a prominent seismicity cluster. It also has the advantage of being in some distance from the central-city-induced seismic noise. It is, however, still within a densely populated area that includes industrial infrastructure. The ground water level is shallow in this area at ~10 m depth. Drilling at this site was conducted in late 2012, during which cutting samples were taken every meter.

From the cuttings it appears that the 288-m-deep Tuzla borehole was drilled into a single limestone formation (E. Arpat, personal comm. and report, 2012). The cuttings have the lithological characteristics of the Tuzla Limestone, a member of the Denizli Köyü formation of late Devonian age. The thickness of the Tuzla Limestone at neighboring Marmara coastal sites is estimated to be ~60 m (Özgül, 2012). However, northeast-southwest-trending tight folds have been mapped in the eastern Istanbul area (Fig. 4.1, right, top), which makes it difficult to obtain a reliable thickness (Özgül, 2012). There is no information available on the inclination of the beddings, but it is possible that the substantial difference between the 288 m thickness obtained from the Tuzla cuttings and the 60 m estimated from outcrops can be explained by a steeply dipping limb of folded limestone beds. This is illustrated in a simplified sketch in Fig. 4.3a. Due to the lack of geological cross sections from the Tuzla area, the sketches in Fig. 4.3 are speculative, but are shown here to guide our interpretation of Tuzla data.

Additional information on the local structure comes from well-logging measurements down to a depth of 258 m (Jochem Kueck, GFZ report, personal comm., 2012). The P- and S-wave velocity profiles from the sonic log are displayed in Fig. 4.4. The sampling of these logs is 10 cm, which is substantially finer than the spatial resolution to be obtained from microearthquake waveform data, suggesting these data need to be averaged. Silva and Stovas (2009) have quantified to what extent different well-log averaging methods preserve lower-frequency seismic properties and how they are suitable for velocity model building. Following their results we generated our velocity model from the sonic log using Equation (4.1) for calculating interval velocities:

$$V_i = \left[\left(\sum_{n=1}^{N} V(n) \right) \middle/ \left(\sum_{n=1}^{N} V(n)^{-1} \right) \right]^{-1/2}, \tag{4.1}$$

where N is the number of sonic log velocity samples $V(n)$ within a given layer. We chose our layer boundaries to be at the sensor depths, at 71 m, 144 m and 215 m. The derived velocity model is presented in Fig. 4.4 and listed in Table 4.2.

Spectra of well log sequences usually follow a power-law scaling of $k^{-\alpha}$ with spatial frequency k and $\alpha \approx 1$. This rule is irrespective of rock type or observation scale (e.g. Shiomi *et al.*, 1997; Leary and Al-Kindy, 2002). The α value of the Tuzla P-wave log is 1.01, a typical value for fractured rock, whereas the value for the S-wave log is 0.28. This suggests that while the V_P log is a valid measure of the local P-wave velocity, the V_S log appears to be unreliable, perhaps due to some aspect of the logging procedure or well conditions.

The P-wave sonic log shows a complex seismic velocity structure. Most significantly, near-surface P-wave velocities of ~3600 m/s lie above a velocity inversion to less than ~3400 m/s

23

at ~90 m depth. This ~50 m thick interval is followed by an increasing trend to ~4100 m/s at the bottom of the well log at 258 m.

This P-wave sonic log seems somewhat at odds with the uniform lithological character of the well cuttings. However, some features of the other types of well logs also indicate a more heterogeneous layering (see Fig. D1 in Appendix D). We observe relatively low resistivity values for the interval of ~85 m to ~105 m, and irregularities in the hole diameter caliper log at ~90 m to ~140 m depth. While these irregularities are not enough to account for the observed low velocities, they do add to their uncertainties. The resistivity and caliper logs might be interpreted as an indication for a weak zone, perhaps of thrust faulting origin. Thus, another possible explanation for the unexpected thickness of the limestone layer could be repetition of the sequence as a result of thrust faulting associated with the local folding (Esen Arpat, personal comm., 2015) (Fig. 4.3b).
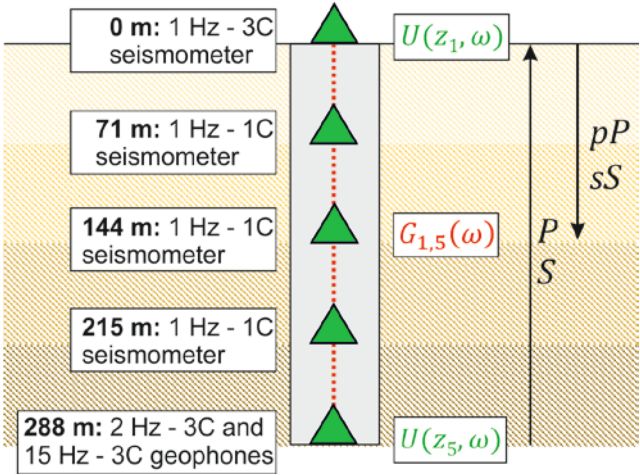

Figure 4.2: Sketch of the GONAF-Tuzla vertical borehole array and experiment geometry. Instruments are indicated with triangles and the direct P- and S-waves (P, S) and their corresponding surface reflections (pP, sS) are sketched with arrows. Details of the instrumentation are described in Prevedel *et al.* (2015).
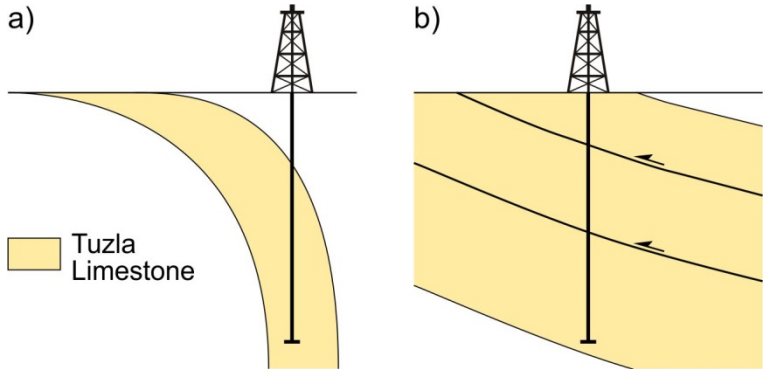

Figure 4.3: Sketch to illustrate two possible models derived for the observed 288 m deep Tuzla Limestone formation. **a)** The borehole was drilled into a steeply dipping limb of folded limestone beds. **b)** The borehole was drilled into a repeating sequence of the Tuzla Limestone caused by thrust faulting.
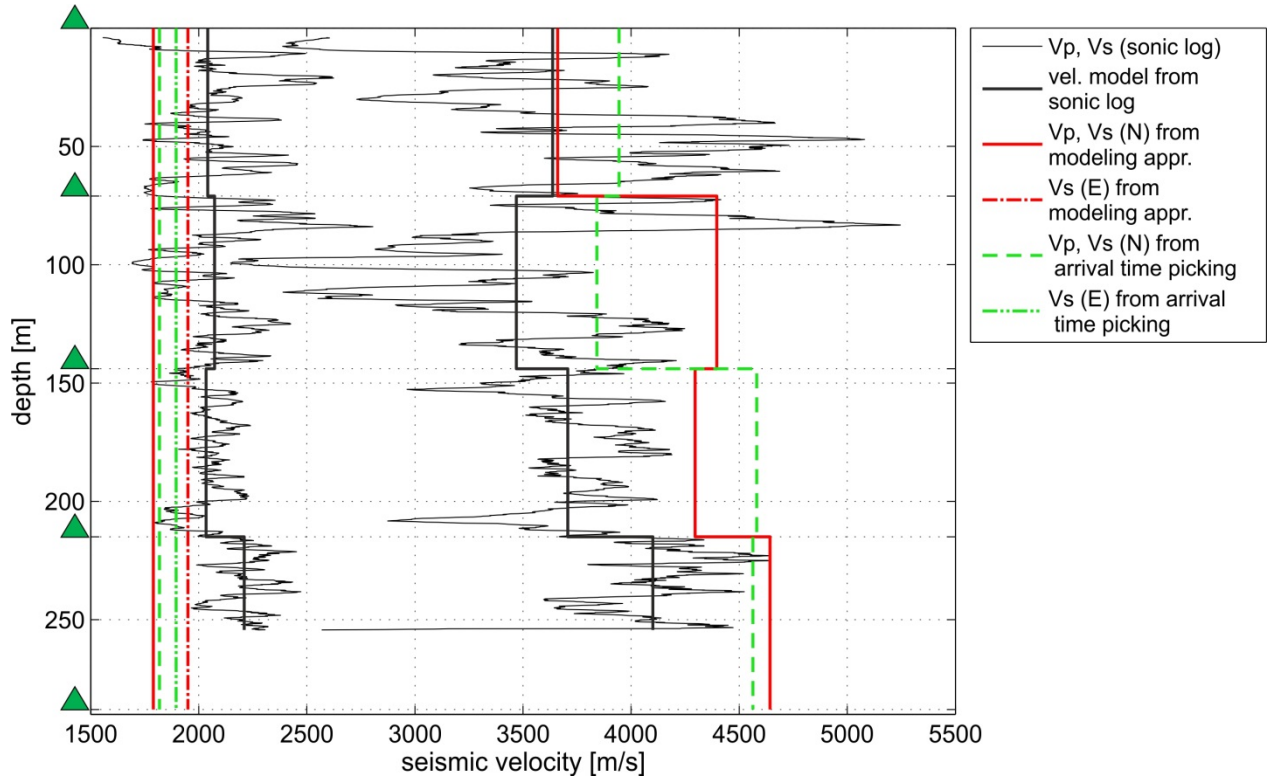
Figure 4.4: Sonic-log velocities (black thin line) and P and S-wave velocity model derived from the sonic log (black bold line) are presented together with the velocity models obtained from the modeling approach and from arrival-time picking in the deconvolved seismograms. For the S-wave velocity different results are obtained from the E and N components, thus both values are shown. Triangles on the left indicate the positions of the borehole geophones along the well (see Fig. 4.2).

4.3 Dataset

We used both GONAF-Tuzla (vertical array) and PIRES (island-based surface stations) waveform recordings to compile a local hypocenter catalog to study near-surface wave propagation effects. For earthquake detection we applied a short-term average / long-term average trigger to the vertical component signals from all of these stations. A seismic event was declared when three or more verticals triggered within a time window of 5 s. We also took into account events that were too weak to be detected on the surface PIRES stations, but detected with the GONAF-Tuzla borehole array. In the May 2013 time period considered here, 188 events were detected by the combined network. Of these, 153 could be located using the *HYPOCENTER* computer code (Lienert *et al.*, 1986) and the optimized 1-D velocity model for the eastern Marmara region of Bulut *et al.* (2009).

For this study we selected events with signal-to-noise ratios > 4 at the GONAF-Tuzla sensor at 215 m depth. The ratio was calculated by dividing the root-mean-square amplitude of the first 0.3 s of the P-wave train by that of a 10 s noise window before the P-wave arrival. A total of 26 events with duration magnitudes from 0.6 to 2.9 and hypocentral distances from 7 to 51 km from the GONAF-Tuzla array fit this criterion (black open circles in Fig. 4.1 and list of earthquakes in Tab. 4.1). The seismograms from all the 1 and 2 Hz sensors for these events were used to analyze the wave propagation effects in the shallowest layers.
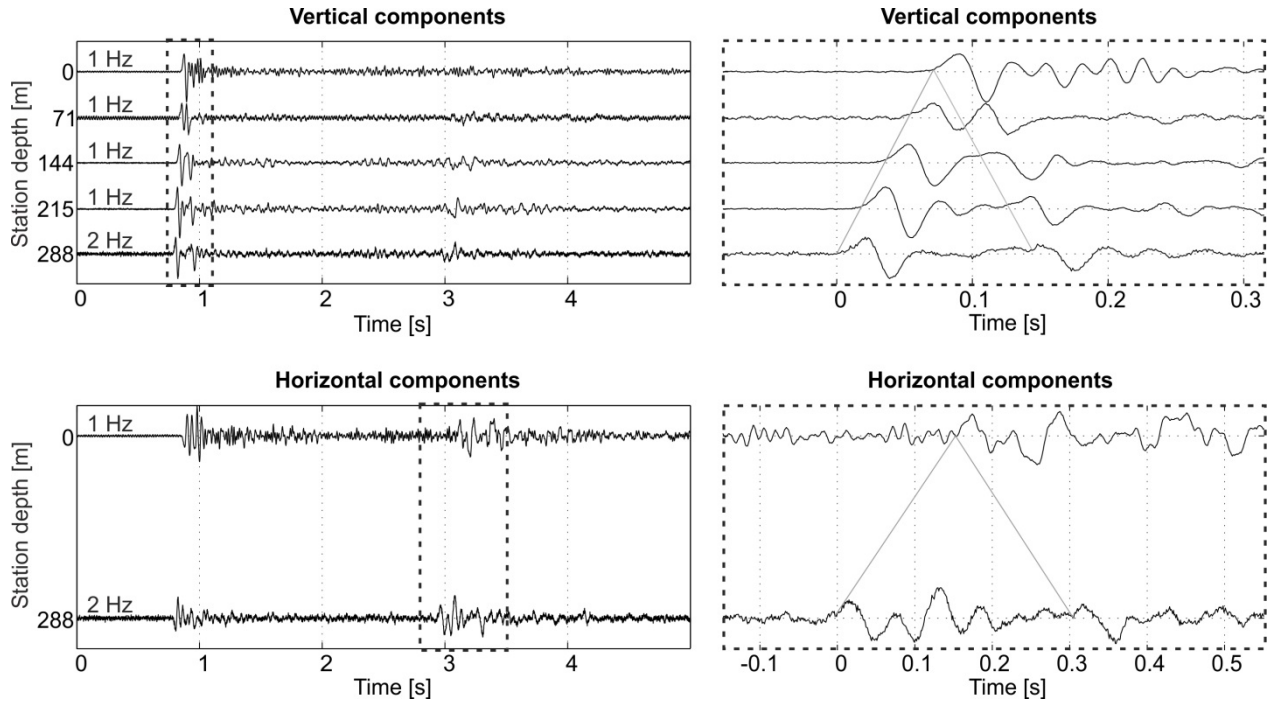
Figure 4.5: Waveform example from vertical and north-south horizontal components of the GONAF-Tuzla array. The respective sensor depth is plotted at the y-axis and each trace is normalized to its maximum. The instrument response has been corrected for and the seismograms are otherwise unfiltered. Note that only the surface station and the very deepest sensor have horizontal components. **Left** hand side figures show complete waveforms of event 18 (Table 4.1) and the **right** side figures present close up windows of the same event containing only the P-wave (top) and S-wave (bottom), respectively. The direct upgoing P- and S-waves and their corresponding downgoing surface reflections are marked with gray lines.

Fig. 4.5 shows an unfiltered, but instrument corrected, waveform example from the GONAF-Tuzla array for event number 18 in Table 4.1. The upgoing direct P- and S-waves and their corresponding downgoing surface reflections (pP and sS) can be clearly seen in these seismograms. As expected, the attenuation of the waves as they travel to the surface and then down again significantly reduces their amplitudes. At the surface station one also sees reverberations following the direct P-wave. As we will discuss, these secondary arrivals are observed for many events and appear to be due to the shallow subsurface structure.

Table 4.1: Source parameters of the 26 earthquakes used for shallow wave-propagation study.

Event	Date, Time (UTC)	Longitude	Latitude	Depth [km]	Magnitude [M_D]	Hypocentral distance [km]
1	2013/5/1 17:43:50.8	29.1680	40.4630	8.2	2.7	41.0
2	2013/5/1 22:43:46.5	29.3020	40.8570	7.8	1.8	9.4
3	2013/5/1 23:13:51.9	29.2940	40.8500	7.3	2.6	8.4
4	2013/05/03 00:36:10.2	29.184	40.771	8.5	2.0	12.4
5	2013/05/03 12:17:23.1	29.282	40.842	7.2	1.1	7.8

6	2013/05/03 09:45:10.7	29.424	40.83	0.4	1.7	12.7
7	2013/05/05 20:34:24.0	29.313	40.856	5.0	-	7.5
8	2013/05/07 09:41:39.8	29.286	40.864	4.6	1.7	7.2
9	2013/05/09 04:53:4.5	29.12	40.685	8.6	2.7	21.3
10	2013/05/09 05:37:9.4	29.126	40.707	11.0	2.2	20.5
11	2013/05/09 06:05:48.5	29.117	40.689	11.6	2.5	22.5
12	2013/05/10 01:59:14.9	29.119	40.691	9.9	1.9	21.5
13	2013/05/10 08:24:42.1	29.119	40.691	9.1	2.4	21.1
14	2013/05/10 23:57:18.9	29.12	40.686	8.7	2.4	21.2
15	2013/05/11 09:52:7.8	29.28	40.85	6.0	0.9	7.2
16	2013/05/12 04:32:39.4	29.118	40.685	7.8	2.4	21.1
17	2013/05/12 23:16:13.6	29.29	40.676	7.2	1.7	17.1
18	2013/05/12 23:43:35.1	29.306	40.682	9.0	2.4	17.5
19	2013/05/14 14:26:49.5	29.288	40.878	0.6	1.2	7.1
20	2013/05/18 20:02:27.1	29.286	40.857	5.6	0.6	7.3
21	2013/05/19 19:42:21.3	29.178	40.472	7.7	2.3	39.8
22	2013/05/19 22:16:41.0	29.12	40.696	11.4	2.5	21.8
23	2013/05/21 10:05:23.3	28.962	40.427	0.0	2.9	50.6
24	2013/05/24 20:24:40.9	29.274	40.738	8.0	-	11.7
25	2013/05/26 00:11:45.8	29.224	40.71	9.1	2.6	15.4
26	2013/05/30 07:49:52.7	29.282	40.838	7.9	1.9	8.3

Table 4.2: Seismic interval velocities between the sensors of the GONAF-Tuzla array derived from sonic logs and arrival-time picking. Velocities are derived from sonic-log measurements using Eq. (4.1) and from arrival-time picking of the direct P- and S-waves in the deconvolved seismograms with the downhole sensor at 288 m depth used as reference (Fig. 4.7a and b, bottom, left).

Depth [m]	Sonic log		Arrival-time picking	
	V_P [m/s]	V_S [m/s]	V_P [m/s]	V_S [m/s] (N/E)
0 – 71	3637	2042	3944 ± 46	
71 – 144	3469	2073	3842 ± 40	$1818 \pm 3 / 1895 \pm 3$
144 – 215	3707	2034	4581 ± 63	
215 – 288	4100	2210	4563 ± 13	

4.4   Method

One aim of the GONAF effort is to determine the P- and S-wave velocity and attenuation structure for each borehole site. A common method used to find the quality factor Q is the spectral ratio technique (e.g. Gibbs *et al.,* 1994; Parolai *et al.,* 2007; Ge *et al.,* 2009). It typically begins by computing the ratio of the Fourier spectra of isolated P and S waves between the surface and downhole seismograms, after taking into account instrument responses and other gain factors not related to attenuation. At the Tuzla site the traveltime differences between P and pP and S and sS at the 288 m deep sensor are only ~0.13 s and ~0.32 s, respectively. These separations are relatively short compared to other studies (e.g. Blakeslee and Malin, 1991; Bethmann *et al.*, 2012). This limits the bandwidth over which the spectral ratios can be fit with a constant Q model, $Q = -\pi \delta t m^{-1}$, m being the slope of the ratio and δt the traveltime difference between the recording levels (Aki and Richards, 2002). These and other interference effects result in meaningless Q values.

In order to make use of the complete wavefield, including the signals from downgoing waves, we chose instead to apply a seismic interferometry approach to determine the characteristics of the Tuzla site. This approach also allowed us to determine the velocity structure between the borehole sensors. Several algorithms exist for interferometry, but here we focus on the deconvolution technique (e.g. Trampert *et al.*, 1993; van Vossen *et al.*, 2004; Mehta *et al.*, 2007; Parolai *et al.*, 2009; Nakata and Snieder, 2012).

We first applied instrument response corrections to each seismogram and assumed near-vertical incidence at the bottom sensor and that all sensors in the borehole are subject to the same source and path effects (from the source to the deepest sensor). The deconvolution of the earthquake signal at sensor at depth z_1 with that at depth z_2 yields the plane wave Green's function $G_{1,2}$ for propagation from z_2 to z_1. This can be written in frequency domain as

$$G_{1,2}(\omega) = \frac{U(z_1, \omega)}{U(z_2, \omega)}, \qquad (4.2)$$

where ω is the angular frequency and $U(\omega)$ is the Fourier spectrum of the seismogram. The fraction in Equation (2) also can be turned around to yield the Green's function for propagation from z_1 to z_2.

Since the signals are band-limited, contaminated by background noise, and contain site related notches in their spectra, the spectral division in Eq. (4.2) is inherently unstable. To prevent this instability a regularized deconvolution is typically used. We tested two different regularizations. The first is used for example by Mehta *et al.* (2007), Parolai *et al.* (2009) and

Nakata and Snieder (2012), and the second is the method of Helmberger and Wiggins (1971) and Dey-Sarkar and Wiggins (1976). The first turned out to be more stable for our data, and is given by:

$$G_{1,2}(\omega) \approx W(\omega) \frac{U(z_1, \omega)}{U(z_2, \omega)},$$
(4.3)

where

$$W(\omega) = \frac{|U(z_2, \omega)|^2}{|U(z_2, \omega)|^2 + \varepsilon}$$
(4.4)

is the filter, hence

$$G_{1,2}(\omega) \approx \frac{U(z_1, \omega) U(z_2, \omega)^*}{|U(z_2, \omega)|^2 + \varepsilon}.$$
(4.5)

The regularization parameter ε refers to a constant added to the denominator to prevent numerical instabilities in Eq. (4.2) (e.g. Parolai *et al.*, 2009). It is chosen as a percentage of the average spectral power of $U(\omega)$ at the station selected as reference. Tests have shown that an ε of 3 % seems to be the appropriate value for our data.

4.5   Data Processing

In order to use the horizontal components of the surface and downhole sensors it is necessary to rotate the downhole horizontal components into N and E directions so that their orientation equals the orientation of the surface horizontal components. How the rotation angle is determined is explained in detail in Appendix A.

After orienting the downhole horizontal components the seismograms of all channels were then rotated into radial and transverse directions and corrected for instrument response and DC offset. As in previous deconvolution studies (Mehta *et al.*, 2007; Parolai *et al.*, 2009), our results were insensitive to the data window selection. Accordingly, we chose to use windows containing the complete signal of the event. This data window was tapered to avoid spectral leakage.

The deconvolution was performed by applying Eq. (4.5). The bandwidth of the deconvolution was set to 0.1 to 40 Hz, as all 26 events have energy at least up to ~40 Hz (see spectra in Fig. D2 – D14 in Appendix D). The lower limit of the bandpass turned out to be helpful in removing very-low-frequency noise, but its influence on the deconvolution result was only minor. Thus, a low corner frequency of 0.1 Hz was chosen to include as many octaves of bandwidth as possible. As the last step all the deconvolved spectra are inverse Fourier transformed into time domain and then stacked to improve the signal-to-noise ratio. The stacking requires the assumption of nearly vertical incidence, meaning equal moveouts along the borehole for all events. We checked these times in the deconvolved seismograms and found only minor traveltime differences of < 0.01 s. Fig. 4.6 shows the surface-to-144 m vertical component deconvolution results for each event and their stacking result.
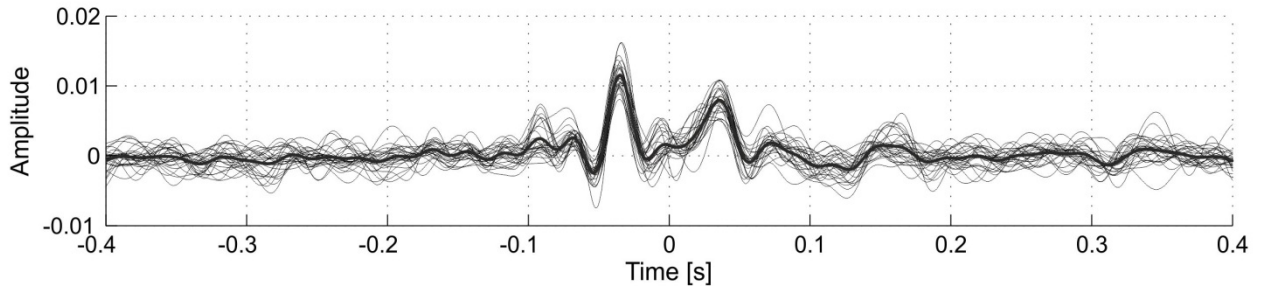
Figure 4.6: Seismograms from the sensor at 144 m depth after deconvolution from the surface signal. Thin traces show the results from each of the 26 events. The bold trace is the stacked deconvolved seismogram.

4.6   Deconvolution results and discussion

Fig. 4.7a and b display the deconvolved seismograms with the surface and 288 m sensor used as reference. When the signal at the surface is used as reference the upgoing waves are mapped onto times before their surface arrival. Thus the up- and down-going waves are symmetric around the surface arrival time, which is taken to be the zero reference. When the 288 m sensor is used as reference, all the signals appear after its arrival time. In Fig. 4.7a each trace is normalized to its maximum to show the relatively small downgoing signal amplitudes at the deepest sensor. To allow for amplitude comparisons between different depth levels, each trace in Fig. 4.7b is normalized to the maximum of the entire array.

Fig. 4.7b shows clearly how the amplitude of the upgoing wave decreases while propagating from 288 m to 71 m depth. However, in the upper tens of meters between the sensor at 71 m depth and the surface the amplitude increases. After correcting for the free surface amplitude factor of 2 the surface sensor still records a 1.7 times stronger signal than the sensor at 71 m. This factor of 2 is only correct for vertically incident and SH waves. For P- and SV-waves it varies with incidence angle and can be even below 1 (Shearer and Orcutt, 1987). The amplitude increase in the upper few tens of meters indicates that in these shallow depths at the Tuzla site amplification due to impedance contrasts influences the waveforms more strongly than the effects of attenuation. If these impedance effects are not taken into account, it is only possible to determine an apparent attenuation, as will be discussed later.

The average seismic velocities between sensors can be calculated from the traveltime differences between them in the deconvolved records (Table 4.2 and Fig. 4.4). Since only the surface sensor and the sensors at 288 m depth have horizontal components, an average S-wave velocity could be determined only between them.

The arrival time picking of the direct upgoing P-wave shows that a strong change in P-wave velocity exists somewhere between 71 m and 215 m depth (Fig. 4.7a and b, bottom left). Further, two reflected P-waves can be seen in the deconvolved seismograms. These are marked with gray dashed lines in Fig. 4.7. The upgoing reflected wave, seen on the bottom left in Fig. 4.7a and b, and the downgoing reflected wave, seen on the top left in Fig. 4.7a and b appear to originate from an interface between the sensors at 71 and 144 m. Such a horizon could correspond to the low-velocity zone evident in the sonic log velocity profile between ~90 and ~140 m depth (Fig. 4.4). Reassuringly, the polarities of the reflected waves agree with the presence of a low-velocity layer. The reverberations after the direct P-wave arrival at the surface sensor seen in the unfiltered seismograms (Fig. 4.5) could be created by multiple reflections from this layer.
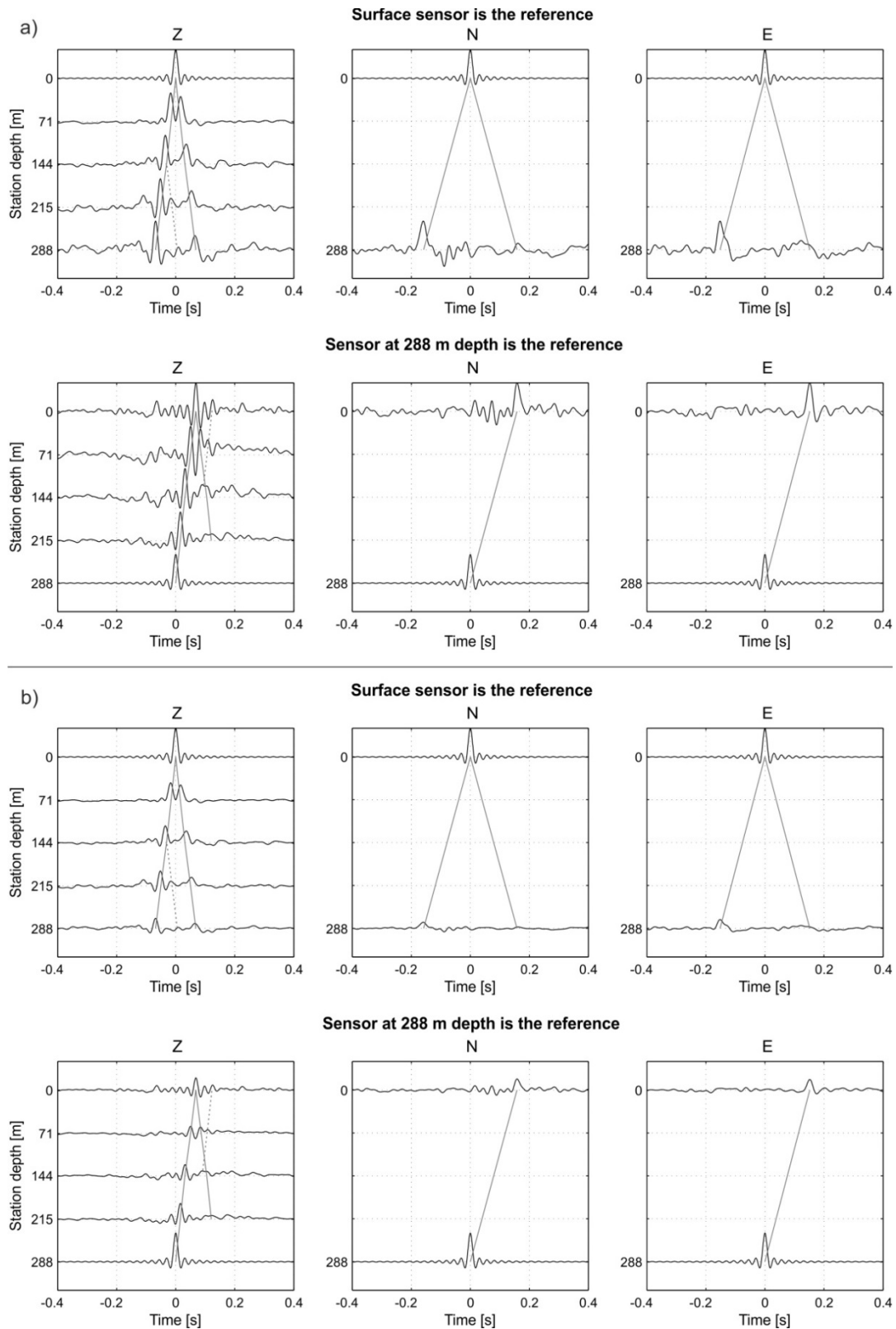
Figure 4.7: Stacked deconvolved seismograms from vertical and horizontal components. Once the surface sensor is used as reference sensor (top) and the other time the sensor at 288 m depth is used as reference (bottom). Gray solid lines mark the traveltimes of the direct up- and down-going waves and dashed gray lines indicate reflected phases. **a)** Each trace is normalized to its maximum. **b)** Each trace is normalized to the maximum of the entire array.

The arrival time picking of the S-wave suggests that the S-wave velocity appears to be 4 % slower on the N component than at the E component. This could be an indication of shear-wave splitting – a difference in S-wave velocity as a function of azimuth – rather than an artefact of the method. The eastern Sea of Marmara is known to show this type of anisotropy as reported by Hurd and Bohnhoff (2012) and Eken *et al.* (2013). The S-anisotropy in the depth range of ~3 to ~10 km was estimated to be ~1 – 3 %. Moreover, Eken *et al.* (2013) also found the fast polarization direction north of the Princes Islands segment to be parallel to the main NAFZ strand, and along maximum horizontal stress direction, S_{Hmax} ~N125°E (Kiratzi, 2002; Bohnhoff *et al.*, 2006). These observations could account for the splitting direction seen at Tuzla. A further indication for having a true shear-wave splitting observation in our data is that following Nakata and Snieder (2012) deconvolution interferometry can be used for shear wave splitting analysis, which however, would be beyond the scope of this study.

4.7 Forward modelling

We modeled the deconvolved seismograms from the Tuzla site with the layered, frequency-wavenumber propagator method of Wang (1999). The source for these time-domain synthetic seismograms was placed 1 km directly below the receiver points. The aim was to obtain a first order estimate of the apparent P- and S-wave Q values and to refine the velocities of the layers between the sensors.

Because of the uncertainties introduced by the unconstrained structures evident at the Tuzla site, we chose to reduce the layering above each sensor to a single, homogeneous, effective unit. This approach allowed us to use a grid search method for the best fit model. It resulted in four different effective P-wave velocity and attenuation models, covering the depth ranges 0 – 71, 0 – 144, 0 – 215, and 0 – 288 m. The effective S-wave velocity and quality factor were determined for a homogeneous layer between the horizontal components at 0 – 288 m. These effective parameters are indicated here by an over-bar, as in $\overline{V_P}$ versus V_P for the interval velocities, and $\overline{Q_P}$ for the effective quality factors. We discuss later how these values relate to ones that might have been obtained for the individual intervals.

After the computation of synthetic seismograms the same processing steps as for the observed waveform data were applied and then the results compared to the observations. In our grid search, we sought to find the minimum misfit between the observed amplitudes and arrival times of the up- and down-going waves (A_u^o, A_d^o and t_u^o, t_d^o) and their corresponding synthetic values (A_u^s, A_d^s and t_u^s, t_d^s), as given by

$$m(V, Q) = \sqrt{(A_u^o - A_u^s)^2 + (A_d^o - A_d^s)^2 + (t_u^o - t_u^s)^2 + (t_d^o - t_d^s)^2} \,. \qquad (4.6)$$

To reduce computation time this 4-D grid search (V_P, Q_P, V_S and Q_S) was separated into two 2-D searches, with the P- and S-wave parameters being determined independently. Q_S and V_S for SH waves are inherently independent of Q_P and V_P. For the P-SV case, the S-parameters are held fixed while determining V_P and Q_P, and similarly for Q_S and V_S. Also, under the assumption of frequency constant Q_P, V_P could be determined independently from the other parameters, since it depends only on the arrival times of the P-wave. Only Q_P has a dependency on both, P- and S-wave velocity, because it is determined from the amplitude of the P-wave recording which in turn depends on the impedance contrast that is controlling the amount of energy reflected and refracted as P-wave and converted S-wave. Under the assumption of vertical incidence, these conversions are reliable. Nevertheless, even if this assumption is broken, if the S-wave velocity is fixed to a value close to the true value the error in Q_P introduced by this simplification will be small, as we will show. For the P- and S-

wave parameters we searched a range of velocities from 3000 – 4600 m/s and 1600 – 2100 m/s, and quality factors from 1 – 100 and 1 – 50, respectively.

The misfit functions are presented in Fig. 4.8, with their minima marked by a white dot. For all three components we observe that in the misfit functions the apparent Q values are well constrained, whereas the velocities appear less well constrained. Nonetheless, clear minima can be observed for the horizontal components, but less so for the vertical components. To better constrain the velocity, tests have shown that the terms in Eq. (4.6) containing the arrival times should be weighted more heavily than the amplitude terms. This however, reduces the capability for resolving Q. Since we already have good velocity information from sonic log data and arrival time picking in the deconvolved seismograms, we decided against a velocity weighted misfit function to obtain better constrained Q values. On the E component the velocity and Q are less constrained compared to the N component. This is because the downgoing wave is poorly resolved on the E component due to interference with two peaks that precede its arrival (Fig. 4.7a, top right).

The best-fit model effective velocities and quality factors are summarized in Table 4.3. We observe increasing Q_P with increasing depth and $\overline{Q_P}(288 \text{ m}) \approx 2\overline{Q_S}(288 \text{ m})$, which is in good correspondence with theory. Overall, the average P-wave velocities obtained from the modeling approach are very similar to the P-wave root-mean-square velocities derived from the arrival time picking. Going from the shallowest homogeneous layer to the deepest these are 3944 m/s, 3892 m/s, 4106 m/s, and 4217 m/s. The effective P-wave velocities obtained from the modeling approach can be transferred to interval velocities using the Dix Equation (Dix, 1955) (see Table 4.3). These values are in contrast to the velocities derived from arrival time picking and the P-wave sonic log: the forward modeling places a more modest low velocity layer at a deeper depth.

Figure 4.9 presents the modeled seismograms computed with the parameters listed in Table 4.3 in comparison to the observed deconvolved seismograms. The modeled up- and down-going S- and P-waves on the N and Z components fit better than on the E component. This can be explained by the weak downgoing S-wave on the E component which interferes with two preceding signals.

Table 4.3: Effective seismic velocities and apparent quality factors obtained from the forward modeling approach. The parameters marked with over-bars are the effective velocities and apparent quality factors corresponding to a homogenous layer between the surface and the sensor. S-wave parameters could be determined for the depth range 0 – 288 m only and they were derived independently on the N and E components. The parameters written without over-bar correspond to a specific depth interval.

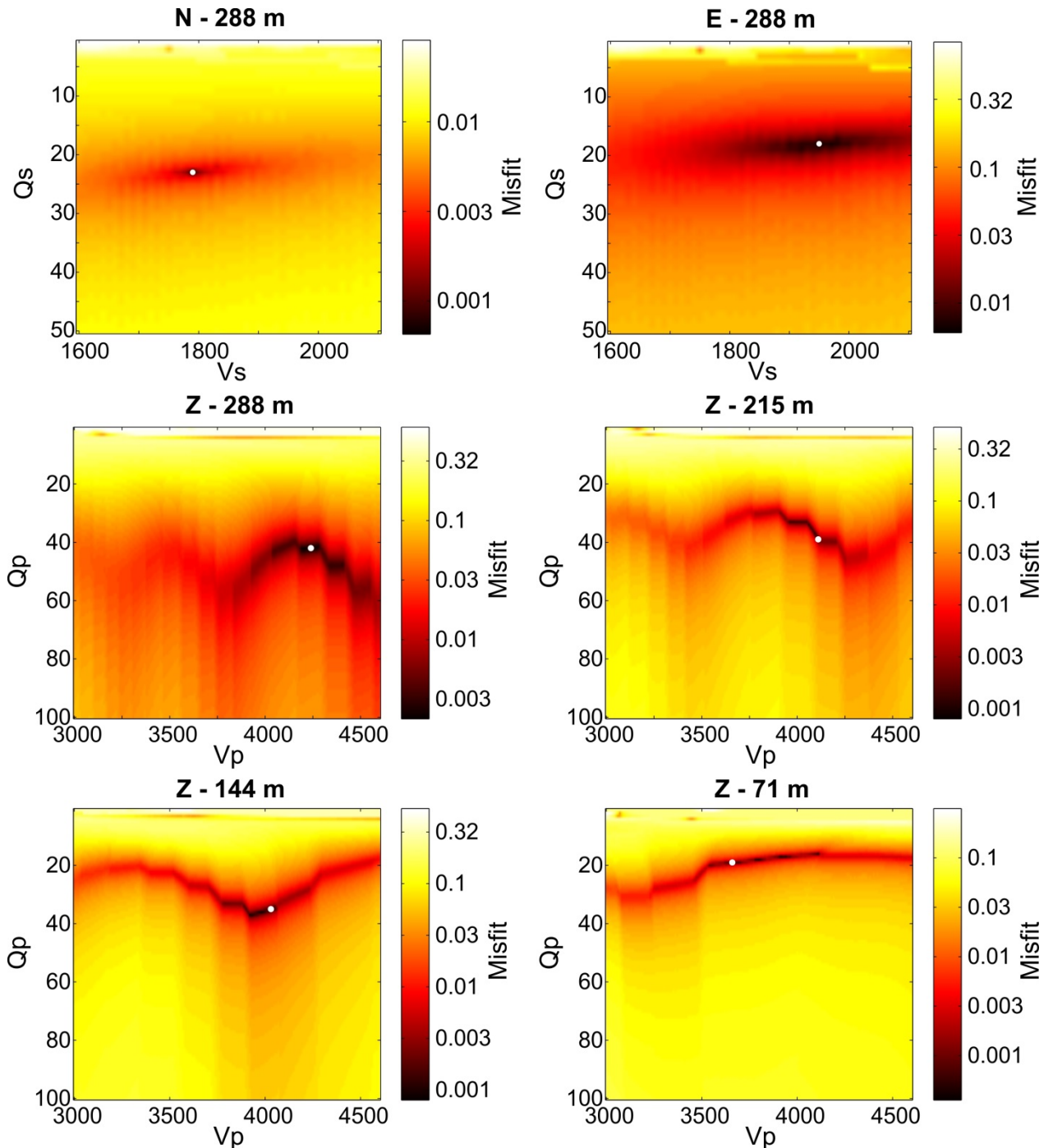| Depth [m]	$\overline{V_P}$ [m/s]	$\overline{Q_P}$	$\overline{V_S}$ [m/s] (N / E)	$\overline{Q_S}$ (N / E)	Depth [m]	V_P [m/s]	Q_P
0 – 71	3660	19			0 – 71	3660	19
0 – 144	4030	35			71 – 144	4396	160
0 – 215	4110	39			144 – 215	4296	54
0 – 288	4240	42	1790 / 1950	23 / 18	215 – 288	4643	56

33

Figure 4.8: Misfit functions of all three components for the sensor at 288 m depth and for all verticals. The horizontal components N and E were used for the determination of V_S and Q_S and the vertical Z components for the determination of V_P and Q_P. The white dot marks the minimum of each misfit function.

4.7.1 Error analysis

From Figures 4.8 and 4.9 it can be concluded that our simple forward modeling approach gives well constrained velocities and apparent quality factors. However, the simplifications of (1) a homogeneous layer and (2) deriving P- and S-wave parameters independent from each other can introduce significant errors. To evaluate these we computed synthetic seismograms for several models. These include one-layer models, two-layer models (with both, a faster

layer over a slower layer and vice versa), and four-layer models based on the sonic logs and the velocities derived from the modeling approach and arrival-time picking. To define S-wave velocities for the shallower layers in the four-layer models a V_P/V_S ratio of 2.27 [i.e. $\overline{V_P}$(288 m)/ $\overline{V_S}$ (288 m)] was assumed. The modeling approach results and the ones from arrival time picking give this same V_P/V_S ratio. For Q values for each layer of the four-layer models we use equation (2) in Tonn (1991) for the calculation of interval Q_P values from the effective values obtained from the modeling approach. The interval Q_P values are 19, 160, 54 and 56 from the shallowest to the deepest layer. The interval Q_S values are set to $Q_P/2$.

We apply to the synthetic data the same forward modeling approach as used for the recorded waveform data. While performing the grid search for V_S and Q_S, the P-wave velocity was fixed to 4200 m/s ($V_{P,mod}$). This is close to the root-mean-square velocity of a homogeneous layer above the sensor at 288 m, as determined from arrival time picking in the deconvolved seismograms. During the grid search over V_P and Q_P the S-wave velocity was fixed to 1850 m/s ($V_{S,mod}$). This is between the two S-wave velocities derived from arrival time picking: 1818 m/s and 1895 m/s on the N and E components, respectively. During the error analysis we evaluate how the error depends on the difference between the fixed velocity (V_{mod}) and the real one (V_{real}). We call the difference between these velocities ΔV.

The error estimates from the one-layer models and the four-layer models are summarized in Table 4.4. As expected the simple one-layer models yield very small errors for V_S and also Q_S. Furthermore, we did not observe a dependency of the S-wave parameters on ΔV, which is also as expected, as they are determined from the SH component which does not contain P-wave energy. The four-layer models also show small errors in V_S, but the errors in Q_S increased noticeably due to the unconstrained impedance contrasts between the sensor levels.
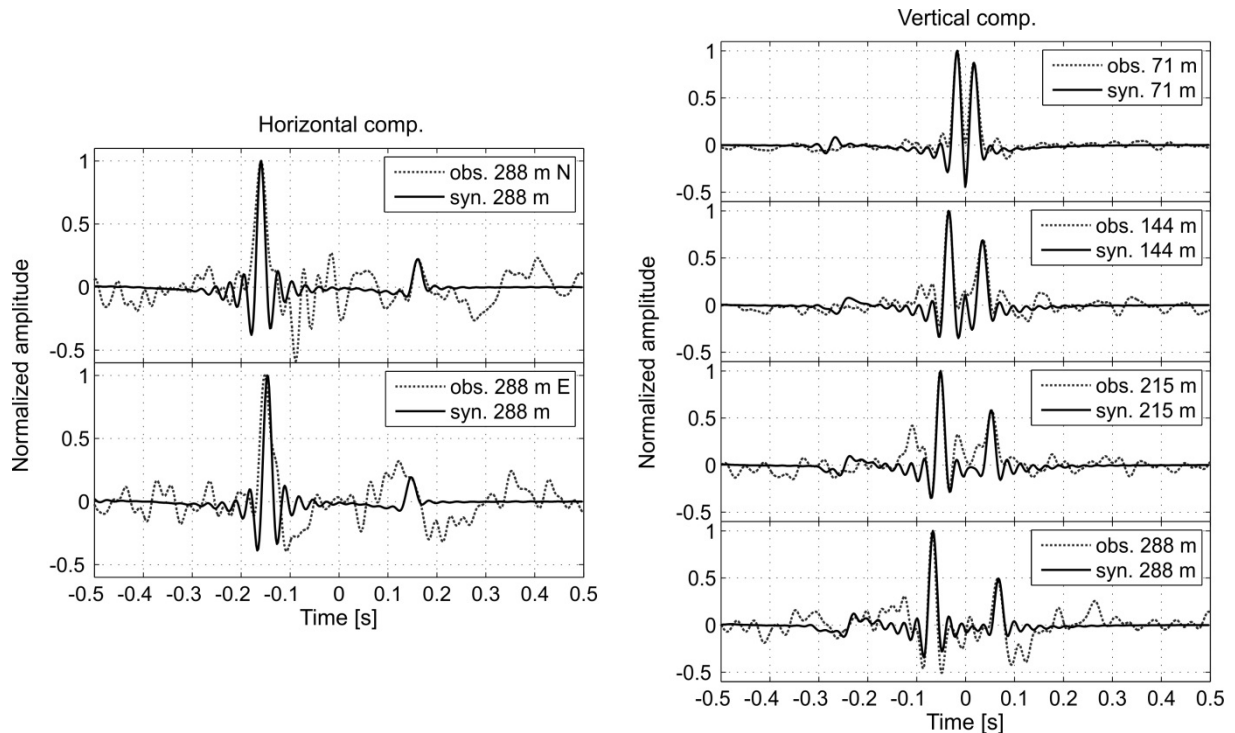

Figure 4.9: Comparison of waveforms of the observed and synthetic deconvolved seismograms. The solid traces show the deconvolved synthetic seismograms for the best fit (parameters are listed in Table 4.3). The observed deconvolved seismograms are plotted with a dotted line.
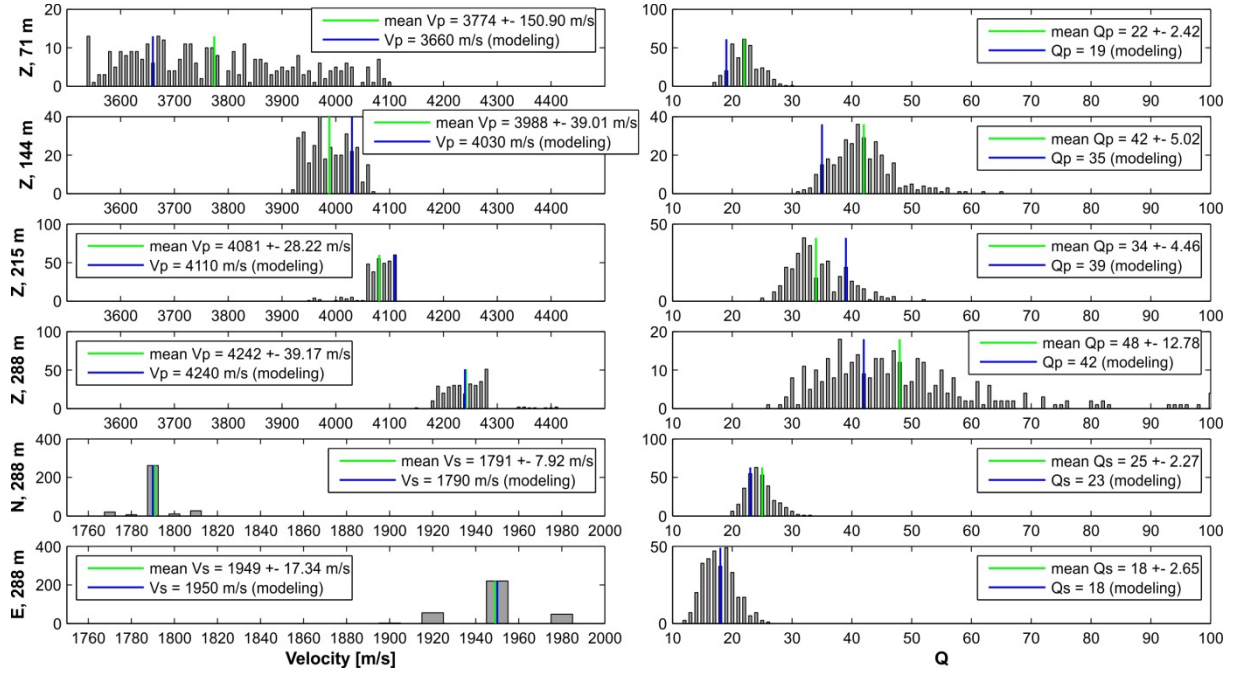
Figure 4.10: Results of Jackknife test. The histograms present the distribution of results obtained from each subset. Left and right figures present the results for P- and S-wave velocity and quality factors, respectively. The mean and standard deviation and results of the modeling approach are marked with lines and given in the legend.

The errors in V_P for the one-layer and four-layer models are similar to the errors of V_S. It also appears that V_P is insensitive to changes in ΔV. In contrast, it is more difficult to evaluate the error in Q_P due to its strong dependency on ΔV. The range of errors in Q_P given in Table 4 are based on the assumption that $V_{S,real}$ differs from $V_{S,mod}$ not more than ± 10 %. The first table value corresponds to -10 % ($V_{S,real} > V_{S,mod}$) and the second to +10 % ($V_{S,real} < V_{S,mod}$). A negative error implies that Q_P is underestimated and positive values correspond to overestimation. We observe that the modeling approach has a tendency to overestimate the P-wave quality factor. Keeping in mind that $V_{S,mod}$ has been chosen based on the S-wave velocity measured on the deepest sensor, $V_{S,real}$ at the shallower sensors is probably smaller than $V_{S,mod}$. Hence the expected error in Q_P corresponds to $\Delta V = +10$ % rather than the value given for -10 %. Considering that $V_{S,mod}$ is close to the S-wave velocity determined from arrival time picking at 288 m depth, the range of ± 10 % is probably too large for the deep sensors. For the shallower sensors this range could be realistic.

In summary, it appears that the simplification of a homogeneous layer over each sensor has only a minor effect on V_S and V_P, while the errors in the P- and S-wave quality factor increase with increasing model complexity. The simplification of determining V_S and Q_S independent from V_P and Q_P only affects the accuracy of Q_P.

The errors of the velocities and Q depend also on the stability of the deconvolution result of the observed data. To evaluate this we performed a Jackknife test. To do this test, we successively removed two different earthquakes from the 26 events. For each subset the stacked deconvolved seismograms were computed and the amplitudes and arrival times of the up- and down-going waves determined. They were then forward modeled by minimizing Eq. (4.6) to determine the velocities and quality factors. These results are presented in Fig. 4.10 in form of histograms which show the distributions of V and Q. Since Q depends on the logarithm of the amplitude ratio between up- and down-going waves we observe a lognormal distribution of Q (Fig. 4.10, right). Hence, for Q, the logarithmic mean and standard deviation was calculated. In contrast to that there is no specific distribution observable for V (Fig. 10, left). We calculate for V the mean and standard deviation of a normal distributed dataset. The

values of the mean and standard deviation of Q and V are given in the legends in Fig. 4.10. These calculations show that the deconvolution results are mostly stable. However, for the sensor at 71 m depth we observe a larger standard deviation of V_P of ~4 % and for the sensor at 288 m depth Q_P has a large standard deviation of ~27 %.

The errors of the velocities derived from arrival time picking in the deconvolved seismograms are determined with the same Jackknife test. These are around 1 % (see Table 4.2).

4.8   Discussion

With deconvolution interferometry we analyzed near-surface wave propagation effects, such as amplification and attenuation and determined the velocity structure below the Tuzla site in southeastern Istanbul. From arrival time picking in the deconvolved seismograms and from forward modeling the Green's functions we derived two different velocity models down to 288 m depth. The first model sees a low-velocity zone between the sensors at 71 and 144 m and the second one between the sensors at 144 and 215 m depth (Fig. 4.4). Since logging measurements confirm a low-velocity zone between ~90 to ~140 m the first velocity model seems to be more reliable. Despite these differences both models have similar root-mean-square velocities. This reflects the common problem of uniqueness, i.e. several models can describe the same observation. In our modeling approach we focused on fitting the amplitudes and traveltimes of the direct upgoing wave and its surface reflection. If we also would have taken into account the arrival times of the phases that are reflected from the low-velocity layer (gray dotted lines in Fig. 4.7a and b) we might have been able to better constrain the low-velocity zone at the right depth. However, this was not possible, since we performed a simple grid search for a homogeneous layer above each sensor. We recommend for future modeling studies to choose more complex techniques, e.g. a full wavefield inversion, to be able to better capture the heterogeneities in the subsurface. Further, additional information from logging would be invaluable.

Table 4.4: Estimated errors of the results from the modeling approach. Summary of error analysis: The errors presented here are the average errors obtained from several one-layer models and four-layer models. The error bounds given for $\overline{Q_P}$ correspond to a range of $\Delta V = $ -10 – +10 % (see explanation in the text). Positive values indicate an overestimation of $\overline{Q_P}$, and negative values an underestimation.

Depth [m]	One-layer models				Four-layer models			
	Err. $\overline{V_S}$ [%]	Err. $\overline{Q_S}$ [%]	Err. $\overline{V_P}$ [%]	Err. $\overline{Q_P}$ [%]	Err. $\overline{V_S}$ [%]	Err. $\overline{Q_S}$ [%]	Err. $\overline{V_P}$ [%]	Err. $\overline{Q_P}$ [%]
71	0.9	6.5	4.4	+100 – -27	3.3	20.3	5.5	+35 – -27
144	0.4	1	1.4	+51 – -6	0.7	8.8	1.2	+81 – +3
215	0.3	0.6	0.6	+34 – -9	0.5	7.9	0.7	+65 – +7
288	0.25	0.1	0.7	+13 – -8	0.5	5.1	0.7	+43 – +7

Both of our P-wave velocity models derived from interferometry overestimate the P-wave sonic log velocities by ~10 – 20 % even though the estimated errors for the velocities are only

~1 to 5 %. One possible reason for an overestimation is the assumption of vertical incidence of the incoming wavefield. If this assumption is not fulfilled, apparent higher velocities will be determined. Another reason for the difference in velocities could be related to the higher frequencies used in sonic log measurements that sample only a few decimeters around the borehole. Thus, the seismic waves sample a larger volume of the rock formations including potential lateral variations. A comparison of our S-wave velocity model with the sonic log S-wave velocity model is not reasonable, since the latter is likely to be erroneous, as discussed in section 'Geology at Tuzla'.

The forward modeling approach allowed us to determine apparent P- and S-wave quality factors. The apparent Q_P values for the depth ranges 0 – 71 m, 0 – 144 m, 0 – 215 m and 0 – 288 m increase with depth and we find $Q_P \approx 2Q_S$, in accordance with theory. Nevertheless, our Q estimates have to be interpreted with caution. They are biased due to the fact that we did not account for impedance changes during the modeling, since we assumed in the model a single homogeneous layer above each sensor. Thus our apparent Q values contain both, intrinsic and scattered attenuation, and impedance effects. The latter means, if waves travel from higher to lower impedance layers, as in our case between the sensors at 288 to 71 m, the decreasing impedance causes amplification due to energy conservation, with energy being proportional to $\rho V A^2$ (ρ density, V velocity and A amplitude). This impedance amplification could lead to apparent higher Q values. On the other hand, increasing impedances, as in our case from the low-velocity zone to the layer above, would lead to apparent lower Q values. Despite this bias, which causes large errors especially in Q_P, our apparent quality factors are similar to the ones found in other studies in the Marmara Sea region. E.g., Parolai *et al.* (2010) estimated Q_S values of 30, 46, and 99 for the depth ranges 0 – 50 m, 0 – 70 m, and 0 – 140 m in Ataköy (western Istanbul). They also used the recordings of a vertical borehole array and fitted the borehole-to-surface spectral ratios with a theoretical transfer function to derive Q_S. Using the ratio between S-wave and coda-wave amplitudes, Gündüz *et al.* (1998) determined a frequency dependent average S-wave attenuation of $Q_s(f) = (50 \pm 1.7)f^{1.09 \pm 0.05}$ for the crust below the Sea of Marmara.

4.9   Conclusions

We studied the first-order wave propagation effects at the GONAF-Tuzla vertical array in southeastern Istanbul, Turkey. Using a seismic interferometry technique based on deconvolution and a simple forward modeling approach we obtained estimates of near-surface apparent quality factors and seismic velocities for P- and S-waves.

The near-surface seismic velocities at the Tuzla site are high compared to other Istanbul sites and other borehole sites around the world with comparable depth. We found P-wave velocities of more than 3600 m/s and S-wave velocities of ~1800 m/s in a 300 m deep borehole. An additional uniqueness comes from a strong impedance change somewhere between 71 and 215 m depth, which is probably related to a velocity inversion observed by sonic logs between ~ 90 and ~140 m depth. These impedance steps introduce reverberations in the recordings of the surface sensor and the high velocities lead to strong interference of up- and down-going waves on the downhole sensors.

Due to the given complicated structure and the resulting impedance contrasts it was not possible to derive attenuation parameters with standard techniques such as spectral ratios. Instead we proposed a forward modeling approach and found that the apparent Q_P increase with depth, with values of 19, 35, 39, and 42 for the depth ranges 0 – 71 m, 0 – 144 m, 0 – 215 m, and 0 – 288 m. For the apparent Q_S we observe a value of ~20 for the depth range 0 – 288 m. These attenuation estimates are interpreted to be biased by the strong heterogeneities observed at the Tuzla site.

If borehole seismometers are installed within a relatively simple almost homogeneous subsurface our forward modeling approach based on a 2-D grid search would be sufficient to derive reliable quality factors. However, in the presence of a complex geological setting, such as at the Tuzla site, it is recommendable to use more comprehensive modeling techniques that invert for Q and impedance contrasts simultaneously and also take the incidence angle into account.

Our results are derived from a carefully selected set of local microseismic events, with a bandwidth between 0.1 to 40 Hz. They were obtained from the first available data from the recently implemented GONAF observatory and are encouraging signs of this networks utility. They reveal not only the complex near-surface factors that need to be considered in ground motion studies of the Tuzla site, but also open the door for more sophisticated analysis and modeling research.

5   *b*-value analysis

Ishimoto and Iida (1939) who studied maximum amplitudes of seismograms in Japan, and Gutenberg and Richter (1944) who compared the frequency of earthquake magnitudes in California with the one from global seismicity, suggested that the distribution of amplitudes/magnitudes follows the same power-law relation worldwide. The cumulative frequency-magnitude distribution (FMD) follows the commonly called Gutenberg-Richter (GR) law, which has the form

$$\log_{10} N(M) = a - bM, \tag{5.1}$$

where $N(M)$ is the number of earthquakes with magnitudes $\geq M$, and a and b are constants. The intercept a varies with analyzed region and time period and presents the productivity level of seismicity, while the slope b is generally ~1. The b-value describes the relative distribution of magnitudes, having a relatively larger amount of small earthquakes with respect to larger ones when b is high, and vice versa.

The logarithmic GR law is linear over all magnitudes, but usually FMDs deviate from this linear trend at the low and high ends of the magnitude range (Figure 5.1). The downward deviation at small magnitudes is due to the incompleteness of the catalog caused by the limited detection capability of the seismometer network. At the high end downward and upward deviations from the linear trend are observed. Depending on the magnitude scale used the downward deviation at large magnitudes reflects the magnitude saturation. To avoid this problem the moment magnitude, M_W, which does not saturate was introduced by Hanks and Kanamori (1979). Nevertheless, also for moment magnitudes FMDs deviate from linearity at large magnitudes. These observed breaks of slope led to the suggestion of alternative more complex empirical relations to describe FMDs (Cosentino *et al.*, 1977; Schwartz and Coppersmith, 1984; Kagan, 1997; Triep and Sykes, 1997). Since these models differ mainly in how they treat the high end of the magnitude range, they will not be discussed here, because this study (presented in chapter 6) focuses on micro to moderate earthquakes which are commonly described with the simple GR law (eq. 5.1). Nevertheless, independent of the choice of model, probabilistic seismic hazard assessment is sensitive to the Gutenberg-Richter b-value (Bender, 1983; Youngs and Coppersmith, 1985). In many probabilistic hazard studies (e.g. Frankel, 1995) the b-value is assumed to be constant for the whole study area, which is in agreement with the global average b-value of ~1 (e.g. Kagan, 1999). However, many local studies report spatial and temporal variations of b, and it has been suggested that incorporating spatially varying b-values improves hazard estimations (e.g. Schorlemmer *et al.*, 2004b).

Furthermore, spatial b-value variations are thought to imply the heterogeneity of stress or other parameters in the crust. Thus, mapping spatial b-value variations is suggested to contribute to a better understanding of the state of stress on a fault (e.g. Wiemer and Wyss, 1997). This idea is adopted in the study presented in chapter 6 in which b-value maps are generated for the Izmit-Düzce region and eastern Sea of Marmara. However, before the analysis of spatiotemporal b-value variations in the study area are presented, this chapter discusses in general the relationship between b and physical properties of the fault after methods of b-value calculation and its uncertainties are described.
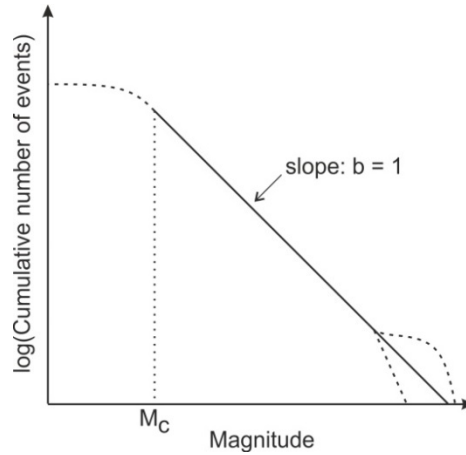
Figure 5.1: Sketch of the cumulative frequency-magnitude distribution (FMD) of an earthquake catalog. The solid line presents the linear Gutenberg-Richter (GR) law (eq. 5.1) with a slope of b = 1. At lower magnitudes (dashed line) the FMD deviates from the GR law due to the incompleteness of the catalog. For magnitudes larger or equal M_c (magnitude of completeness) the catalog is regarded as complete. At the high end of the magnitude range (dashed lines) some models suggest an upward deviation from the GR law and others a downward deviation (see text for references).

5.1   Computation of the *b*-value

An obvious approach to compute b is to fit the slope of the FMD with a regression line by the least-squares method. However, this technique is very sensitive to variations of the largest events in the catalog since it weights too strongly the few large events compared to the more numerous smaller events. Furthermore, synthetic studies showed that the least-squares method underestimates the b-value (Amorèse *et al.*, 2010). Instead, it is more appropriate and more common to use the maximum likelihood method by Utsu (1965) and Aki (1965) or similar forms of it.

5.1.1   Maximum likelihood method

The probability density function (PDF) of magnitude M is given by Aki (1965) as

$$f(M|\beta) = \begin{cases} 0 & \text{for } M < M_\text{c}, \\ \beta \exp[-\beta(M - M_\text{c})] & \text{for } M \geq M_\text{c}, \end{cases} \tag{5.2}$$

with

$$\beta = b \ln(10). \tag{5.3}$$

The magnitude is assumed to be a continuous variable of infinitive range above the minimum magnitude or magnitude of completeness M_c, also called threshold magnitude. If magnitudes are independent from each other, the joint PDF of N magnitudes M_i ($i = 1, \dots, N$) is equal to the product of each individual PDF, $f(M_i|\beta)$. Likewise, the likelihood function, which describes the likelihood with which the parameter β yields the set of N magnitudes is

$$L(\beta|_{M_1,\ldots,M_N}) = \prod_{i=1}^{N} f(M_i|_\beta) = \prod_{i=1}^{N} \beta\exp[-\beta(M_i - M_c)]. \tag{5.4}$$

To find the β that maximizes the likelihood function its first derivative has to be set to zero. Since it is easier to differentiate a sum than a product the logarithmic likelihood function is used. The logarithmic maximum likelihood condition is written as

$$\frac{d\ln(L)}{d\beta} = \sum_{i=1}^{N} \frac{d}{d\beta}[\ln(\beta) - \beta(M_i - M_c)] = 0. \tag{5.5}$$

Solving for β and inserting the mean magnitude $\langle M \rangle = 1/N \sum_{i=1}^{N} M_i$ results into the classical Aki-Utsu maximum-likelihood estimate of β,

$$\beta = \frac{1}{\langle M \rangle - M_c}. \tag{5.6}$$

5.1.2 Maximum likelihood method for a limited range of magnitudes

The Aki-Utsu maximum likelihood estimate unrealistically assumes a range of magnitudes that is continuous and unbounded on top. In reality earthquake catalogs contain a maximum magnitude depending on geological conditions of the fault and the time that is covered by the catalog. Page (1968) showed that when taking the maximum magnitude in the catalog, $M_{\max}$, into account the PDF takes the form

$$f(M|_\beta) = \begin{cases} 0 & \text{for } M < M_c \text{ and } M > M_{\max}, \\ \dfrac{\beta\exp[-\beta(M - M_c)]}{1 - \exp[-\beta(M_{\max} - M_c)]} & \text{for } M_c \leq M \leq M_{\max}. \end{cases} \tag{5.7}$$

After conducting the same steps as in equations 5.2 to 5.6 the maximum likelihood estimation of β of Page (1968) follows,

$$\frac{1}{\beta} = \langle M \rangle - M_c + \frac{(M_{\max} - M_c)\exp[-\beta(M_{\max} - M_c)]}{1 - \exp[-\beta(M_{\max} - M_c)]}. \tag{5.8}$$

This equation requires numerical solution. To estimate β analytically the Aki-Utsu estimate β_0 (eq. 5.6) is corrected by the expected bias calculated by approximating equation 5.8 with the accuracy of the Taylor expansion of second degree (Gibowicz and Kijko, 1994). The β value corrected for $M_{\max}$ then becomes

$$\beta = \beta_0(1 - \kappa), \tag{5.9}$$

with

$$\kappa = \beta_0 \frac{(M_{\max} - M_c)\exp[-\beta_0(M_{\max} - M_c)]}{1 - \exp[-\beta_0(M_{\max} - M_c)]}. \tag{5.10}$$
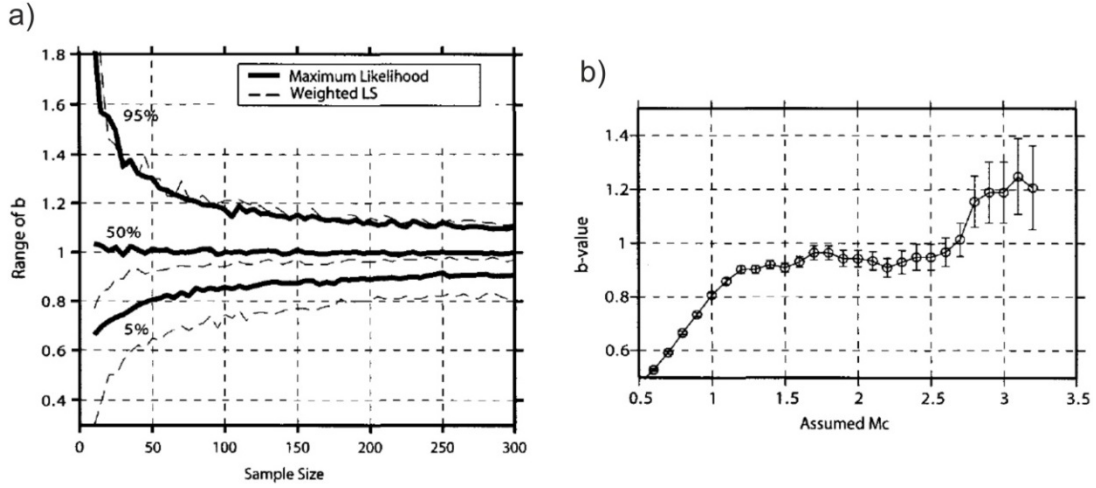
Figure 5.2: a) Range of *b*-values as a function of sample size based on a synthetic dataset of 5000 events with a *b*-value of 1. A sample of size N was drawn randomly. For each sample the *b*-value was calculated with the maximum likelihood (solid lines) and weighted least-squares method (dashed lines). This procedure was repeated 1000 times. For each sample size the 5, 50 and 95 percentiles are plotted. **b)** *b* as a function of assumed M_c with error bars based on a Parkfield dataset from 1980 - 2000. From Wiemer and Wyss (2002).

A further drawback of the Aki-Utsu estimate, next to neglecting the upper bound of the magnitude range, is the assumption of a continuous magnitude distribution. Therefore, Bender (1983) introduces a maximum likelihood estimate for a grouped magnitude dataset. This is especially an issue for datasets that are based on historical seismicity catalogs, e.g. intensity catalogs with wide intervals of 0.6 magnitude units.

Pickering *et al.* (1995) tested different methods for determining the *b*-value. They conclude that to obtain a reliable estimate of *b* with the maximum likelihood method a magnitude interval of 0.1 is sufficient (note the discussion of the study of Marzocchi and Sandri (2003) in section 5.2.1), and the range of magnitudes between M_c and M_{max} should be at least 2 orders of magnitudes. They suggested that for datasets with a shorter range of magnitudes the maximum-likelihood estimate of Page (1968) is most suitable. Thus, in the study presented in chapter 6 the approximated estimator of Page (eq. 5.9) is used for the computation of *b*.

5.1.3 Accuracy of *b*-value estimates

Based on the central limit theorem the standard deviation of β, σ_β, was given by Aki (1995) as $\sigma_\beta = \beta/\sqrt{N}$. The standard deviation of *b* is then $\sigma_b = \sigma_\beta/\ln(10)$. More commonly used because more accurate is the formula derived by Shi and Bolt (1982) which accounts for slow temporal changes of β,

$$\sigma_\beta = \beta^2 \sqrt{\frac{\sum_{i=1}^{N}(\langle M \rangle - M_i)^2}{N(N-1)}}. \tag{5.11}$$

Nevertheless, Shi and Bolt (1982) underestimated the uncertainties of *b* since equation 5.11 does not take the errors in the determination of magnitudes and M_c into account. Therefore, in more recent studies a bootstrap technique is applied to derive more realistic errors in *b* (e.g. Schorlemmer *et al.*, 2003; Amorèse *et al.*, 2010), i.e. from a dataset of N events, N events are

drawn while each event can be drawn more than once. From the reshuffled dataset M_c and b are computed. This procedure is repeated many times and the standard deviation of the b-values is taken as the uncertainty of b. With such bootstrap techniques it is possible to incorporate into the b-value uncertainty the uncertainty of M_c. However, they still neglect the uncertainty of each individual magnitude itself. This is apparent from the fact that most earthquake catalogs do not provide magnitude uncertainties. In contrast, the uncertainty of each magnitude in this study (chapter 6) is known and is taken into account as described in section 6.3.2.

An important parameter that influences the accuracy of b is the sample size. This was analyzed in many studies based on random sampling of synthetic power-law distributions (Bender, 1983; Pickering *et al.*, 1995; Wiemer and Wyss, 2002). The results of Wiemer and Wyss (2002) are presented in Figure 5.2a. Additionally, the authors tested the maximum-likelihood method against a weighted least-squares fit and obtained less biased b-values with the maximum-likelihood method. Figure 5.2a shows that the uncertainty of b-increases rapidly with sample size smaller 50.

Another parameter with a strong influence on the b-value is the magnitude of completeness as illustrated in Figure 5.2b (from Wiemer and Wyss, 2002). Figure 5.2b shows the b-value for different assumed M_c based on a dataset from Parkfield, California. When M_c is underestimated ($M_c < 1.2$) the b-value decreases as well, because of the incompleteness of the catalog that leads to a flattening of the cumulative FMD at magnitudes smaller than M_c. The increasing uncertainty of b-with increasing M_c is related to the reduced sample size.

5.2 Causes of *b*-value variations

Local studies report spatial and temporal variations of b between ~0.3 – 2.5 (El-Isa and Eaton, 2014) for which numerous possible interpretations are offered. Here the most common suggested interpretations and geological/geophysical causes of b-value variations will be discussed, after some causes of artificial b-value variations are mentioned.

5.2.1 Artificial *b*-value variations

The statistical significance of b-value variations is under debate (Frohlich and Davis, 1993; Kagan, 1999; Marzochi and Sandri, 2003; Amorèse *et al.*, 2010). Artificial b-value variations are caused by systematic errors in the catalog or the method of b-value calculation. Errors in the catalog are related to changes in the seismometer network, e.g. station density, type of instruments, or to changes in the data processing routines, like triggering algorithms or magnitude determination. This can lead to spatiotemporal variations of the magnitude of completeness in the catalog. Therefore, to ensure that spatiotemporal variations in b are not just caused by changes of M_c, M_c should be determined for each individual bin in space and time for which the b-value is calculated. Another option is to use a global threshold which should be the largest M_c in the region or time period. Often with the latter approach too many events are rejected to still yield a good coverage of the study area.

Another source of artificial b-value variations is the mixture of different magnitude scales and erroneous magnitude determinations. The dataset in this study provides an example of both problems. The dataset will be introduced in more detail in section 6.2, but a few remarks will be made here. It is a compilation of three different catalogs, two providing duration magnitudes, and the third moment magnitudes. An inspection of the FMDs of the three catalogs reveals for all of them anomalous FMDs (Figure 6.4, black curves). The catalogs

based on duration magnitudes yield unusual high *b*-values of 2.96 and 2.49. In contrast to the first two catalogs, the third catalog based on moment magnitudes results in a significantly lower *b*-value of 0.81. This catalog covers the same area as the catalog with the *b*-value of 2.49, but corresponds to a different time period. Nevertheless, this apparent significant *b*-value change is certainly mainly related to differences in the magnitude determination and not to temporal changes of physical properties in the crust. Thus, when merging different catalogs, the catalogs should report the same magnitude scale and the magnitudes should have been determined with the same processing routines to rule out systematic errors. Therefore, for this study the magnitudes have been recalculated.

Furthermore, the deviation of FMDs from the GR law results in unprecise estimates of the GR parameters as discussed for example by Lasocki and Papadimitriou (2006) who observed multimodal FMDs of different areas in Greece. Bimodality effects can originate from the mixture of two fracturing processes as observed in induced seismicity (Urban *et al.*, 2016), leading to invalidity of the GR law.

Marzocchi and Sandri (2003) discussed possible errors in the determination of the *b*-value itself. They showed that the *b*-value based on the Aki-Utsu estimate (eq. 5.6) is biased towards larger *b* by approximately 0.13, because of neglecting the fact that the magnitudes are binned and not continuous, leading to a wrong estimate of the mean magnitude $\langle M \rangle$ and the threshold magnitude M_c. Nevertheless, most studies use the Aki-Utsu estimate instead of corrected formulas given for example by Bender (1983). This might be explained by the statement of Bender (1983) and Pickering *et al.* (1995) that the bias which arouses from the wrong $\langle M \rangle$ is negligible when the magnitude binning is 0.1 or less. However, these statements did not take into account the stronger effect of the wrong estimate of M_c as shown by Marzocchi and Sandri (2003). Nevertheless, when applying the same method for calculating *b* to the whole dataset, possible biases introduced by the method are contained equally in all results, and hence, relative *b*-value changes can still be compared.

In this study artificial *b*-value variations are avoided by creating a homogeneous magnitude dataset, determining M_c space and time dependent, using the same *b*-value estimate throughout the whole study, and neglecting FMDs which deviate too strongly from the GR law. Furthermore, several parameter settings are tested to assess their influence on the result, and strict quality criteria are applied.

5.2.2 Negative correlation of *b* with stress

The *b*-value is considered to provide important constraints on the stress level of faults. This point of view is represented much stronger in the literature than opposing opinions that doubt the significance in *b*-value fluctuations (El-Isa and Eaton, 2014). It is commonly accepted that the *b*-value negatively correlates with stress. This is supported by theoretical models (Scholz, 1968), numerical modeling (Amitrano, 2003), laboratory experiments (Scholz, 1968; Goeble *et al.*, 2013) and field observations (Scholz, 2015).

Scholz (1968) observed from acoustic emissions (AE) in rock fracture experiments that the *b*-value of the AEs decreases with increasing differential stress $(\sigma_1 - \sigma_3)$, where σ_1 and σ_3 are the maximum and minimum compressive stresses. To explain this observation Scholz (1968) derived a theoretical model of microfracturing that describes rock deformation in laboratory and crustal scales and relates the stress in a rock to the *b*-value. He describes the size distribution of fractures in an inhomogeneous medium as a power function of fracture size, which reads
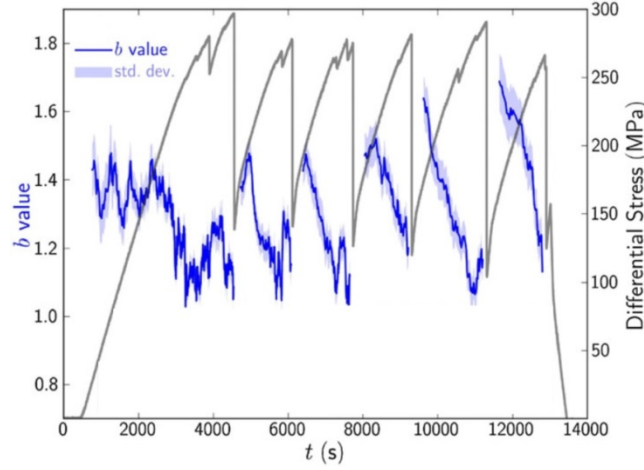
Figure 5.3: Influence of cyclical stress changes during stick-slip type fault movement on temporal b-value variations. Both differential stress (gray line) and b-values (blue line) exhibit a characteristic saw-toothed pattern but with opposite sense. Standard errors in b-are indicated by blue-shaded areas. From Goebel *et al.* (2013).

$$N(A) = A^{-[1-F(S|\bar{\sigma})]}. \tag{5.12}$$

$N(A)$ is the number of fractures with a fracture area larger than A, $F(S|\bar{\sigma})$ is the probability density function of the local stress σ to exceed the strength S of the material, and $\bar{\sigma}$ is the uniformly applied stress on the rock or a portion of the earth's crust. Comparing equation 5.1 and 5.12 it follows that

$$b \sim [1 - F(S|\bar{\sigma})]. \tag{5.13}$$

In this simple heuristic model the b-value is negatively proportional to stress, since $F(S|\bar{\sigma})$ increases with increasing stress.

Support for this hypothesis comes from laboratory experiments where stress conditions can be controlled. For example, in stick-slip experiments of Goebel *et al.* (2013), which are a laboratory analogy of earthquakes (Brace and Byerlee, 1966), it was observed that the b-value decreases during differential stress buildup. After stress is released by a stick-slip event the b-value suddenly increases and then starts to decrease again during the stress-buildup phase of the next stick-slip event. Such a saw-tooth pattern of the b-value and differential stress, is shown in Figure 5.3.

In most b-value studies the relationship between b and differential stress is utilized to interpret observed b-value variations in crustal seismicity in terms of varying stress along the fault. Starting from the Coulomb-Mohr failure criterion (eq. 5.14) some basic observations can be explained.

$$\tau = \tau_0 + (\sigma_n - P)\tan(\phi). \tag{5.14}$$

The Coulomb failure criterion describes how much shear stress τ can be applied to a surface subjected to a normal stress σ_n before it fails (Stein and Wysession, 2003). The pore pressure P is taken into account by the effective normal stress $\sigma'_n = \sigma_n - P$. In equation 5.14 τ_0 is the cohesive strength of the material, $\tan(\phi) = \mu$ is the internal friction coefficient, where ϕ is the internal angle of friction. The shear and normal stresses on a fault with an angle θ to the maximum compressive stress σ_1 expressed with the differential stress $\Delta\sigma = \sigma_1 - \sigma_3$ and mean stress $\bar{\sigma} = (\sigma_1 + \sigma_3)/2$ are (Zoback and Townend, 2001)

$$\tau = \frac{\Delta\sigma}{2}\sin(2\theta) \tag{5.15}$$

and

$$\sigma_n = \frac{\Delta\sigma}{2}\cos(2\theta) + \bar{\sigma}. \tag{5.16}$$

In the following it will be described how the differential stress behaves in the three endmember stress configurations (normal, strike-slip, and thrust faulting). Following Zoback and Townend (2001) equations 5.15 and 5.16 are substituted into equation 5.14, as well as the approximate σ_1 and σ_3 for the different stress regimes, which are

$$\begin{aligned}
\sigma_{1,normal} &= \sigma_v, & \sigma_{3,normal} &= \sigma_v - \Delta\sigma, \\
\sigma_{1,strike-slip} &= \sigma_v + \Delta\sigma/2, & \sigma_{3,strike-slip} &= \sigma_v - \Delta\sigma/2, & (\sigma_{2,strike-slip} = \sigma_v), \\
\sigma_{1,thrust} &= \sigma_v + \Delta\sigma, & \sigma_{3,thrust} &= \sigma_v,
\end{aligned} \tag{5.17}$$

where $\sigma_v = \rho g z$ is the vertical stress resulting from the overburden of the crust, ρ is rock density, and g the gravitational acceleration. Then the differential stress for the three different stress regimes reads with $A = 1/\cos(\phi)$

$$\begin{aligned}
\Delta\sigma_{normal} &= \frac{2}{A+\mu}(\tau_0 + (\sigma_v - P)\mu), \\
\Delta\sigma_{strike-slip} &= \frac{2}{A}(\tau_0 + (\sigma_v - P)\mu), \\
\Delta\sigma_{thrust} &= \frac{2}{A-\mu}(\tau_0 + (\sigma_v - P)\mu).
\end{aligned} \tag{5.18}$$

How the differential stress in different stress regimes (eq. 5.18) changes with depth and pore pressure is illustrated in Figure 5.4. It follows that the differential stress increases with increasing depth, and decreases with increasing pore pressure. Additionally, Figure 5.4 shows that the differential stress is largest in thrust, intermediate in strike-slip, and smallest in normal faulting regimes. Accordingly, a b-value decrease with increasing depth or decreasing pore pressure is explained with an increase of differential stress (Bachmann *et al.*, 2012; Spada *et al.*, 2013). Likewise, b-value variations across different stress regimes are also explained with changes of differential stress (Schorlemmer *et al.*, 2005).
Due to the negative correlation of b and stress, in some studies spatial b-value maps are used to identify asperities by low b-value anomalies (Wiemer and Wyss, 1997). Asperities are fault patches of high strength (strong coupling) which are under high stress relative to the average stress on the fault (Lay and Kanamori, 1981). Similarly, creeping and locked fault patches are suggested to be identified by low and high b-value anomalies, respectively (Schorlemmer *et al.*, 2004a). Temporal b-value variations are interpreted in terms of asperity loading and unloading. For example, a b-value decrease prior to an earthquake is interpreted as stress buildup (Gulia *et al.*, 2016).
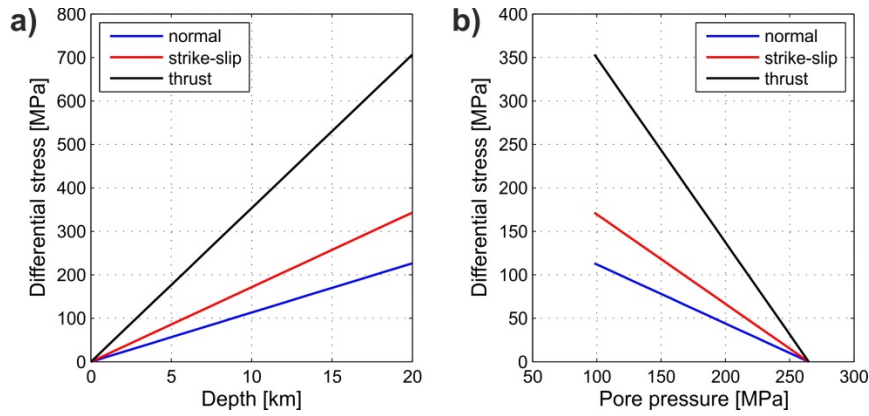
Figure 5.4: Dependency of differential stress on depth **(a)** and pore pressure **(b)** in different stress regimes based on equations 5.18 in which τ_0 is set to zero, corresponding to frictional sliding on pre-existing fractures, and the rock density is 2700 kg/m³. For the friction coefficient μ the approximate average value in the crust of 0.6 is used (Zoback and Townand, 2001). **a)** Here a hydrostatic pore pressure is assumed. **b)** The pore pressure is increased from hydrostatic to lithostatic, while the depth is set to 10 km.

5.2.3   Correlation of *b* with other geological/geophysical parameters

Further, numerous parameters are correlated with spatial *b*-value variations. Some of them suggest driving forces behind *b*-value fluctuations different from stress.

For example, Mogi (1962) observed in laboratory experiments with materials of various structures that *b* increases with increasing material heterogeneity. Based on this hypothesis he explained the decreasing *b*-values with depth with an increased homogeneity at deeper crust.

Amitrano (2003) proposed as cause for the *b*-value changes with depth the macroscopic behavior (brittle/ductile) of the material, i.e. that the *b*-value decrease is mainly driven by the increase of ductile deformation of the rock with increasing depth. Amitrano (2003; 2012) further concluded that it is mainly the internal friction coefficient which controls the brittleness of the material and thus the *b*-value.

High *b*-values in earthquake swarms are discussed in conjunction with the correlation dimension[3] (describing the earthquake epicenter distribution; small/high correlation dimension corresponding to distributed/localized epicenter distribution). However, in some cases a negative, in others a positive correlation between *b* and correlation dimension is observed (Hirata, 1989; Henderson *et al.*, 1994). Nevertheless, since swarm-like earthquake activity consists mainly of small magnitude events it is reasonable to expect a high *b*-value for earthquake swarms.

The *b*-value can also be related to the damage distribution described with the parameter D, which is the power-law exponent of the fracture length distribution in the crust. Note that equation 5.12 which describes the distribution of fracture length can be reformulated as

$$N(A) = A^{-D} \tag{5.19}$$

and thus in analogy to equation 5.13 it can be concluded that a dependency of *b* and *D* exists. A small D value corresponds to localized damage on relatively large fractures which goes along with comparatively large magnitude earthquakes that lead to a small *b*-value, while a

---

[3] In the literature it is common to use for the correlation dimension the term 'fractal dimension', but also the parameter D (described in the paragraph below) is referred to as fractal dimension in the literature. To prevent confusion, for neither of them this term is used here.

large D indicates a diffuse damage distribution on many small cracks resulting in a high b-value (Meredith *et al.*, 1990).

At the present state there is no consensus on the cause or driving force for b-value variations. Since numerous parameters control the state of stress on the fault, its heterogeneity et cetera, and since these parameters are not independent from each other, b-values cannot be interpreted unambiguously.

5.3   Application to the western North Anatolian Fault Zone

The methodologies used in the study presented in chapter 6 for determining the moment magnitude and magnitude of completeness are described here.

5.3.1   Computation of moment magnitude

The choice of magnitude scale for this study is the moment magnitude, M_W, because in contrast to other magnitude scales it directly relates to the strength of the earthquake and does not saturate. It is given by Hanks and Kanamori (1979) as

$$M_\text{W} = \frac{2}{3}(\log_{10}(M_0) - 9.1),\tag{5.20}$$

where M_0 is the seismic moment, or scalar moment in Newton-meter. It is related to the earthquake faulting process in terms of rigidity of the material μ, average slip on the fault D, and fault area A by (Stein and Wysession, 2003)

$$M_0 = \mu D A.\tag{5.21}$$

For a shear source the seismic moment is directly related to the low-frequency level Ω_0 of the P- or S-wave far-field displacement spectrum at frequencies $f \to 0$ (Fig. 5.5)

$$M_0 = \frac{4\pi\rho v^3 \Omega_0}{RS}.\tag{5.22}$$

ρ is the density, r hypocentral distance, and v the P- or S-wave velocity at the hypocenter. R and S are the radiation pattern correction coefficient and free-surface correction factor, respectively.

In this study, to objectively determine the spectral level Ω_0 the methodology of Andrews (1986) and Snoke (1987) who introduced the J and K integrals is used. The integral J of the square of the velocity spectrum is given by Snoke (1987) as

$$J = 2\int_0^\infty |V(\omega)|^2 df = 2\int_0^\infty |\omega U(\omega)|^2 df$$

$$= \frac{2}{3}[U(\omega_1)\omega_1]^2 f_1 + 2\int_{f_1}^{f_2} |\omega U(\omega)|^2\, df + 2|\omega_2 U(\omega_2)|^2 f_2 ,\tag{5.23}$$
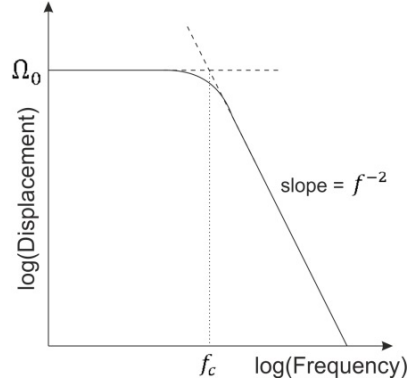
Figure 5.5: Schematic sketch of a displacement spectrum in a double-logarithmic plot. The low-frequency spectral level at $f \to 0$ is denoted with Ω_0 and the corner frequency with f_c. At frequencies higher than f_c the spectrum falls off with a slope of f^{-2}.

where $V(\omega)$ and $U(\omega)$ are the velocity and displacement spectra, respectively, and $\omega = 2\pi f$ is the angular frequency. Since the bandwidth of the seismic instrument is limited, the integral J is corrected for the lower and higher cutoff frequencies f_1 and f_2 assuming a constant amplitude of $U(\omega_1)$ for $f < f_1$, and a f^{-2} fall-off for $f > f_2$. The integral K of the square of the displacement spectrum corrected for the limited bandwidth is given by Snoke (1987) as

$$K = 2 \int_0^\infty |U(\omega)|^2 df = 2|U(\omega_1)|^2 f_1 + 2 \int_{f_1}^{f_2} |U(\omega)|^2 \, df + \frac{2}{3}|U(\omega_2)|^2 f_2 \,. \qquad (5.24)$$

Assuming Brune's source model (Brune, 1970) the spectral level is related to J and K by

$$\Omega_0 = \left(\frac{4K^3}{J}\right)^{1/4} \qquad (5.25)$$

Once the spectral level Ω_0 is known the seismic moment can be calculated from equation 5.22 and the moment magnitude from equation 5.20.

5.3.2 Underestimation of magnitudes

The largest Izmit aftershock in the dataset used here occurred on Sep 13th 1999 at 11:55 am. Studies of Izmit aftershocks report for this event a magnitude $M_L 6.2$ and $M_W 5.8$ (Örgülü and Aktar, 2001; Özalaybey *et al.*, 2002). In contrast, the Izmit aftershock catalog used here, after the recalculation of moment magnitudes, states a magnitude M_W of 4.9. Thus, the magnitude of this event is significantly underestimated.
Methodological reasons for this can be a selection of a too short S-wave data window from which the magnitude was determined, wrong assumptions about the velocity model, ρ, Q, S and R (see eq. 5.22), and a wrong instrument response correction. The data window, all parameters from equation 5.22, and the quality factor (for correcting for attenuation) were changed in various combinations, but the magnitude did not change by more than ± 0.2. Furthermore, a wrong instrument correction, or wrong assumptions about the quality factor, or the parameters from equation 5.22 would lead to a general under- or over-estimation of the magnitude, also of smaller magnitude events which is not the case. To further evaluate the

magnitudes determined in this study they were compared to the magnitudes given by Örgülü and Aktar (2001) and Özalaybey *et al.* (2002) which range between *M* 3.7 – 4.5 (the *M*~6 event is not included into this comparison). The average deviation of the magnitudes from this study from their magnitudes is -0.18, which is a very good fit. Probably the *M*~6 event is underestimated in this study, because its magnitude determination is solely based on recordings of short-period instruments, which are not designed to record strong earthquakes. For example, on two stations the waveform recordings were even clipped.

Due to the lack of recordings of broadband seismometers, the magnitudes of the largest events in the catalog (> *M*4) are slightly underestimated. Only the *M*~6 event is significantly underestimated. However, this does not change the distribution of large to small events, since the largest events in the catalog remain the largest events in spite of their magnitudes being underestimated. Hence, also the distribution of high and low *b*-value areas is not affected. This is validated by calculating the same *b*-value map and depth sections as presented in chapter 6 (Fig. 6.6) with the initial magnitudes of the Izmit aftershocks. The results are shown in Figure 5.6. Comparing Figures 5.6 and 6.6 shows that the location of areas with relatively higher and relatively lower *b*-values does not change.

5.3.3 Determination of M_c

A simple to apply automatic procedure for determining M_c is the maximum curvature technique (MAXC) which defines M_c as the point of maximum curvature of the cumulative FMD, or equivalently as the magnitude that yields the maximum of the noncumulative FMD (Woessner and Wiemer, 2005). With this technique the FMDs in this study were not always fitted well. Therefore, another method based on the goodness of fit method (GOF) proposed by Wiemer and Wyss (2000) was applied in a slightly modified way.

In this method each magnitude bin, M_i, in the range of *M* of the catalog is tested as possible M_c. Therefore β is computed with eq. 5.9 in which M_c is set to M_i. Then the corresponding synthetic FMD, S_{M_i}, is calculated. Based on the assumption that seismicity obeys the Gutenberg-Richter law the synthetic FMD is (Gibowicz and Kijko, 1994)
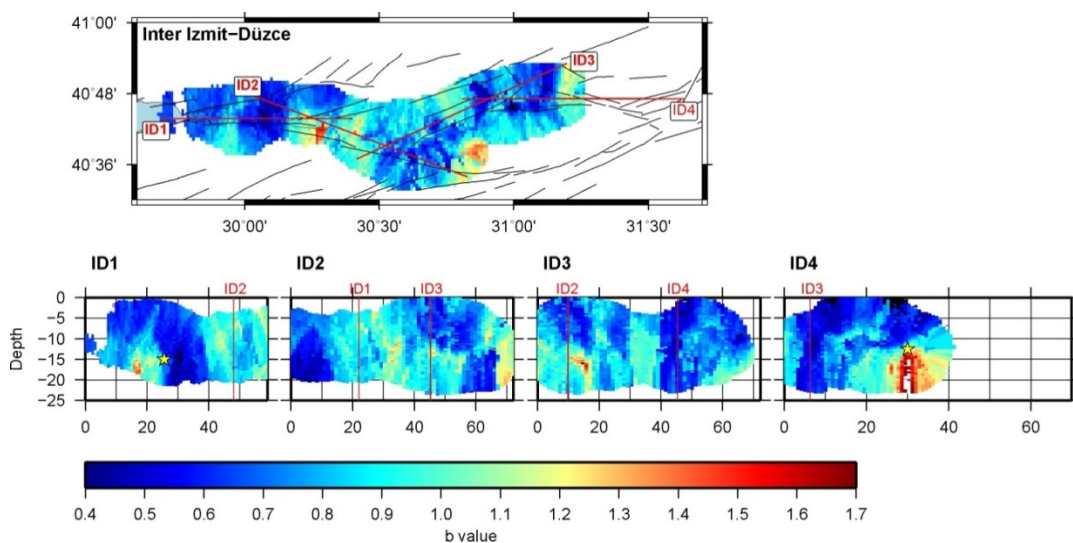
Figure 5.6: *b*-value map and depth sections calculated with the initial magnitudes of the Izmit aftershock catalog.

$$S_{M_i}(M) = N_{M_i} \exp\left(-\beta(M - M_i)\right), \tag{5.27}$$

where M is the complete range of magnitudes in the dataset, and N_{M_i} is the number of events with magnitudes larger or equal M_i. Then the goodness of fit, R, between the synthetic FMD and the observed one, B_{M_i}, is

$$R(M_i) = 100 - 100 \frac{\sum_{k=1}^{k=n} \left| B_{M_i,k} - S_{M_i,k} \right|}{\sum_{k=1}^{k=n} B_{M_i,k}}. \tag{5.28}$$

The subscript M_i indicates that the fit between S and B is only evaluated in the range $M_i \leq M \leq M_{\max}$, where $M_{\max}$ is the maximum magnitude in the dataset. n is the number of magnitude bins in the range $M_i \leq M \leq M_{\max}$. A high goodness of fit value indicates a good fit between the synthetic and observed FMDs. However, if M_c is simply picked at maximum R it can be overestimated (see Fig. 6.5b, right). Therefore, Wiemer and Wyss (2000) assigned a threshold of $R = 90\%$, i.e. they defined M_c as the smallest magnitude that gives a 90% fit to the data. Their choice of a constant threshold of $R = 90\%$ is not applicable to the dataset used here since a large spatial variation of R is observed. Thus, an alternative approach is proposed, which is illustrated in Fig. 6.5. First, an initial $M_{c,\text{ini}}$ is determined by selecting the maximum of the noncumulative FMD (Fig. 6.5, left). Second, a ΔM is selected ($\Delta M = 0.2$) and M_c is defined as the magnitude that yields the maximum R in the range $M_{c,\text{ini}} \pm \Delta M$ (Fig. 6.5, right). Furthermore, the R value is an objective measure of how well the FMD fits the GR law. Thus, it is used as one stability criterion in this study.

The performance of both techniques (MAXC and GOF) is compared in Figure 5.7. In the case of a catalog with magnitudes of low quality, e.g. the dataset of this study with original magnitudes (Fig. 5.7, top row), the GOF method results in a better fit to the FMD than the MAXC method. After recalculating the magnitudes of the whole dataset the differences between the GOF and MAXC method are small, which can be assigned to the improved quality of the dataset (Fig. 5.7, middle and bottom row).
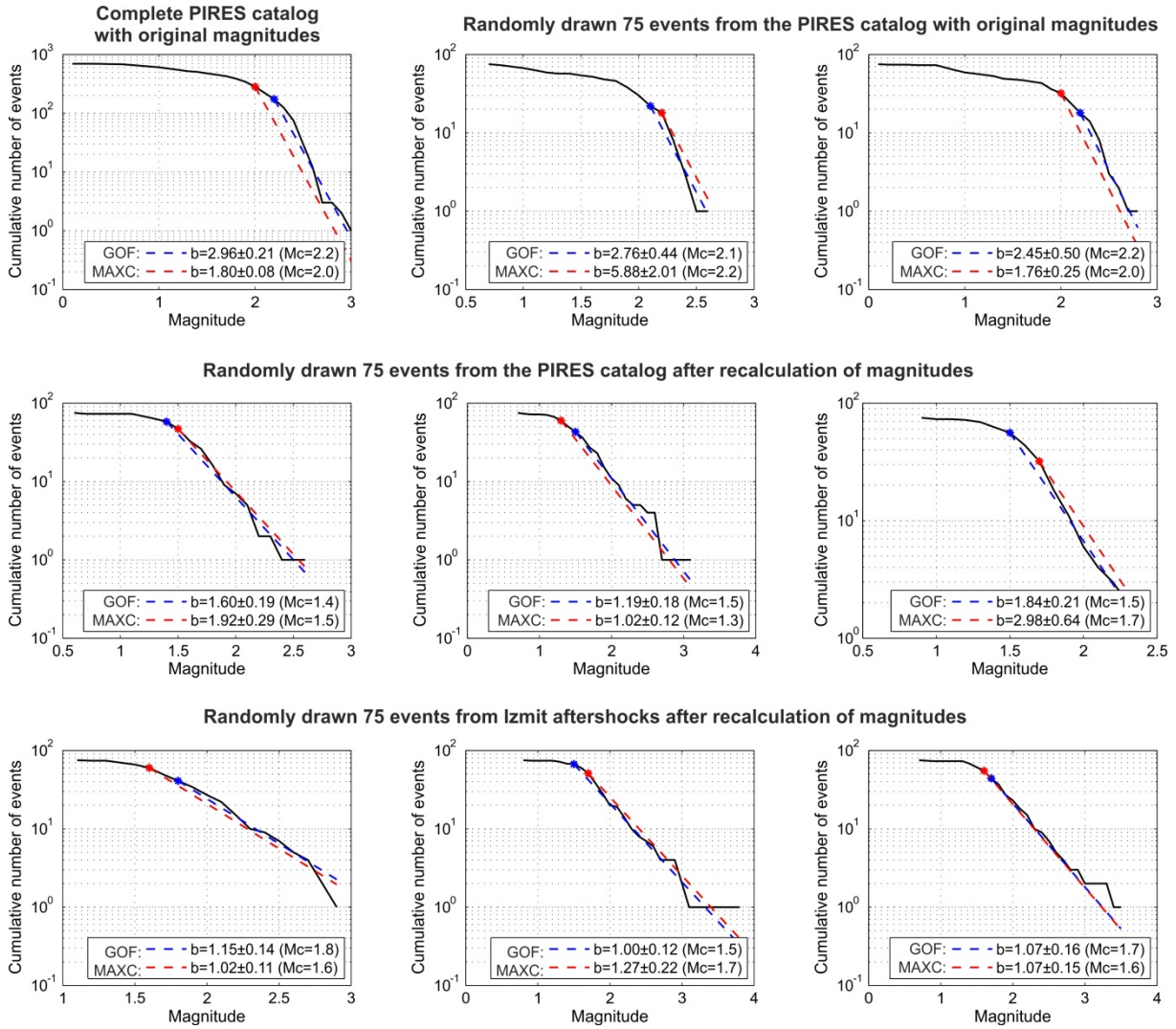
Figure 5.7: Comparison of the maximum curvature method (MAXC) and the goodness of fit method (GOF) for determining M_c. The M_c values are marked with stars and the corresponding linear power-law functions are plotted as red and blue dashed lines. The error given for b in the legend is calculated from the Shi and Bolt (1982) standard deviation (eq. 5.11). The top row presents examples of the original PIRES catalog based on duration magnitudes which deviate strongly from the linear GR-law resulting in a large scatter of b. The middle and bottom row present FMDs from the PIRES and Izmit aftershock catalogs based on the newly computed moment magnitudes. For each example 75 events were drawn randomly from the catalog.

6 Variation of seismic *b*-value at different stages of the seismic cycle along the North Anatolian Fault Zone in northwestern Turkey[4]

Summary

We studied spatiotemporal *b*-value variations along the North Anatolian Fault Zone (NAFZ) in northwestern Turkey with a focus on the combined 1999 Izmit and Düzce rupture and the eastern Sea of Marmara. We used a local seismicity catalog of the Izmit-Düzce region covering a time span from 2.5 years prior to the Izmit until 14 months after the Düzce mainshock and a four-year hypocenter catalog in the eastern Sea of Marmara. We consistently calculated moment magnitudes to ensure a homogeneous dataset and applied strict quality criteria. This allows studying variations of *b*-values throughout the region and at different stages of the seismic cycle. With a standard gridding technique *b*-value maps, depth sections and time series were calculated which reveal a very heterogeneous *b*-value distribution in the study area. The variety of *b*-value observations cannot be interpreted unambiguously, given that the *b*-value most likely depends on a combination of fault-zone characteristics like local stress conditions, heterogeneity of the crust and damage distribution. By presenting a comprehensive set of possible interpretations we point out that a biased discussion of the results towards stress or another individual parameter may lead to erroneous conclusions. Furthermore, the applied data discretization scheme influences the appearance of the final *b*-value distribution leading to potential misinterpretations.

6.1 Introduction

The frequency-magnitude distribution (FMD) of earthquake catalogs is commonly thought to follow the Gutenberg-Richter law (Gutenberg and Richter, 1944)

$$\log_{10} N(M) = a - bM, \tag{6.1}$$

where N is the number of earthquakes with magnitude larger or equal to M. The constants a and b represent the earthquake productivity of the analyzed area within certain time period, and the relative distribution of earthquake magnitudes, respectively. For a particular area and time period, a low b-value corresponds to a relatively high number of large events with respect to smaller ones and vice versa.

The global average b-value is assumed to be ~1 (e.g. Kagan, 1999). In contrast, many local studies report spatial and temporal variations of b between ~0.3 – 2.5 (see review of various studies in El-Isa and Eaton, 2014). The statistical significance of b-value fluctuations is still under debate (Frohlich and Davis, 1993; Kagan, 1999; Amorèse *et al.*, 2010; Urban *et al.*, 2016). If b-value changes are not artifacts resulting from the calculation method and/or incompleteness of the catalog, the seismic b-value is considered to provide important constraints on the stress level of faults. It is commonly accepted that the b-value generally correlates negatively with differential stress. This relation has been observed across a wide range of scales, from acoustic emissions in laboratory experiments (Scholz, 1968; Goebel *et al.*, 2013) over induced seismicity (Bachmann *et al.*, 2012) to global natural seismicity (Scholz, 2015). Other factors suggested to control the b-value are material heterogeneity (Mogi, 1968), damage distribution, and frictional properties on the fault (Amitrano 2003; 2012).

Mapping spatial b-value distributions along active faults has been used to identify asperities (areas of low b), which are assumed to possess an increased probability of rupturing in a future earthquake (Wyss *et al.*, 2000; Wyss, 2001). Furthermore, Schorlemmer *et al.* (2004a) studied seismicity along the Parkfield segment of the San Andreas Fault and showed that low and high b-value anomalies can be associated with locked and creeping fault segments, respectively.

Recent studies focused on evaluating whether temporal b-value variations reflect the state of stress of a fault at different stages of the seismic cycle. Tormann *et al.* (2015) analyzed b-values prior and after the 2011 Tohoku-oki earthquake in Japan and found a correlation between temporal b-value changes and loading and unloading of the fault. They observed an increase of b during the aftershock phase followed by a quick decrease to its preseismic level which they interpreted as quick reloading of the fault. Schurr *et al.* (2014) and Gulia *et al.* (2016) observed a systematic b-value decrease during the period before the 2014 Iquique earthquake in Chile and 2009 L'Aquila earthquake in Italy, respectively.

In this study we analyze spatiotemporal b-value variations along the western North Anatolian Fault Zone (NAFZ). The NAFZ is one of the largest plate-bounding transform faults, separating the Anatolian and Eurasian plates and extending for 1200 km between Eastern Anatolia and the Northern Aegean (e.g. Şengör *et al.*, 2005; Le Pichon *et al.*, 2015; Bohnhoff *et al.*, 2016a). The current right-lateral slip rate along the NAFZ with respect to stable Eurasia is 20-30 mm/yr (e.g. Barka, 1992; McClusky et al., 2000). During the 20th century, the NAFZ has ruptured over 900 km of its length (Ambraseys, 1970) with a series of $M > 7$ strike-slip earthquakes migrating overall westward towards the Istanbul-Marmara region in NW Turkey. The most recent major events on the NAFZ occurred in 1999, the $M_W 7.4$ Izmit (Aug 17th) and $M_W 7.1$ Düzce (Nov 12th) earthquakes (Fig. 6.1) (e.g. Tibi *et al.*, 2001; Barka *et al.*, 2002;

Bohnhoff *et al.*, 2016b), leaving the Marmara segment as the only NAFZ portion that has not sustained a major earthquake since 1766 (Parsons, 2004; Bohnhoff et al., 2013).

The spatial *b*-value distribution along the western NAFZ has already been analyzed previously. Westerhaus *et al*. (2002) analyzed the local seismicity between 29.8°E and 31.2°E in the years of 1985 – 1995, and Öncel and Wyss (2000) presented a *b*-value map for the Sea of Marmara region and the Izmit-Düzce area obtained from local seismicity between 1983 and 1999, prior to the Izmit earthquake. Both studies revealed low *b*-values in the vicinity of the Izmit epicenter, which they interpreted as a highly stressed asperity. Izmit aftershocks have been studied by Aktar *et al.* (2004) who focused on the first 45 days of Izmit aftershocks, and Görgün *et al*. (2009) analyzed the last 25 days of aftershocks, prior to the Düzce earthquake.

The previously mentioned studies in the Izmit-Düzce area are based on different earthquake catalogs involving different magnitude scales and different methodologies for calculating *b*. Thus, no direct comparison of absolute *b*-values between these studies is possible. However, it is an important issue to uniformly study the spatial and temporal *b*-value distribution in relation to the Izmit and Düzce earthquakes in general, and in the light of the forthcoming Marmara earthquake in particular.

Here we present the first study focusing on *b*-value variations based on a catalog with uniform magnitude scale throughout the region and time. We focus on the *b*-value distribution along the combined Izmit-Düzce rupture and the eastern Sea of Marmara segment of the NAFZ. The combined catalogs include high-resolution seismicity covering 2.5 years prior to the Izmit to 14 months after the Düzce mainshock and a four-year hypocenter catalog from a near-fault seismic network at the Princes Islands segment where a *M*>7 earthquake is pending. We re-evaluated all available waveform data to consistently calculate moment magnitudes ensuring a homogeneous dataset. This allows studying spatial and temporal variations of *b* with unprecedented detail and at different stages of the seismic cycle. The observed heterogeneities of the temporal and spatial *b*-value distribution in the eastern Sea of Marmara and Izmit-Düzce region are discussed in conjunction with several possible *b*-value interpretations linked to changes in stress conditions, heterogeneity of the crust, or damage distribution, and point out that a biased presentation of the results towards either one of the fault characteristics may lead to erroneous conclusions.
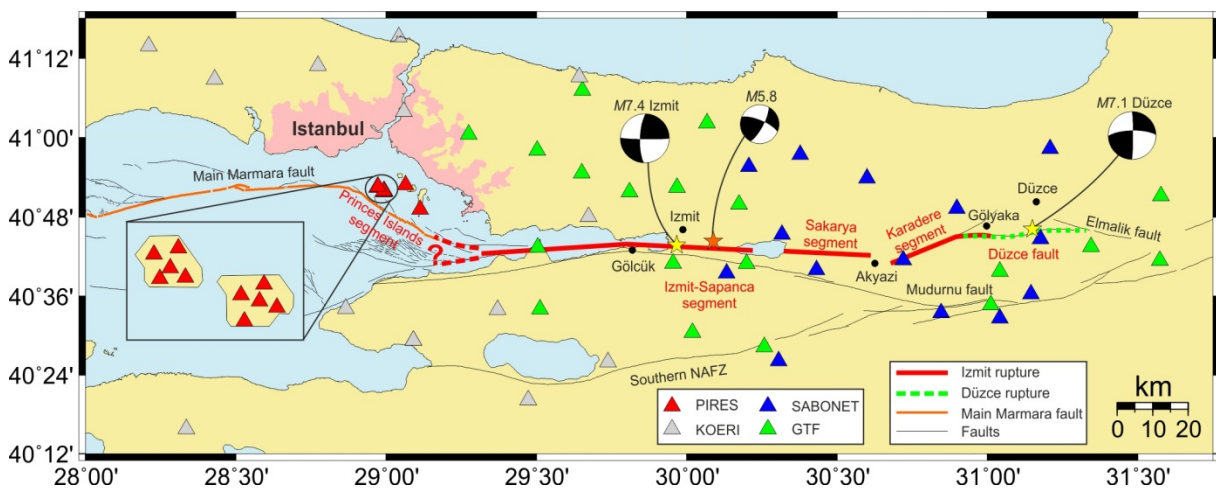
Figure 6.1: Distributions of seismometer stations of the SABONET, GTF, and PIRES networks, and selected stations from the permanent regional Kandilli Observatory and Earthquake Research Institute (KOERI) network. The Izmit and Düzce rupture are highlighted with bold red and green lines, respectively. Faults in the Sea of Marmara are after Armijo et al. (2005). In the Izmit-Düzce region faults are taken from the Turkey General Directorate of Mineral Research and Exploration. The orange star marks the largest Izmit aftershock in this dataset. Focal mechanism solutions of the Izmit and Düzce earthquakes and the M_W5.8 aftershock are from Özalaybey et al. (2002) and Örgülü and Aktar (2001).

6.2   Seismicity dataset

We used a recently compiled hypocenter catalog covering the time period from Jan 1997, (31 months prior to the Izmit earthquake), to Jan 2001, (14 months after the Düzce earthquake) (Ickrath *et al.*, 2015; Bohnhoff *et al.*, 2016b). This catalog is derived from recordings of 14 out of the 15-station short-period permanent SApanca-BOlu NETwork (SABONET, Fig. 6.1, blue triangles) operating since 1996 (Milkereit *et al.*, 2000), and 20 out of the 21-station short-period temporary network of the German Task Force for Earthquakes (GTF, Fig. 6.1, green triangles) installed four days after the Izmit mainshock and operating for two months, thus improving the station coverage along the Izmit rupture during the aftershock period (Baumbach *et al.,* 2003; Bindi *et al.*, 2007).

We separated the dataset into three different time periods. The SABONET catalog with absolute hypocenter locations covers the pre-Izmit time from Jan 1997 to end of 1998 and the post-Düzce time from Jan 2000 to Jan 2001. The Izmit aftershock time period recorded by the combined GTF-SABONET network spans from Aug 24th to Oct 19th 1999, between the Izmit and Düzce mainshocks, and is referred to as inter Izmit-Düzce time. The Izmit aftershocks were relocated by Bulut *et al.* (2007). These time periods were adopted from previous research of Ickrath *et al.* (2015) and Bohnhoff *et al.* (2016b) who focused on stress field orientation, and spatiotemporal seismicity distribution in relation to co- and post-seismic slip, respectively. Selecting the same time periods for this study creates an ideal basis for comparing their findings with the spatiotemporal *b*-value variations described below.

After removing quarry blasts and events with insufficient location accuracy (see supplementary material) the combined hypocenter catalog for the Izmit-Düzce region consists of a total of 6532 events. The seismicity along the Izmit-Düzce rupture, separated for the three different time periods is presented in Fig. 6.2 in map view and in four different depth sections (ID1, ID2, ID3 and ID4).

For the eastern Sea of Marmara region, we use a relocated seismicity catalog containing 756 events from Oct 2006 to the end of 2009. The events were recorded with the permanent local island-based PIRES (Prince Islands Real-time Earthquake System) network, consisting of up to 16 stations from which we used 10 short-period and 2 broadband stations (Fig. 6.1, red triangles). In addition we also used 13 selected broadband stations of permanent regional networks (Fig. 6.1, grey triangles) (see Bohnhoff et al., 2013, for details). The seismicity in the eastern Sea of Marmara is presented in Figure 6.3. Two depth profiles have been selected for this area. Profile EM1 is parallel to the Princes Islands segment as the main fault branch of the NAFZ, and EM2 is perpendicular to the fault extending throughout the pull-apart Çınarcık basin.

6.3   Methodology

6.3.1   Magnitude determination

The seismicity catalogs described above corresponding to different network configurations involve different magnitude scales. This precludes the comparison of absolute *b*-values between the time periods and along NAFZ sections since different magnitude scales lead do different frequency-magnitude distributions (Wiemer and Wyss, 2002). Therefore, we recalculated the magnitudes for all catalogs to form a consistent dataset of homogeneous magnitude.

The SABONET and PIRES catalogs originally include duration magnitudes (M_D). Plotting the FMD of the original catalogs allowed to identify a bias due to subjective manual picking of the coda length (Fig. 6.4a, b), leading to a deviation from the self-similar Gutenberg-Richter relation. The relocated Izmit aftershock catalog already includes moment magnitudes (M_W), but the magnitudes of moderate earthquakes are systematically overestimated (Fig. 6.4c). Hence, we also recomputed M_W for the Izmit aftershocks.

To determine M_W we used a methodology based on J and K integrals (Andrews, 1986; Snoke, 1987), where J and K are the integrated squared velocity and displacement spectra of S-waves, respectively.

The S-wave waveforms are first selected on both horizontal components, transformed to Fourier's domain, and then corrected for instrument response, spectral bandwidth and attenuation. The bandwidths used for the calculation of J and K integrals (see equations 3 and 8 in Snoke, 1987) were 1 – 40 Hz and 1 – 20 Hz for the eastern Sea of Marmara and the Izmit-Düzce region, respectively. The different bandwidths can be attributed to differences in sampling rate, signal-to-noise ratio at high frequencies, event-station distance, and magnitude range in both regions. Regarding the attenuation correction, we used a frequency independent Q operator determined by manually inspecting the spectral fall-off at high frequencies. The resulting Q values for the eastern Sea of Marmara and the Izmit-Düzce region are set to 350 and 700, respectively. The smaller Q value for the eastern Sea of Marmara region might be related to the presence of up to 3.5 km thick sediment layers in the Çınarcık basin (Carton *et al.*, 2007).

From the J and K integrals the low-frequency spectral level, Ω_0, of the displacement spectrum is estimated by

$$\Omega_0 = \left(\frac{4K^3}{J}\right)^{1/4}.$$ (6.2)

The spectral level is used to calculate the seismic moment, M_0, with

$$M_0 = \frac{4\pi\rho v^3 \Omega_0}{RS}.$$ (6.3)

The rock density ρ is here set to 2.7 g/cm^3, r is the hypocentral distance and v is the S-wave velocity at the hypocenter taken from the velocity models of Bulut *et al.* (2009) for the eastern Sea of Marmara and of Bulut *et al.* (2007) for the Izmit-Düzce region. R is the radiation-pattern correction factor, averaged to 0.63, and S is the free-surface correction factor set to 1.5. The seismic moment is then converted to moment magnitude using the relationship given by Hanks and Kanamori (1979),

$$M_W = \frac{2}{3}(\log_{10}(M_0) - 9.1).$$ (6.4)

We estimate the earthquake's magnitude from the mean value of moment magnitudes calculated at each station. The corresponding uncertainties are estimated as 2 times the standard deviation of the magnitudes calculated at each station.

Figure 6.4a–c presents the comparison of FMDs using initial magnitudes (black) and the newly computed M_W (blue). The initial duration magnitudes from the PIRES and SABONET catalogs give high b-values up to 3, which we consider an artifact. The M_D magnitude distribution of the PIRES catalog is bimodal with a rather high magnitude of completeness,

M_c, reducing the range of magnitudes above M_c. This results in an apparent increase of b, which is commonly observed in datasets with a short magnitude range (Schorlemmer *et al.*, 2003). The M_D of the SABONET catalog seems to be biased by an overestimation of the occurrence of $M\sim2$ events and underestimation of larger events which reduces the magnitude range, again leading to an increased b-value. In contrast, the recalculated moment magnitudes M_W result in FMDs with b-values that are closer to 1. Also the FMD of the PIRES catalog is no longer bimodal. The b-value and M_c were determined following a procedure described in the next section.

Table 1 summarizes the number of events for all different datasets, mean hypocenter location accuracy, b-value, and M_c. Figure 6.5 (left and middle column) shows FMDs for the different areas and time periods.

6.3.2 Magnitude of completeness and *b*-value determination

For the calculation of b-value maps we defined a 2D grid with a binning of 0.01° in latitude and longitude direction. For the depth sections the depth sampling is 0.2 km. For each bin the closest N events, based on epicentral or hypocentral distance, above or equal to M_c (see below for details on calculation) were selected for the b-value computation. We chose $N = 50$, as described in the supplementary material. If the selected events are outside a radius of 10 km no b-value is computed for this bin. Due to selecting events based on a number of events with $M \geq M_c$ instead of choosing all events within a fixed radius each bin samples a different area or volume, thus the resolution is higher in seismically active areas.

For particular areas temporal b-value variations were analyzed in more detail (Fig. 6.6 and 6.7, areas A-G). For these areas, b-value time series were computed in a chronological order with a moving time window containing 75 events, and a step of 10 events. Since M_c varies with time and space we estimated M_c for each bin on the map and depth sections and for each time individually.

Table 6.1: List of catalogs used in this study with information about their b-value, M_c and mean hypocenter location precision (vertical and horizontal error, and rms). For the SABONET catalog the values given correspond to the catalog after it was cleaned from events with unprecise hypocenter location (see Appendix C).

Catalog	Time period	Number of events	b value	M_c	Hor. error [km]	Ver. error [km]	rms
Izmit-Düzce area							
Pre-Izmit							
SABONET	3rd Jan. 1997 – 30th Dec. 1998	328	1.4	1.8	3.48	4.68	0.25
inter Izmit-Düzce							
Izmit aftershocks (relocated)	24th Aug. 1999 – 19th Oct. 1999	3155	1.31	1.8	0.331	0.394	0.03
Post-Düzce							
SABONET	9th Jan. 2000 – 27th Jan. 2001	2493	1.31	1.6	3.23	4.0	0.21
Eastern Sea of Marmara							
PIRES (relocated)	4th Oct. 2006 – 21st Dec. 2009	556	1.43	1.4	0.099	0.124	0.08
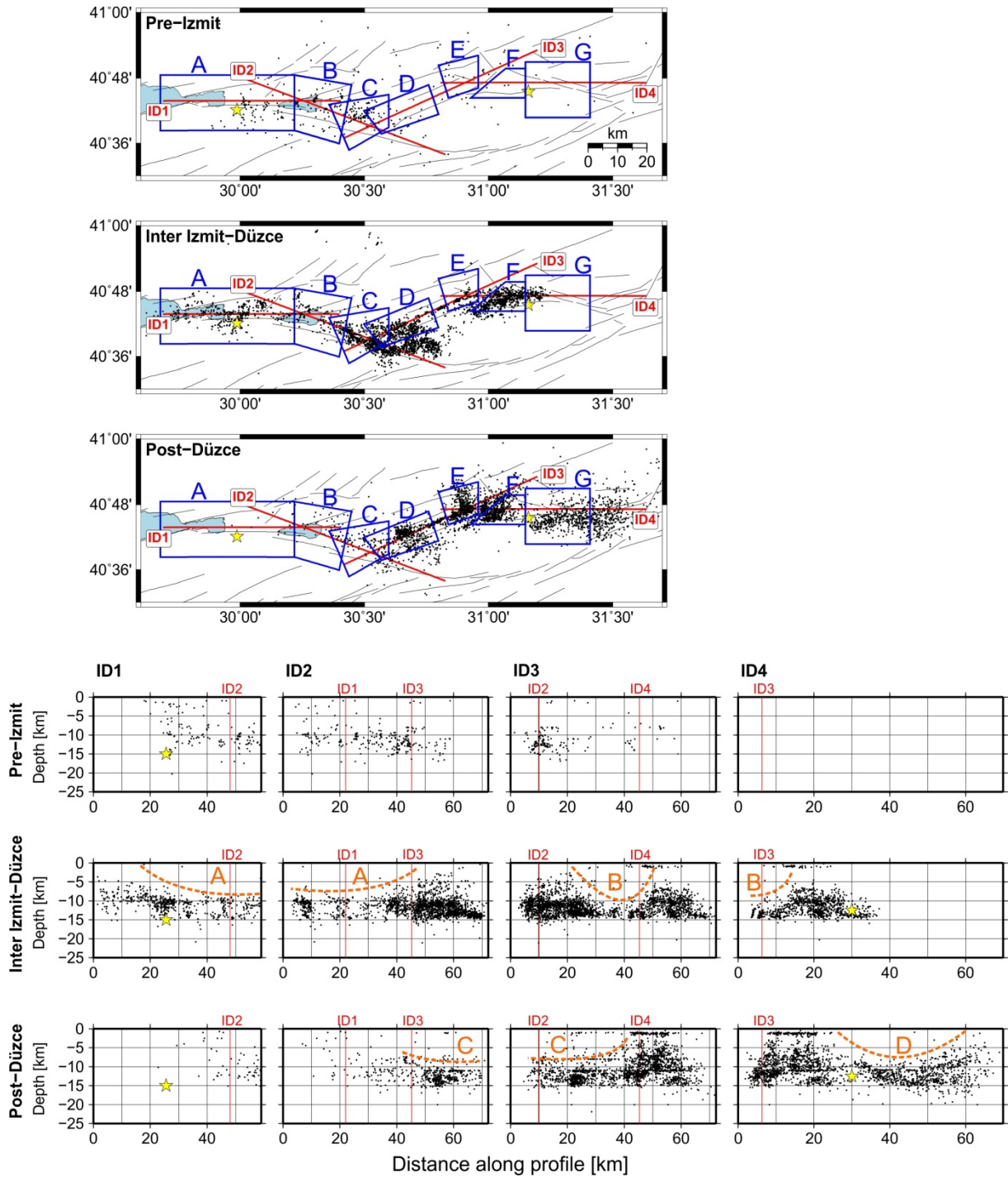
Figure 6.2: Distribution of seismicity during the three analyzed time periods in the Izmit-Düzce region in map and depth view. The locations of the four depth sections (ID1, ID2, ID3 and ID4) are marked with red lines. All events within 10 km of the depth profiles are plotted. The red lines in the depth sections mark the intersection points of the depth sections. For the blue areas A – G *b*-value time series are computed (Fig. 6.10). The orange areas A – D in the depth sections mark the aseismic patches after Bohnhoff et al. (2016). Izmit and Düzce hypocenters are indicated by yellow stars.
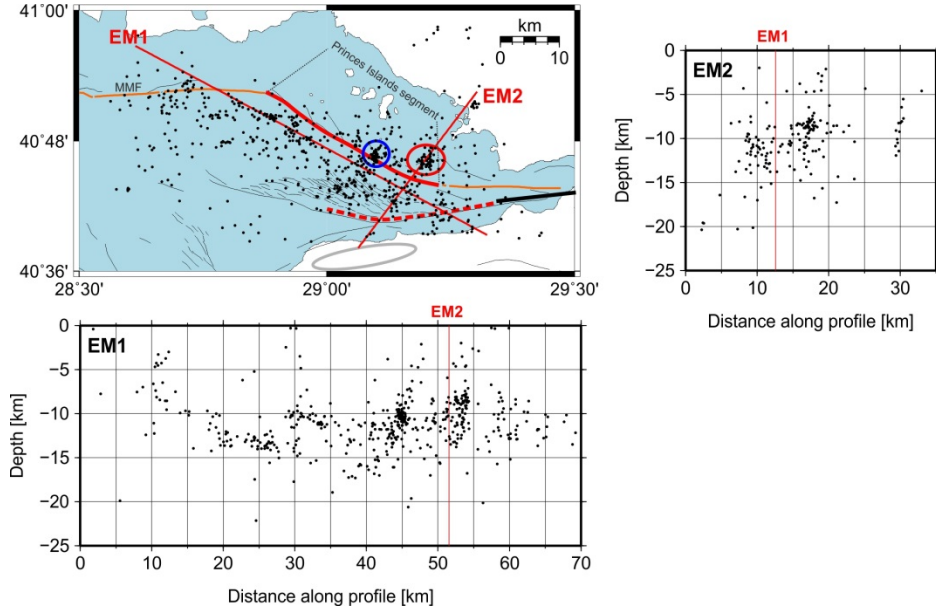
Figure 6.3: Seismicity in the eastern Sea of Marmara in map and depth view. The locations of the depth sections EM1 and EM2 and their intersection in the depth sections are marked with red lines. The seismicity plotted in the depth section is within 8 km to the profile. The orange fault is the Main Marmara Fault (MMF), from which the Princes Islands segment is highlighted in red. The Izmit rupture is indicated by a black bold line. The dashed red line marks the 'Çınarcık basin segment'. Red and blue circles outline the Tuzla and Baliciada cluster, respectively. The gray ellipse indicates the location of the ongoing Yalova swarm activity (not part of our dataset).

The b-value is calculated following Page (1968). This technique is based on the maximum-likelihood method (Aki, 1965). In addition, the method accounts for the maximum magnitude in the catalog, M_{max}, to correct for the limited range of magnitudes in the dataset. The Shi and Bolt (1982) estimate for the standard deviation of the maximum likelihood b-value is a commonly used measure of b-value uncertainties. The approach underestimates the uncertainties of b since it mainly reflects the total number of events from which b was calculated and neglects uncertainties in M and M_c (Page, 1968; Schorlemmer *et al.*, 2004a). To account for the magnitude uncertainties of each event, from the original dataset a new synthetic set of magnitudes is created by randomly perturbing the magnitude of each event within its 95% confidence interval. This procedure is repeated one hundred times. Then M_c and the b-value are computed from each of the one hundred modified datasets and the mean and one standard deviation are taken as the final b-value and the measure of uncertainty.

To generate robust results, a correct estimate of the magnitude of completeness is crucial. To determine M_c, a modified version of the goodness-of-fit method by Wiemer and Wyss (2000) is applied. Instead of assuming a constant threshold of a goodness of fit of $R = 90\%$ (see Wiemer and Wyss (2000) for details), we used an alternative approach, which is illustrated in Figure 6.5. First, an initial $M_{c,ini}$ is determined by selecting the maximum of the noncumulative FMD (Fig. 6.5, left). Second, we select a ΔM and define M_c as the magnitude that yields the maximum goodness of fit in the range $M_{c,ini} \pm \Delta M$ (Fig. 6.5, right).

6.3.3 Stability tests

Artificial b-value variations may originate from systematic errors in the catalog or the method of b-value calculation. Therefore, we tested the influence of M_c, ΔM, N, and the location

precision of hypocenters on the obtained b-value maps. These tests showed that the main features in the b-value maps remain stable when varying different parameters (see Appendix C for details).

To further ensure that we only consider real b-value variations, we selected stable results based on three criteria. 1) We neglect areas with a range of magnitudes above M_c smaller than one order, since we observe a correlation between patches of very high b-value with large standard deviation and a very small range of M (see Fig. C1b, C2b in Appendix C). This is related to the fact that the maximum likelihood procedure is based on the assumption of an infinite maximum magnitude. The minimum range of M for which the maximum likelihood method yields stable results is estimated to be two orders (Pickering *et al.*, 1995). For smaller magnitude ranges it is suggested to use the modified maximum likelihood method by Page (1968) as applied here. The lower limit of one order of range of M is a somewhat arbitrary choice. However, a sufficient range of M is a common problem in local seismicity catalogs over short time periods, resulting in many b-value studies based on catalogs with similarly short ranges of M (e.g. Wiemer and McNutt, 1997; Schorlemmer *et al.*, 2003; Vorobieva *et al.*, 2016). 2) Areas that have a standard deviation of b larger than 0.2 are neglected (Fig. C1c, C2c in Appendix C). 3) We disregard areas with a goodness of fit smaller than 85% (Fig. C1d, C2d in Appendix C), since a low goodness of fit value indicates a deviation from a power-law distribution, e.g. in the case of a bimodal FMD. The remaining areas with a b-value in the Izmit-Düzce area and the eastern Sea of Marmara have an average standard deviation of b of 0.12, an average goodness of fit of 92%, an average range of M of 1.6 and 1.3 orders, and an average radius around each bin of 6.5 and 7.5 km, respectively. Also for the b-value time series the three stability criteria are applied.

6.4   Results and Discussion

We discuss the results for separate structural regions along the NAFZ (Fig. 6.1) and show b-value maps and depth sections for the Izmit-Düzce and eastern Sea of Marmara region before (Fig. 6.6 and 6.8) and after (Fig. 6.7 and 6.9) applying the stability criteria described above. The b-value time series are presented in Figure 6.10.

6.4.1   Izmit-Düzce area

For the Izmit-Düzce area (Fig. 6.6 and 6.7) we find a distribution of low and high b-value patches in good agreement with earlier findings by Westerhaus *et al.* (2002), Aktar *et al.* (2004) and Görgün *et al.* (2009) irrespective of the different methods of estimating b-values used in these studies.

The observed variability of b-values in the Izmit-Düzce area ranging between 0.5 – 1.7 within a relatively small area indicates a very complex structural setting and local stress field. Since b-value variations may not be related to stress heterogeneity only, but possibly also to damage varying in space and time (Amitrano, 2003), changes in frictional properties (Amitrano, 2012), and material heterogeneity (Mogi, 1962), we discuss several correlations between the b-value and geological/geophysical parameters to pose the large variety in possible b-value interpretations, and thus the difficulty in identifying the cause of b-value fluctuations.
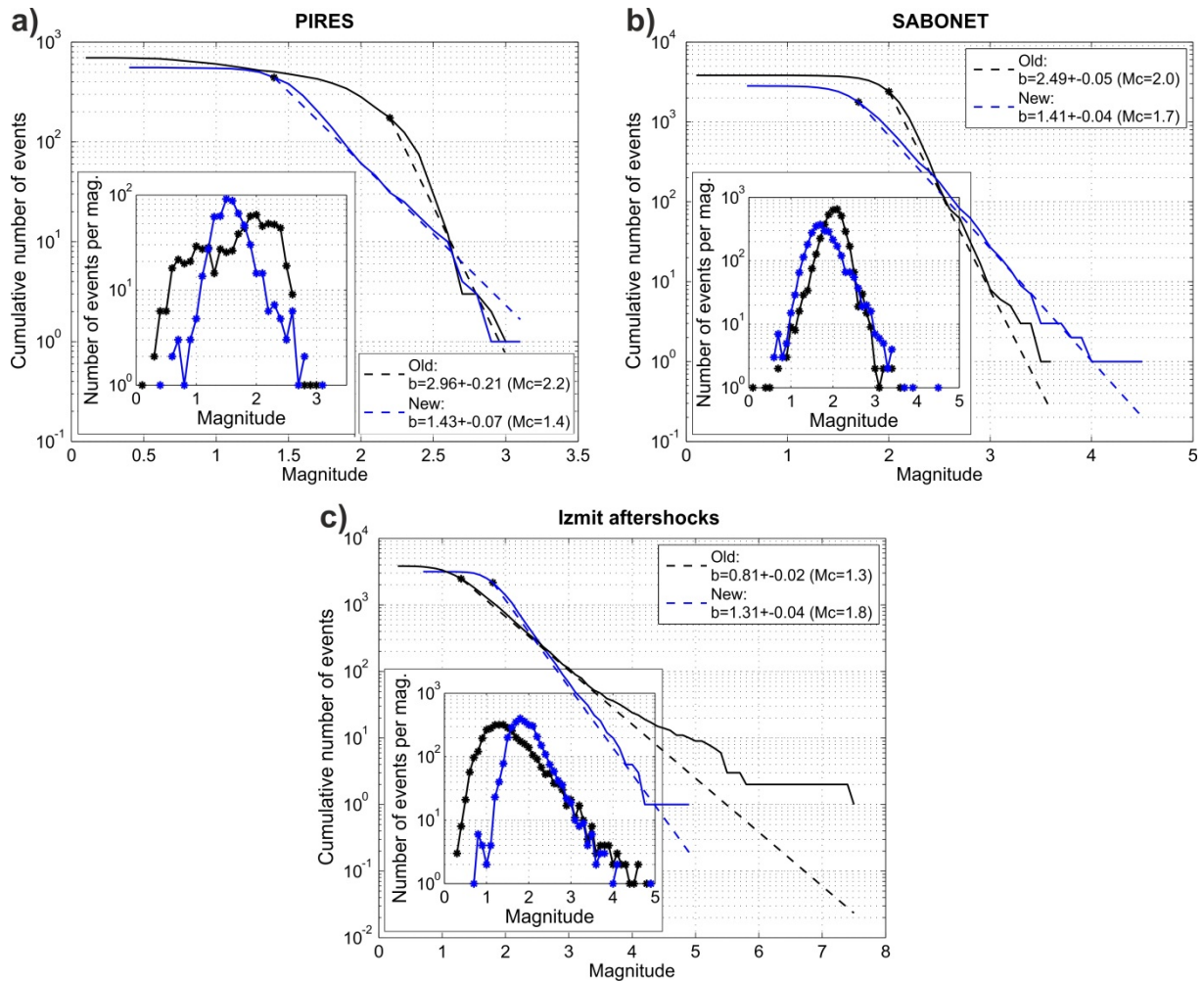
Figure 6.4: Comparison of initial (black) and new moment (blue, this study) magnitudes for the eastern Sea of Marmara (PIRES network) **(a)**, and Izmit-Düzce (SABONET network) **(b)**, and Izmit aftershock **(c)** regions, respectively (see text for details).

Furthermore, we used the opportunity to compare our results with the results of the studies of Ickrath *et al.* (2015) and Bohnhoff *et al.* (2016b) since they are based on the same dataset separated into the same time periods. Bohnhoff *et al.* (2016b) observed four aseismic patches in the upper 10 km of the crust during the Izmit and Düzce aftershock periods (Fig. 6.2, orange patches A – D in the depth sections). We do not observe a correlation with the *b*-value distribution and these aseismic patches, which is discussed in Appendix B.

Izmit-Sapanca segment

The Izmit earthquake nucleated on the strike-slip Izmit-Sapanca fault segment (Fig. 6.7, box A). This fault segment was identified previously as a seismic gap with the potential for a *M*>6 earthquake (Toksöz *et al.*, 1979). Furthermore, low *b*-values in pre-Izmit seismicity were interpreted to indicate a high-stressed asperity on this fault segment (Öncel and Wyss, 2000; Westerhaus *et al.*, 2002). This interpretation is supported by high coseismic slip of the Izmit earthquake at depth in the hypocentral region observed in several inversion results of seismologic and geodetic data (Reilinger *et al.*, 2000; Tibi *et al.*, 2001; Bouchon *et al.*, 2002, Delouis *et al.*, 2002).
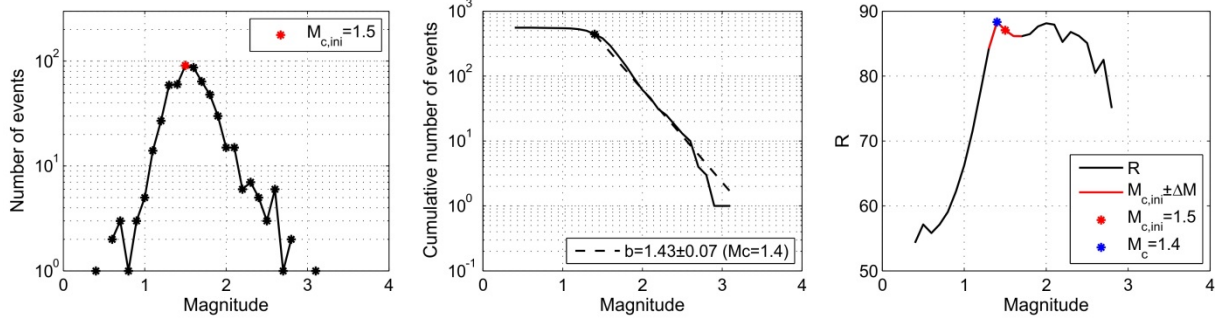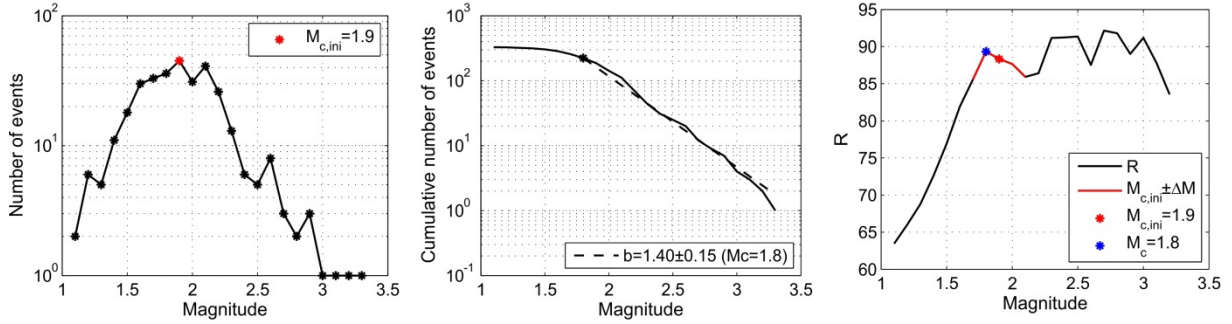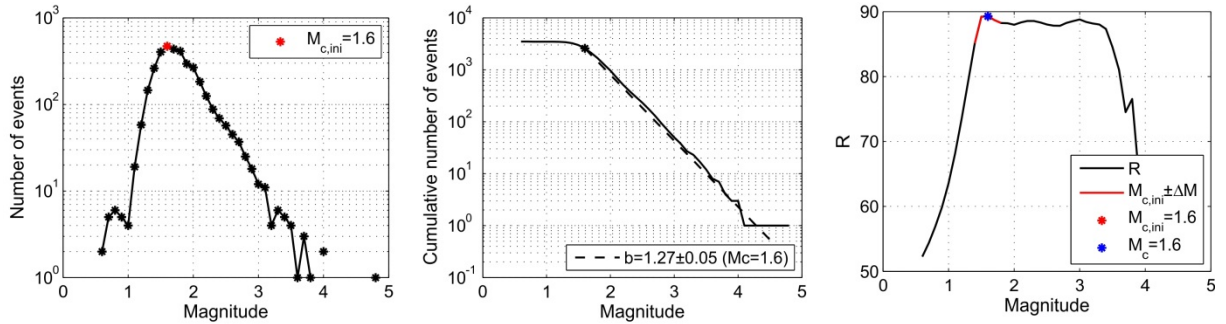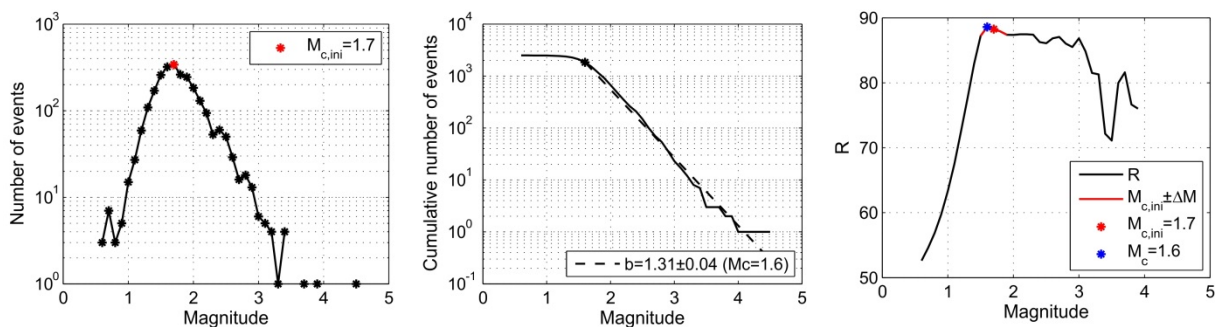
Figure 6.5: Illustration of estimation of M_c for the catalogs of the eastern Sea of Marmara **(a)**, and the Izmit-Düzce region for the time periods pre-Izmit **(b)**, inter Izmit-Düzce **(c)**, and post-Düzce **(d)**. **Left** figures show the noncumulative frequency-magnitude distribution (FMD) from which the maximum is taken as the initial $M_{c,ini}$. **Middle** figures present the cumulative FMDs and the corresponding *b*-values. In the **right** figures the goodness of fit, *R*, is plotted to illustrate how the magnitude with the maximum *R* in the range $M_{c,ini} \pm \Delta M$ is chosen as M_c ($\Delta M = 0.2$).

Interestingly, the Izmit aftershocks indicate the lowest *b*-values down to 0.5 on the Izmit-Sapanca segment (Fig. 6.7, box A). However, high *b*-values are expected for asperities that experienced large stress release during the mainshock (Sobiesiak *et al.*, 2007; Tormann *et al.*,

2015) and large coseismic slip (Wiemer and Katsumata, 1999). If the b-value is interpreted to serve as a stress-meter, either this asperity experienced very quick stress reloading during the first week for which no aftershock recordings are available to us, or this fault segment had comparatively small coseismic stress release with respect to the accumulated shear stress, and thus, may be still under higher stress than the eastern segments of the fault. The first option seems unlikely since the suggested reloading times of other studies indicate reloading periods of weeks or month rather than days (Hardebeck, 2012; Ickrath *et al.*, 2014; Tormann *et al.*, 2015).

Aktar *et al.* (2004) computed spatial b-value variations for Izmit aftershock seismicity including data from the first days and also obtained generally low b-values in the Izmit-Sapanca area. However, in agreement with our study Aktar *et al.* (2004) observed some slightly higher b-values directly to the west of the Izmit epicenter (Fig. 6.7, box A) and interpreted them as a signature of existing asperity.

In the pre-Izmit time period the lowest b-values (~0.9 – 1) in the Izmit-Düzce region are observed on the Izmit-Sapanca segment. Unfortunately, for this time period we only obtained stable b-value estimates for small areas due to the limited seismicity before the Izmit earthquake and strict quality criteria. A more detailed analysis of the time evolution of b can be seen in Figure 6.10, column A. The b-value of ~1 during the pre-Izmit time is lower than the b-values during most of the inter Izmit-Düzce time period, especially after Sep 14th (see below). The differences are small and we only have a single data point for the pre-Izmit time, but nevertheless this may support the interpretation of Aktar *et al.* (2004) of elevated b-values on an asperity during the aftershock period. However, the observed shallower seismicity west of the Izmit epicenter and temporal variations of the stress field orientation may also explain the higher b-values in this area.

Ickrath *et al.* (2015) found a significant rotation of the stress field following the Izmit mainshock from a strike-slip to a normal-faulting regime, which is supported by focal mechanisms of Izmit aftershocks of strike-slip and normal-faulting in this area (Örgülü and Aktar, 2001; Özalaybey *et al.*, 2002; Bohnhoff *et al.*, 2006; Stierle *et al.*, 2014). Ickrath *et al.* (2014) observed a systematic recovery of the stress orientation to the pre-mainshock stress regime based on focal mechanism inversions for the whole Izmit rupture area. The b-value time series of the inter Izmit-Düzce time contains periods of increased b-values, which may indicate a variable proportion of strike-slip and normal-faulting mechanisms. However, also in areas where Ickrath *et al.* (2015) did not identify temporal variations of the stress field (e.g. Düzce fault (Fig. 6.10, column F)) the b-value varies significantly during the inter Izmit-Düzce time.

The abrupt change of b after Sep 14th can be assigned to the occurrence of the strongest Izmit aftershock in our dataset. The M_W5.8 earthquake with strike-slip focal mechanism occurred on Sep 13th between the Izmit epicenter and Lake Sapanca at 17 km depth (Örgülü and Aktar, 2001; Özalaybey *et al.*, 2002, Fig. 6.1, orange star). The M_W5.8 event correlates with the beginning of significant b-value perturbations (starting with an increase) in the areas A, C, D, and F. The increasing b-values possibly indicate stress release and unclamping of the fault. However, in the areas C and D the increase already starts short before the M_W5.8 event. Furthermore, the highest b-values from the time series of area A coincide with pronounced shallower seismicity between Sep 24th and Oct 6th (orange box in Fig. 6.10) that occurs between 29.7°E and 30°E directly west of the Izmit epicenter where the b-value map shows the highest b-values in area A. The shallow depth distribution of the aftershocks in this region (see Fig. 6.2, depth profile ID1) suggests that the higher b-values west to the Izmit epicenter could also be related to a reduced differential stress at shallower depth in agreement with other studies that observe decreasing b-values with depth (e.g. Spada *et al.*, 2013).
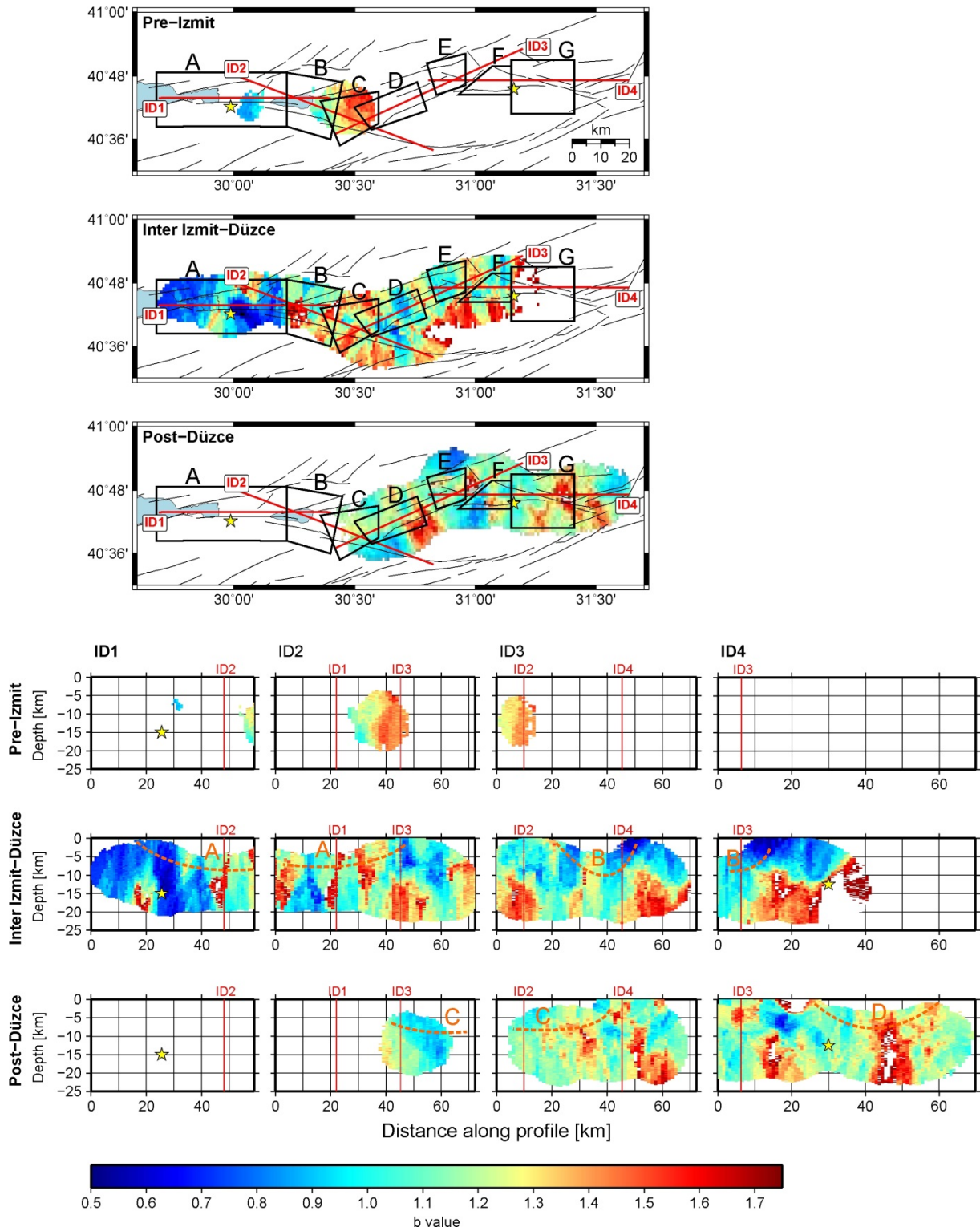
65

Figure 6.6: *b*-value maps and depth sections before applying stability criteria in the Izmit-Düzce region. The locations of the four depth sections (ID1, ID2, ID3 and ID4) are marked with red lines on the maps. The red lines in the depth sections mark the intersection points of the depth sections. For the blue areas A – G *b*-value time series are computed (Fig. 6.10). The area inside the orange lines A – D in the depth sections mark the aseismic patches after Bohnhoff et al. (2016). Izmit and Düzce hypocenter are indicated by yellow stars.
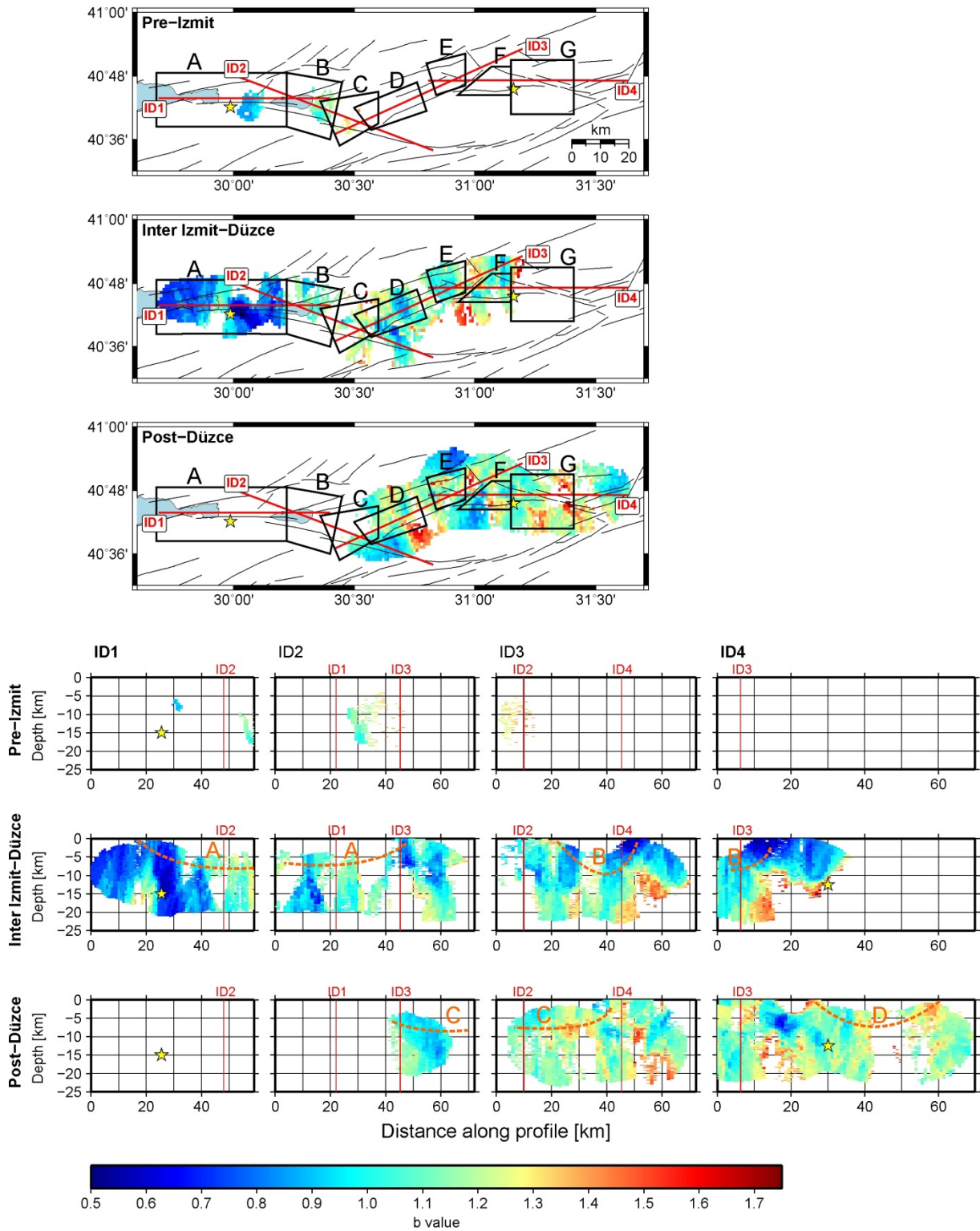
Figure 6.7: *b*-value maps and depth sections after applying the stability criteria in the Izmit-Düzce region. See further description in Figure 6.6.

It is therefore conceivable that the Izmit mainshock caused rather short-term stress field perturbations on the Izmit-Sapanca fault. Prior to the earthquake, this area experienced only sparse seismicity and a few months afterwards the activity was again very low. The fluctuations in the *b*-value time series may arise from the occurrence of the $M_W 5.8$ event and

temporal changes in the depth distribution of seismicity. After the 4th of October, the b-value returned to the pre-Izmit level of ~1.

The relatively low b-values on this fault segment prior and after the Izmit earthquake also can be related to the fault structure and fracture distribution in the crust. The Izmit-Sapanca strike-slip segment is a relatively simple geological structure compared to the more complex eastern fault segments in the study area. Therefore, the crust in this area may hosts rather few large fractures instead of many small, distributed ones, promoting the occurrence of comparatively large magnitude events resulting in low b-values. This interpretation is supported by Meredith *et al.* (1990), who discussed that fracture distribution and b are positively correlated.

Sakarya segment

Along the strike-slip Sakarya fault segment east of Lake Sapanca (Fig. 6.7, box B, Fig. 6.10, column B) the largest coseismic surface slip of ~5 m occurred during the Izmit earthquake (Barka *et al.*, 2002). Since high coseismic slip is observed to coincide with areas of high b-values (Wiemer and Katsumata, 1999), Aktar *et al.* (2004) interpreted high b-values along the Sakarya segment and below the Akyazi basin to result from a ruptured asperity, which goes along with the assumption of lower b-values before the mainshock.

In contrast to this assumption our study shows stationary intermediate b-values ranging between ~1-1.3 in the Sakarya segment before and after the Izmit earthquake. Additionally, no significant stress rotation in the Sakarya segment was found (Ickrath *et al.*, 2015), and the depth of seismicity throughout the time period considered here remains constant extending between ~8-16 km.

Akyazi basin

The fault structure of the Akyazi pull-apart basin is complex with a surface slip deficit >3 m (Barka *et al.*, 2002). Ickrath *et al.* (2014) suggested a coseismic rotation of the stress regime from strike-slip to normal-faulting below the Akyazi basin, followed by a back-rotation to original orientation within a few weeks after the Izmit earthquake. However, they refined their conclusion in a follow-up study based on a new seismicity catalog including pre-Izmit background seismicity (Ickrath *et al.*, 2015) and found that also during the pre-Izmit time a predominantly east-west extensional normal faulting regime was present. The stationary stress field is reflected in on average consistently high b-values observed in the Akyazi basin. The strong b-value variations during the inter Izmit-Düzce time (Fig. 6.10, column C) will be discussed later together with the b-value fluctuations on the southern Karadere segment (see below).

Also Aktar *et al.* (2004) and Görgün *et al.* (2009) observed generally high b-values in the Akyazi basin during the inter Izmit-Düzce time, and Westerhaus *et al.* (2002) obtained high b-values in the Akyazi basin from pre-Izmit seismicity. These observations suggest that fault structure and stress state in the Akyazi basin did not change significantly following the Izmit event.

The generally high b-values in the Akyazi basin are in accordance with several features. 1) The predominant normal-faulting stress field implies lower differential stresses. 2) Geological complexity is generally correlated with high b-values (López Casado *et al.*, 1995), because the complexity indicates a heterogeneous subsurface which is suggested by laboratory experiments to correlate positively with b (Mogi, 1962). Crustal heterogeneity in the Akyazi basin can be assumed due to the presence of the fault triple junction of the Sakarya, Karadere and Mudurnu fault, and the seismic velocity contrasts detected across the Sakarya (Bulut *et al.*, 2012) and Karadere faults (Najdahmadi *et al.*, 2016). 3) Similarly, it can be assumed that the fracture distribution in the Akyazi basin is diffuse due to the heterogeneous stress field

resulting from the geological complexity. Thus, many small, distributed fractures result in small-magnitude earthquakes leading to a high *b*-value. This is in contrast to the Izmit-Sapanca segment, where the low *b*-values may originate from a localized fracture distribution. 4) Heat flow density mapping and thermal spring studies by Pfister *et al.* (1998) revealed the presence of thermal springs in the Akyazi basin. Pfister pointed out that thermal springs occur more frequently in transtensional-extensional tectonic regimes where fluid pathways exist. The mapping of thermal springs in this region already prior to the Izmit mainshock indicates that this region is in general subjected to enhanced fluid flow. This goes along with increased heat flow and pore pressure in the basin. Elevated heat flow in volcanic areas has been found to correlate with high *b*-values (Wiemer and McNutt, 1997), and also pore pressure increase was observed to correlate positively with *b* (Bachmann *et al.*, 2012). Interestingly, Stierle *et al.* (2014) observed significant non-double-couple components in seismic moment tensors calculated from early Izmit aftershocks in the Akyazi basin. These moment tensors were interpreted to relate to tensile fracturing on pre-existing faults reflecting the pronounced fluid motion.

Southern Karadere segment

Due to sparse seismicity east of the Akyazi basin prior to the Izmit mainshock, the Karadere fault can only be discussed for the inter Izmit-Düzce and post-Düzce times. The SW-NE trending strike-slip Karadere fault is subdivided into a southern and northern part (Fig. 6.7, box D and E), following Ickrath *et al.* (2015) who found distinctly different stress field orientations for both areas. The southern Karadere fault partly overlaps with the ~5 km wide Akyazi gap with no surface slip, and the predominant normal-faulting stress regime in the inter Izmit-Düzce and post-Düzce times (Ickrath *et al.*, 2015) indicates a strong influence of the Akyazi pull-apart basin.

In contrast to the fault segments discussed above, we observe a change from low to high *b*-values between the inter Izmit-Düzce period and post-Düzce period. The *b*-value time series of the inter Izmit-Düzce time (Fig. 6.10, column D) shows a step from ~1-1.2 to 1.5 around Sep 12th 1999, coinciding with a decrease in seismicity rate from ~15-40 events per day before Sep 12th to ~3-8 events per day afterwards, which further decreased after May 2000. Accordingly, for the inter Izmit-Düzce time the low *b*-values seen in the map and depth sections reflects mainly the early Izmit aftershock period before Sep 12th.

Comparing the depth distribution of seismicity in the area of box D before and after the Düzce earthquake in the Akyazi basin and southern Karadere fault segment (see Fig. 6.2), we observe almost no shallow seismicity after the Düzce event. However, the shallow seismicity in the inter Izmit-Düzce time occurred only during particular time periods as marked in Figure 6.10 with orange boxes.

The low *b*-values observed in the first month after the Izmit mainshock may reflect a stress concentration due to a slip deficit in the Akyazi gap and lateral variations of coseismic slip along the Izmit rupture. Subsequently, the increased stress in this region triggered shallow seismicity resulting in postseismic relaxation and distributed brittle damage in the upper crust which leads to an increase of the *b*-value. This scenario is in agreement with Wang *et al.* (2010) who analyzed potential physical mechanisms of postseismic relaxation after the Izmit earthquake. The authors applied a viscoelastic damage rheology model to fit numerically the observed aftershock rates and postseismic displacement measurements of GPS stations. In particular, Wang *et al.* (2010) suggested that areas of increased aftershock activity (Akyazi basin, southern Karadere segment) accumulate increasing damage accommodating inelastic relaxation. They found that up to 50% of the measured surface displacements and the high

69

rate of aftershocks may be related to damage formation in the first month after the Izmit mainshock.

Similar to the Izmit-Sapanca segment, temporal b-value variations of the seismicity at the Akyazi basin and southern Karadere segment start just prior to the $M_W 5.8$ aftershock. This event and the increased shallow aftershock seismicity indicate that the Akyazi basin was subjected to strong but transient stress field perturbations. To some extent this may have caused the strong b-value variations in this region observed after the Izmit earthquake.

Northern Karadere segment

The Düzce earthquake occurred 87 days after the Izmit event activating the Düzce fault, and its rupture terminated in the west at the fault junction with the Karadere fault. The northern part of the Karadere fault reflects a strike-slip regime before and after the Düzce earthquake (Ickrath *et al.*, 2015). Nevertheless, temporal b-value changes are visible. In the map and depth sections (Fig. 6.7, box E, and in the depth sections around the intersection of ID3 and ID4), lower b-values (0.5 – 1.1) can be seen during the inter Izmit-Düzce time compared to post-Düzce ($b \sim 1 – 1.7$). During the inter Izmit-Düzce time the seismicity is concentrated between 12-15 km depth. In contrast, during the post-Düzce time seismicity is spread over the whole depth from 3-15 km. This depth distribution of seismicity and the corresponding b-values are in good agreement with observations of other studies indicating a b-value decrease with depth (Spada *et al.*, 2013).

The western termination of the Düzce rupture at the junction of the Düzce and Karadere faults likely caused a stress concentration on the northern Karadere segment. Presumably this triggered shallow aftershock seismicity on the northern Karadere segment after the Düzce earthquake resulting in strong b-value variations in the post-Düzce time series (Fig. 6.10, column E).
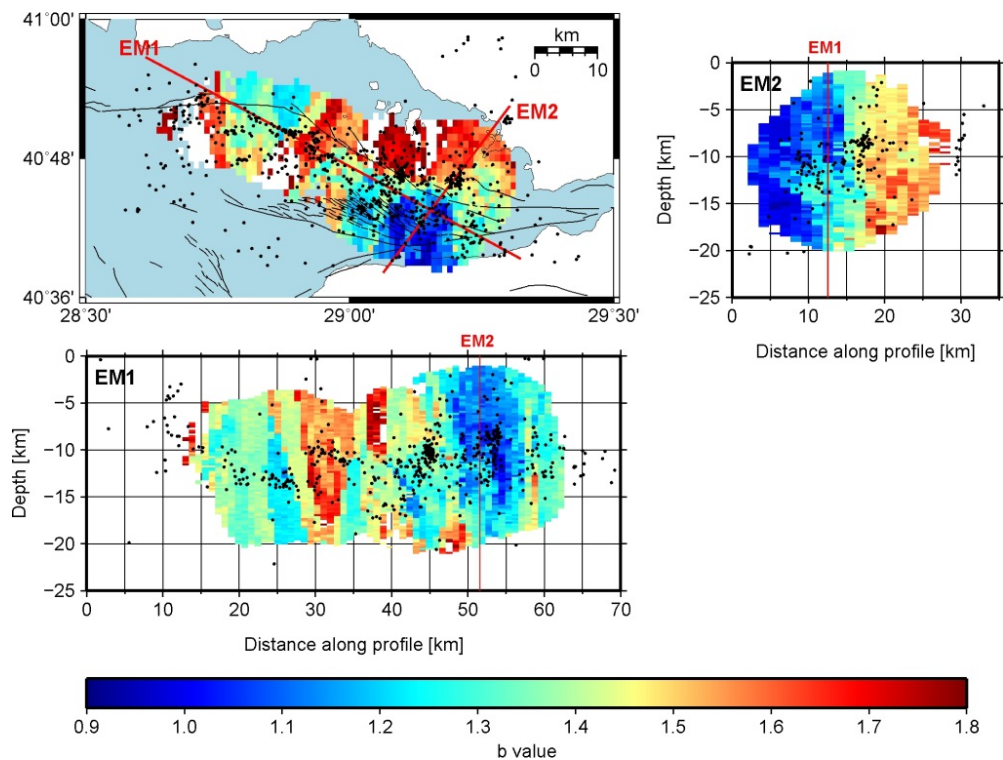
Figure 6.8: b-value map and depth sections before applying stability criteria for the eastern Sea of Marmara. Red lines on the map mark the locations of the depth sections EM1 and EM2, and in the depth sections they mark the point of intersection. b-values plotted in white on the map correspond to values that are higher than 1.8.
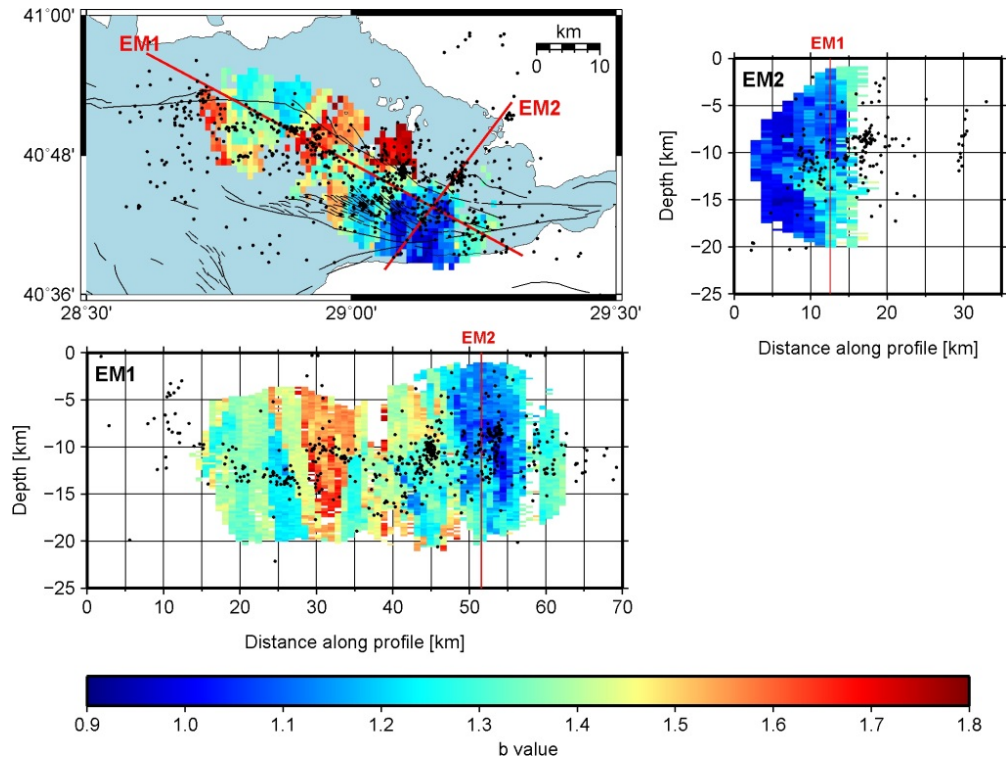
Figure 6.9: *b*-value map and depth sections after applying stability criteria in the eastern Sea of Marmara. See further description in Figure 6.8.

Düzce fault

The E-W trending strike-slip Düzce fault dips ~65° to the north (Bouin *et al.*, 2004). It is located at the southern border of the Düzce basin and splays out to the west from the Karadere fault forming a releasing wedge in the Gölyaka basin. The fault hosted the Düzce main shock, which produced a symmetric bidirectional rupture ~40 km in length with coseismic horizontal surface slip distributed along the whole Düzce fault up to 5 m in the epicentral region and rapidly decreasing slip at both ends of the rupture (Akyüz *et al.*, 2002; Pucci *et al.*, 2007).

The western Düzce segment partly ruptured already during the Izmit earthquake (Fig. 6.7, box F, west of the Düzce epicenter; Hartleb *et al.*, 2002). It experienced oblique coseismic slip with a significant normal component at depth (Bouin *et al.*, 2004, Akyüz *et al.*, 2002; Hartleb *et al.*, 2002; Pucci *et al.*, 2007). This is in contrast to the central part and the eastern segment of the fault where the slip is almost purely right-lateral (Fig. 6.7, box G, east of the Düzce epicenter). Furthermore, the surface rupture of the Düzce earthquake follows in the western segment the saw-toothed trajectory of an old complex fault system, while the eastern segment produced a simple E-W trending linear rupture trace that cuts across the en-échelon pattern of the old fault system (Pucci *et al.*, 2007). We calculated the *b*-value time series separately for both segments since the different rupture dynamics on the western and eastern Düzce segment may be reflected in *b*-value differences. However, we do not observe pronounced differences in *b* (Fig. 6.7, depth section ID4 kilometer 10-30 (western segment) and 30-50 (eastern segment)). This is in agreement with the observation of Ickrath *et al.* (2015) who found a strike-slip stress regime along the entire Düzce fault.

The Izmit earthquake triggered strong aftershock activity on the western Düzce segment, from which we obtained low *b*-values (0.5 – 0.9) in the upper 10 km of the crust, in agreement with Görgün *et al.* (2009) who suggested high stress on the Düzce fault. After the Düzce event, higher *b*-values are observed. Considering the large coseismic slip during the Düzce

71

earthquake, the *b*-value increase may be related to stress released by the Düzce mainshock. However, this observation is only obvious in the depth section, but not in the map view (Fig. 6.7). The *b*-values in the map view are probably affected by the two-dimensional projection which neglects the hypocenter depth, and thus, mixes deep (>10 km) and shallow seismicity. This is especially critical on the western Düzce segment, where the seismicity in the inter Izmit-Düzce time below 10 km results in unstable very high *b*-values up to 1.7.

During the inter Izmit-Düzce time a significant amount of seismicity occurred below 10 km depths off the Düzce fault towards the south. This mixture of on- and off-fault seismicity results in larger *b*-value uncertainties for the inter Izmit-Düzce time and may cause the unusual high *b* values at depth below 10 km. In contrast, the Düzce aftershock seismicity on the western Düzce segment is concentrated on the fault, and the corresponding *b*-value time series reveals stationary *b*-values around 1.

Also the *b*-value time series for the eastern Düzce segment (area G) does not show strong variations with $b \approx 1.5$ in the inter Izmit-Düzce and post-Düzce time until June 2000, decreasing to 1.1 afterwards.

Elmalik fault

Towards the east the Düzce fault connects with the single trace of the NAFZ via a right-releasing step-over formed by the WNW–ESE trending Elmalik fault (Pucci *et al.*, 2007). Despite the absence of coseismic slip of the Düzce earthquake on this fault, strong aftershock seismicity was triggered there.

The *b*-values are depth-invariant and similar to that obtained for the eastern Düzce segment (Fig. 6.7, depth section ID4, 50-70 km). Due to the lack of supporting information, we refrained from interpreting the *b*-values on the Elmalik fault.

6.4.2   Eastern Sea of Marmara

Coulomb stress field modeling of King *et al.* (2001) showed that the Izmit earthquake loaded adjacent faults to the east and west of the Izmit rupture. This resulted in the $M_W7.1$ Düzce earthquake on the eastern side, but towards the west the next major earthquake is still pending. In the eastern Sea of Marmara the NAFZ splits into two major (Princes Islands segment in the north and Armutlu fault in the south) and several minor branches. The western termination of the Izmit rupture is off-shore in the Sea of Marmara but its exact location is still under debate. Based on modeled coseismic displacement at depth it is estimated to be near the city of Yalova at 29.3°E on the Armutlu fault segment (Reilinger *et al.*, 2000; Wright *et al.*, 2001; Delouis *et al.*, 2002). In contrast, from Izmit aftershock seismicity it is suggested that the rupture may have propagated further west ending around 29.1°E (Karabulut *et al.*, 2002). The distribution of Izmit aftershocks reveals four clearly separated regions of seismicity in the eastern Sea of Marmara (Karabulut *et al.*, 2011). 1) An E-W striking band of seismicity along the central Çınarcık basin, the Çınarcık basin segment (dashed red line in Fig. 6.3). On this segment strong Izmit aftershock seismicity may have indicated the westernmost portion of the Izmit rupture. 2) A pronounced seismicity cluster was activated two days after the Izmit earthquake near the Tuzla peninsula (Fig. 6.3, red circle). This Tuzla cluster is currently active with constant location and size (Bulut *et al.*, 2009; Bohnhoff *et al.*, 2013). 3) On the NW-SE trending Princes Islands segment (Fig. 6.3, bold red line) the aftershock activity was triggered immediately following the Izmit earthquake but diminished rapidly within a few weeks. This fault segment is considered to be the main NAFZ branch connecting to the central Marmara segment further to the west. 4) The strongest Izmit

aftershock activity was located to the south of the eastern Sea of Marmara on the Armutlu peninsula, which is outside of our study area (Fig. 6.3, gray circle).

Bohnhoff *et al.* (2013) investigated the microseismic activity below the eastern Sea of Marmara between 2006 and 2009 and identified a potentially locked ~30 km long and ~10 km deep aseismic region below the Princess Islands segment. This contention is based on historical earthquakes in the Sea of Marmara throughout the past 2000 years, and the absence of a major earthquake on the Princes Islands segment since 1766.

For the Sea of Marmara available geodetic data is limited without GPS stations directly south of the fault. This makes it difficult to decide to what extent the Princes Islands segment is creeping or locked (Ergintav *et al.*, 2014). Schmittbuhl *et al.* (2015) suggested for the Princes Islands segment a locking depth of ~10 km, based on the studies of Bohnhoff *et al.* (2013) and Ergintav *et al.* (2014).

In the following, we discuss the mapped *b*-value distribution in the Çınarcık basin.

Comparison to *b*-values in the Izmit-Düzce Region

The *b*-value distribution in the eastern Sea of Marmara is shown in map view and as depth section before (Fig. 6.8) and after (Fig. 6.9) applying the stability criteria (section 6.3.3). We observe strong spatial variations in the *b*-values similar to that visible in the Izmit-Düzce region. This may reflect a strongly heterogeneous stress field, in accordance to the complex tectonic setting of an extensional pull-apart basin, which is cut through by strike-slip faults of different orientations separated by fault bends. However, the absolute *b*-values found in the eastern Sea of Marmara (0.9 – 1.8) are higher than those in the Izmit-Düzce region (0.5 – 1.75).

Although we paid careful attention to compiling a homogeneous dataset so that absolute *b*-values in both study areas can be compared, the generally higher *b*-values in the eastern Sea of Marmara suggest a possible relation to systematic differences in the calculation of magnitudes. For both areas we computed M_W with the same methodology. However, a few systematic differences remain: the bandwidth of frequency over which the seismic moment is computed, the velocity model, the quality factor, and the seismic instruments recording the seismicity. Excluding systematic errors, the random errors on the absolute *b*-values in both study areas are less or equal to 0.2.

High *b*-values in the northern Çınarcık basin

Below the eastern Sea of Marmara the highest *b*-values are observed north of the Princes Islands segment, close to the Baliciada (Fig. 6.3, blue circle) and Tuzla (Fig. 6.3, red circle) clusters. The *b*-values related to the Tuzla cluster did not fulfill the imposed stability criteria due to a limited range of magnitudes of 0.9 above M_c. However, other studies (e.g. Wiemer and McNutt, 1997) discuss *b*-values obtained over magnitude ranges as small as ~0.5, and we consider the uncertainties of the *b*-values around the Tuzla cluster acceptable. The Baliciada cluster was identified as an earthquake swarm that occurred on a splay fault near the Princes Islands segment (Bulut *et al.*, 2011). This cluster consists of 77 events at 10-11.5 km depth that are highly clustered in space (few km²) and time (less than 24h). Bulut *et al.* (2011) concluded that the Baliciada cluster was triggered by fluid transport or fluid pressure variations along the fault network. A similar microseismicity swarm was detected northeast of the Tuzla cluster containing ~100 events of magnitudes between ~-0.5-1.7 (Prevedel *et al.*, 2015). This swarm occurred within a few days framing Apr 20th 2013 northeast of the Tuzla cluster at ~7 km depth. However, even when excluding the Baliciada cluster from the dataset

and repeating the calculation of the *b*-value map the general trend of higher *b*-values north of the Princes Islands segment remain.

Magnetotelluric measurements across the Çınarcık basin indicate a highly conductive anomaly between the Princes Islands and the Çınarcık basin segments extending in depths below ~10 km and possibly continuing down to the upper mantle (Kaya *et al.*, 2013). The authors observe that seismicity is mainly clustered surrounding the conductive body at the Princes Islands segment and south of the Çınarcık basin segment, and suggested that the abundant swarm activity on splay faults north of the Princes Islands segment may be explained by fluids migrating from the deep conductive zone south of the Princes Islands segment to the north. This is similar to seismic swarm activity in volcanically active regions and induced seismicity in hydrothermal fluid injection experiments, which have been observed to coincide with high *b*-value areas (Wiemer and McNutt 1997; Bachmann *et al.* 2012; Tormann *et al.* 2015). This also corroborates the common view that the Yalova cluster south of the Cirnarcik basin is related to hydrothermal activity on the Armutlu peninsula (Karabulut *et al.*, 2002; 2011), where Aktar *et al.* (2004) observed relatively high *b*-values in Izmit aftershocks.

Aktar *et al.* (2004) took the high *b*-values in the Yalova and Tuzla clusters and in the area between them as indication for a pre-existing highly fractured fluid-filled zone, which was reactivated by coseismic stress changes. In contrast to Aktar *et al.* (2004) we obtained significantly lower *b*-values south of the Tuzla cluster. Possibly the difference may be attributed to short-term stress perturbations similar to the strong *b*-value fluctuations after the Izmit and Düzce mainshocks that we observed in the Izmit-Düzce region (Fig. 6.10).

b-value variations along the main fault trace

Southeast of the Princess Islands segment, we observe the lowest *b*-values, coinciding with the fault bend where the main fault trace changes its orientation from E-W to NW-SE. Another low *b*-value patch is located directly south of Istanbul at the other bend of the fault. In this bend the largest event from the catalog (M_W3.1) occurred. In both bending points, fault plane solutions reveal an oblique strike-slip mechanism with a thrust faulting component, which is more pronounced in the northwestern than the southeastern bend (Karabulut *et al.*, 2002; Bulut *et al.*, 2009). The thrust faulting component indicates high compressional stresses at the fault bends in accordance with the observation of low *b*-values (Schorlemmer *et al.*, 2005). Coulomb stress modelling of the Izmit rupture supports the high stresses on the southeastern bend (Hubert-Ferrari *et al.*, 2000; Parsons *et al.*, 2000; King *et al.* 2001). Interestingly, it was exactly at this location where a M_W4.2 earthquake occurred on Jun 25th 2016. This was the largest event below the eastern Sea of Marmara in several years.

On the Princes Islands segment between the low *b*-value areas at the bending points of the NAFZ significantly higher *b*-values are observed which coincide with the aseismic region discussed by Bohnhoff *et al.* (2013). Wiemer and Wyss (1997) suggested that earthquakes likely nucleate in areas of low *b*-values and stop in regions of high *b*-values. Also Wyss (2001) suggested that the rupture of the 1868 *M*6.8 earthquake on the Hayward fault stopped on a fault segment showing high *b*-values. Following their reasoning, the Princes Islands segment could be a creeping or low-stressed fault segment, which may have stopped the Izmit rupture. This also would explain the absence of shallow seismicity. However, the hypothesis of Wiemer and Wyss (1997) neglects the aspect that strong asperities may also act as barriers. For example, the Izmit rupture stopped in the east in a low *b*-value area as indicated by Görgün et al. (2009) and our study.

75
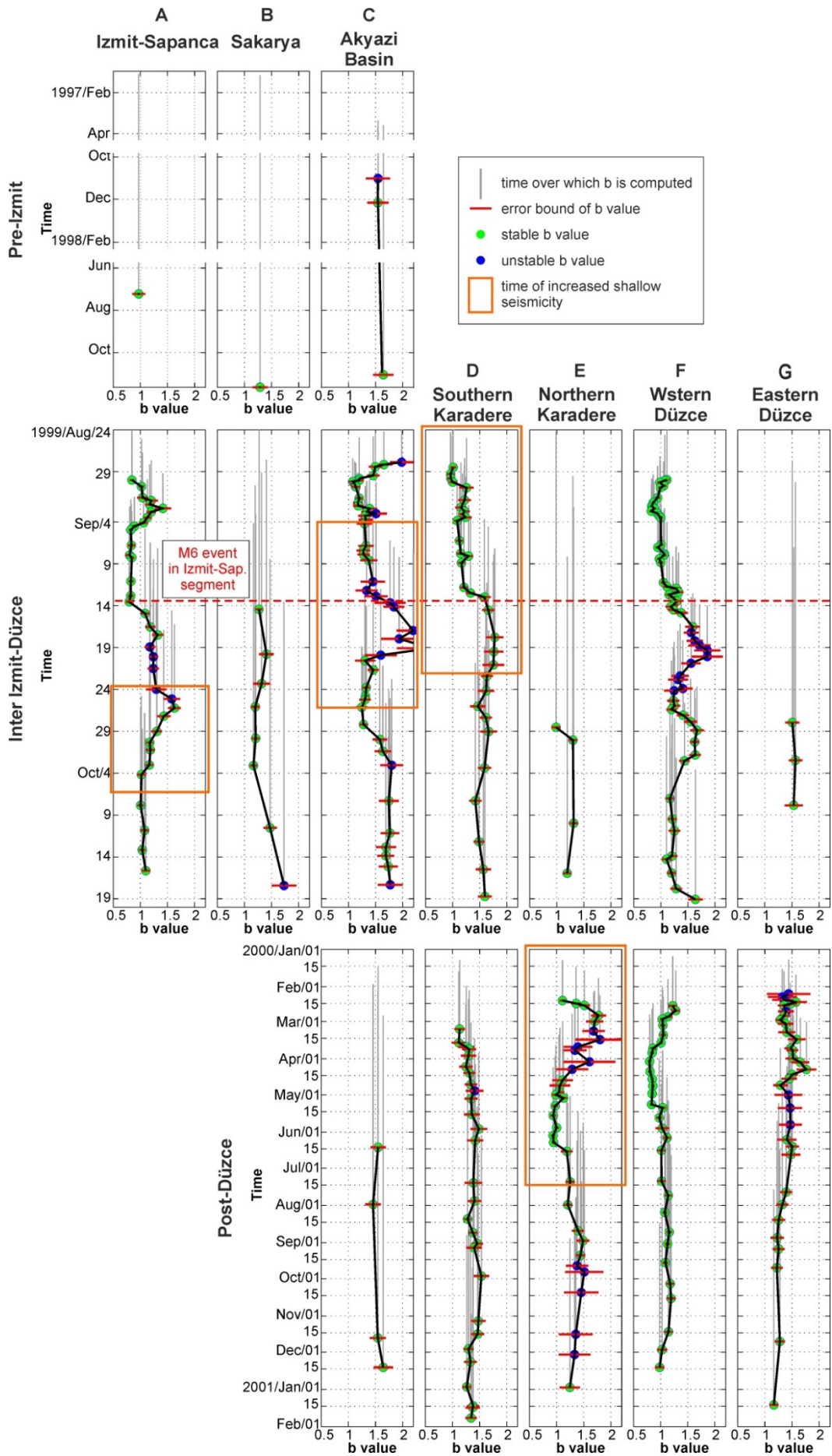
Figure 6.10: *b*-value time series for the areas A – G marked with black boxes in Figure 6.7, and blue boxes in Figure 6.2. Green and blue dots mark stable and unstable *b*-values, respectively, identified by stability criteria (section 6.3.3). Gray vertical lines indicate the timespan over which each *b*-value is computed and uncertainties are presented by red horizontal lines. The red dashed line across the inter Izmit-Düzce time period mark the occurrence of the largest Izmit aftershock in the catalog (*M*5.8). Orange boxes indicate timespans of pronounced shallow seismicity (<10 km depth).

As pointed out earlier, the gridding technique to produce *b*-value maps and depth sections lead to a mixture of different seismicity populations in complex fault systems. Considering that Bulut *et al.* (2011) identified several seismicity clusters on splay faults surrounding the Princes Islands segment, it may be that a mixture of different seismicity populations causes the high *b*-values on the Princes Islands segment, similar to the western Düzce segment. Furthermore, if the Princes Islands segment is locked, it is conceivable that slip is transferred to splay faults surrounding the main fault trace. Thus, the resulting *b*-values on the Princes Islands segment would not be representative for the main fault trace, but rather reflect properties of the splay faults.

6.5   Conclusions

Based on a combined hypocenter catalog, a dataset of homogeneous moment magnitudes was generated to analyze spatiotemporal *b*-value variations in the Izmit-Düzce region for pre-, inter- and post-seismic time periods, as well as the spatial *b*-value distribution in the eastern Sea of Marmara.

The strong variations of *b*-values between 0.5 – 1.8 result from significant complexity of the study area and highlight a variety of possible mechanisms that may explain the observed *b*-values. They are linked to changes in stress conditions on the fault (e.g. Scholz, 1968), or structural parameters, like heterogeneity of the crust (Mogi, 1962) or damage distribution (Meredith *et al.*, 1990; Amitrano, 2003).

Since the stress conditions and structural parameters of the fault are not independent from each other it is difficult to delineate the influence of each individual parameter, and to determine the cause of the observed *b*-value variations. As an example, we observed low *b*-values on the Izmit-Sapanca segment before and after the Izmit mainshock. This is in contrast to the coseismic rotation of the stress regime (Ickrath *et al.*, 2015) from which one could expect elevated *b*-values during the aftershock period due to large stress release. However, when the effect of stress release on the *b*-value may be overprinted by the fault-structural dependency of *b*, the absence of significant *b*-value increase during the aftershock period would not allow to infer the stress state on the fault.

We emphasize the importance of the applied gridding technique, choice of projection (map / depth section), and the choice of temporal separation of the dataset on the interpretation of spatial and temporal *b*-value changes. In complex fault systems, different populations of seismicity (off-fault/on-fault, shallow/deep, or seismicity from adjacent faults) may be easily mixed due to insufficient hypocenter location precision or inappropriate grid selection, potentially leading to misinterpretations of spatial *b*-value distributions.

As a consequence of to the ambiguity of the *b*-value it is not possible to answer the question whether or not the Princes Island segment is locked or creeping. The relatively high *b*-values on the Princes Island segment may 1) be an artefact from mixing different seismicity populations, 2) indicate a weak or creeping fault segment (when *b* is more stress related), 3) indicate a damage zone surrounding the main fault trace (when *b* is more structure related). Finally, the main fault trace may be locked and strain may be transferred to surrounding splay

faults. In this case, b-values from this part may not carry any information about the main fault trace.

7   Conclusions and Discussion

For realistic seismic hazard assessment a comprehensive understanding of all components involved in creating hazard is necessary. However, due to the complex nature of the earth one has to rely on simplified assumptions which are based to a great deal on observations. Therefore, the downhole Geophysical Observatory of the North Anatolian Fault (GONAF) was designed to improve the seismic monitoring of the eastern Sea of Marmara region, with its first borehole array completed on the Tuzla peninsula. Analyses of the first recordings available from the GONAF-Tuzla array proved the goal of lowering the magnitude-detection threshold below zero and improving the quality of microseismicity recordings to be successfully accomplished, as demonstrated by the detection of an earthquake swarm that occurred within a few days around Apr 20th 2013 and comprises ~100 events of magnitudes between ~-0.5 and 1.6.

Subsequently, from a set of 26 local earthquake recordings from the Tuzla borehole array of good signal-to-noise ratio, near-surface Q values and P- and S-wave velocities were estimated with seismic interferometry. In general, estimates of Q are imprecise and which method of determination is most suitable depends on the specific situation given by signal-to-noise ratio, geology, and recording conditions (Tonn, 1991). Borehole recordings are interfered by downgoing reflections from the surface and reflectors between the surface and the borehole sensor. When standard methods such as the spectral ratio technique fail due to interference effects the method proposed here is a good alternative, since it takes advantage of the complete wavefield including downgoing waves. With deconvolution interferometry Green's functions for the individual depth levels of the instruments were obtained with an excellent signal-to-noise ratio. These were forward modeled to infer the near-surface parameters. However, the forward modeling approach used here is based on two simplifications: 1) a single homogeneous layer above each borehole sensor and 2) that P- and S-wave parameters can be determined independently. Due to assumption (1) it was not possible to constrain with the modeling approach the depth of the low velocity layer. Only precise velocities of an effective homogeneous layer above each borehole sensor were obtained. Furthermore, assumption (1) leads to increasing uncertainties in the P- and S-wave quality factors with increasing model complexity since impedance effects that alter the amplitude of the wave are neglected, while assumption (2) only affects the accuracy of Q_P. Therefore, more sophisticated modeling techniques are needed to derive results of great precision at sites of complex geology and to constrain the depth of layer interfaces.

The Tuzla site reveals unusual high seismic velocities and a low-velocity layer at ~90-140 m depth. The velocity inversion may have consequences for ground motion predictions at the Tuzla site, as discussed in the following.

To account for site effects in ground motion predictions the site's site-response is classified by their site conditions which are commonly described with the international standard parameter V_{S30}, i.e. the average S-wave velocity in the upper 30 m. A common method to obtain site specific V_{S30} values is modeling horizontal-to-vertical spectral ratios (HVSR) of seismic noise recordings (Di Giacomo *et al.*, 2005). However, site-response characteristics obtained from noise and earthquake recordings differ, due to different composition and propagation path of the wavefields (Di Giacomo *et al.*, 2005). The differences are especially significant in the presence of a velocity inversion, as it is the case for the Tuzla site. As illustrated in Figure 7.1 (top, right) the waves of the seismic noise triggered on the surface propagate laterally and are mainly composed of surface waves, while the earthquake waves, incident from below, are affected by the impedance contrasts in the heterogeneous subsurface. Hence, if site-response classifications are based on V_{S30} only, neglecting geological complexity may lead to unexpected amplification due to velocity inversions (Kanlı, 2006;

Gallipoli and Mucciarelli, 2009). Accordingly, refined classification parameters are suggested (Steidl, 2000). Such new methodologies can be tested best when the subsurface structure is well known. Thus, as outlined in the next section the GONAF borehole array forms a good basis for testing new methodologies for site characterization.

In the second study of this thesis spatiotemporal variations of the Gutenberg-Richter b-value in the Izmit-Düzce region and eastern Sea of Marmara were analyzed in the attempt to better understand the current state of stress on the Princes Islands segment of the NAFZ and to evaluate b-value variations at different stages of the seismic cycle. As a first step the dataset was homogenize by recalculating moment magnitudes for all events in the hypocenter catalogs. Subsequently b-value maps and depths sections were generated with a standard gridding technique, and for the Izmit-Düzce region b-value time series were computed for seven sub-regions.

Although the Izmit and Düzce earthquakes are two of the best studied transform-fault earthquakes of the world the observed spatiotemporal b-value distribution in the Izmit-Düzce region could not be interpreted unambiguously, and often the observed b-values were not as expected from simple assumptions. For example on the Izmit-Sapanca segment low b-values are observed during the inter Izmit-Düzce time, although one could expect high aftershock b-values because of the rotation of the stress regime which implies large stress release and observed large coseismic displacement on the Izmit-Sapanca segment. This suggests that also structural parameters like fault geometry or fracture distribution affect the b-value. However, fault-structural parameters and the state of stress on a fault are not independent from each other, and it is difficult to discriminate which parameter affects the b-value most. Thus, the b-value analysis in the Izmit-Düzce region points out that b-value interpretations should be regarded with care, and the interpretation needs to incorporate all available information in order to limit the possibility for erroneous conclusions. As a consequence, due to the limited knowledge about the Princes Islands segment the b-values in that area did not help to constrain the state of stress on the Princes Islands segment, since they can be interpreted in various ways. Furthermore, the data discretization scheme influences the appearance of the final b-value distribution leading to potential misinterpretations of erroneous b-values that arise from mixing different seismicity populations.

Nevertheless, even when the cause of b-value variations is not well understood, in the majority of b-value studies the spatial variation is regarded as real due to numerous observations in the laboratory and field. Hence, the trend in probabilistic seismic hazard assessment (PSHA) is towards incorporating recurrence models with spatially varying b-values (Schorlemmer $et\ al.$, 2004b; Pace $et\ al.$, 2006; Wiemer $et\ al.$, 2009). Independent of the choice of model for describing the frequency-magnitude distribution of the largest events on a fault (e.g. characteristic or truncated GR law) the b-value is needed to describe the background seismicity of small to moderate magnitudes, as illustrated in Figure 7.1 (top, left). In current PSHA for the Marmara region the background seismicity is described with a constant b-value throughout the region (Erdik $et\ al.$, 2004; Kalkan $et\ al.$, 2008). The strong variety of b-values in the eastern Sea of Marmara suggests that it may be reasonable to incorporate spatial variations. However, the PIRES catalog with microseismicity between M_W~1-3 is an unusual dataset for determining the b-value of background seismicity in PSHA, since usually for that purpose catalogs containing earthquakes of magnitude up to 5 or 6 are used. However, according to the concept of self-similarity the b-value derived from microseismicity could be extrapolated to larger magnitudes. Still, the four-year time period of the PIRES catalog is too short, and even when self-similarity holds true the absence of larger magnitude events in the catalog precludes a prediction of background seismicity with statistical relevance. Nevertheless, the b-value variation in the region indicates that a regional constant b-value may not be a realistic assumption.

79

The study of near-surface properties at the Tuzla site and the *b*-value analysis suggest that the models on which seismic hazard estimates in the Istanbul region are based are too simplified, which would lead to an under- or over-estimation of the seismic hazard. In PSHA such epistemic errors, arising from wrong model assumptions, are reduced by using logic trees to consider several conceivable models. An example is given in Fig. 7.1, bottom. First seismic sources are defined. For example, if the fault system is well known a fault segmented model can be used in which each fault is characterized by its kinematics and credible maximum magnitude. Then various recurrence models can be considered, e.g. models that consider a constant or variable *b*-value, for example an individual *b*-value for each fault segment. Furthermore, different so called attenuation relations can be taken into account, which are models to account for site effects. When enlarging the number of models in the logic tree epistemic uncertainties are possibly reduced. Finally, to design seismic hazard assessment as site and fault specific as possible, analyses of near-surface rock characteristics and spatial *b*-value variations are indispensable.
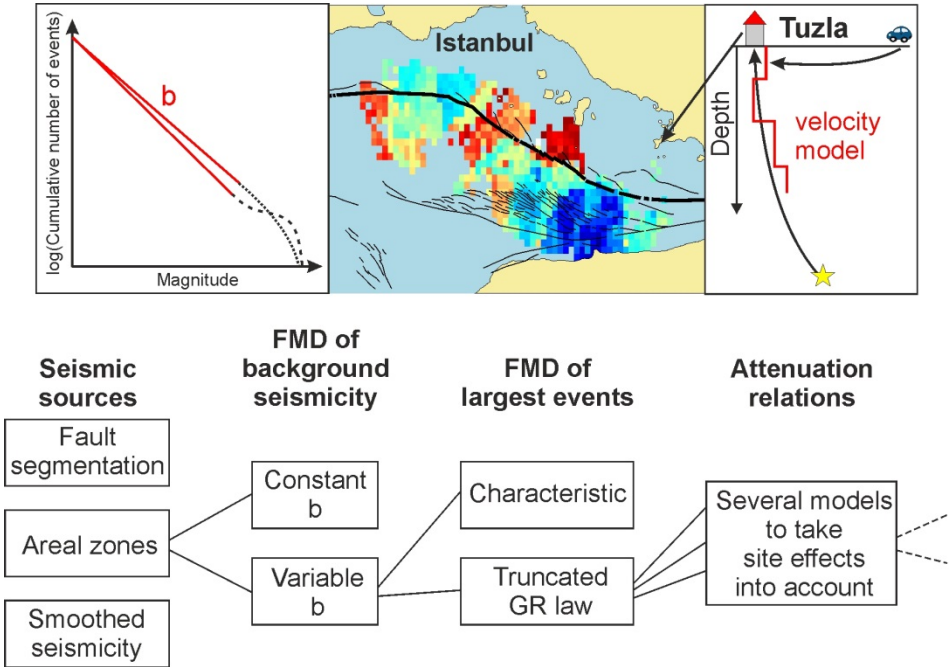
Figure 7.1: Bottom: Overview of different components that are considered in probabilistic seismic hazard assessment (PSHA) in form of a logic tree which can be arbitrarily extended: Models for defining seismic sources (column 1), recurrence models to predict future seismicity (column 2 and 3), and several models of attenuation relations to account for site effects (column 4). The **top right** figure illustrates how the velocity inversion below the Tuzla site affects waves which incident from below, while waves which are radiated from noise sources at the surface do not propagate through the velocity inversion (depending on their wavelength). The **top left** figure is a sketch of two different recurrence models. The predicted background seismicity of small to moderate magnitude (red lines) depends mainly on the *b*-value. The prediction of recurrence periods of the largest credible earthquakes on the fault depends strongly on the choice of model (e.g. characteristic (dashed line), truncated GR law (dotted line)). The **top middle** figure shows a map of the eastern Sea of Marmara together with the *b*-value distribution determined in this study. The black bold line marks the main trace of the NAFZ.

7.1   Perspectives

So far, the study of near-surface rock properties was focused on data from the Tuzla site as the first completed borehole array. Now that seven GONAF boreholes are completed the study can be extended to the other boreholes. Since all borehole arrays are equipped equally systematic differences due to variable recoding systems can be ruled out, making the GONAF borehole network ideal for comparative studies. A joint study of near-surface wave propagation and associated site effects with the seven GONAF borehole arrays allows for example to discriminate between and address the role of different geological formations. For example, the Tuzla well penetrates mostly carbonatic formations, while the Büyükada well is drilled into a solid Quartzite. Furthermore, the applicability of different techniques for determining near-surface characteristics can be tested on different sites. For example, the forward modeling procedure used in this study should be extended to take heterogeneities between the borehole seismometer depth levels as well as the incident angle of the incoming earthquake waves into account. Furthermore, the derived near-surface rock properties should be translated to standard parameters like V_{S30} to facilitate the use of the results in existing ground motion prediction equations and standard site classifications. Afterwards, new classification parameters can be evaluated. Since the borehole arrays will be complemented in future with a strong-motion and broadband instrument at the surface, different instrumentations can be incorporated into the tests as well. Especially the strong-motion recordings will be of great value in the case of a strong earthquake, to address the question of how well the previously from weak motion estimated site responses predict strong ground motions.

To extend the b-value study to the central and western Sea of Marmara hypocenter catalogs from the regional seismometer networks from KOERI (Kandilli Observatory and Earthquake Research Institute) and AFAD (Disaster and Emergency Management Presidency of Turkey) can be incorporated into the study. From both institutes the catalogs date back to 1900. Incorporating these datasets into the existing ones will enlarge the study area in space and time, and will add seismicity of moderate magnitude to the dataset which are needed to estimate the background seismicity with statistical relevance. However, it will be a challenging task to ensure a homogeneous magnitude scale in such a combined catalog, and to assess the magnitude of completeness which varies during the long time period.

Since the gridding technique used here to generate b-value maps and depth sections are not ideal for complex fault systems, different techniques for grouping the events should be tested. Instead of grouping events around each grid cell it may be more reasonable to group events based on distance to the fault. The evaluation of the quality of different event-selection techniques will be limited by hypocenter precision and knowledge about the fault geometry.

Finally, to address the question to what extend damage distribution affects the b-value, further laboratory or field experiments are necessary, since laboratory studies that evaluate the b-value in conjunction with damage are less frequently presented in science than studies that focus on the dependency on stress, because the latter is easily measurable during the experiment. A possible analysis to evaluate the b-value dependency on damage may be as follows. Laboratory experiments indicate that typically the density of damage in the rock, i.e. fracture density, decreases with increasing distance to the rupture plane of the macro-rupture, which is in accordance to field observations where the density of seismicity in the crust decreases with distance to the fault. Therefore, it should be tested if this is reflected in spatial b-value variations within the damage zone.

Appendix

A.   Orientation of downhole horizontal components[5]

During the deployment of the downhole three-component geophones the vertical component of the instruments follows the direction of the well path, which deviates from verticality by less than 2° (Prevedel *et al.*, 2015), whereas the orientation of the horizontal components cannot be controlled due to rotation of the instruments around their vertical axis while they are lowered into the hole. Therefore, before comparing with each other the horizontal components of the surface and downhole sensors, the downhole horizontal components need to be rotated into the same direction as the orientation of the surface components, i.e. into N and E directions.

The rotation angle is determined by calculating cross-correlations between the horizontal components of the surface sensor with rotated horizontal components of the downhole sensor. Thereby the downhole sensor is clockwise rotated in 1° steps. The angle that yields the larges cross-correlation coefficient is regarded as the angle of deviation from N and E.

To avoid a false angle determination due to scattered high-frequency waves we low-pass filtered the data below the first trough in the downhole spectra of the P- and S-waves at ~3 Hz. Thus for this analysis we had to select a second dataset of well recorded regional and teleseismic events that have a sufficiently strong content of low-frequency energy. Eleven events with hypocentral distances between 114 km and 1614 km and magnitudes of 4.7 – 6.4 were selected from KOERI catalog. Due to their lack of high-frequency energy these eleven events are not part of the dataset used in the shallow wave propagation study.

For the cross-correlation analysis we selected the whole signal (P- and S-waves) and used instrument corrected recordings. The cross-correlation functions for all eleven events are presented in Fig. 4.11. They are very coherent, thus present a stable result. Averaging the maximum cross-correlation coefficients yields the angle of deviation from N and E of 313° ± 15°. Thus, as first processing step of the shallow wave propagation study, the downhole horizontal components of the sensor at 288 m depth are clockwise rotated by 313°.
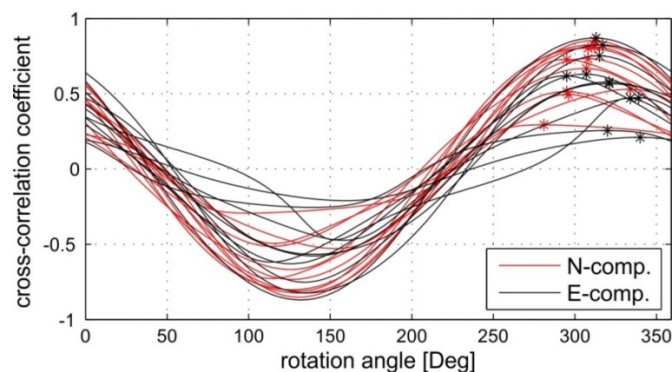
Figure A.1: Cross-correlation functions of the 2 Hz geophone at 288 m depth from all eleven events that were selected for the orientation of the downhole horizontal components. The maximum cross-correlation coefficient is marked by a star.

---

[5] Appendix of the publication Raub *et al.* (2016) (chapter 4).

B.   Aseismic patches in the Izmit-Düzce region and *b*-values[6]

Bohnhoff *et al.* (2016b) observed four aseismic patches in the upper 10 km of the crust during the Izmit and Düzce aftershock periods (Fig. 2, orange patches A – D in the depth sections). The authors related patches A and B to the aseismic afterslip cumulated during the 75 days following the Izmit event, and the aseismic patches C and D to the cumulative ~2 years afterslip of the combined Izmit and Düzce earthquakes.

We do not observe a correlation with the *b*-value distribution for the corresponding time periods, inter Izmit-Düzce (A, B) and post-Düzce (C, D), see Figure 7. Patch A stretches for about 40 km below the Izmit-Sapanca and Sakarya segments. We find low *b*-values (0.5 – 0.9) in the west and higher ones (0.9 – 1.2) in the east. Along the ~30 km long aseismic patch B below the Karadere fault we observe *b*-values between 0.5 – 1.3. For patch C, which spans ~40 km from Lake Sapanca across the Akyazi basin and large portions of the Karadere segment, we only obtained *b*-values for its eastern part with values ranging between ~1 – 1.4. Patch D (~40 km long) located below the eastern Düzce segment and Elmalik fault coincides with high *b*-values up to 1.5.

The location of the aseismic patches during the inter Izmit-Düzce time suggests a relation between the distribution of aftershock seismicity, fault geometry, and stress distribution (Bohnhoff *et al.*, 2016b). Patches A and B are located on strike-slip segments with large coseismic lateral slip at the surface (1-5 m, Barka *et al.*, 2002) and in the upper crust (e.g. Delouis *et al.*, 2002) indicating a relaxation of the fault due to large stress release. Between the aseismic patches A and B is a high-seismicity area in the Akyazi basin at the triple junction of the Sakarya, Karadere, and Mudurnu faults. To the northwest patch B is bounded by another high-seismicity area at the southwestern border of the Düzce basin. In the Akyazi and Düzce pull-apart basins a broad zone of shearing without a clear surface rupture was observed (Barka *et al.*, 2002; Hartleb *et al.*, 2002). Thus, Bohnhoff *et al.* (2016b) suggested high coseismic stress release on the patches A and B and a stress concentration on the ending points of rupture segments where strong aftershock activity was triggered. Accordingly, we could expect for the inter Izmit-Düzce time to find high *b*-values at patches A and B, and low *b*-values in the Akyazi and Düzce basins. However, this does not match our observation and those of other *b*-value studies of Izmit aftershocks (Aktar *et al.*, 2004; Görgün *et al.*, 2009).

---

[6] Appendix of the manuscript Raub *et al.* (submitted to *Tectonophysics*) (chapter 6).

C. Supplementary material of the *b*-value study[7]

Stability tests

The parameters strongly affecting the *b*-value in the methodology used here are N, M_c, and ΔM, the latter since it influences the determination of M_c. Therefore, to evaluate the stability of the results we test different parameter settings. Tests with $\Delta M = 0.2$ and 0.3 produced very similar *b*-values and we decided to use a ΔM of 0.2 for the whole study.

The influence of M_c was tested by repeating the analysis with a M_c that was held constant for the whole study area, instead of determining M_c individually for each bin. The spatiotemporally varying M_c values from the goodness of fit method range between 1.2 and 2.2 in the Izmit-Düzce region, and 1.3 and 1.8 in the eastern Sea of Marmara (see map of M_c in Fig. C1,2(a)). We tested as constant M_c values between $1.6 - 1.9$ (only a very small area in the Izmit-Düzce region has a larger M_c). As expected, the choice of M_c affects the *b*-value most, but the main features of the *b*-value variations remain. When M_c is set to 1.6 it is in some areas lower than the value estimated from the goodness of fit method. This results in an underestimation of *b*, which can be observed in Figure C3,4. Nevertheless it is also not practicable to use the maximum M_c observed in the study area since then the limitation of using $N = 50$ events above M_c is only fulfilled by a few bins. Therefore, to make use of as many events as possible we use for our analysis a spatiotemporally varying M_c.

A further parameter affecting the *b*-value results is the accuracy of the hypocenter locations. This is particularly important for the SABONET catalog containing some events with comparatively large hypocenter location errors. We tested different subsets of the SABONET catalog, chosen based on location precision. The first subset contains all events independent of the error in location, and the second and third subsets contain only events that have a hypocenter location error < 10 and 5 km and a rms < 0.5 and 0.3 s, respectively. Figure C5 shows *b*-value maps that were computed with the three different subsets and different N (50, 75, 100). Figure C6 shows *b*-value maps computed with the PIRES catalog and different N. We do not test $N < 50$ because below this value the uncertainties of *b* increase rapidly (Wiemer and Wyss, 2002). These tests show that the main features of the spatial and temporal *b*-value variations in the study area remain, independent of the choice of N and event location precision. Mainly the spatial resolution of *b*-value anomalies and the coverage of the area for which a *b*-value can be computed are affected, because the larger N the larger the area from which the events are selected for each bin, and the smaller N the more bins fulfill the condition of having the closest N events within a radius of 10 km. Therefore, to obtain a large spatial coverage and a fine resolution, we use an N of 50, and for the SABONET catalog location errors of up to 10 km and a rms of up to 0.5 s is allowed, yielding mean horizontal and vertical location errors of 3.3 and 4.1 km, respectively, and a mean rms of 0.22 s. These location errors only apply to the SABONET catalog. From the relocated Izmit aftershocks and the PIRES catalog all events can be used, since they have good relative location accuracy.

---

[7] The section 'Stability tests' is submitted as electronical supplement of the manuscript Raub *et al.* (submitted to Tectonophysics) (chapter 6).

a)

85

b)

ID1   ID2   ID3   ID4

Distance along profile [km]

M_{range}

C)

87
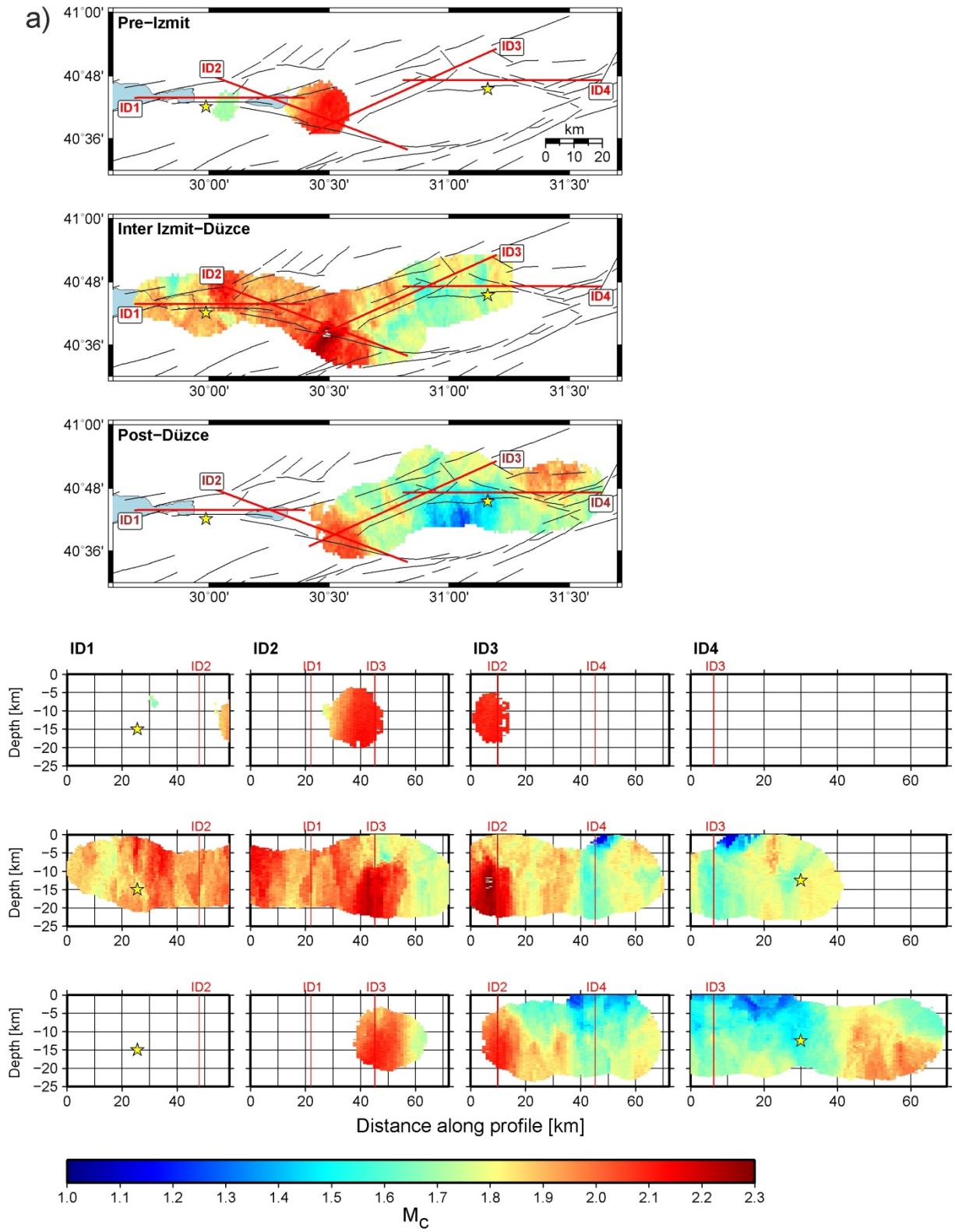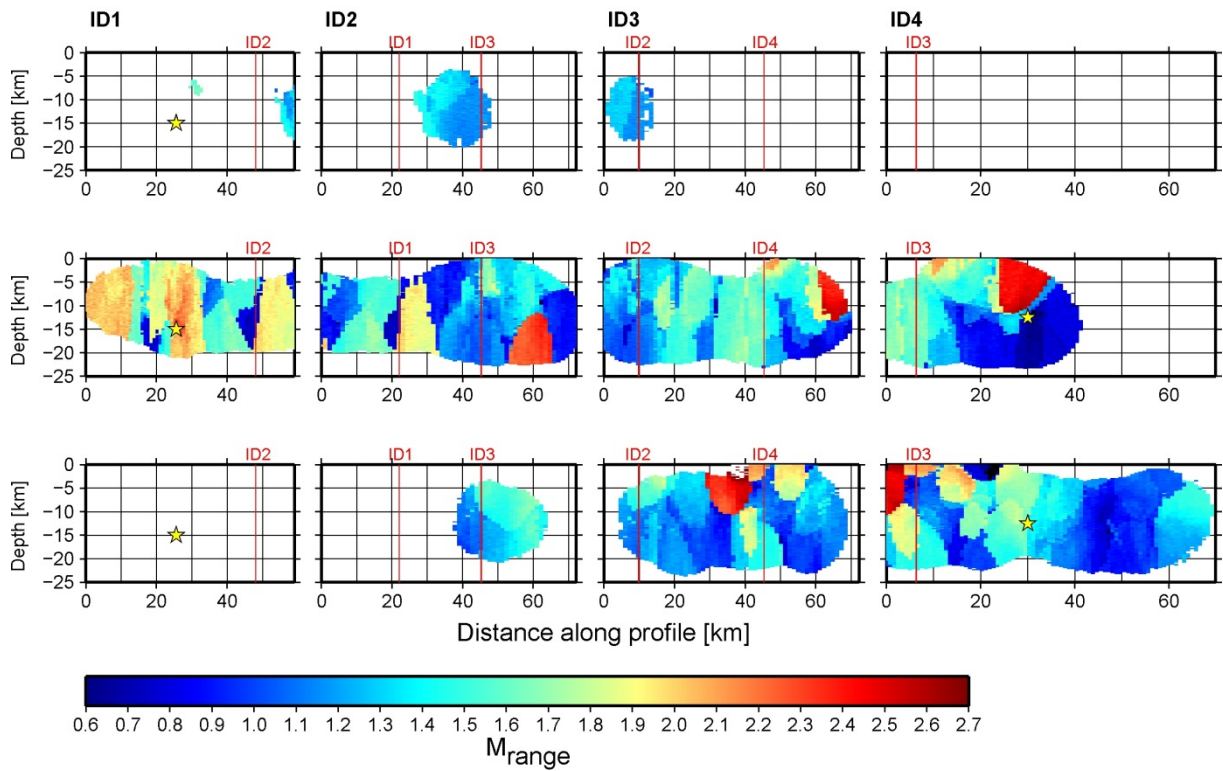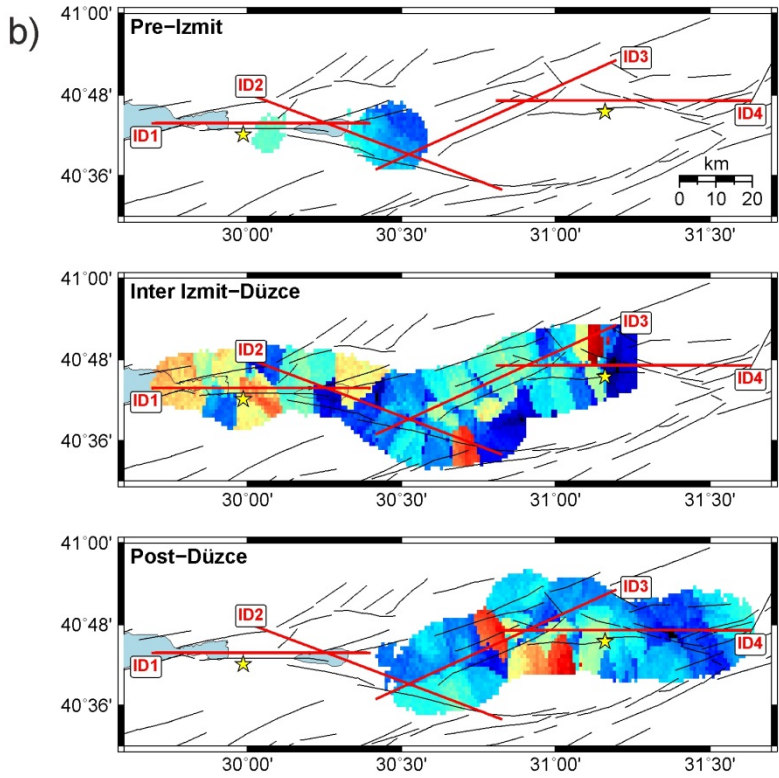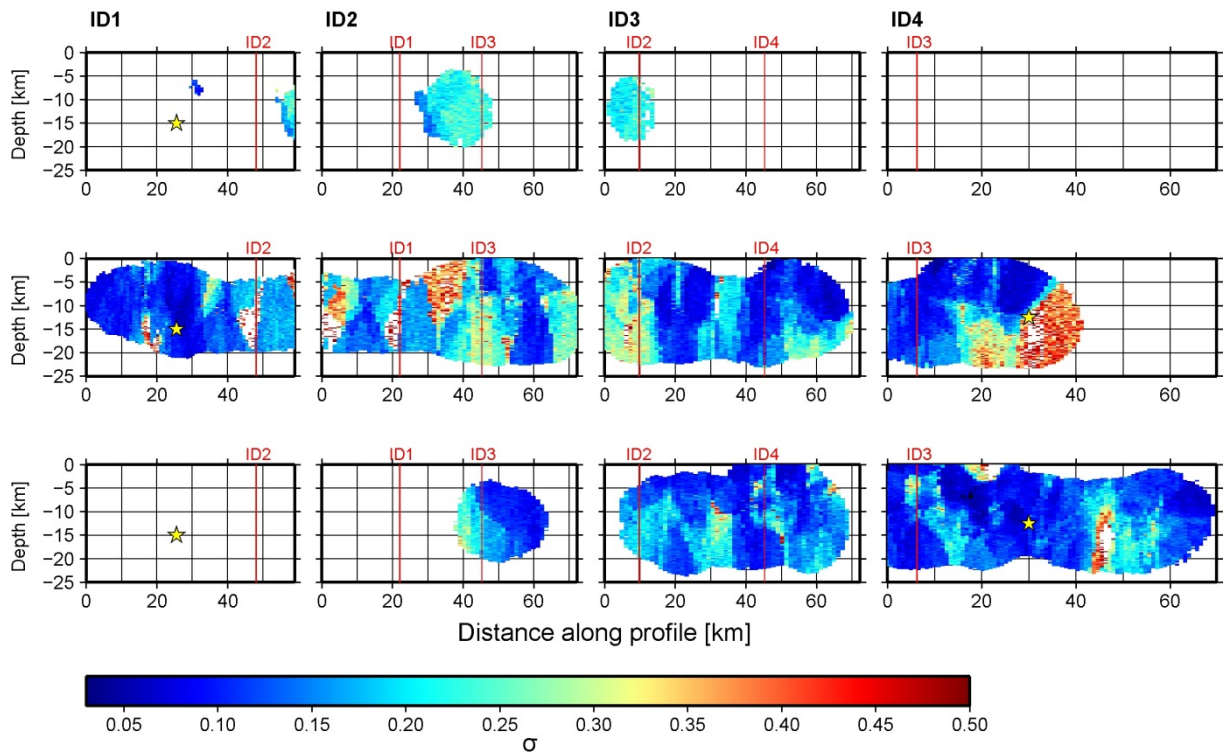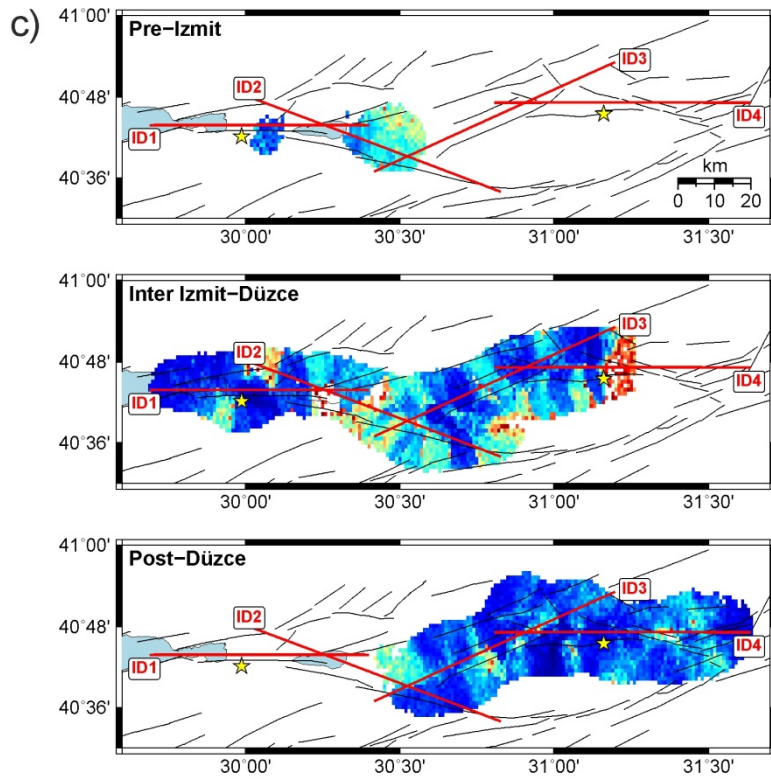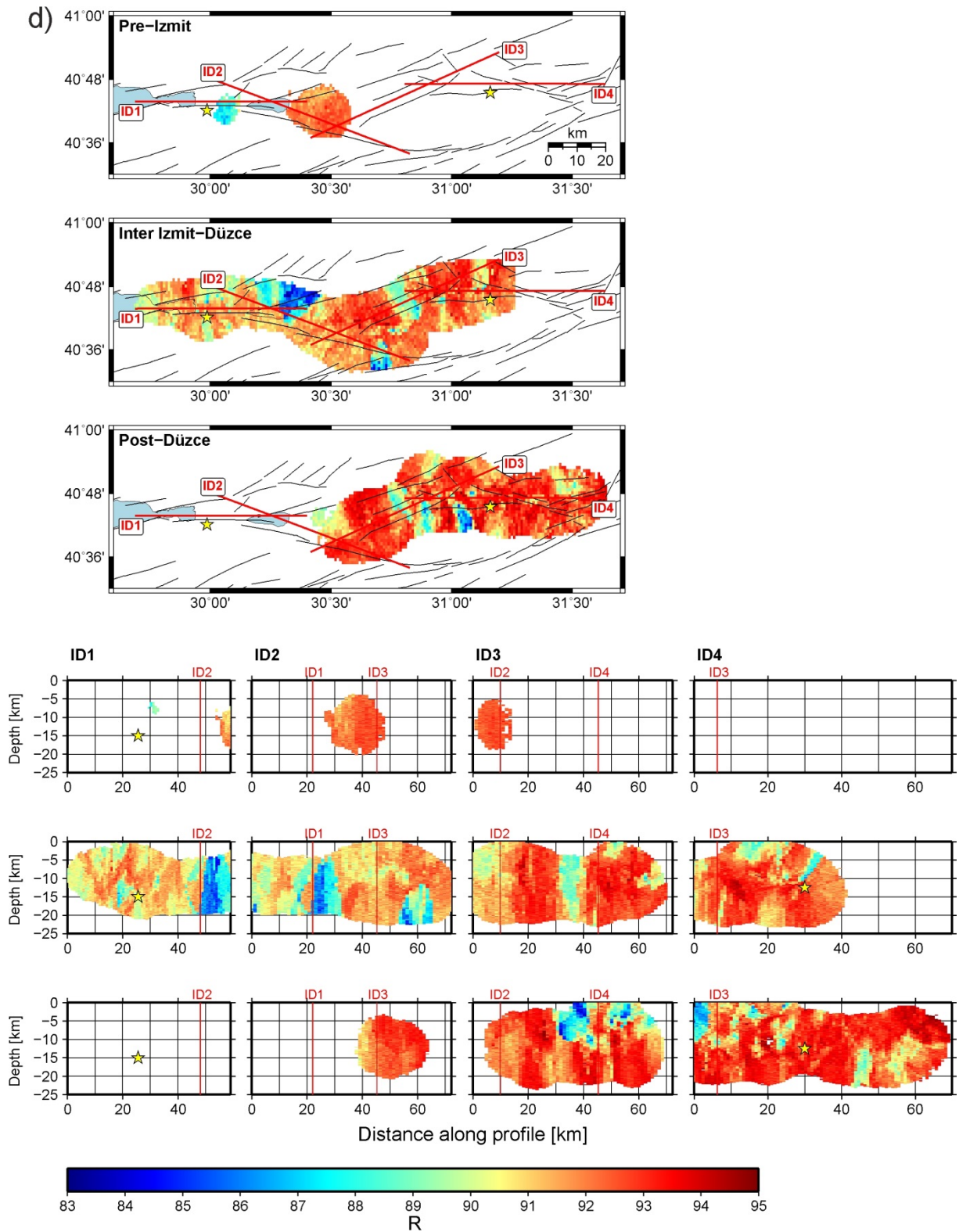
Figure C.1: Maps and depth sections of **(a)** magnitude of completeness, **(b)** range of M above M_c, **(c)** standard deviation of b and **(d)** the goodness of fit value R in the Izmit-Düzce region.
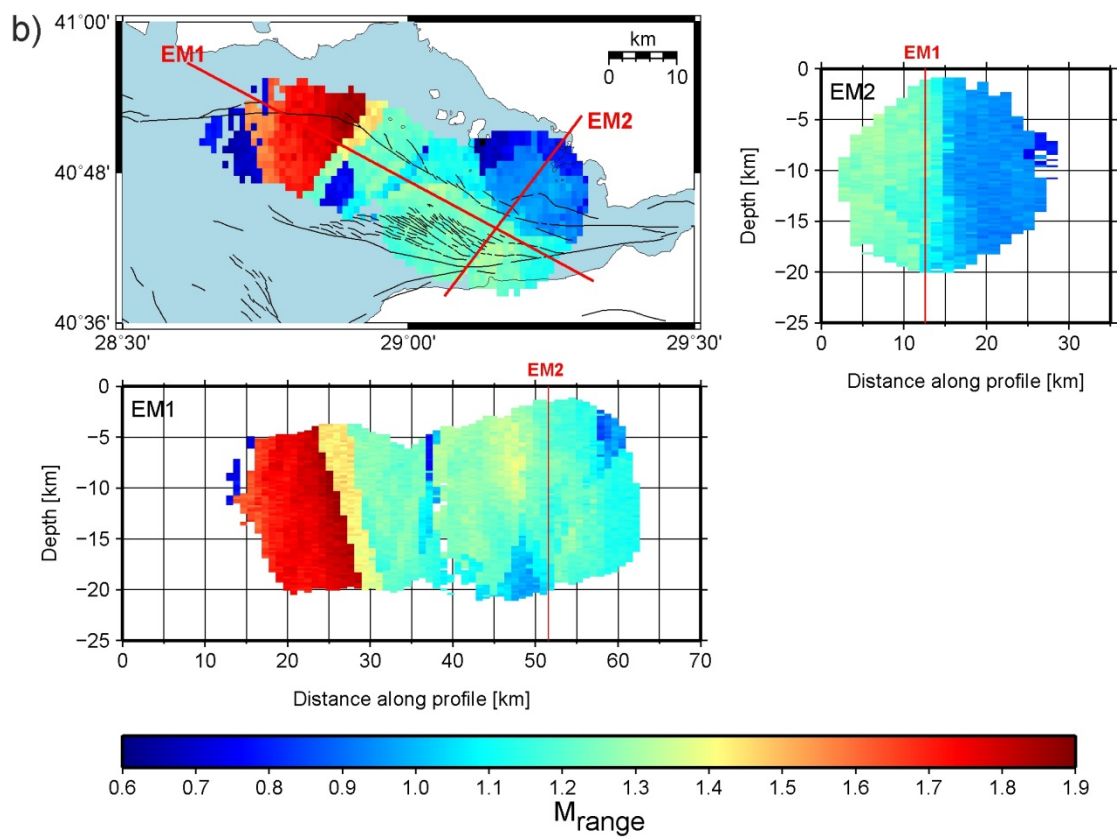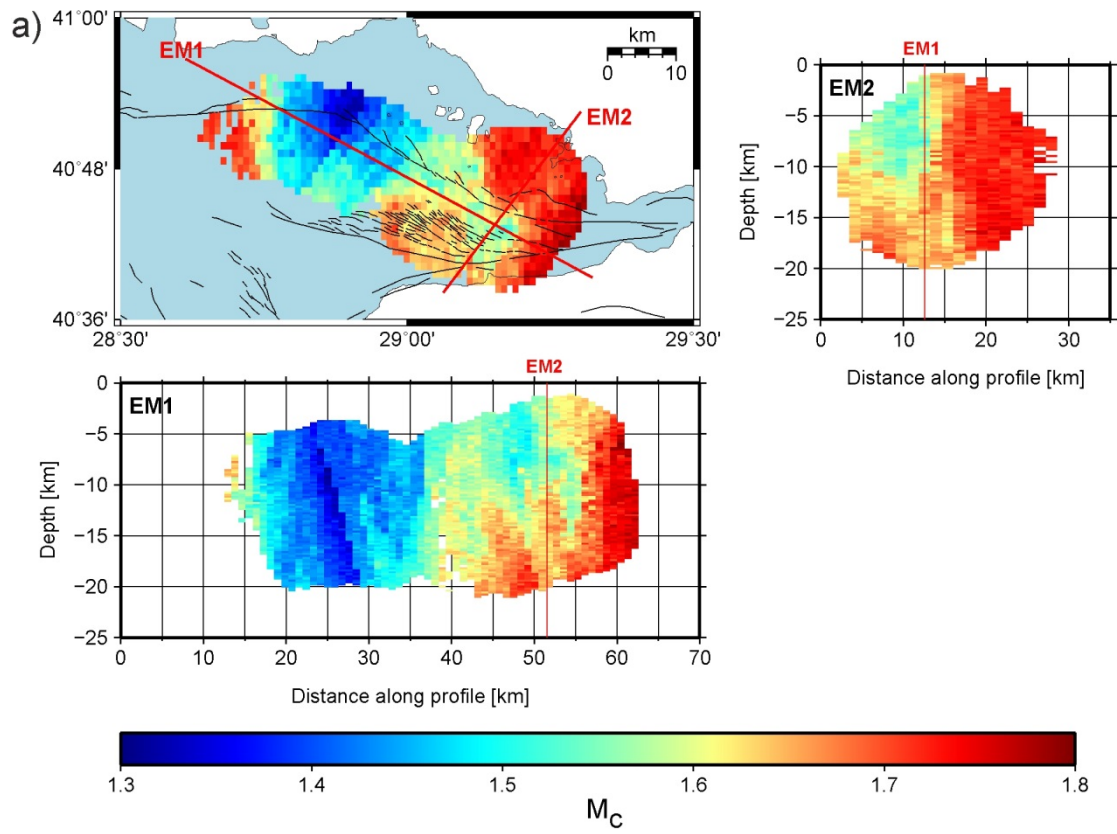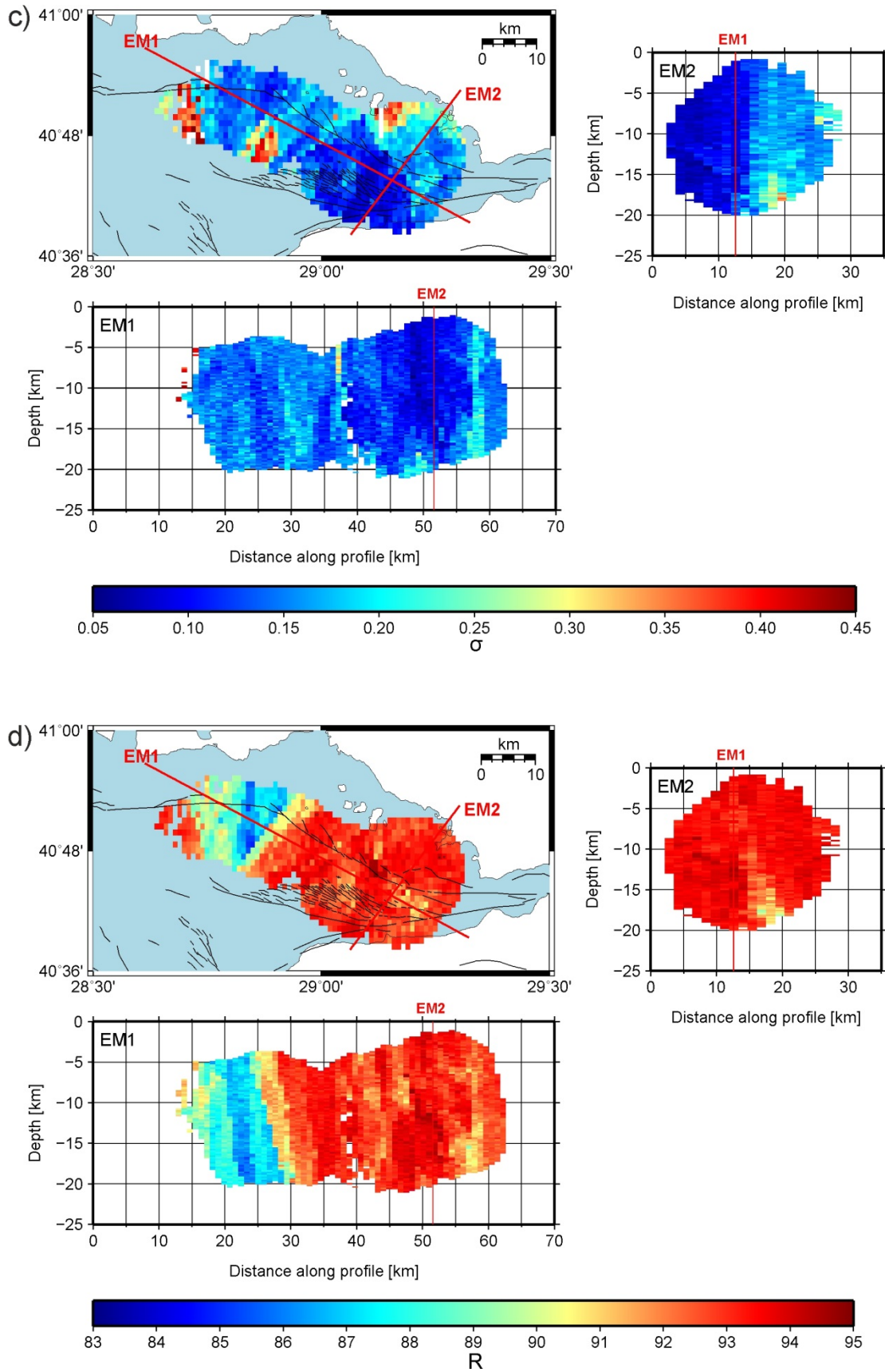
Figure C.2: Maps and depth sections of **(a)** magnitude of completeness, **(b)** range of M above M_c, **(c)** standard deviation of b and **(d)** the goodness of fit value R in the eastern Sea of Marmara.
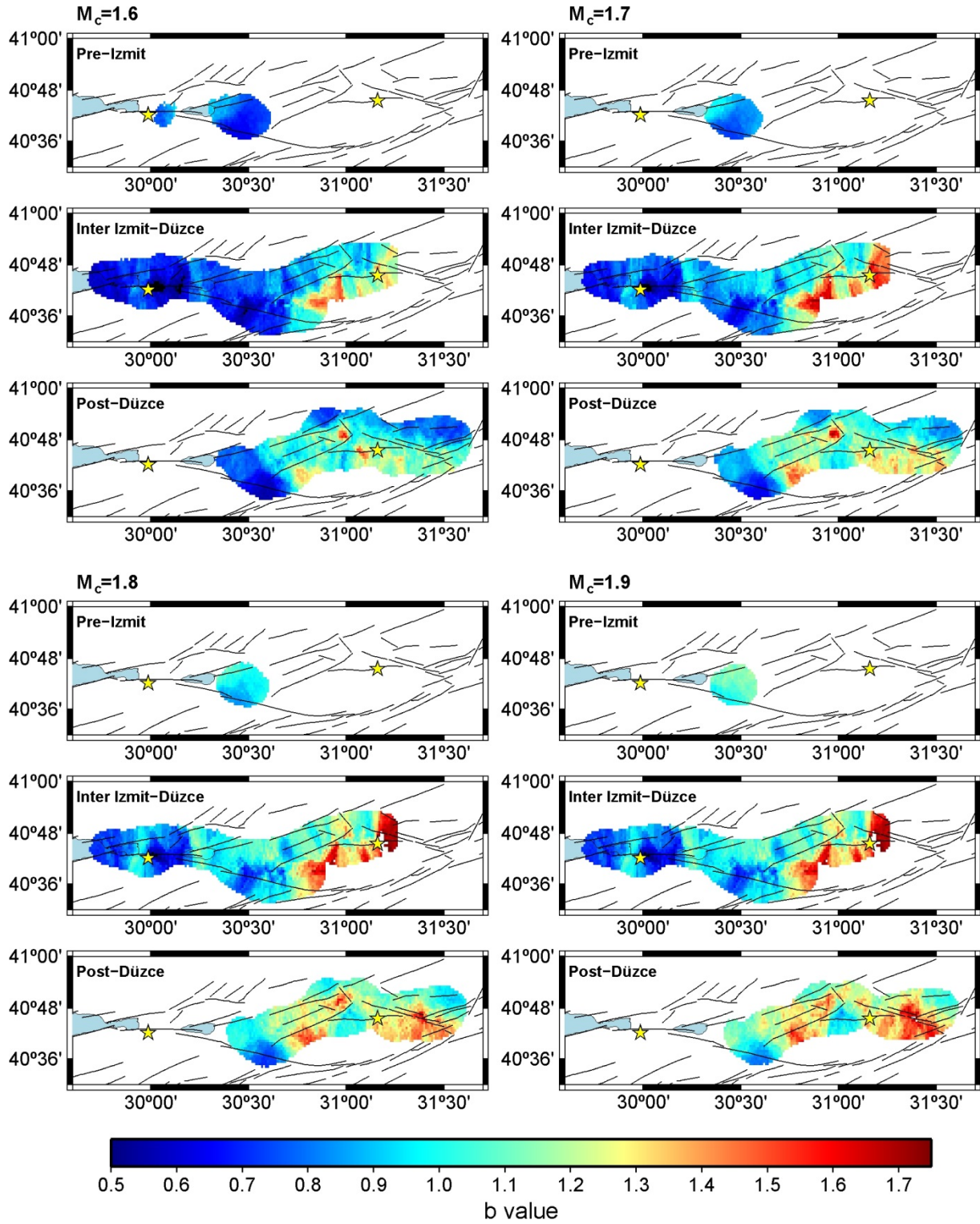
Figure C.3: Test of different values for M_c (1.6, 1.7, 1.8, 1.9) that were held constant for the whole study area, instead of determining M_c individually for each bin in the Izmit-Düzce region.
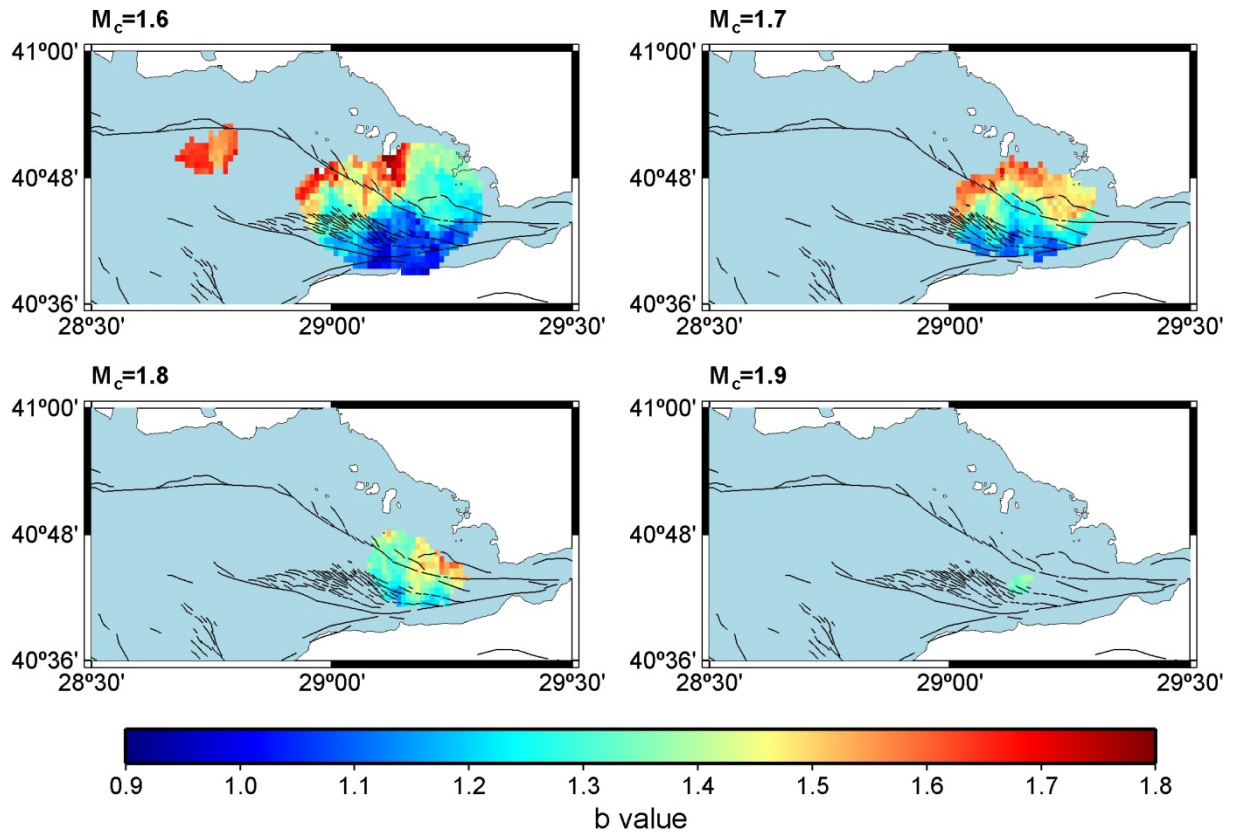
Figure C.4: Test of different values for M_c (1.6, 1.7, 1.8, 1.9) that were held constant for the whole eastern Sea of Marmara, instead of determining M_c individually for each bin.
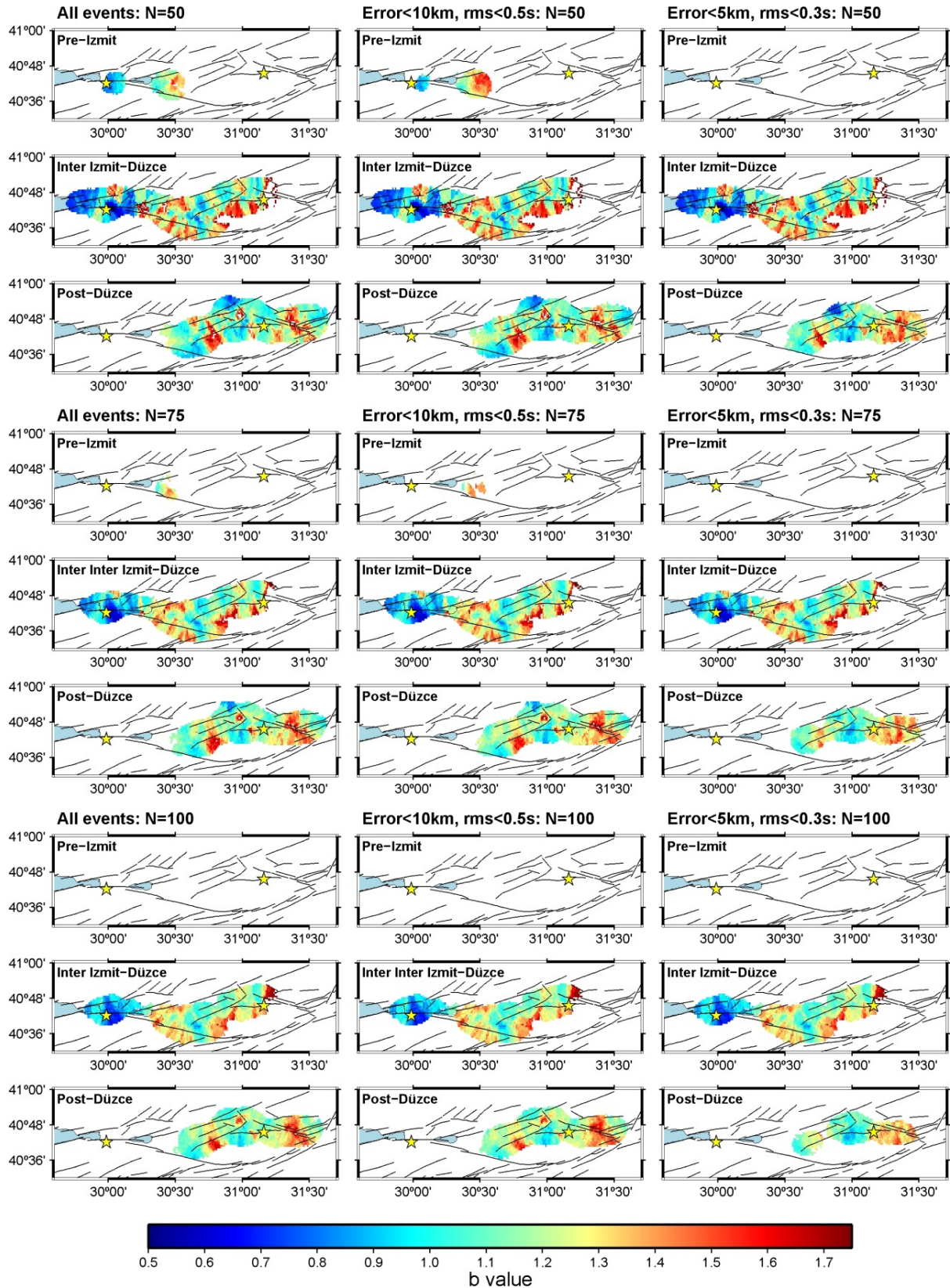
Figure C.5: Test of different N (50, 75, 100) and threshold of event location precision. In the left column all events were used independent of location error, and in the middle and right columns thresholds of location error < 10 and 5 km and rms < 0.5 and 0.3s were tested in the Izmit-Düzce region.
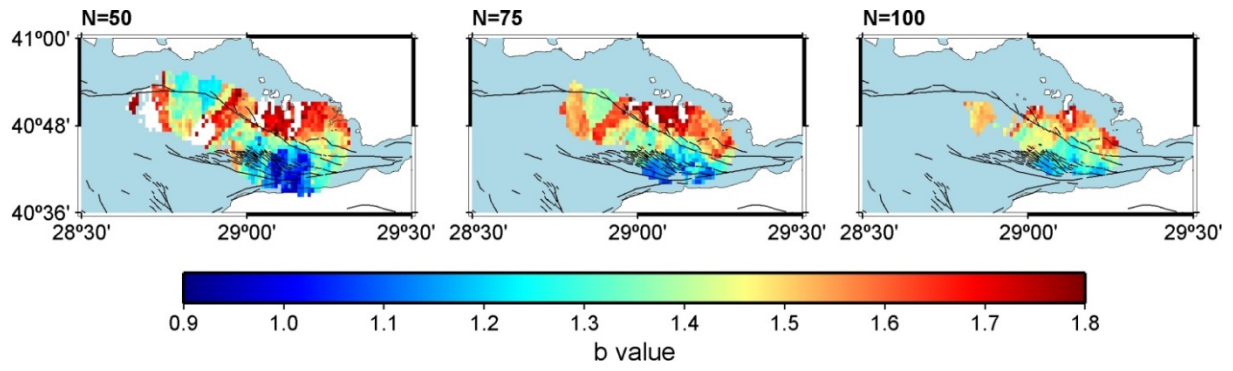
Figure C.6: Test of different N (50, 75, 100) in the eastern Sea of Marmara.

D.   Supplementary material of the GONAF-Tuzla study[8]

This electronic supplement contains figures that present the resistivity and caliper logs in comparison with the *P*- and *S*-wave sonic log measurements (Fig. A.1) and the spectra of all 26 events used in the shallow wave propagation study (Figs. A.2–A.14).
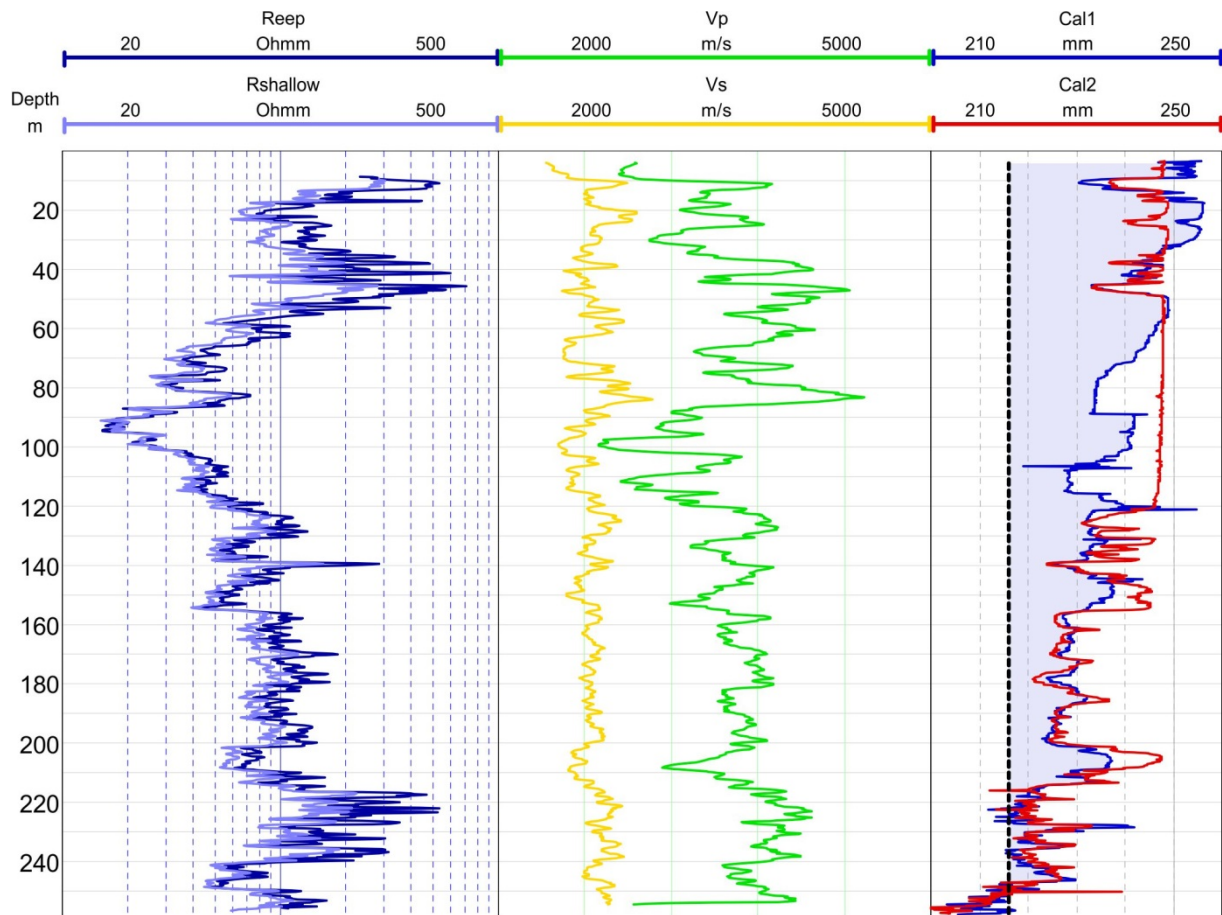
Figure D.1: Composite log showing resistivity, P- and S-wave velocity and caliper.
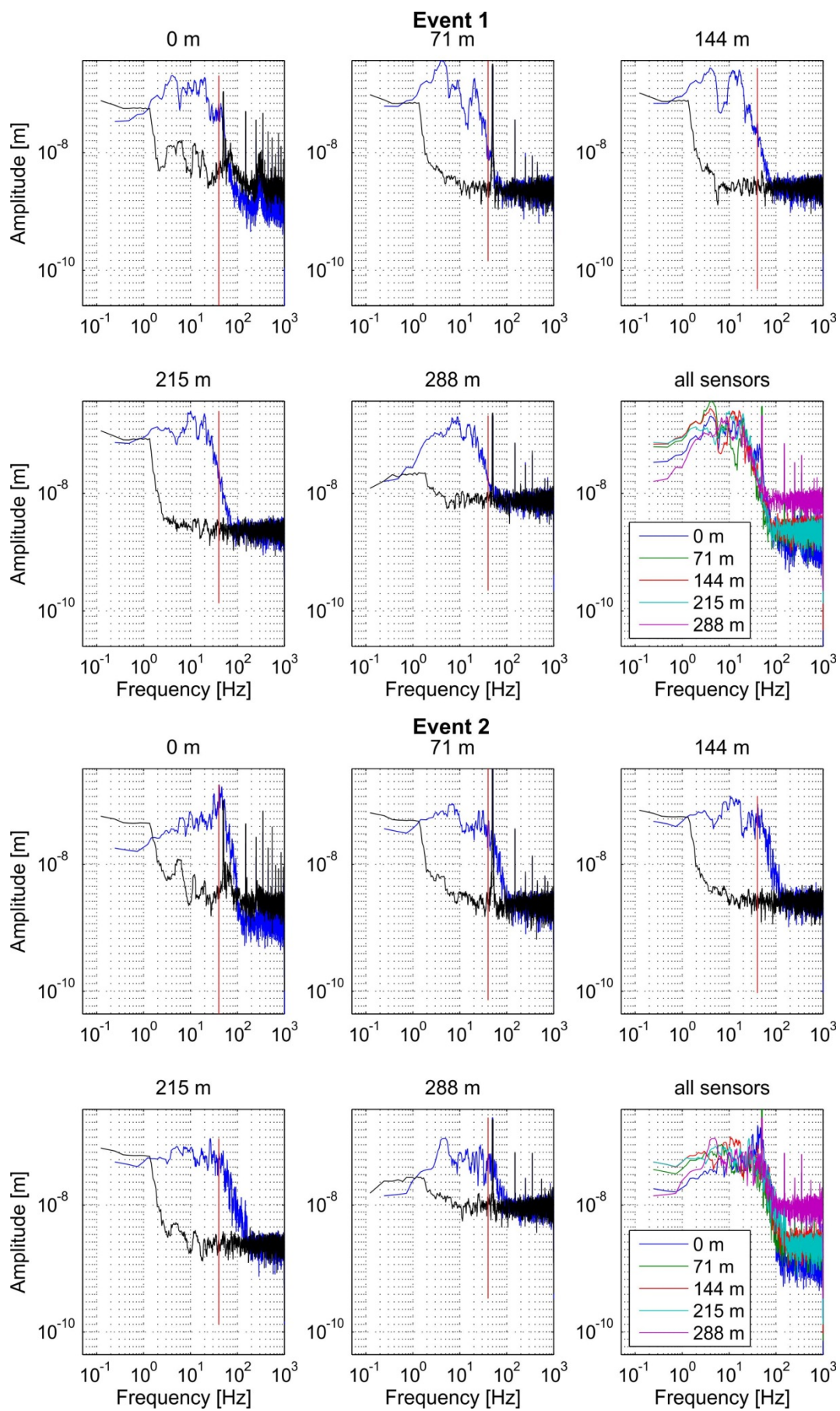
Figure D.2: Spectra of events 1 and 2.
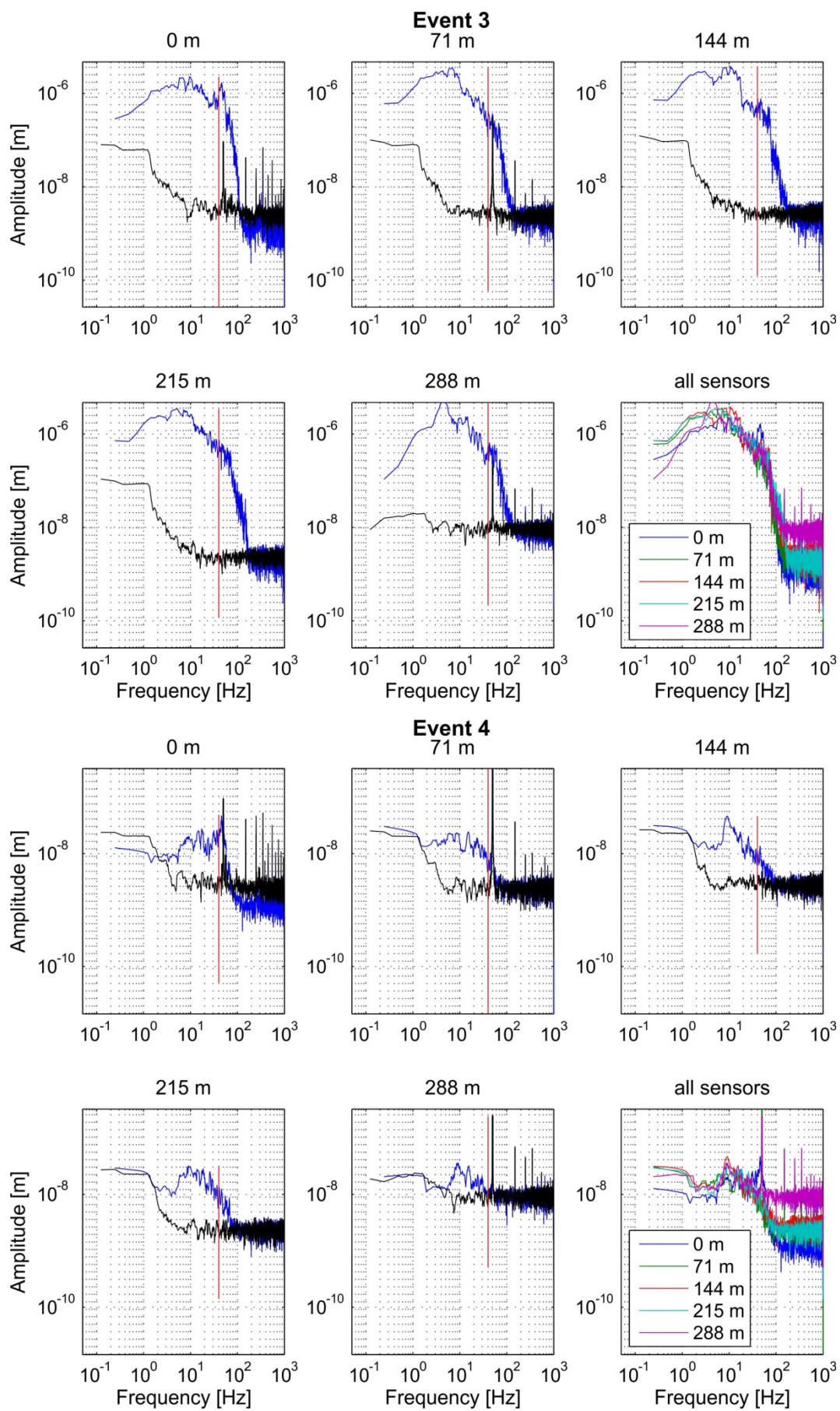
Figure D.3: Spectra of events 3 and 4.
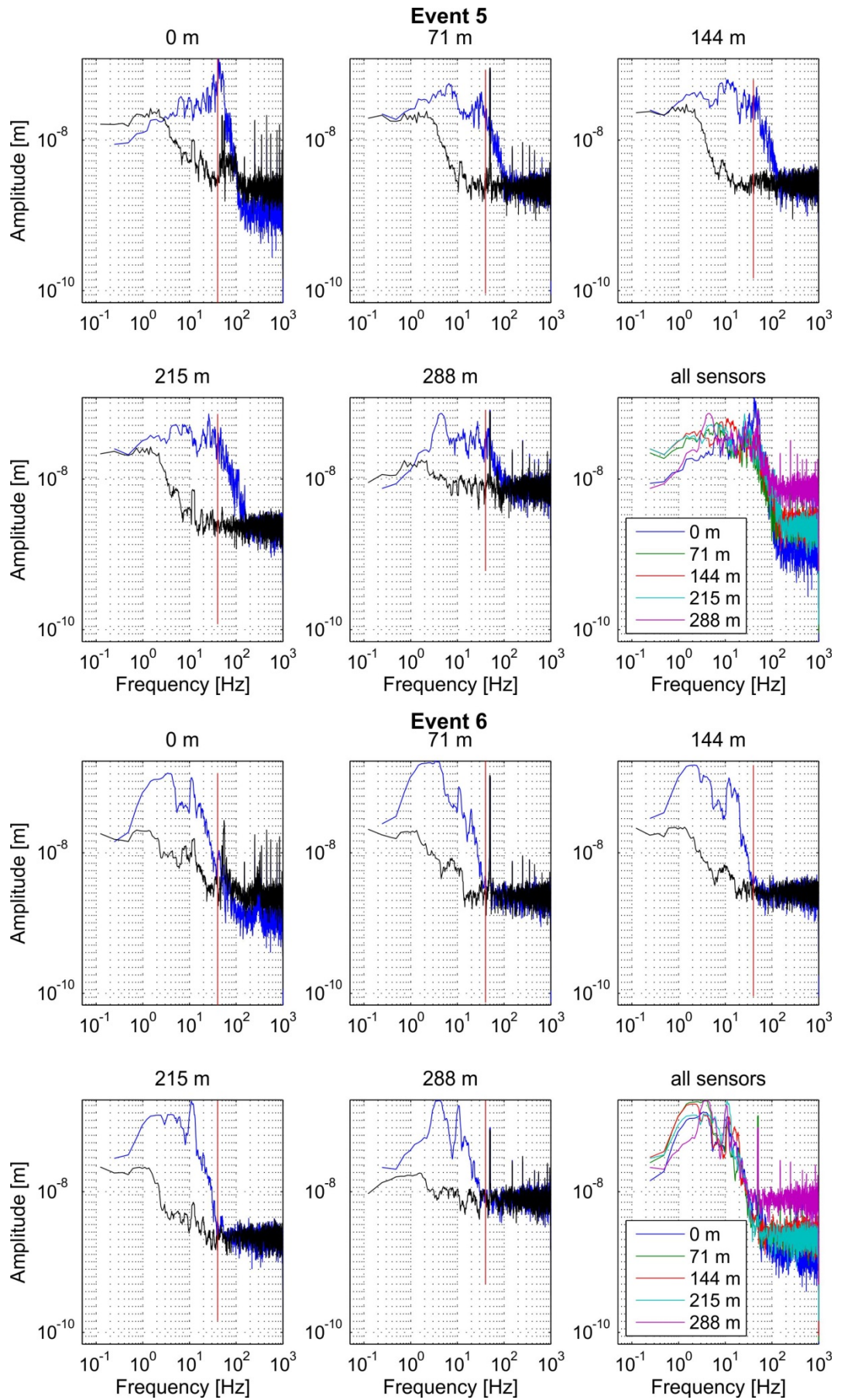
Figure D.4: Spectra of events 5 and 6.
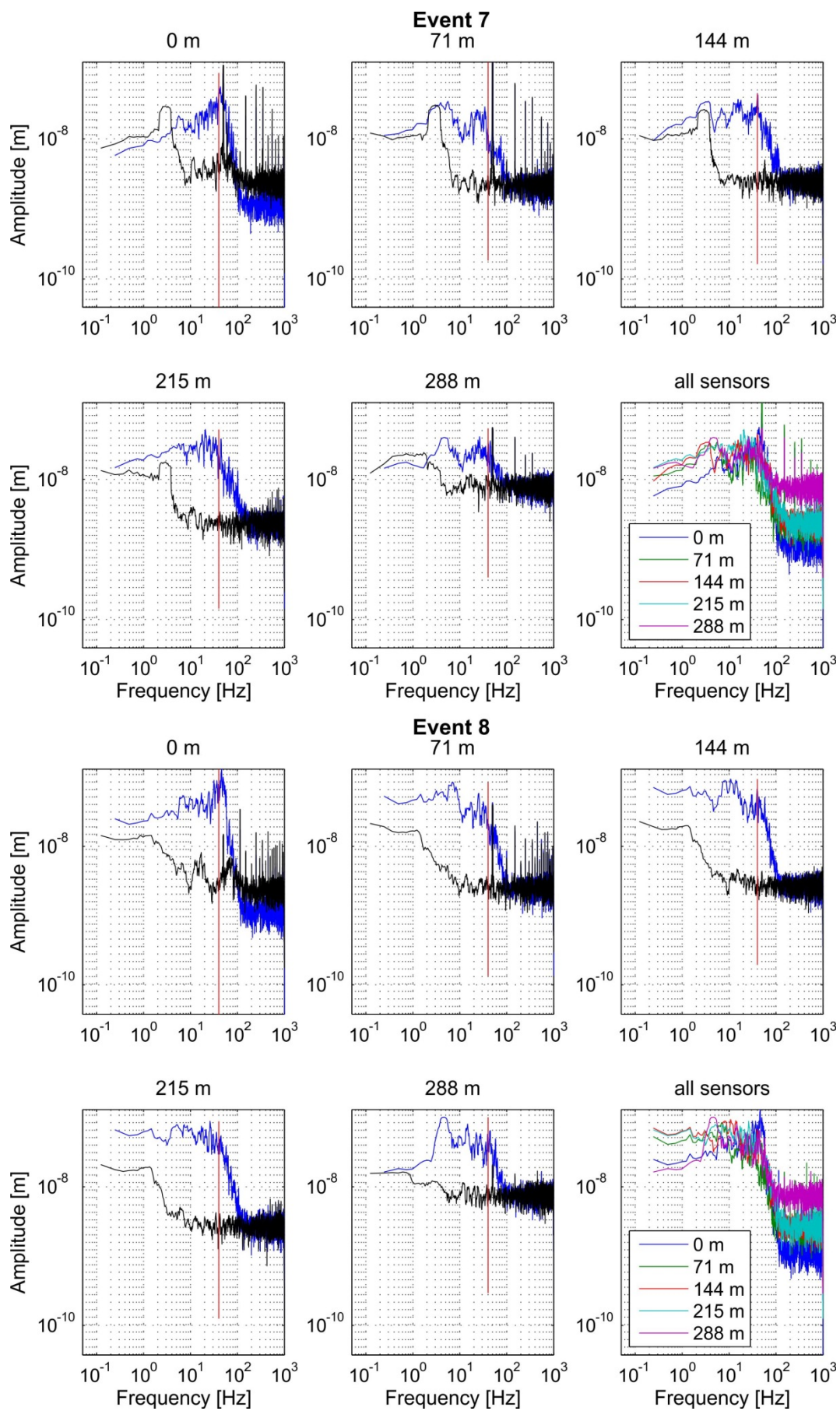
Figure D.5: Spectra of events 7 and 8.
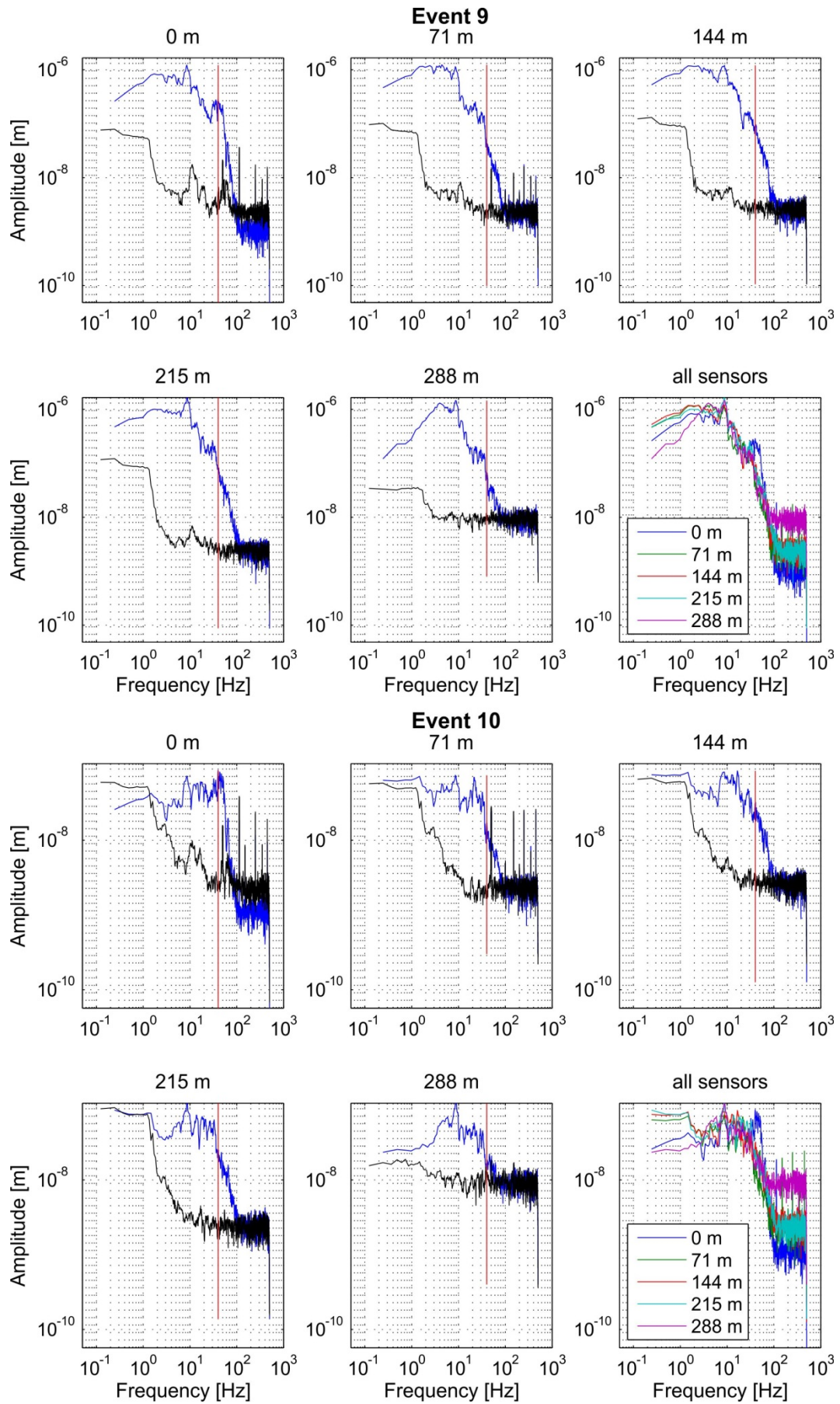
Figure D.6: Spectra of events 9 and 10.
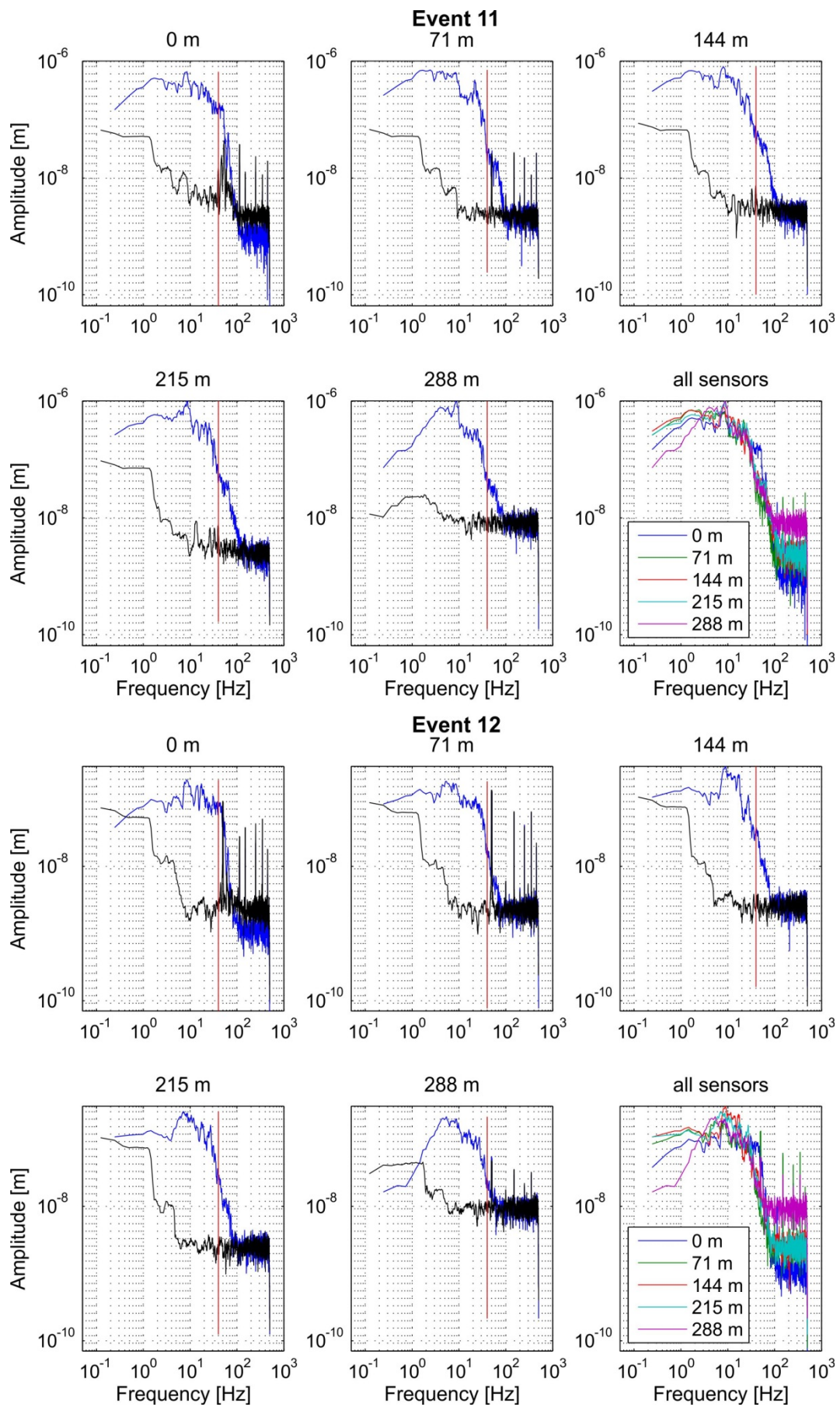
Figure D.7: Spectra of events 11 and 12.
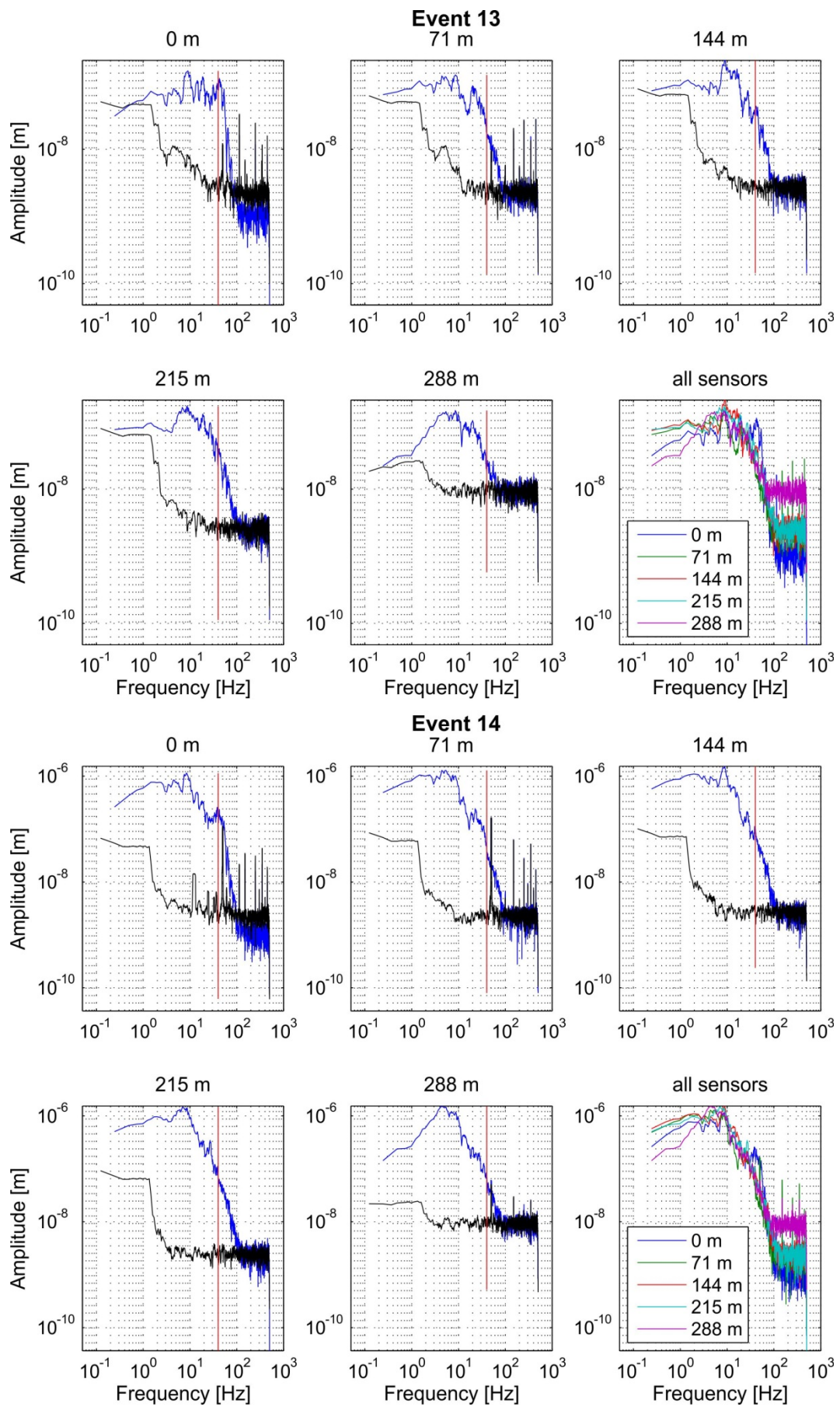
Figure D.8: Spectra of events 13 and 14.
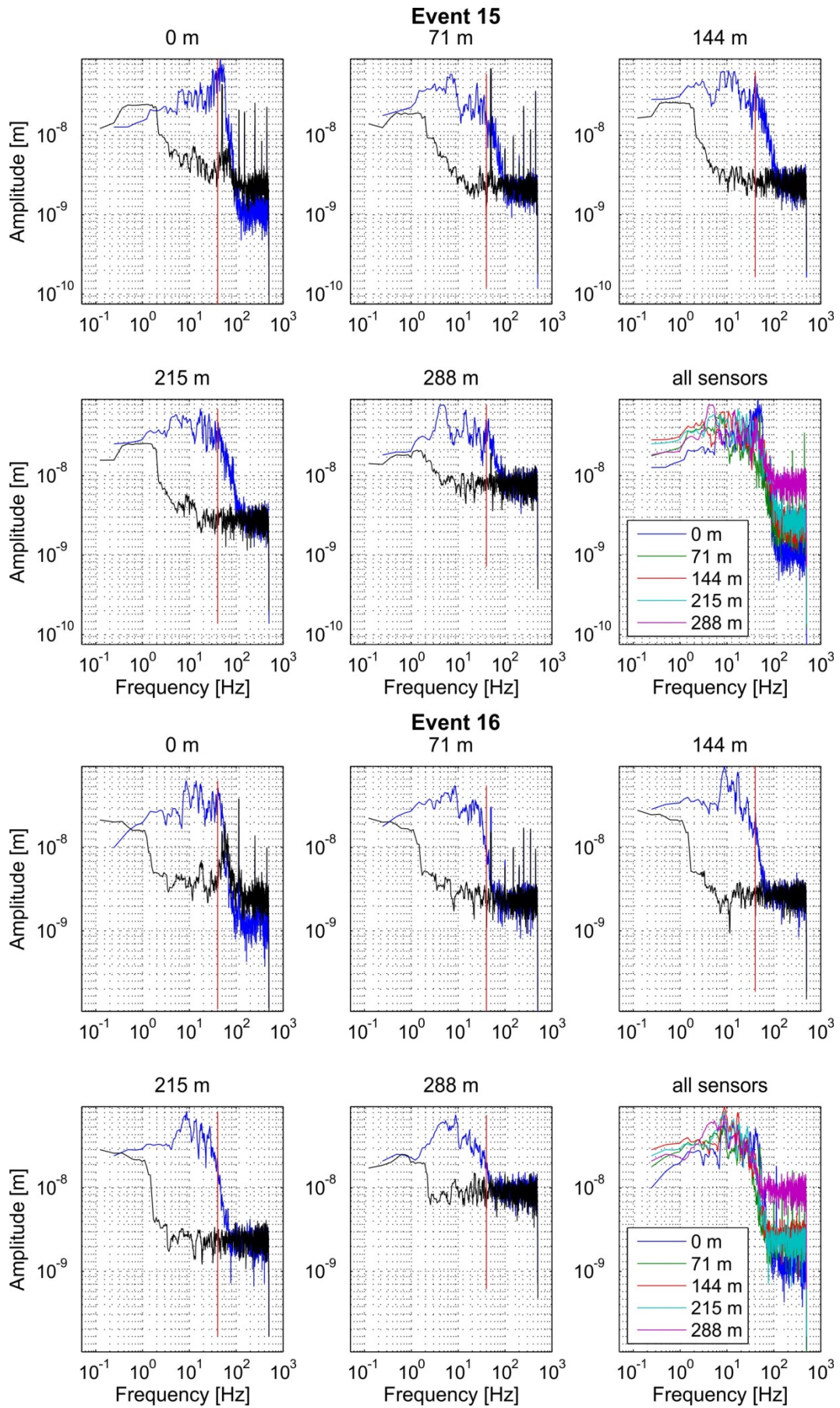
Figure D.9: Spectra of events 15 and 16.
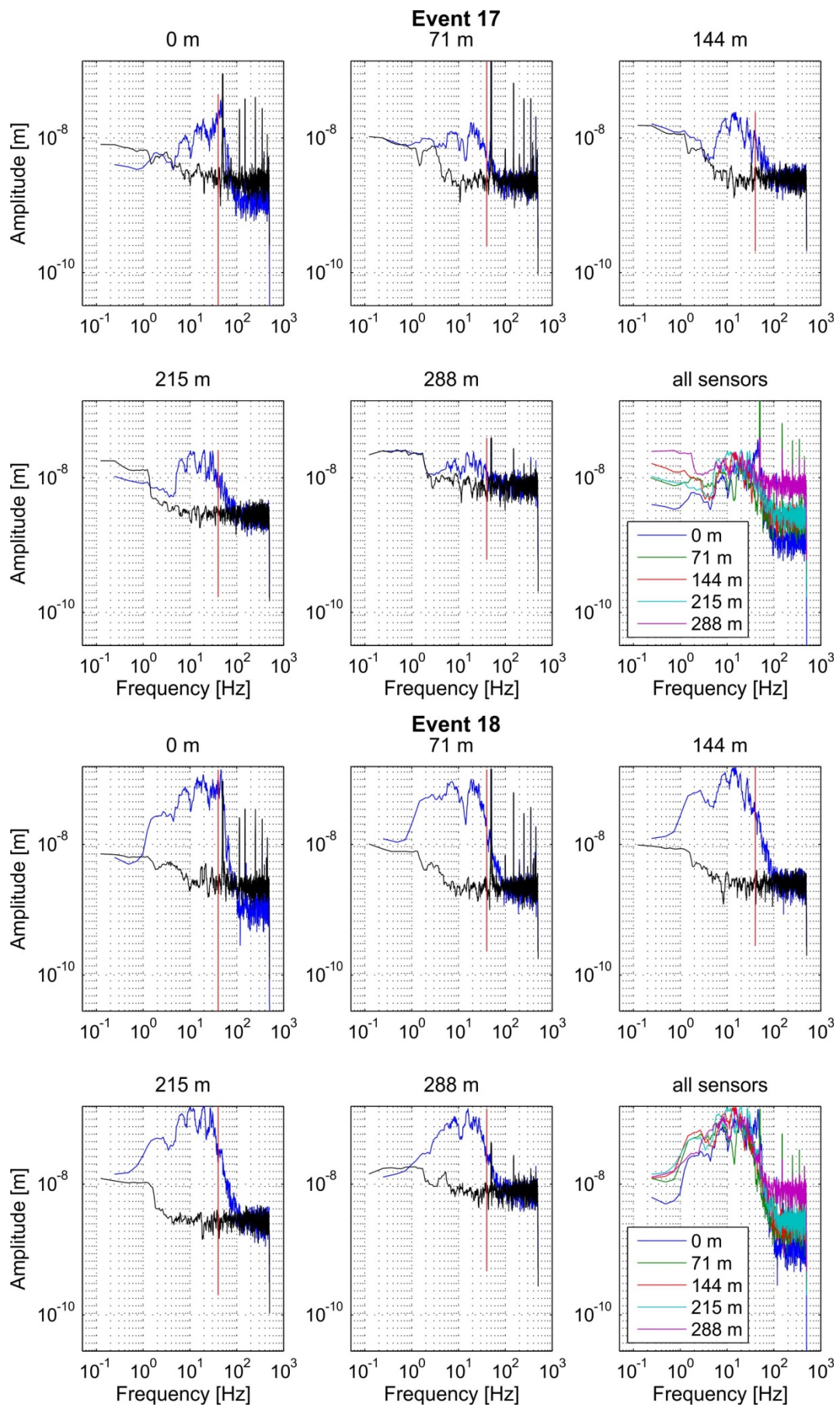
Figure D.10: Spectra of events 17 and 18.
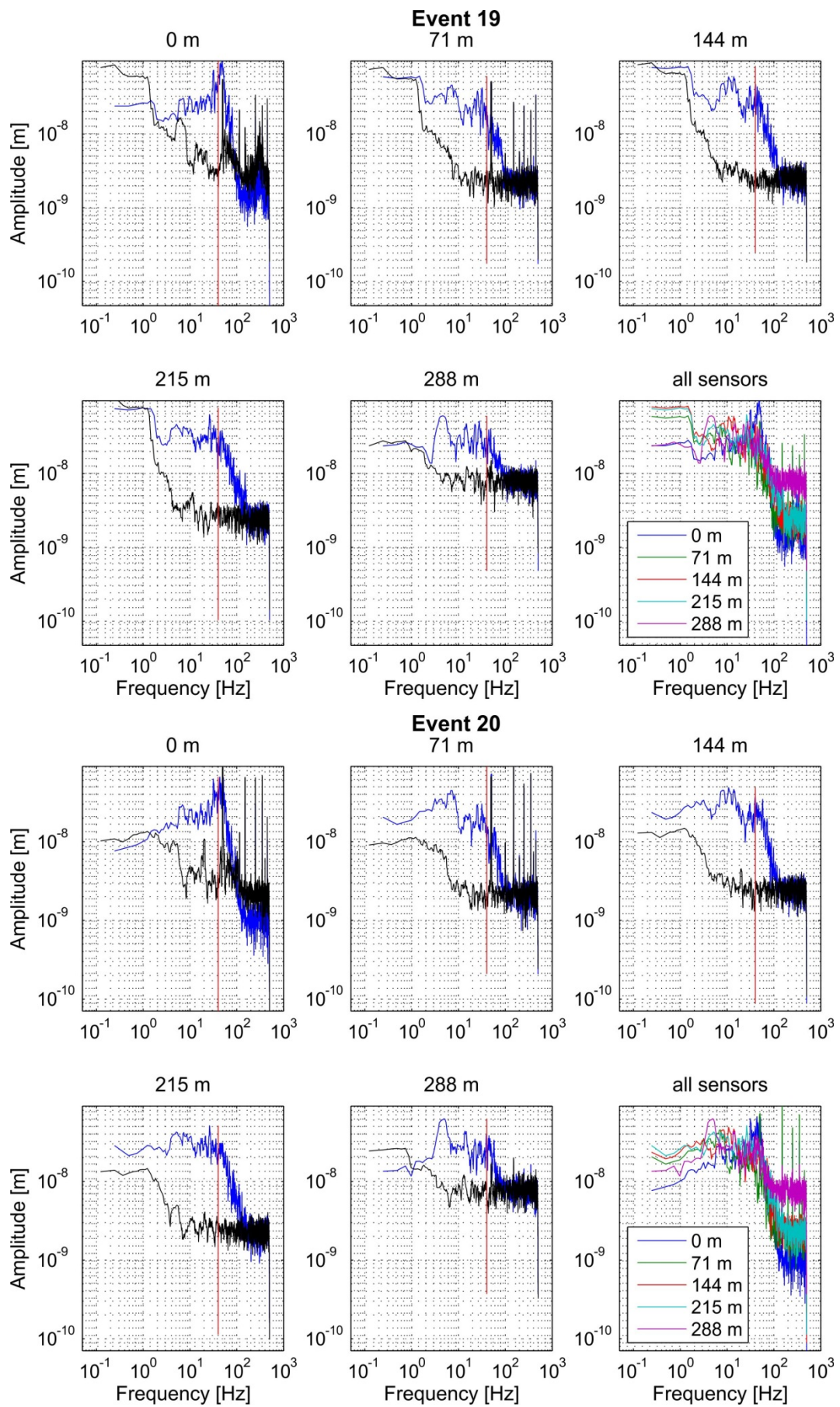
Figure D.11: Spectra of events 19 and 20.
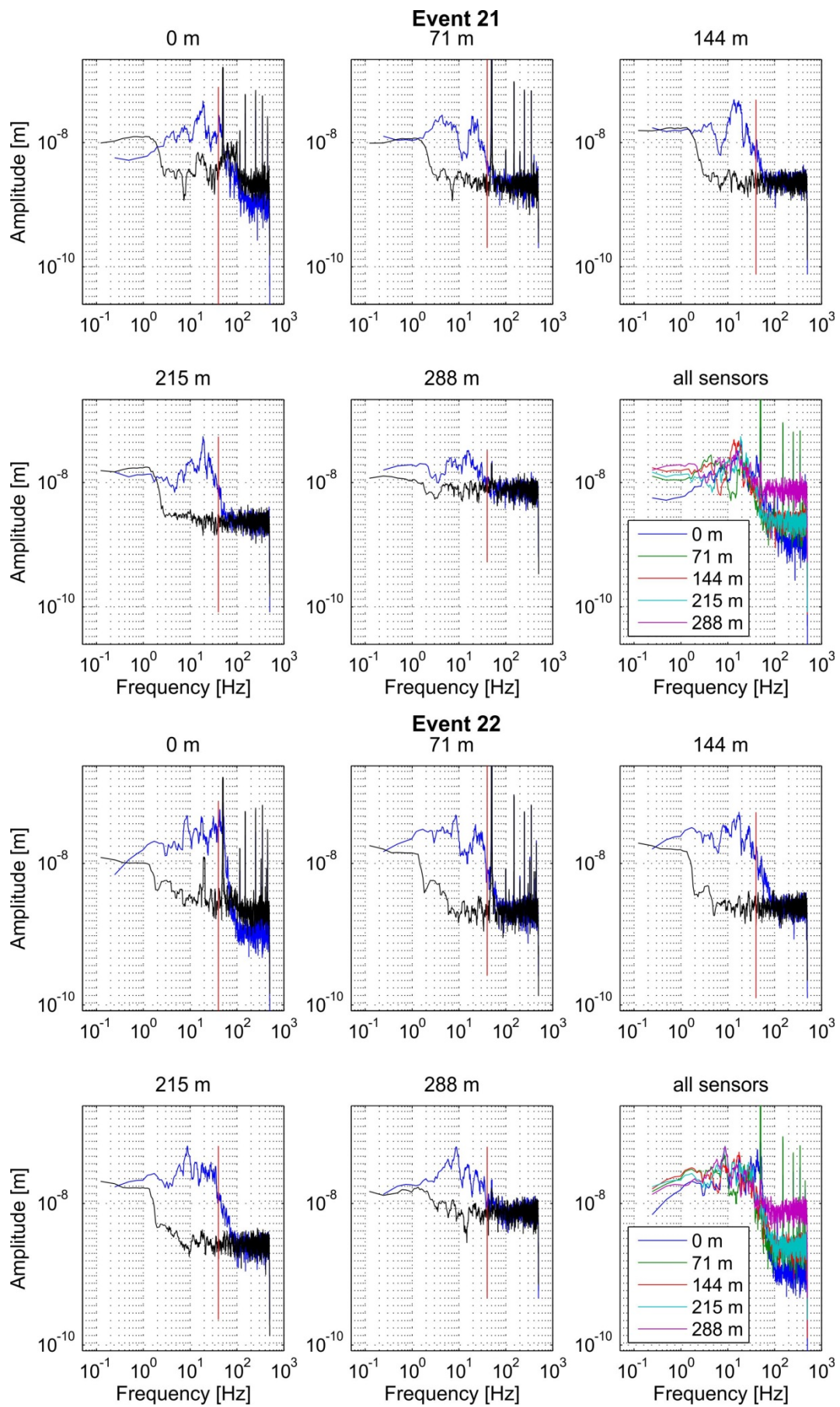
Figure D.12: Spectra of events 21 and 22.
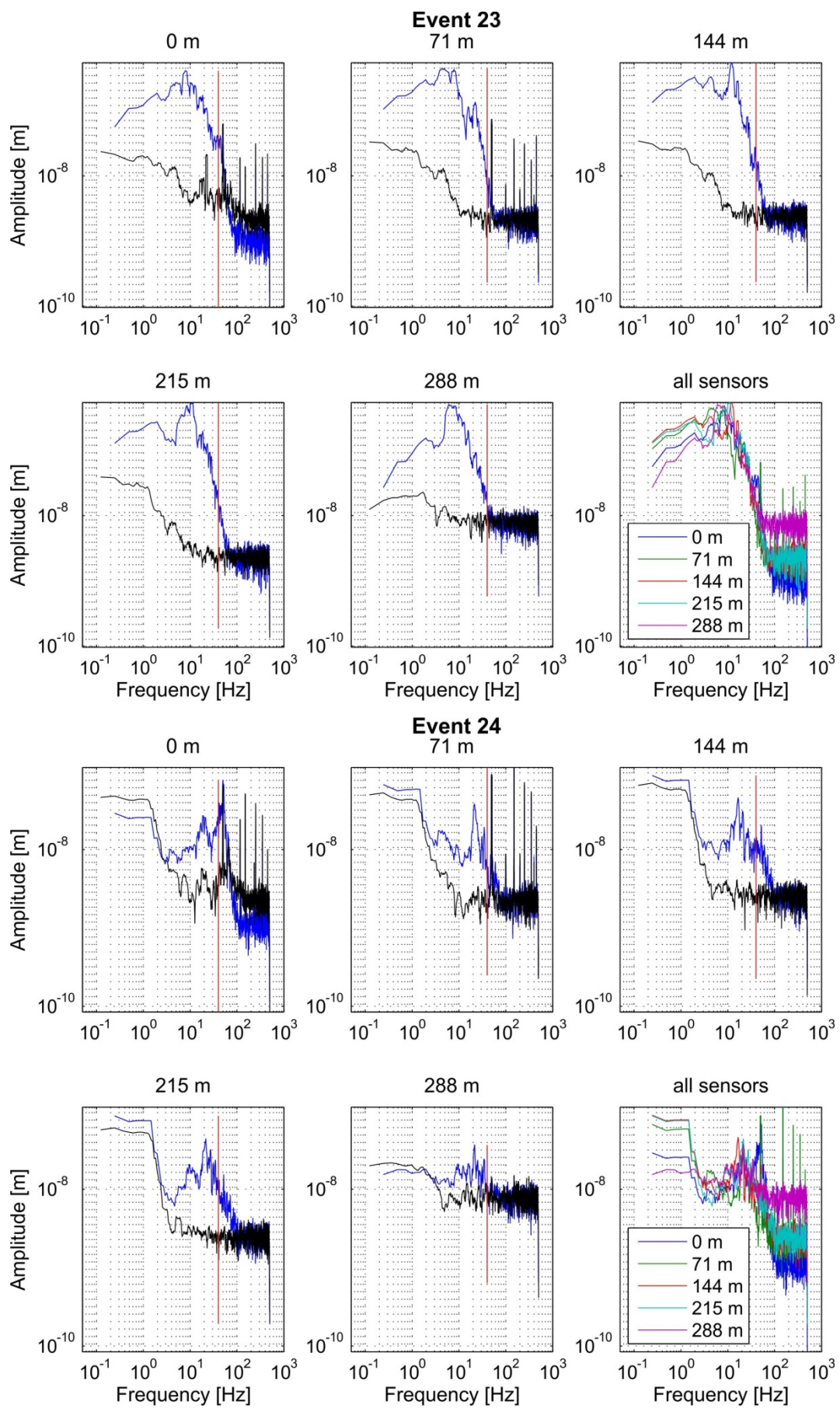
Figure D.13: Spectra of events 23 and 24.

107
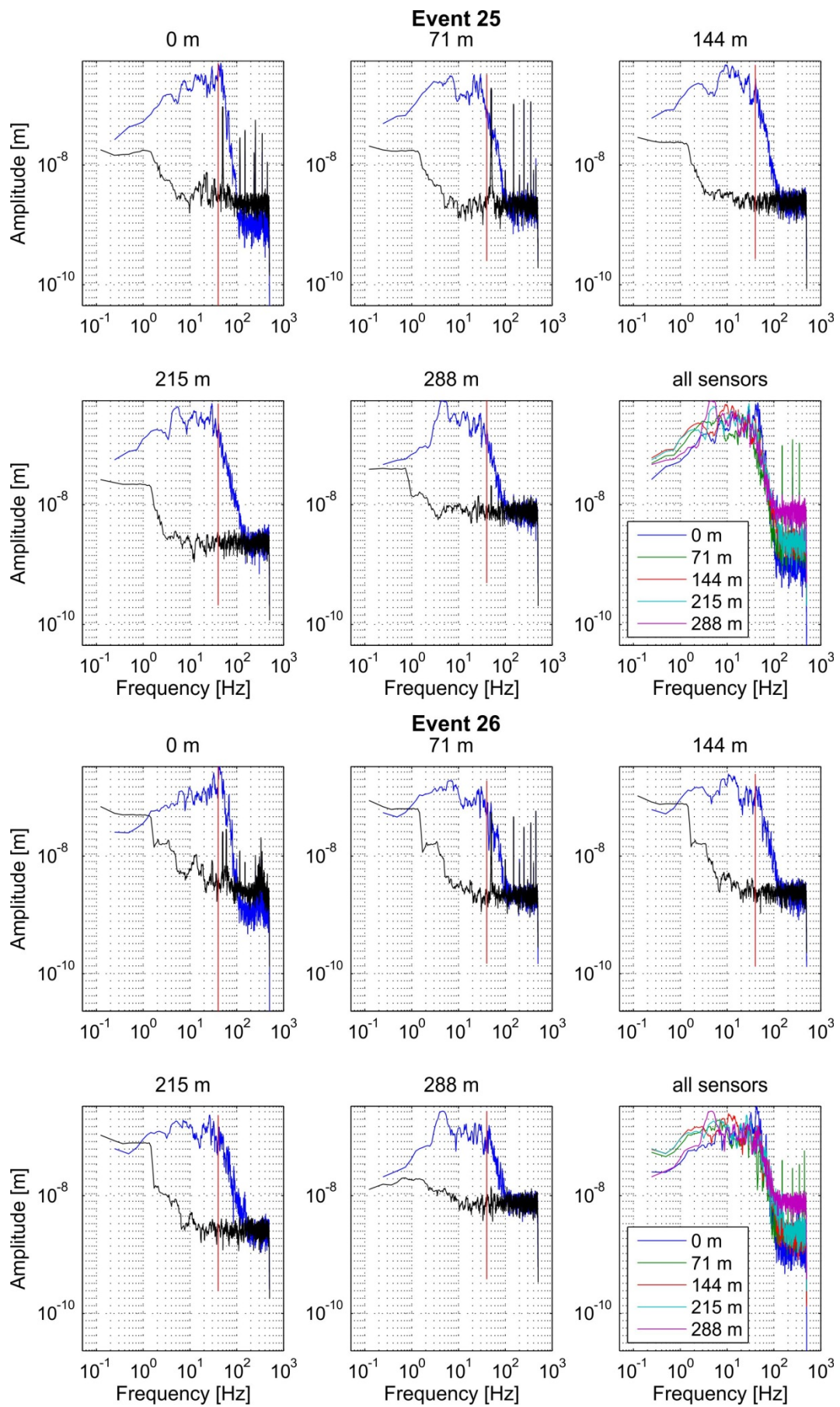
Figure D.14: Spectra of events 25 and 26.

References

Abercrombie, R. and P. Leary (1993). Source parameters of small earthquakes recorded at 2.5 km depth, Cajon Pass, southern California: Implications for earthquake scaling, *Geophys. Res. Lett.,* **20,** 1511-1514.

Aki, K. (1965). Maximum Likelihood Estimate of *b* in the Formula $\log N = a - bM$ and its Confidence Limits, *Bull. Earthq. Res. Inst.,, Univ. Tokyo,* **43,** 237-239.

Aki, K. and P. G. Richards (2002). *Quantitative Seismology: Theory and Methods,* W. H. Freeman and Company, New York.

Aktar, M., S. Özalaybey, M. Ergin, H. Karabulut, M.P. Bouin, C. Tapırdamaz, F. Biçmen, A. Yörük and M. Bouchon (2004). Spatial variation of aftershock activity across the rupture zone of the 17 August 1999 Izmit earthquake, Turkey, *Tectonophysics,* **391,** 325-334.

Akyüz, H.S., R. Hartleb, A. Barka, E. Altunel, G. Sunal, B. Meyer and R. Armijo (2002). Surface Rupture and Slip Distribution of the 12 November 1999 Düzce Earthquake (M 7.1), North Anatolian Fault, Bolu, Turkey, *Bull. Seism. Soc. Am,* **92,** 61-66.

Ambraseys, N.N. (1970). Some characteristic features of the Anatolian fault zone, *Tectonophysics,* **9,** 143-165.

Amitrano, D. (2003). Brittle-ductile transition and associated seismicity: Experimental and numerical studies and relationship with the b value, *J. Geophys. Res.,* **108,** 2044, doi:10.1029/2001JB000680, B1.

Amitrano, D. (2012). Variability in the power-law distributions of rupture events, *Eur. Phys. J. ST,* **205,** 199-215.

Amorèse, D., J.R. Grasso and P.A. Rydelek (2010). On varying b-values with depth: results from computer-intensive tests for Southern California, *Geophys. J. I.*, **180,** 347-360.

Andrews, D.J. (1986). Objective Determination of Source Parameters and Similarity of Earthquakes of Different Size. *in Earthquake Source Mechanics*, American Geophysical Union, 259-267.

Aochi, H. and T. Ulrich (2015). A probable earthquake scenario near Istanbul determined from dynamic simulations, *Bull. Seism. Soc. Am.,* **105,** 1468-1475.

Armijo, R., N. Pondard, B. Meyer, G. Uçarkus, B. M. de Lépinay, J. Malavieille, S. Dominguez, M.-A. Gustcher, S. Schmidt, C. Beck, N. Çagatay, Z. Çakir, C. Imren, K. Eris, B. Natalin, S. Özalaybey, L. Tolun, I. Lefèvre, L. Seeber, L. Gasperini, C. Rangin, O. Emre and K. Sarikavak (2005). Submarine fault scarps in the Sea of Marmara pull-apart (North Anatolian Fault): Implications for seismic hazard in Istanbul, *Geochem. Geophys.,* **6,** Q06009.

Assimaki, D., W. Li, J. H. Steidl and K. Tsuda (2008). Site Amplification and Attenuation via Downhole Array Seismogram Inversion: A Comparative Study of the 2003 Miyagi-Oki Aftershock Sequence, *Bull. Seism. Soc. Am.,* **98,** 301-330.

Bachmann, C.E., S. Wiemer, B.P. Goertz-Allmann and J. Woessner (2012). Influence of pore-pressure on the event-size distribution of induced earthquakes, *Geophys. Res. Lett.,* **39**.

Barka, A. A. (1992). The North Anatolian fault zone, *Ann. Tetonicae,* **6,** 164 - 195.

Barka, A., H. S. Akyüz, E. Altunel, G. Sunal, Z. Çakir, A. Dikbas, B. Yerli, R. Armijo, B. Meyer, J. B. de Chabalier, T. Rockwell, J. R. Dolan, R. Hartleb, T. Dawson, S. Christofferson, A. Tucker, T. Fumal, R. Langridge, H. Stenner, W. Lettis, J. Bachhuber and W. Page (2002). The Surface Rupture and Slip Distribution of the 17 August 1999 İzmit Earthquake (M 7.4), North Anatolian Fault, *Bull. Seism. Soc. Am.,* **92,** 43-60.

Baumbach, M., D. Bindi, H. Grosser, C. Milkereit, S. Parolai, R. Wang, S. Karakisa, S. Zünbül and J. Zschau (2003). Calibration of an ML Scale in Northwestern Turkey from 1999 Izmit Aftershocks, *Bull. Seism. Socc Am.,* **93,** 2289-2295.

Bender, B. (1983). Maximum likelihood estimation of *b* values for magnitude grouped data, *Bull. Seism. Soc. Am.,* **73,** 831-851.

Bethmann, F., N. Deichmann and P. M. Mai (2012). Seismic wave attenuation from borehole and surface records in the top 2.5 km beneath the city of Basel, Switzerland, *Geophys. J. Int.,* **190,** 1257-1270.

Bindi, D., S. Parolai, E. Görgün, H. Grosser, C. Milkereit, M. Bohnhoff and E. Durukal (2007). ML Scale in Northwestern Turkey from 1999 Izmit Aftershocks: Updates, *Bull. Seism. Soc. Am.,* **97,** 331-338.

Bindi, D., B. Petrovic, S. Karapetrou, M. Manakou, T. Boxberger, D. Raptakis, K. D. Pitilakis and S. Parolai (2015). Seismic response of an 8-story RC-building from ambient vibration analysis, *Bull. Earthq. Eng.,* **13,** 2095-2120.

Blakeslee, S. and P. Malin (1991). High-frequency site effects at two Parkfield downhole and surface stations, *Bull. Seism. Soc. Am.,* **81,** 332-345.

Bohnhoff, M., H.-P. Harjes and T. Meier (2005). Deformation and stress regimes in the Hellenic subduction zone from focal Mechanisms, *J. Seismol.,* **9,** 341-366.

Bohnhoff, M., H. Grosser and G. Dresen (2006). Strain partitioning and stress rotation at the North Anatolian fault zone from aftershock focal mechanisms of the 1999 Izmit Mw= 7.4 earthquake, *Geophys. J. Int.* **166,** 373-385.

Bohnhoff, M., F. Bulut, G. Dresen, P. E. Malin, T. Eken and M. Aktar (2013). An earthquake gap south of Istanbul, *Nat. Commun.,* **4**.

Bohnhoff, M., P. Martínez-Garzón, F. Bulut, E. Stierle and Y. Ben-Zion (2016a). Maximum earthquake magnitudes along different sections of the North Anatolian fault zone, *Tectonophysics,* **674,** 147-165.

Bohnhoff, M., M. Ickrath and G. Dresen (2016b). Seismicity distribution in conjunction with spatiotemporal variations of coseismic slip and postseismic creep along the combined 1999 Izmit-Düzce rupture, *Tectonophysics,* **686,** 132-145.

Bohnhoff, M., G. Dresen, U. Ceken, F.T. Kadirioglu, R.F. Kartal, T. Kilic, M. Nurlu, K. Yanik, D. Acarel, F. Bulut, H. Ito, W. Johnson, P.E. Malin and D. Mencin (submitted to *Scientific drilling*). GONAF - A borehole Geophysical Observatory around the North Anatolian Fault in the Eastern Sea of Marmara

Bouchon, M., M.N. Toksöz, H. Karabulut, M.-P. Bouin, M. Dietrich, M. Aktar and M. Edie (2002). Space and Time Evolution of Rupture and Faulting during the 1999 İzmit (Turkey) Earthquake, *Bull. Seism. Soc. Am.,* **92,** 256-266.

Bouin, M.P., M. Bouchon, H. Karabulut and M. Aktar (2004). Rupture process of the 1999 November 12 Düzce (Turkey) earthquake deduced from strong motion and Global Positioning System measurements, *Geophys. J. Int.,* **159,** 207-211.

Brace, W.F. and J.D. Byerlee (1966). Stick-Slip as a Mechanism for Earthquakes. *Science,* **153**(3739), 990–992.

Brune, J.N. (1970). Tectonic stress and the spectra of seismic shear waves from earthquakes, *J. Geophys. Res.,* **75,** 4997-5009.

Bulut, F., M. Bohnhoff, M. Aktar and G. Dresen (2007). Characterization of aftershock-fault plane orientations of the 1999 İzmit (Turkey) earthquake using high-resolution aftershock locations, *Geophyis. Res. Lett.,* **34,** L20306.

Bulut, F., M. Bohnhoff, W. L. Ellsworth, M. Aktar and G. Dresen (2009). Microseismicity at the North Anatolian Fault in the Sea of Marmara offshore Istanbul, NW Turkey, *J. Geophys. Res.,* **114,** B09302.

Bulut, F., W. L. Ellsworth, M. Bohnhoff, M. Aktar and G. Dresen (2011). Spatiotemporal Earthquake Clusters along the North Anatolian Fault Zone Offshore İstanbul, *Bull. Seism. Soc. Am.,* **101**, 1759-1768.

Bulut, F., Y. Ben-Zion and M. Bohnhoff (2012). Evidence for a bimaterial interface along the Mudurnu segment of the North Anatolian Fault Zone from polarization analysis of P waves, *Earth Planet. Sci. Lett.,* 327–328, 17-22.

Bourry, C., B. Bertrand Chazallon, J.-L. Charlou, J.-P. Donval, L. Ruffin, P. Henry, L. Geli, M.N. Cagatay, S. Iˈnan and M. Moreau (2009), Free gas and gas hydrates from the Sea of Marmara, Turkey: chemical and structural characterization, *Chem. Geol.,* **264**(1–4), 197–206.

Carton, H., S.C Singh, A. Hirn, S. Bazin, B. de Voogd, A. Vigner, A. Ricolleau, S. Cetin, N. Ocakoglu, F. Karakoç and V. Sevilgen, (2007). Seismic imaging of the three-dimensional architecture of the Çınarcık Basin along the North Anatolian Fault, *J. Geophys. Res.,* **112**, B06101, doi:10.1029/2006JB004548.

Cornell, C.A. (1968). Engineering seismic risk analysis, *Bull. Seism. Soc. Am.,* **58,** 1583-1606.

Cosentino, P., V. Ficarra and D. Luzio (1977). Truncated exponential frequency-magnitude relationship in earthquake statistics, *Bull. Seism. Soc. Am.,* **67,** 1615-1623.

Curtis, A., P. Gerstoft, H. Sato, R. Snieder and K. Wapenaar (2006). Seismic interferometry - turning noise into signal, *The Leading Edge,* **25,** 1082-1092.

Delouis, B., D. Giardini, P. Lundgren and J. Salichon (2002). Joint Inversion of InSAR, GPS, Teleseismic, and Strong-Motion Data for the Spatial and Temporal Distribution of Earthquake Slip: Application to the 1999 İzmit Mainshock, *Bull. Seism. Soc. Am.,* **92,** 278-299.

Dey-Sarkar, S. K. and R. A. Wiggins (1976). Source deconvolution of teleseismic P wave arrivals between 14° and 40°, *J. Geophys. Res.,* **81,** 3633-3641.

Di Giacomo, D., M.R. Gallipoli, M. Mucciarelli, S. Parolai, and S.M. Richwalski (2005). Analysis and Modeling of HVSR in the Presence of a Velocity Inversion: The Case of Venosa, Italy, *Bull. Seism. Soc. Am.,* **95,** 2364-2372.

Dix, C. H. (1955). Seismic velocities from surface measurements, *Geophysics,* **20,** 68-86.

Eken, T., M. Bohnhoff, F. Bulut, B. Can and M. Aktar (2013). Crustal Anisotropy in the Eastern Sea of Marmara Region in Northwestern Turkey, *Bull. Seism. Soc. Am.,* **103,** 911-924.

El-Isa, Z.H. and D.W. Eaton (2014). Spatiotemporal variations in the b-value of earthquake magnitude–frequency distributions: Classification and causes, *Tectonophysics,* 615–616, 1-11.

Erdik, M., M. Demircioglu, K. Sesetyan, E. Durukal and B. Siyahi (2004). Earthquake hazard in Marmara Region, Turkey, *Soil Dyn. Earthq. Eng.,* **24,** 605-631.

Ergintav, S., R. E. Reilinger, R. Çakmak, M. Floyd, Z. Cakir, U. Doğan, R. W. King, S. McClusky and H. Özener (2014). Istanbul's earthquake hot spots: Geodetic constraints on strain accumulation along faults in the Marmara seismic gap, *Geophys. Res. Lett.,* **41,** 5783-5788.

Flerit, F., R. Armijo, G. King and B. Meyer (2004). The mechanical interaction between the propagating North Anatolian Fault and the back-arc extension in the Aegean, *Earth Planet. Sci. Lett.,* **224,** 347-362.

Frankel, A. (1995). Mapping Seismic Hazard in the Central and Eastern United States, *Seismol. Res. Lett.,* **66,** 8-21.

Frohlich, C. and S.D. Davis (1993). Teleseismic b values; Or, much ado about 1.0, *J. Geophys. Res.,* **98,** 631-644.

Gallipoli, M.R. and M. Mucciarelli (2009). Comparison of Site Classification from VS30, VS10, and HVSR in Italy, *Bull. Seism. Soc. Am.,* **99,** 340-351.

Ge, J., J. Pujol, S. Pezeshk ans S. Stovall (2009). Determination of Shallow Shear-Wave Attenuation in the Mississippi Embayment Using Vertical Seismic Profiling Data, *Bull. Seism. Soc. Am.,* **99,** 1636-1649.

Geli, L., 21 co-authors and the Marnaut Scientific Party (2008). Gas emissions and active tectonics within the submerged section of the North Anatolian Fault zone in the Sea of Marmara, *Earth Planet. Sci. Lett.,* **274,** 34–39.

Gibbs, J. F., D. M. Boore, W. B. Joyner and T. E. Fumal (1994). The attenuation of seismic shear waves in quaternary alluvium in Santa Clara Valley, California, *Bull. Seism. Soc. Am.,* **84,** 76-90.

Gibowicz, S.J. and A. Kijko (1994). *An Introduction to Mining Seismology*, Vol. 55 of International geophysics series, Academic Press.

Goebel, T.H., D. Schorlemmer, T.W. Becker, G. Dresen and C.G. Sammis (2013). Acoustic emissions document stress changes over many seismic cycles in stick-slip experiments, *Geophys. Res. Lett.,* **40,** 2049-2054.

Görgün, E., A. Zang, M. Bohnhoff, C. Milkereit and G. Dresen (2009). Analysis of Izmit aftershocks 25 days before the November 12th 1999 Düzce earthquake, Turkey, *Tectonophysics,* **474,** 507-515.

Gulia, L., T. Tormann, S. Wiemer, M. Herrmann and S. Seif (2016). Short-term probabilistic earthquake risk assessment considering time-dependent b values, *Geophys. Res. Lett.,* **43,** 2015GL066686.

Gündüz, H., K.-Ö. Ayşe, B.-G. Aysun and T. Niyazi (1998). S-wave attenuation in the Marmara Region, northwestern Turkey, *Geophys. Res. Lett.,* **25,** 2733-2736.

Gutenberg, B. and C.F. Richter (1944). Frequency of earthquakes in California, *Bull. Seism. Soc. Am.,* **34,** 185-188.

Hanks, T.C. and H. Kanamori (1979). A moment magnitude scale, *J. of Geophys. Res.,* **84,** 2348-2350.

Hardebeck, J.L. (2012). Coseismic and postseismic stress rotations due to great subduction zone earthquakes, *Geophys. Res. Lett.,* **39,** L21313.

Hartleb, R.D., J.F. Dolan, H.S. Akyüz, T.E. Dawson, A.Z. Tucker, B. Yerli, T.K. Rockwell, E. Toraman, Z. Çakir, A. Dikbaş and E. Altunel (2002). Surface Rupture and Slip Distribution along the Karadere Segment of the 17 August 1999 İzmit and the Western Section of the 12 November 1999 Düzce, Turkey, Earthquakes, *Bull. Seism. Soc. Am.,* **92,** 67-78.

Haskell, N.A. (1953). The dispersion of surface waves on multilayered media, *Bull. Seism. Soc. Am.,* **43,** 17-34.

Hauksson, E., T.-L. Teng and T. L. Henyey (1987). Results from a 1500 m deep, three-level downhole seismometer array: Site response, low Q values, and fmax, *Bull. Seism. Soc. Am.,* **77,** 1883-1904.

Helmberger, D. and R. A. Wiggins (1971). Upper mantle structure of midwestern United States, *J. Geophys. Res.,* **76,** 3229-3245.

Henderson, J., I.G. Main, R.G. Pearce and M. Takeya (1994). Seismicity in north-eastern Brazil: fractal clustering and the evolution of the b value, *Geophys. J. Int.,* **116,** 217-226.

Hirata, T. (1989). A correlation between the b value and the fractal dimension of earthquakes, *J. Geophys. Res.*, **94,** 7507-7514.

Hubert-Ferrari, A., A. Barka, E. Jacques, S. S. Nalbant, B. Meyer, R. Armijo, P. Tapponnier and G. C. P. King (2000). Seismic hazard in the Marmara Sea region following the 17 August 1999 Izmit earthquake, *Nature,* **404,** 269-273.

Hurd, O. and M. Bohnhoff (2012). Stress and Structural-Induced Shear-Wave Anisotropy Along the 1999 Izmit Rupture, Northwest Turkey, *Bull. Seismol. Soc. Am.,* **102**(5), 2177-2188.

Ickrath, M., M. Bohnhoff, F. Bulut and G. Dresen (2014). Stress rotation and recovery in conjunction with the 1999 Izmit Mw 7.4 earthquake, *Geophys. J. Int.*, **196,** 951-956.

Ickrath, M., M. Bohnhoff, G. Dresen, P. Martínez-Garzón, F. Bulut, G. Kwiatek and O. Germer (2015). Detailed analysis of spatiotemporal variations of the stress field orientation along the Izmit-Düzce rupture in NW Turkey from inversion of first-motion polarity data, *Geophys. J. Int.,* **202,** 2120-2132.

Ishimoto, M. and Iida, K. (1939). Observations of earthquakes registered with the microseismograph constructed recently. *Bull. Earthq. Res. Inst. Tokyo*, **17,** 443–478.

Kagan, Y.Y. (1997), Seismic Moment-frequency Relation for Shallow Earthquakes: Regional Comparison, *J. Geophys. Res.,* **102,** 2835–2852.

Kagan, Y.Y. (1999). Universality of the Seismic Moment-frequency Relation, *Pure Appl. Geophys.,* **155,** 537-573.

Kalkan, E., P. Gülkan, N.Y. Öztürk, and M. Çelebı (2008). Seismic Hazard in the Istanbul Metropolitan Area: A Preliminary Re-Evaluation, *J. Earthquake Eng.,* **12,** 151-164.

Kanlı, A.I., P. Tildy, Z. Prónay, A. Pınar and I. Hermann (2006). VS30 mapping and soil classification for seismic site effect evaluation in Dinar region, SW Turkey, *Geophys. J. Int.,* **165,** 223-235.

Karabulut, H., M.-P. Bouin, M. Bouchon, M. Dietrich, C. Cornou and M. Aktar (2002). The Seismicity in the Eastern Marmara Sea after the 17 August 1999 İzmit Earthquake, *Bull. Seism. Soc. Am.,* **92,** 387-393.

Karabulut, H., J. Schmittbuhl, S. Özalaybey, O. Lengliné, A. Kömeç-Mutlu, V. Durand, M. Bouchon, G. Daniel and M.P. Bouin (2011). Evolution of the seismicity in the eastern Marmara Sea a decade before and after the 17 August 1999 Izmit earthquake, *Tectonophysics,* **510,** 17-27.

Kaya, T., T. Kasaya, S.B. Tank, Y. Ogawa, M.K. Tunçer, N. Oshiman, Y. Honkura and M. Matsushima (2013). Electrical characterization of the North Anatolian Fault Zone underneath the Marmara Sea, Turkey by ocean bottom magnetotellurics, *Geophys. J. Int.,* **193,** 664-677.

King, G.C.P., A. Hubert-Ferrari, S.S. Nalbant, B. Meyer, R. Armijo and D. Bowman (2001). Coulomb interactions and the 17 August 1999 Izmit, Turkey earthquake, *Earth Planet. Sci.,* **333,** 557-569.

Kiratzi, A. A. (2002). Stress tensor inversions along the westernmost North Anatolian Fault Zone and its continuation into the North Aegean Sea, *Geophys. J. Int.,* **151,** 360-376.

Korkusuz Öztürk, Y., N. Meral Özel and A.D. Özbakir (2015). States of local stresses in the Sea of Marmara through the analysis of large numbers of small earthquakes, *Tectonophysics,* **665,** 37-57.

Lasocki, S. and E.E. Papadimitriou (2006). Magnitude distribution complexity revealed in seismicity from Greece, *J. Geophys. Res.,* **111,** B11309, doi:10.1029/2005JB003794.

Lay, T. and H. Kanamori (1981). An Asperity Model of Large Earthquake Sequences. *in Earthquake Prediction*, pp. 579-592, American Geophysical Union.

Leary, P. C. and F. Al-Kindy (2002). Power-law scaling of spatially correlated porosity and log(permeability) sequences from north-central North Sea Brae oilfield well core, *Geophys. J. Int.,* **148,** 426-442.

Le Pichon, X., A.M.C. Şengör, J. Kende, C. İmren, P. Henry, C. Grall and H. Karabulut (2015). Propagation of a strike-slip plate boundary within an extensional environment: the westward propagation of the North Anatolian Fault, *Can. J. Earth Sci.,* **53,** 1416-1439.

Lienert, B. R., E. Berg and L. N. Frazer (1986). HYPOCENTER: An earthquake location method using centered, scaled, and adaptively damped least squares, *Bull. Seism. Soc. Am.,* **76,** 771-783.

López Casado, C., C. Sanz de Galdeano, J. Delgado and M.A. Peinado (1995). The b parameter in the Betic Cordillera, Rif and nearby sectors. Relations with the tectonics of the region, *Tectonophysics,* **248,** 277-292.

Malin, P. E., J. A. Waller, R. D. Borcherdt, E. Cranswick, E. G. Jensen and J. V. Schaack (1988). Vertical seismic profiling of Oroville microearthquakes: Velocity spectra and particle motion as a function of depth, *Bull. Seism. Soc. Am.,* **78,** 401-420.

Marzocchi, W. & Sandri, L., 2003. A review and new insights on the estimation of the b-valueand its uncertainty, *Ann. of Geophys.,* **46,** 1271-1282.

McClusky, S., S. Balassanian, A. Barka, C. Demir, S. Ergintav, I. Georgiev, O. Gurkan, M. Hamburger, K. Hurst, H. Kahle, K. Kastens, G. Kekelidze, R. King, V. Kotzev, O. Lenk, S. Mahmoud, A. Mishin, M. Nadariya, A. Ouzounis, D. Paradissis, Y. Peter, M. Prilepin, R. Reilinger, I. Sanli, H. Seeger, A. Tealeb, M. N. Toksöz and G. Veis (2000). Global Positioning System constraints on plate kinematics and dynamics in the eastern Mediterranean and Caucasus, *J. Geophys. Res.,* **105,** 5695-5719.

Mehta, K., R. Snieder and V. Graizer (2007). Extraction of near-surface properties for a lossy layered medium using the propagator matrix, *Geophys. J. Int.,* **169,** 271-280.

Meredith, P.G., I.G. Main and C. Jones (1990). Temporal variations in seismicity during quasi-static and dynamic rock failure, *Tectonophysics,* **175,** 249-268.

Milkereit, C., S. Zünbül, S. Karakisa, Y. Iravul, J. Zschau, M. Baumbach, H. Grosser, E. Günther, N. Umutlu and T. Kuru (2000). Preliminary aftershock analysis of the Mw = 7.4 Izmit and Mw = 7.1 Düzce earthquake in western Turkey, in *The 1999 Izmit and Düzce Earthquakes: Preliminary Results,* pp. 179–187, edited by Kozaci, Ö and A. Barka, Istanbul Technical University.

Mogi, K. (1962). Magnitude-frequency relations for elastic shocks accompanying fractures of various materials and some related problems in earthquakes, *Bull. Earthquake Res. Inst. Univ. Tokyo,* **40,** 831–853.

Najdahmadi, B., M. Bohnhoff and Y. Ben-Zion (2016). Bimaterial interfaces at the Karadere segment of the North Anatolian Fault, northwestern Turkey, *J. Geophys. Res.,* **121,** 931-950.

Nakata, N. and R. Snieder (2012). Estimating near-surface shear wave velocities in Japan by applying seismic interferometry to KiK-net data, *J. Geophys. Res.,* **117,** B01308.

Oglesby, D.D. and P.M. Mai (2012). Fault geometry, rupture dynamics and ground motion from potential earthquakes on the North Anatolian Fault under the Sea of Marmara, *Geophys. J. Int.,* **188,** 1071-1087.

Öncel, A.O. and M. Wyss (2000). The major asperities of the 1999 Mw = 7.4 Izmit earthquake defined by the microseismicity of the two decades before it, *Geophys. J. Int.,* **143,** 501-506.

Örgülü, G. and M. Aktar (2001). Regional moment tensor inversion for strong aftershocks of the August 17, 1999 Izmit Earthquake (Mw=7.4), *Geophys. Res. Lett.,* **28,** 371-374.

Özalaybey, S., M. Ergin, M. Aktar, C. Tapirdamaz, F. Biçmen and A. Yörük (2002). The 1999 İzmit Earthquake Sequence in Turkey: Seismological and Tectonic Aspects, *Bull. Seism. Soc. Am.,* **92,** 376-386.

Özgül, N. (2012). Stratigraphy and Some Structural Features of the İstanbul Palaeozoic, *Turkish J. Earth Sci.,* **21,** 817–866.

Pace, B., L. Peruzza, G. Lavecchia and P. Boncio (2006). Layered Seismogenic Source Model and Probabilistic Seismic-Hazard Analyses in Central Italy, *Bull. Seism. Soc. Am.,* **96,** 107-132.

Page, R. (1968). Aftershocks and microaftershocks of the great Alaska earthquake of 1964, *Bull. Seism. Soc. Am.,* **58,** 1131-1168.

Parolai, S., M. Mucciarelli, M. R. Gallipoli, S. M. Richwalski and A. Strollo (2007). Comparison of Empirical and Numerical Site Responses at the Tito Test Site, Southern Italy, *Bull. Seism. Soc. Am.,* **97,** 1413-1431.

Parolai, S., A. Ansal, A. Kurtulus, A. Strollo, R. Wang and J. Zschau (2009). The Ataköy vertical array (Turkey): insights into seismic wave propagation in the shallow-most crustal layers by waveform deconvolution, *Geophys. J. Int.,* **178,** 1649-1662.

Parolai, S., D. Bindi, A. Ansal, A. Kurtulus, A. Strollo and J. Zschau (2010). Determination of shallow S-wave attenuation by down-hole waveform deconvolution: a case study in Istanbul (Turkey), *Geophys. J. Int.,* **181,** 1147-1158.

Parolai, S., R. Wang and D. Bindi (2012). Inversion of borehole weak motion records observed in Istanbul (Turkey), *Geophys. J. Int.,* **188,** 535-548.

Parsons, T., S. Toda, R.S. Stein, A. Barka and J.H. Dieterich (2000). Heightened Odds of Large Earthquakes Near Istanbul: An Interaction-Based Probability Calculation, *Science,* **288,** 661-665.

Parsons, T. (2004). Recalculated probability of M ≥ 7 earthquakes beneath the Sea of Marmara, Turkey, *J. Geophys. Res.,* **109**.

Pfister, M., L. Rybach S. Simsek (1998). Geothermal reconnaissance of the Marmara Sea region (NW Turkey): surface heat flow density in an area of active continental extension, *Tectonophysics,* **291,** 77-89.

Pickering, G., J.M. Bull and D.J. Sanderson (1995). Sampling power-law distributions, *Tectonophysics,* **248,** 1-20.

Prevedel, B., F. Bulut, M. Bohnhoff, C. Raub, R. Kartal, F. Alver and P. Malin (2015). Downhole geophysical observatories: best installation practices and a case history from Turkey, *Int. J. Earth. Sci. (Geol. Rundsch.)*, 1-11.

Pucci, S., D. Pantosti, M.R. Barchi and N. Palyvos (2007). A complex seismogenic shear zone: The Düzce segment of North Anatolian Fault (Turkey), *Earth Planet. Sci. Lett.,* **262,** 185-203.

Pulido, N., A. Ojeda, K. Atakan and T. Kubo (2004). Strong ground motion estimation in the Sea of Marmara region (Turkey) based on a scenario earthquake, *Tectonophysics,* **391,** 357-374.

Reilinger, R.E., S. Ergintav, R. Bürgmann, S. McClusky, O. Lenk, A. Barka, O. Gurkan, L. Hearn, K.L. Feigl, R. Cakmak, B. Aktug, H. Ozener and M.N. Töksoz (2000). Coseismic and Postseismic Fault Slip for the 17 August 1999, M = 7.5, Izmit, Turkey Earthquake, *Science,* **289,** 1519-1524.

Şafak, E. (1997). Models and methods to characterize site amplification from a pair of records, *Earthq. Spectra,* **13,** 97-129.

Schmittbuhl, J., H. Karabulut, O. Lengliné and M. Bouchon (2015). Seismicity distribution and locking depth along the Main Marmara Fault, Turkey, *Geochem. Geophys.,* 17, 954-965.

Scholz, C.H. (1968). The frequency-magnitude relation of microfracturing in rock and its relation to earthquakes, *Bull. Seism. Soc. Am.,* **58,** 399-415.

Scholz, C.H. (2015). On the stress dependence of the earthquake b value, *Geophys. Res. Lett.,* **42,** 1399-1402.

Schorlemmer, D., G. Neri, S. Wiemer and A Mostaccio (2003). Stability and significance tests for b-value anomalies: Example from the Tyrrhenian Sea, *Geophys. Res. Lett.,* **30,** 1835, doi:10.1029/2003GL017335.

Schorlemmer, D., S. Wiemer and M. Wyss (2004a). Earthquake statistics at Parkfield: 1. Stationarity of b values, *J. Geophys. Res.,* **109,** B12307, doi:10.1029/2004JB003234.

Schorlemmer, D., S. Wiemer, M. Wyss and D.D. Jackson (2004b). Earthquake statistics at Parkfield: 2. Probabilistic forecasting and testing, *J. Geophys. Res.,* **109,** B12308, doi:10.1029/2004JB003235.

Schorlemmer, D., S. Wiemer and M. Wyss (2005). Variations in earthquake-size distribution across different stress regimes, *Nature,* **437,** 539-542.

Schurr, B., G. Asch, S. Hainzl, J. Bedford, A. Hoechner, M., Palo, R. Wang, M. Moreno, M. Bartsch, Y. Zhang, O. Oncken, F. Tilmann, T. Dahm, V. Victor, S. Barrientos and J.-P. Vilotte (2014). Gradual unlocking of plate boundary controlled initiation of the 2014 Iquique earthquake, *Nature,* **512,** 299-302.

Schwartz, D.P. and K.J. Coppersmith (1984). Fault behavior and characteristic earthquakes: Examples from the Wasatch and San Andreas Fault Zones, *J. Geophys. Res.,* **89,** 5681-5698.

Şengör, A.M.C., O. Tüysüz, C. İmren, M. Sakınç, H. Eyidoğan, N. Görür, X.L. Pichon and C. Rangin (2005). The North Anatolian Fault: a new look, *Annu. Rev. Earth and Planet. Sci.,* **33,** 37-112.

Shearer, P. M. and J. A. Orcutt (1987). Surface and near-surface effects on seismic waves - theory and borehole seismometer results, *Bull. Seism. Soc. Am.,* **77,** 1168-1196.

Shi, Y. and B.A. Bolt (1982). The standard error of the magnitude-frequency b value, *Bull. Seism. Soc. Am.,* **72,** 1677-1687.

Shiomi, K., H. Sato and M. Ohtake (1997). Broad-band power-law spectra of well-log data in Japan, *Geophys. J. Int.,* **130,** 57-64.

Silva, M. B. C. and A. Stovas (2009). Comparison of averaging methods for velocity model building from well logs, *J. Geophys. Eng.,* **6,** 172.

Sleep, N.H. and B.A. Erickson (2014). Nonlinear attenuation of S-waves and Love waves within ambient rock, *Geochem. Geophys.,* **15,** 1419-1440.

Snieder, R. and E. Şafak (2006). Extracting the Building Response Using Seismic Interferometry: Theory and Application to the Millikan Library in Pasadena, California, *Bull. Seism. Soc. Am.,* **96,** 586-598.

Snoke, J.A. (1987). Stable determination of (Brune) stress drops, *Bull. Seism. Soc. Am.,* **77,** 530-538.

Sobiesiak, M., U. Meyer, S. Schmidt, H.J. Götze and C.M. Krawczyk (2007). Asperity generating upper crustal sources revealed by *b* value and isostatic residual anomaly grids in the area of Antofagasta, Chile, *J. Geophys. Res.,* 112, B12308, doi:10.1029/2006JB004796.

Sørensen, M.B., I. Oprsal, S. Bonnefoy-Claudet, K. Atakan, P.M. Mai, N. Pulido and C. Yalciner (2006). Local site effects in Ataköy, Istanbul, Turkey, due to a future large earthquake in the Marmara Sea, *Geophys. J. Int.,* **167,** 1413-1424.

Sørensen, M.B., N. Pulido and K. Atakan (2007). Sensitivity of Ground-Motion Simulations to Earthquake Source Parameters: A Case Study for Istanbul, Turkey, *Bull. Seism. Soc. Am.,* **97,** 881-900.

Spada, M., T. Tormann, S. Wiemer and B. Enescu (2013). Generic dependence of the frequency-size distribution of earthquakes on depth and its relation to the strength profile of the crust, *Geophys. Res. Lett.,* **40,** 709-714.

Steidl, J.H., A.G. Tumarkin and R.J. Archuleta (1996). What is a reference site?, *Bull. Seism. Soc. Am.,* **86,** 1733-1748.

Steidl, J.H. (2000). Site Response in Southern California for Probabilitistic Seismic Hazard Analysis. *Bull. Seism. Soc. Am.*, **90,** 149-169.

Stein, R.S., A.A. Barka and J.H. Dieterich (1997). Progressive failure on the North Anatolian fault since 1939 by earthquake stress triggering, *Geophys. J. Int.,* **128,** 594-604.

Stein, S. and M. Wysession (2003). *An Introduction to Seismology, Earthquakes, and Earth Structure*, Blackwell Publishing.

Stierle, E., M. Bohnhoff and V. Vavryčuk (2014). Resolution of non-double-couple components in the seismic moment tensor using regional networks - II: application to aftershocks of the 1999 Mw 7.4 Izmit earthquake, *Geophys. J. Int.,* **196,** 1878-1888.

Thomson, W.T. (1950). Transmission of Elastic Waves through a Stratified Solid Medium, *J. Appl. Phys.,* **21,** 89-93.

Tibi, R., G. Bock, Y. Xia, M. Baumbach, H. Grosser, C. Milkereit, S. Karakisa, S. Zünbül, R. Kind and J. Zschau (2001). Rupture processes of the 1999 August 17 Izmit and November 12 Düzce (Turkey) earthquakes, *Geophys. J. Int.,* **144,** F1-F7.

Toksöz, M.N., A.F. Shakal and A.J. Michael (1979). Space-time migration of earthquakes along the North Anatolian fault zone and seismic gaps, *Pure Appl. Geoph.,* **117,** 1258-1270.

Tonn, R. (1991). The determination of the seismic quality factor Q from VSP data: a comparison of different computational methods, *Geophys. Prospect.,* **39,** 1-27.

Tormann, T., B. Enescu, J. Woessner and S. Wiemer (2015). Randomness of megathrust earthquakes implied by rapid stress recovery after the Japan earthquake, *Nature Geosci.,* **8,** 152-158.

Trampert, J., M. Cara and M. Frogneux (1993). SH Propagator Matrix and Qs Estimates From Borehole- and Surface-Recorded Earthquake Data, *Geophys. J. Int.,* **112,** 290-299.

Triep, E.G. and L.R. Sykes (1997). Frequency of occurrence of moderate to great earthquakes in intracontinental regions: Implications for changes in stress, earthquake prediction, and hazards assessments, *J. Geophys. Res.,* **102,** 9923-9948.

Urban, P., S. Lasocki, P. Blascheck, A.F. do Nascimento, N. Van Giang and G. Kwiatek (2016). Violations of Gutenberg–Richter Relation in Anthropogenic Seismicity, *Pure Appl. Geophys.,* **173,** 1517-1537.

Utsu, T. (1965). A method for determining the value of b in a formula $\log n = ba - M$ showing the magnitude-frequency relation for earthquakes (with English summary), *Geophys. Bull. Hokkaido Univ.,* **13,** 99-103.

Vasconcelos, I. and R. Snieder (2008a). Interferometry by deconvolution: Part 1 - Theory for acoustic waves and numerical examples, *Geophysics,* **73,** S115-S128.

Vasconcelos, I. and R. Snieder (2008b). Interferometry by deconvolution: Part 2 - Theory for elastic waves and application to drill-bit seismic imaging, *Geophysics,* **73,** S129-S141.

van Vossen, R. v., J. Trampert and A. Curtis (2004). Propagator and wave-equation inversion for near-receiver material properties, *Geophys. J. Int.,* **157,** 796-812.

Vorobieva, I., P. Shebalin and C. Narteau (2016). Break of slope in earthquake size distribution and creep rate along the San Andreas Fault system, *Geophys. Res. Lett.,* 43, 6869-6875.

Wang, L., S. Hainzl, M. Sinan Özeren and Y. Ben-Zion (2010). Postseismic deformation induced by brittle rock damage of aftershocks, *J. Geophys. Res.,* **115,** B10422, doi:10.1029/2010JB007532.

Wang, R. (1999). A simple orthonormalization method for stable and efficient computation of Green's functions, *Bull. Seism. Soc. Am.,* **89,** 733-741.

Westerhaus, M., M. Wyss, R. Yilmaz and J. Zschau (2002). Correlating variations of b values and crustal deformations during the 1990s may have pinpointed the rupture initiation of the Mw = 7.4 Izmit earthquake of 1999 August 17, *Geophys. J. Int.,* **148,** 139-152.

Wiemer, S. and K. Katsumata (1999). Spatial variability of seismicity parameters in aftershock zones, *J. Geophys. Res.*, **104,** 13135-13151.

Wiemer, S. and S.R. McNutt (1997). Variations in the frequency-magnitude distribution with depth in two volcanic areas: Mount St. Helens, Washington, and Mt. Spurr, Alaska, *Geophys. Res. Lett.*, **24,** 189-192.

Wiemer, S. and M. Wyss (1997). Mapping the frequency-magnitude distribution in asperities: An improved technique to calculate recurrence times?, *J. Geophys. Res.,* **102,** 15115-15128.

Wiemer, S. and M. Wyss (2000). Minimum Magnitude of Completeness in Earthquake Catalogs: Examples from Alaska, the Western United States, and Japan, *Bull. Seism. Soc. Am.,* **90,** 859-869.

Wiemer, S. and M. Wyss (2002). Mapping spatial variability of the frequency-magnitude distribution of earthquakes, *Adv Geophys.,* **45,** 259-302.

Wiemer, S., D. Giardini, D. Fäh, N. Deichmann and S. Sellami (2009). Probabilistic seismic hazard assessment of Switzerland: best estimates and uncertainties, *J. Seismol.,* **13,** 449-478.

Woessner, J. and S. Wiemer (2005). Assessing the Quality of Earthquake Catalogues: Estimating the Magnitude of Completeness and Its Uncertainty, *Bull. Seism. Soc. Am.,* **95,** 684-698.

Wright, T., E. Fielding and B. Parsons (2001). Triggered slip: Observations of the 17 August 1999 Izmit (Turkey) Earthquake using radar interferometry, *Geophys. Res. Lett.,* **28,** 1079-1082.

Wyss, M. (2001). Locked and creeping patches along the Hayward Fault, California, Geophys. Res. Lett., **28,** 3537–3540, doi:10.1029/2001GL013499.

Wyss, M., D. Schorlemmer and S. Wiemer (2000). Mapping asperities by minima of local recurrence time: San Jacinto-Elsinore fault zones, *J. Geophys. Res.,* **105,** 7829-7844.

Youngs, R.R. and K.J. Coppersmith (1985). Implications of fault slip rates and earthquake recurrence models to probabilistic seismic hazard estimates, *Bull. Seism. Soc. Am.,* **75,** 939-964.

Zoback, M.D. and J. Townend (2001). Implications of hydrostatic pore pressures and high crustal strength for the deformation of intraplate lithosphere, *Tectonophysics,* **336,** 19-30.

Acknowledgements